

A Global 86 GHz VLBI Survey of Compact Radio Sources

Dissertation

zur

Erlangung des Doktorgrades (Dr. rer. nat.)

der

Mathematisch-Naturwissenschaftlichen Fakultät

der

Rheinischen Friedrich-Wilhelms-Universität Bonn

vorgelegt von

Sang-Sung Lee

aus

Daegu, Korea

Bonn, 2007

Angefertigt mit Genehmigung der Mathematisch-Naturwissenschaftlichen Fakultät
der Rheinischen Friedrich-Wilhelms-Universität Bonn

1. Referant: Prof. Dr. Uli Klein

2. Referant: Priv.-Doz. Dr. Huchtmeier

Tag der Promotion: 31.10.2007

Diese Dissertaion ist auf dem Hochschulschriftenserver der ULB Bonn
(http://hss.ulb.uni-bonn.de/diss_online) elektronisch publiziert.

To Jae-Chun and Solhee.

A Global 86 GHz VLBI Survey of Compact Radio Sources

Abstract

Studies of compact radio sources since the discovery of quasars have revealed a variety of physical properties: both in morphology and kinematics from sub-parsec to Mega-parsec scales, radiation mechanisms at frequencies from the radio to γ -rays, theoretical models for relativistic jets, etc. The frontier discovery of VLBI observations for the compact extragalactic radio sources have triggered the extensive studies to investigate the underlying physics of the relativistic jets. In this context, the highest resolution VLBI surveys of ultra-compact radio sources provides the potentially important statistical basis for future study.

We present results from a large global VLBI survey of compact radio sources at 86 GHz. The main goal of the survey is to increase the total number of objects accessible for future 3-mm VLBI imaging by factors of 3–5. The survey observations reach the baseline sensitivity of 0.1 Jy and image sensitivity of better than 10 mJy/beam. The total of 127 compact radio sources have been observed. The observations have yielded images for 109 sources, extending the database of the sources imaged at 86 GHz with VLBI observation by a factor of 5, and only 6 sources have not been detected. The remaining 12 objects have been detected but could not be imaged due to insufficient closure phase information. Radio galaxies are less compact than quasars and BL Lacs in sub-milliarcsecond scale. Flux densities and sizes of core and jet components of all imaged sources have been estimated using Gaussian model fitting. From these measurements, brightness temperatures have been calculated, taking into account resolution limits of the data. The cores of 70% of the imaged sources are resolved. The core brightness temperatures of the sources peak at $\sim 10^{11}$ K and only 1% have brightness temperatures higher than 10^{12} K. Cores of Intraday Variable (IDV) sources are smaller in angular size than non-IDV sources, and so yield higher brightness temperatures.

The intrinsic properties of relativistic jets in the compact radio sources such as the intrinsic brightness temperature T_0 , the Lorentz factor γ_j , and the viewing angle θ_j can be related to the observed values: the observed brightness temperature T_b and the apparent jet speed β_{app} . These relations enable us to deduce the intrinsic brightness temperature, under the assumptions: (1) all jets have the same Lorentz factor and the intrinsic brightness temperature, and (2) the jet is straight with no bends. The deduced intrinsic brightness temperature is $T_0 = 6.5_{-0.8}^{+1.1} \times 10^9$ K for 85 sources selected from our 3 mm-survey data. This value is less than the one found from the database at 15 GHz in the case of the median-low state by a factor of ~ 5 . Despite the difference in both samples, the decrease of T_0 may imply that the ultra compact cores in AGNs at 86 GHz are magnetic field dominated. Under the equipartition condition between the magnetic field energy and particle energy density, the absolute distance of the VLBI core can be predicted. From the database of VLBI survey at lower frequencies (2, 8, 15 GHz) and our measurement, the brightness temperatures in source frame are investigated in the sub-parsec scale of the compact radio sources. From the very vicinity of the central engine, the brightness temperatures increase slowly and then rise with steeper slope. This implies that the jets are collimated and accelerated by the magnetically driven force, as predicted by the relativistic jet models for the magnetic acceleration. The relativistic jets can be explained as a collection of relativistic shocks. The difference of the intrinsic brightness temperatures derived leads to the fact that the jet emission should evolve substantially already on the sub-milliarcsecond scales. The observed brightness temperatures of the jet components in our survey are in a good agreement with the predicted values of the brightness temperatures obtained from a single set of model parameters with the assumption that each of the jet components is an independent relativistic shock with adiabatic energy losses dominating the emission.

Contents

Abstract	iii
1 Introduction	1
1.1 Extragalactic Compact Radio Sources	1
1.2 VLBI observations	2
1.3 Structure of the Dissertation	3
1.4 Main Results	3
2 Basics of VLBI	5
2.1 Interferometry	5
2.1.1 Spatial coherence function of electromagnetic field	5
2.1.2 Data acquisition and cross correlation	7
2.1.3 Special characteristics of VLBI	8
2.2 Data analysis	8
2.2.1 Fringe fitting	8
2.2.2 Amplitude calibration	9
2.3 Imaging	9
2.3.1 Fourier inversion	10
2.3.2 Deconvolution	10
2.3.3 Closure quantities	12
2.3.4 Self-calibration	12
2.4 Model fitting	13
2.4.1 Imaging as an inverse process	13
2.4.2 Error estimation	14
2.4.3 Estimating the brightness temperature from VLBI data	15
3 Physics of Compact Radio Sources	19
3.1 Compact radio sources	19
3.2 Synchrotron Radiation	19
3.2.1 Total radiated power	20
3.2.2 Spectrum of synchrotron radiation	21
3.2.3 Synchrotron self-absorption	22
3.3 Brightness temperature (T_b) limits	24
3.3.1 Inverse Compton scattering	24
3.3.2 Inverse Compton limits of T_b	25
3.3.3 Equipartition limits of T_b	26
3.3.4 Relaxation of the limits of T_b	26
3.4 Relativistic jets as compact radio sources	27
3.4.1 Relativistic outflows	27
3.4.2 Innermost region of relativistic jets	28
3.4.3 Accelerating and decelerating jet models	29
3.4.4 Matter content of jets	30
3.5 VLBI observations as a tool to investigate relativistic jets	30
3.5.1 Multi-epoch VLBI observations	31
3.5.2 Multi-frequency VLBI observations	32
3.5.3 VLBI surveys	32

4	A Global 3 mm-VLBI Survey	37
4.1	Introduction	37
4.2	Survey observations	37
4.2.1	Source selection	37
4.2.2	Snapshot observations with GMVA	38
4.3	Data reduction	38
4.3.1	Fringe-fitting: <i>fourfit</i> and <i>FRING</i>	44
4.3.2	Fringe detection	46
4.3.3	Amplitude calibration	46
4.4	Imaging	46
4.4.1	Model fitting	50
4.4.2	Hybrid mapping	50
4.4.3	Measuring image parameters	51
4.5	Results of the survey	52
4.5.1	Images	52
4.6	Discussion	92
4.6.1	Source compactness	92
4.6.2	Brightness temperature T_b	93
4.6.3	Intraday variable sources	93
4.7	Summary	95
5	Intrinsic Properties of Compact Radio Sources	103
5.1	Introduction	103
5.2	Intrinsic brightness temperature	103
5.3	Compact jets on sub-parsec scales	106
5.4	Do Jets expand adiabatically?	112
5.5	Conclusion	112
6	Conclusions	115
	Bibliography	117
	Acknowledgements	124
	Curriculum Vitae	127

List of Tables

1.1	Characteristic scales in the nuclear regions in active galaxies	2
4.1	VLBI surveys at 86 GHz	38
4.2	Source list	40
4.2	Source list (<i>continued</i>)	41
4.2	Source list (<i>continued</i>)	42
4.3	Log of survey observation	43
4.4	Participating telescopes	43
4.5	Average antenna gain corrections	49
4.6	Image parameters	54
4.5	Image parameters (<i>continued</i>)	55
4.5	Image parameters (<i>continued</i>)	56
4.6	Model fit parameters of sources	57
4.6	Model fit parameters of sources (<i>continued</i>)	58
4.6	Model fit parameters of sources (<i>continued</i>)	59
4.6	Model fit parameters of sources (<i>continued</i>)	60
4.6	Model fit parameters of sources (<i>continued</i>)	61
4.7	Statistics of IDV and non-IDV selected sources	94
5.1	Synchrotron luminosity	110
5.1	Synchrotron luminosity (<i>continued</i>)	111

List of Figures

2.1	Basic picture of radio source – interferometer geometry.	6
2.2	Basic features of a two-element interferometer.	7
2.3	Clockwise from the upper left panel: the uv -coverage (sampling function), the synthesized beam, the dirty beam, and the “CLEAN” map for the observation of 3C 84 made on October 24 2002 at 86 GHz with the global mm-VLBI array.	11
2.4	Confidence intervals in dimensions of parameter 1 and 2. The same fraction of measured points (here 68 %) lies (i) between the two vertical lines, (ii) between the two horizontal lines, (iii) within the ellipse (taken from Press et al. (1992b), sec. 14.5).	14
3.1	A schematic for helical motion of a particle in a uniform magnetic field.	20
3.2	Radiation patterns: (a) Dipole radiation pattern for particle at rest, and (b) Angular distribution of radiation emitted by a particle with perpendicular acceleration and velocity.	21
3.3	(a) Synchrotron spectrum from a power-law distribution of electrons. (b) Synchrotron self-absorbed spectrum of III Zw 2, taken from Falcke et al. (1999).	23
3.4	(a) The Compton effect: The scattering of a photon by a free electron. (b) The inverse Compton effect: The scattering of a low energy photon by a relativistically moving electron.	24
3.5	Sketch of accelerating jet model and decelerating jet model.	29
3.6	Apparent superluminal velocity as a function of the viewing angle θ for $\gamma=1.5,2,4,5,10$	31
3.7	(a) Component tracks near the core of 3C345 and (b) position angle of the ejection point of the different components (they are referred to as C1,C2,C3,...etc)	32
3.8	Sketch of a “core” position at different frequencies.	33
3.9	Distribution of the turnover frequency of parsec-scale jet in 3C 345. The contours are drawn at 0.1...15 GHz, which are indicated with numbers.	33
3.10	Prediction for flux density per unit length of relativistic jets by various jet models.	35
4.1	The sky-distribution of 86 GHz VLBI sources	39
4.2	uv -plots of 0003-066 and 0016+731 at low and high declinations of -06 and 73 degrees, respectively.	39
4.3	Fringe detections on each baseline for epoch A (Oct. 2001) and epoch C (Oct. 2002).	47
4.4	Mk4 Fringe Plots of 2209+236 on the baseline of Haystack-Pico Veleta.	48
4.5	Distribution of fringe detection SNR of the sources.	49
4.6	Distribution of the image quality factor ξ_r	51
4.7	Distributions of the correlated flux density ratios (a) R_S and (b) R_L	52
4.8	123 contour maps of 109 sources with the distributions of the uv -sampling and of the visibility amplitude against uv -radius.	62
4.7	- continued.	63
4.7	-continued.	64
4.7	-continued.	65
4.7	-continued.	66
4.7	-continued.	67
4.7	-continued.	68
4.7	-continued.	69
4.7	-continued.	70
4.7	-continued.	71
4.7	-continued.	72
4.7	-continued.	73
4.7	-continued.	74

4.7	-continued.	75
4.7	-continued.	76
4.7	-continued.	77
4.7	-continued.	78
4.7	-continued.	79
4.7	-continued.	80
4.7	-continued.	81
4.7	-continued.	82
4.7	-continued.	83
4.7	-continued.	84
4.7	-continued.	85
4.7	-continued.	86
4.7	-continued.	87
4.7	-continued.	88
4.7	-continued.	89
4.7	-continued.	90
4.7	-continued.	91
4.7	-continued.	92
4.8	Distributions of the total flux density, S_{86} (top left), the CLEAN flux density, S_{CLEAN} (middle left), the correlated flux density on the longest baseline, S_L (bottom left), compactness indices on milliarcsecond scales S_{CLEAN}/S_{86} (top right) and sub-milliarcsecond scales S_L/S_S (middle right), and the core dominance $S_{\text{core}}/S_{\text{CLEAN}}$ of the imaged sources.	96
4.9	Normalized mean amplitude of the visibility function in terms of uv -radius for the survey sample.	97
4.10	Distributions of the flux density (top panel) and the the angular size (middle and bottom panel) of the core components for the imaged sources.	98
4.11	Distributions of the source frame brightness temperatures in the core components.	99
4.12	Distributions of the correlated flux density at the longest baseline S_L (top left), the compactness index S_L/S_S (middle left), the core dominance $S_{\text{core}}/S_{\text{CLEAN}}$ (bottom left), the core flux density S_{core} (top right), the size of core component d_{core} (middle right), and the brightness temperature T_b (bottom right) for IDV selected and non-IDV selected sources (see text for reference).	100
4.13	Comparison percentile plots of Kolmogorov-Smirnov (KS) test with the distributions shown in Figure 4.12 for IDV selected and non-IDV selected sources.	101
4.14	Normalized mean amplitude of the visibility function in terms of uv -radius for IDV and non-IDV sources.	102
5.1	Apparent jet speed versus observed brightness temperature	104
5.2	Plot of the apparent jet speed versus the observed brightness temperature	105
5.3	Brightness temperatures in source frame	107
5.4	Power law fit of brightness temperatures.	109
5.5	Adiabatic expansion of relativistic jet.	112

Chapter 1

Introduction

1.1 Extragalactic Compact Radio Sources

In the early 1900's, the discoveries of strong, broad emission lines in NGC 1068 (Fath 1913; Slipher 1917) and the jet in M87 (Curtis 1918) indicated a “non-stellar” activity in the nuclei of galaxies. After these discoveries, the systematic analysis of the first sample of the non-stellar activities by Seyfert (1943) drew the focus of astronomers to this new class of galaxies. In the mean time, modern radio astronomy began with the discovery of radio emission from our Galaxy by K. Jansky (Jansky 1932). Eight years after this pioneering work, G. Reber (Reber 1940) confirmed Jansky's work and discovered the first indication of “discrete radio sources”, which were revealed as strong and fluctuating radio sources by Hey et al. (1946). Subsequently, the discrete sources were identified as extragalactic radio sources (Baade & Minkowski 1954), and explained as incoherent synchrotron emission produced by a non-thermal population of relativistic electrons (Alfvén & Herlofson 1950).

A high energy estimate of the radio sources (Burbidge 1956) lead to the explanation of such energy with the release of gravitational potential energy (Hoyle & Fowler 1963). In the same year, identifying observations of the compact radio sources with point-like optical sources discovered *quasars* – quasi-stellar sources (Schmidt 1963). The discovery of quasars with enormous energies suggested that such phenomena could be related to the central engine (e.g. *black hole*, Zeldovich 1964; Salpeter 1964) in the core of a host galaxy, which is called the *active galactic nucleus (AGN)*. The black hole model received limited attention until the *accretion disk* around the black hole – an efficient way to explain the energetic phenomena – was suggested (Lynden-Bell 1969). On explaining the observed aspects of AGN many theoretical models were suggested. Among those, most acceptable models were mainly based on three fundamental assumptions: relativistic beaming (Shklovskii 1963), relativistic injection from galactic nuclei (Rees 1966), and accretion of matter onto a central black hole (see Begelman et al. 1984).

Extragalactic radio sources have been largely divided into three regions: the megaparsec-scale diffuse emission region far away from the host galaxy (Miley 1980), the narrow jets and hot spots connecting between the diffuse region and the nuclei of the host galaxy (Bridle & Perley 1984; Ferrari 1998), and the compact sources very close to the galactic nuclei (Kellermann & Pauliny-Toth 1981; Zensus 1997). To explain the observed aspects, phenomenological scenarios (e.g., *unification scheme*) in which various observational classes of AGN are interpreted as different manifestations of the same type of central engine, with different powers and geometries, have been developed (Antonucci 1993; Urry & Padovani 1995). The key elements in these unification models are an unresolved accretion disk on scales of $\ll 1$ pc and the twin opposite jets that are accelerated perpendicular to its plane. In particular, both twin jets are fully visible when they are perpendicular to the observer's line of sight, which is the case in extended radio galaxies (“FRI” and “FR II”) and “radio-loud quasars”. The jets are not clearly distinguishable at kpc-scales when they are seen with very small angles to the line-of-sight, but their emission in this case is relativistically Doppler boosted in frequency and luminosity, which is the case of “blazars” and compact radio galaxies. Weaker AGN would produce small jets, and the above classes would become “Seyfert 2” (large angles to the line of sight), “Seyfert 1” (smaller angles), and “BL Lacs” (very small angles).

The activity in AGN is observed throughout the entire range of the electromagnetic spectrum, due to contributions from the various physical components located in the nuclear environment of active galaxies. The nuclear constituents in AGN can be roughly divided into six categories: accretion disk and infalling material, broad-line and narrow-line region, obscuring torus, bipolar outflows (jets), nuclear stellar population,

Table 1.1: Characteristic scales in the nuclear regions in active galaxies

	l [R_g]	l_8 [pc]	θ_{Gpc} [mas]	τ_c [yr]	τ_{orb} [yr]
Event horizon:	1–2	10^{-5}	5×10^{-6}	0.0001	0.001
Ergosphere:	2	10^{-5}	5×10^{-6}	0.0001	0.001
Accretion disk:	10^1 – 10^3	10^{-4} – 10^{-2}	0.005	0.001–0.1	0.2–15
Corona:	10^2 – 10^3	10^{-3} – 10^{-2}	5×10^{-3}	0.01–0.1	0.5–15
Broad line region:	10^2 – 10^5	10^{-3} –1	0.05	0.01–10	0.5–15000
Molecular torus:	$>10^5$	>1	>0.5	>10	>15000
Narrow line region:	$>10^6$	>10	>5	>100	>500000
Jet formation:	$>10^2$	$>10^{-3}$	$>5 \times 10^{-4}$	>0.01	>0.5
Jet visible in the radio:	$>10^3$	$>10^{-2}$	>0.005	>0.1	>15

Column designation: l – dimensionless scale in units of the gravitational radius, GM/c^2 ; l_8 – corresponding linear scale, for a black hole with a mass of $5 \times 10^8 M_\odot$; θ_{Gpc} – corresponding largest angular scale at 1 Gpc distance; τ_c – rest frame light crossing time; τ_{orb} – rest frame orbital period, for a circular Keplerian orbit. Adapted from (Lobanov & Zensus 2007)

secondary black holes (Lobanov & Zensus 2007). The scales of the nuclear environment are ranging from ~ 1 – $2 R_g$ (gravitational radius) to ~ 100 parsecs, as listed in Table 1.1.

1.2 VLBI observations

A few years after Jansky’s discovery with his *directional antenna*, a parabolic *dish* radio telescope was developed by Reber (1940), increasing the collecting area and directional power of the radio antenna for very weak “cosmic static”. The compact radio sources were observed at a sub-arcsecond resolution after the development of the *aperture synthesis* method (Ryle & Hewish 1960). In the late 60s, an observing technique using the aperture synthesis method, *Very Long Baseline Interferometry* (VLBI), was introduced and applied to observe compact radio sources (e.g., Clark et al. 1968; Cohen et al. 1968). In 1971, VLBI observations discovered *superluminal expansion* of extragalactic compact radio sources (Cohen et al. 1968; Moffet et al. 1971; Whitney et al. 1971). Subsequent follow-up VLBI observations revealed the superluminal expansions in many extragalactic objects (Zensus & Pearson 1987) and triggered extensive studies on kinematics, morphology, polarization, and physical properties of these objects (Hughes 1991; Zensus 1997; Zensus et al. 2003; Wiita 2006)

Answering to the demand for higher angular resolutions to reveal the inner most structure of extragalactic compact radio sources, the length of VLBI baselines have been extended up to 10^4 km on the ground and 2×10^4 km to “space” (Hirabayashi et al. 2000). The observing wavelength range also has been extended to millimeter wavelengths (Barvainis & Phillips 1997; Greve & Krichbaum 1999). The highest resolving power has been obtained by increasing the baseline length and the observing frequency (*global millimeter VLBI*). Millimeter VLBI (mm-VLBI) provides a unique tool for exploring the physical nature of compact Galactic and extragalactic radio sources. The higher resolution provided by millimeter wavelengths, which is a factor of ~ 10 better than that of the space-VLBI at centimeter wavelengths, allows us to image directly the “VLBI core” and the “knots”. Furthermore, synchrotron radiation from compact radio sources becomes optically thin at wavelengths between 1 cm and 1 mm (Stevens et al. 1994). Therefore, mm-VLBI makes it possible to look deeper into the central regions of the compact radio sources, which is invisible at centimeter wavelengths.

In 1995, a global mm-VLBI array, the Coordinated Millimeter VLBI Array (CMVA), began to operate at 86 GHz with support from millimeter observatories throughout the world (Rogers et al. 1995). The number of participating telescopes has gradually increased from 3 to 12 until the CMVA stopped operating mm-VLBI experiments in 2000. The participation of large and sensitive European antennas (e.g. the 100m RT at Effelsberg, the 30m MRT at Pico Veleta, the 6×15 m interferometer on Plateau de Bure) provides a single baseline sensitivity of up to ~ 0.1 Jy, an image sensitivity of better than 10 mJy/beam, and a global uv-coverage. The mm-VLBI experiments have been continued at the Global mm-VLBI Array (GMVA), the successor to the CMVA. The GMVA performs regular, coordinated global VLBI observations at 86 GHz

with up to 14 telescopes, providing good quality images with a typical angular resolution of 50–70 micro-arcseconds (μas).

1.3 Structure of the Dissertation

Chapter 2 describes the basic principles of Very Long Baseline Interferometry (VLBI) observations. A detailed discussion on estimating physical parameters (e.g., brightness temperature) from the VLBI observations is also included. In Chapter 3, the physical aspects of compact radio sources are described. Inverse Compton limits and equipartition limits of the brightness temperatures of the compact radio sources are discussed. The currently accepted paradigm of AGN is presented and an approach for distinguishing between different kinematic models of the inner jet using 3 mm-VLBI observations is suggested. Chapter 4 presents results of the global 86 GHz VLBI survey of compact radio sources. The observations and post-processing procedures are summarized. A new method developed and implemented for achieving a higher fringe-detection rate is described. The post-processing includes set of tasks and methods for imaging and estimating physical parameters of each component. Hybrid maps and model fits to the source structure are presented for all sources detected in the survey data. The corresponding distributions of uv -data are shown graphically. Source compactness, and the intraday variable (IDV) sources in the sample are discussed. In Chapter 5, a detailed analysis of the survey results is presented, focused on the intrinsic properties of the compact radio sources. A method to deduce the intrinsic brightness temperature using the apparent jet speeds is presented. The observed brightness temperatures at 86 GHz are compared with those measured at lower frequencies to investigate the inner jet region of the compact jets. Adiabatic expansion of the relativistic jets is discussed. Chapter 6 gives a summary of the main findings of this work.

1.4 Main Results

The main results from the work presented in this thesis can be summarized as follows:

1. A global 86 GHz VLBI survey of 127 compact radio sources has been carried out. This survey resulted in high resolution VLBI images for 109 sources. The survey has yielded first 86 GHz VLBI images for 90 sources. Overall number of sources imaged at 86 GHz with VLBI has been increased by a factor of 5.
2. A specific procedure to search interferometric fringes of weak sources observed with a snapshot mode is developed. A detailed post-processing method for 3 mm-VLBI observations is described. Image quality of each VLBI map is quantified by determining the properties of residual noise. The sources are modeled with Gaussian components, resulting in flux densities and sizes of individual fitted components. Uncertainties of the model fit parameters are discussed and described.
3. Compactness at sub-milliarcsecond and milliarcsecond scales of the sources is described. The analysis of the normalized visibility functions is made for quasars, BL Lacs, and radio galaxies. Comparison of IDV and non-IDV sources for estimated parameters is made.
4. Physical properties of the compact radio sources are discussed and summarized. Brightness temperature limits are introduced and derived. Theoretical models for the innermost region of the relativistic jets are described.
5. Intrinsic brightness temperatures are determined in a sample of 85 sources from the 3 mm-VLBI-survey data. Brightness temperatures of compact jets in sub-parsec scale regions are investigated, and applied to test physical models for the inner jets. The effect of adiabatic expansion in relativistic jet is discussed on the basis of brightness temperature changes along the jet.

Chapter 2

Basics of VLBI

The fundamentals of Very Long Baseline Interferometry (VLBI) are reviewed in this chapter. We first discuss the fundamental principles of radio interferometry and the application to VLBI observations, data analysis and imaging. Practical aspects of model fitting interferometric visibility data are then discussed in detail. Finally, methods for estimating the physical parameters from VLBI data and images are described. Theoretical reviews of the underlying concepts of interferometry can be found in Thompson et al. (1991). Practical aspects of radio interferometry and synthesis imaging are presented in Taylor et al. (1999) and Zensus et al. (1995b). We use these references to summarize the basics of VLBI.

2.1 Interferometry

In radio astronomy, the resolution of observations has been a critical issue. Early discoveries in radio astronomy were made with single telescopes reaching an angular resolution of $\sim 1^\circ$, but many radio sources in the Universe have turned out to be smaller than this angular size. Optical observations are generally limited by atmospheric seeing to a resolution of $\sim 1''$. In order to reach a comparable resolution at radio wavelengths, telescopes with a large diameter are required. For example, a telescope of 200 km in diameter is needed at a wavelength of 1 m. The only practical way to achieve this is to use smaller telescopes separated by several hundreds of kilometers and connected as an interferometer array. In this section, we present a brief review of the technique of very long baseline interferometry.

2.1.1 Spatial coherence function of electromagnetic field

For the case of a very distant celestial radio source located at a position \mathbf{R} (hereafter, boldface symbols indicate vectors), the source radiation is described by a time variable electric field, $\mathbf{E}(\mathbf{R}, t)$, at the source location (Figure 2.1). The field can be represented as a sum of *quasi-monochromatic components* $\mathbf{E}_\nu(\mathbf{r})$ which are the coefficients of the Fourier expansion of the electric field,

$$\mathbf{E}(\mathbf{R}, t) = \mathcal{F}[\mathbf{E}_\nu(\mathbf{r})]. \quad (2.1)$$

The corresponding electric field at the observer's location \mathbf{r} is:

$$\mathbf{E}_\nu(\mathbf{r}) = \int P_\nu(\mathbf{R}, \mathbf{r}) \mathbf{E}_\nu(\mathbf{R}) dS. \quad (2.2)$$

The integral indicates a superposition of the field components from every point of the source. Integration must be done over the whole source. The function $P_\nu(\mathbf{R}, \mathbf{r})$ is called the *propagator*, and describes propagation of the electric field from \mathbf{R} to \mathbf{r} . In the empty space between the observer and the radio source,

$$P_\nu = \frac{1}{|\mathbf{R} - \mathbf{r}|} \exp(2\pi i \nu |\mathbf{R} - \mathbf{r}|/c), \quad (2.3)$$

so that a quasi-monochromatic component of the field can be written as:

$$\mathbf{E}_\nu(\mathbf{r}) = \int \frac{\mathbf{E}_\nu(\mathbf{R}) e^{2\pi i \nu |\mathbf{R} - \mathbf{r}|/c}}{|\mathbf{R} - \mathbf{r}|} dS. \quad (2.4)$$

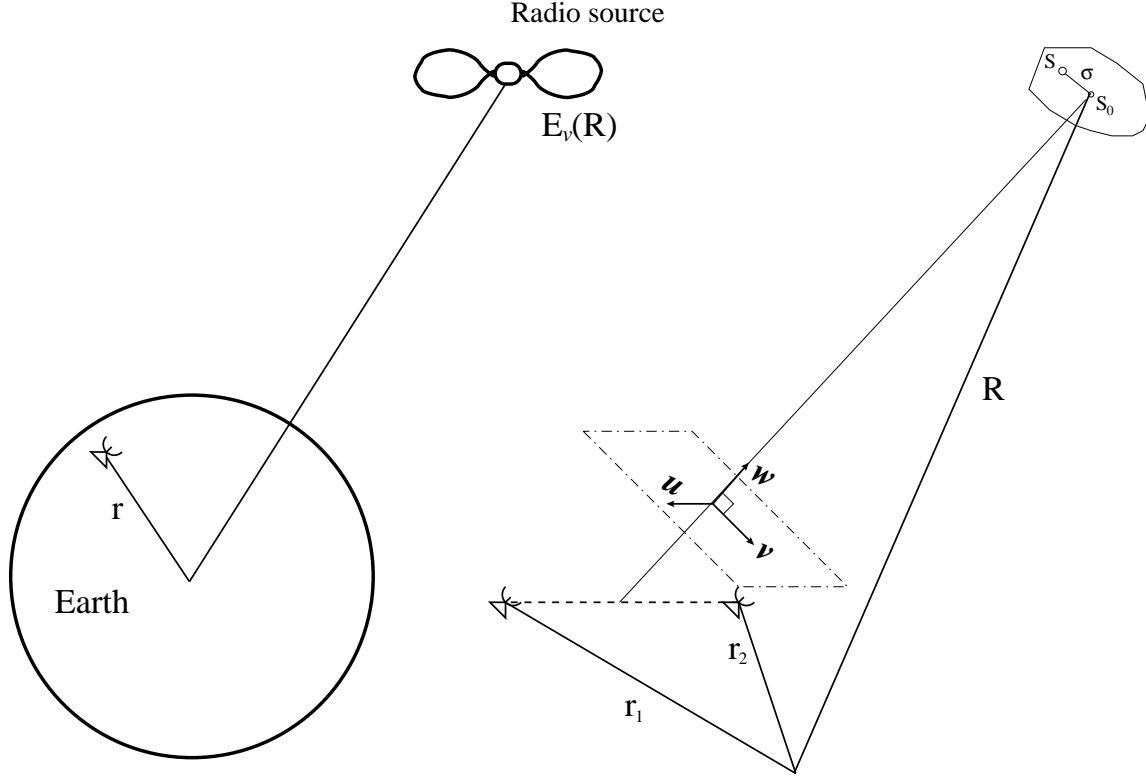


Figure 2.1: Basic picture of radio source – interferometer geometry.

This equation is the general form of the quasi-monochromatic component of the electric field at a frequency ν produced by a distant celestial radio source.

One of the properties of $\mathbf{E}_\nu(\mathbf{r})$ is the correlation of the field at two different locations, \mathbf{r}_1 and \mathbf{r}_2 . The correlation is defined as the expectation of the product of the fields at the given locations:

$$\mathbf{V}_\nu(\mathbf{r}_1, \mathbf{r}_2) = \langle \mathbf{E}_\nu(\mathbf{r}_1) \mathbf{E}_\nu^*(\mathbf{r}_2) \rangle, \quad (2.5)$$

where the asterisk indicates the complex conjugate. Using equation (2.4), the expectation of the product is:

$$\mathbf{V}_\nu(\mathbf{r}_1, \mathbf{r}_2) = \langle \int \int \mathbf{E}_\nu(\mathbf{R}_1) \mathbf{E}_\nu(\mathbf{R}_2) \frac{e^{2\pi i \nu |\mathbf{R}_1 - \mathbf{r}_1|/c}}{|\mathbf{R}_1 - \mathbf{r}_1|} \frac{e^{-2\pi i \nu |\mathbf{R}_2 - \mathbf{r}_2|/c}}{|\mathbf{R}_2 - \mathbf{r}_2|} dS_1 dS_2 \rangle. \quad (2.6)$$

In order to simplify this expression, two assumptions are employed:

1. The radiation from astronomical objects is not spatially coherent, so, the *emitted* fields are spatially incoherent: $\langle \mathbf{E}_\nu(\mathbf{R}_1) \mathbf{E}_\nu(\mathbf{R}_2) \rangle \equiv 0$ for $\mathbf{R}_1 \neq \mathbf{R}_2$,
2. The distance to the celestial radio sources is much greater than the distance to different sites of observation, $|\mathbf{R}| \gg |\mathbf{r}|$, so terms of order $|\mathbf{r}/\mathbf{R}|$ can be safely ignored.

Introducing a unit vector, $\mathbf{s} = \mathbf{R}/|\mathbf{R}|$, in the direction of \mathbf{R} , and substituting the area element of integration, dS , with the element of solid angle, $d\Omega$, we can rewrite (2.6) as:

$$V_\nu(\mathbf{r}_1, \mathbf{r}_2) = \int I_\nu(\mathbf{s}) e^{-2\pi i \nu \mathbf{s} \cdot (\mathbf{r}_1 - \mathbf{r}_2)/c} d\Omega, \quad (2.7)$$

where $I_\nu = |\mathbf{R}|^2 \langle |\mathbf{E}|^2 \rangle$ – the observed *intensity* of the radiation field. This function, V_ν , is the *spatial coherence function* of the field $\mathbf{E}_\nu(\mathbf{r})$, and it can be directly measured by interferometric devices.

If the size of the radiating source is small, the unit vector \mathbf{s} can be approximated as $\mathbf{s} = \mathbf{s}_0 + \boldsymbol{\sigma}$ (see Figure 2.1). If we introduce a coordinate system (u, v, w) in which $\mathbf{r}_1 - \mathbf{r}_2 = (u, v, w)c/\nu$, $\mathbf{s}_0 = (0, 0, 1)$ and the unit vector $\mathbf{s} = (0, 0, 1) + (l, m, 0) = (l, m, 1)$, we can rewrite (2.7) as

$$V'_\nu(u, v, w) = e^{-2\pi i w} \int \int I_\nu(l, m) e^{-2\pi i (ul + vm)} dl dm. \quad (2.8)$$

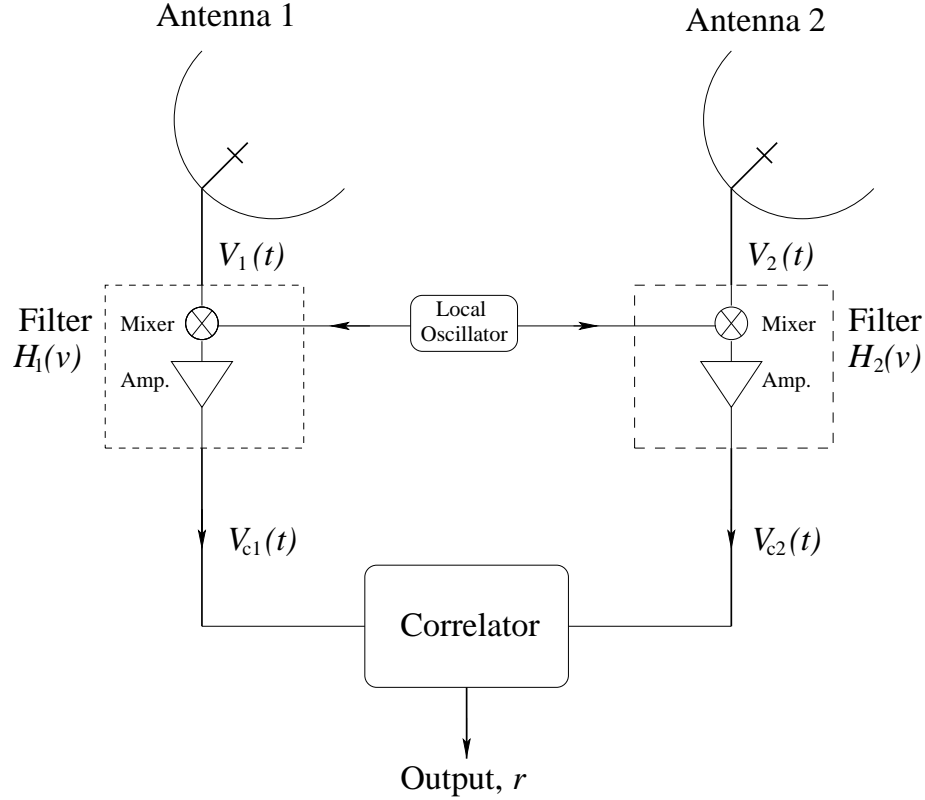


Figure 2.2: Basic features of a two-element interferometer.

By considering the quantity $V_\nu(u, v) = e^{2\pi i w} V'_\nu(u, v, w)$, we can absorb the factor $e^{-2\pi i w}$ in (2.8), which is the factor related to the phase difference between two antennas, and (2.8) can be independent of w :

$$V_\nu(u, v) = \iint I_\nu(l, m) e^{-2\pi i (ul + vm)} dl dm. \quad (2.9)$$

Equation (2.9) describes the basic relation between quantities described in the *spatial frequency domain* (u, v) , and those in the *image domain* (l, m) . Because antenna elements are not ideal, the *primary beam* or *normalized reception pattern*, $G_\nu(l, m)$ must be included into the integral in (2.9), in order to account for the directional sensitivity of the elements.

2.1.2 Data acquisition and cross correlation

A general scheme of a simple interferometer is shown in Figure 2.2. When the two antennas of the interferometer receive radiation from a distant celestial radio source, the output signals, V_1 and V_2 from the two antenna elements pass through filters with frequency responses H_1 and H_2 , and are then cross-correlated. An antenna with an angular reception pattern $G_\nu(\theta)$ responding to a radio source electric field distribution $E_\nu(\theta)$ will produce an output

$$V_\nu = \int E_\nu(\theta) G_\nu(\theta) d\theta. \quad (2.10)$$

In the filter, the output of the antenna is mixed with a local oscillator (LO) signal and is put through one or more intermediate frequency (IF) amplifiers. The outputs of the two filters in the Figure (2.2) are:

$$V_{c1}(\nu) = V_1(\nu) H_1(\nu), \quad (2.11)$$

and

$$V_{c2}(\nu) = V_2(\nu) H_2(\nu). \quad (2.12)$$

Cross correlation of these two signals in the correlator yields

$$r(\tau) = \lim_{T \rightarrow \infty} \frac{1}{2T} \int V_{c1T}(t) V_{c2T}^*(t - \tau) dt. \quad (2.13)$$

The subscript T indicates the truncation applied to the time variability of the subscripted functions. The delay τ reflects the source geometry with respect to the two antennas and various instrumental delays. Some of the contributions to the total delay are corrected for (e.g., instrumental delays, earth rotation, antenna clock rate and the atmosphere). However, errors in the calculated delays always exist in VLBI observations and they have to be corrected using the technique of *fringe fitting*.

2.1.3 Special characteristics of VLBI

A simple radio interferometer (e.g. the one shown in Figure 2.2) consists of two antennas connected together via a coaxial cable or radio link (*connected element interferometry*). The two antennas operate in real time using the local oscillator connected to the mixers within both antenna systems, and the output signals from different antennas are correlated with each other after traveling through the coaxial cable or via a radio link.

The principles of VLBI are basically the same as those of the connected element interferometry. The specific property of VLBI is that the antennas record information independently of each other. At each antenna, the signals are converted to a baseband of frequencies and are recorded onto magnetic tapes or disks together with precise time marks. The station clock is tuned by frequency standard. The phase of the local oscillator is also controlled by the frequency standard at each antenna. Since the frequency of the frequency standards are not precisely determined, there is a frequency offset and time error in the data recorded at each antenna. These errors will cause the delay error during the correlation later and they should be corrected using a two-dimensional search for *fringes* in time and frequency.

Another difference between VLBI and the connected element interferometry is the length of the baselines, which are usually more than two orders of magnitude longer in VLBI experiments. This results in larger phase errors in time and frequency. There are also much fewer unresolved sources that can be used as calibrators in VLBI experiments. In a connected element interferometry, there is generally a suitable calibration source within a few degrees of the target source that can be observed every few minutes. Thus, there is no fundamental limits on integration time.

2.2 Data analysis

2.2.1 Fringe fitting

To increase the speed of data analysis, VLBI data should be reduced in volume, which requires averaging the data in time and frequency. However, errors in the correlator model and wave propagation can cause significant reduction of the visibility amplitude and increase the phase noise in the averaged data. These errors must be corrected before the averaging can be made. The delays obtained from the correlation can be affected by a number of errors: errors in the source or antenna position used, errors in the earth model, errors in the clock epoch and rate at each antenna, and errors in the atmospheric model. The interferometer phase is related to the delay by the simple relationship:

$$\phi_{t,\nu} = 2\pi\nu\tau_t, \quad (2.14)$$

where $\phi_{t,\nu}$ is the interferometer phase, ν is the observing frequency, and τ_t is the interferometer delay. By differentiating equation (2.14), the phase errors $\Delta\phi_{t,\nu}$ caused by errors in the delays are given by

$$\Delta\phi_{t,\nu} = 2\pi\nu\Delta\tau_t. \quad (2.15)$$

In the time and frequency domain, a first order expansion of the error in interferometer phase is:

$$\Delta\phi_{t,\nu} = \phi_0 + \left(\frac{\partial\phi}{\partial\nu}\Delta\nu + \frac{\partial\phi}{\partial t}\Delta t \right), \quad (2.16)$$

where ϕ_0 is the phase error at the reference time and frequency, $\partial\phi/\partial\nu$ is the *delay* or *delay residual*, and $\partial\phi/\partial t$ is the *rate* or *delay rate*. The equation (2.16) holds for each individual antenna and it is most likely that the delay error in the correlated model consists of contributions from each antenna. The baseline dependent errors between any two antennas i and j can then be expressed as the difference of antenna dependent errors:

$$\begin{aligned} \Delta\phi_{i,j} &= \Delta\phi_i - \Delta\phi_j \\ &= \phi_{i,0} - \phi_{j,0} + \left(\left[\frac{\partial\phi_i}{\partial\nu} - \frac{\partial\phi_j}{\partial\nu} \right] \Delta\nu + \left[\frac{\partial\phi_i}{\partial t} - \frac{\partial\phi_j}{\partial t} \right] \Delta t \right). \end{aligned} \quad (2.17)$$

Several techniques used for estimating the delay rates and delay residual are referred to as *fringe fitting*. For the VLBI survey data presented in this dissertation, baseline-based fringe fitting and *global* fringe fitting (Schwab & Cotton 1983; Walker 1989), which is antenna-based fringe fitting, were used. For both techniques, equation (2.17) is applied to determine the antenna-based phase, delay rate, and delay residuals. The general procedure of fringe fitting is shown in Cotton (1995) and the details of the procedure applied for fringe fitting the data from the 86 GHz VLBI survey can be found in section 4.3.

2.2.2 Amplitude calibration

The observed visibility V_{ij} between antennas i and j can be expressed as:

$$V_{ij}(\nu, t) = \mathcal{G}_{ij}(\nu, t)V'_{ij}(\nu, t) + \epsilon_{ij}, \quad (2.18)$$

where V'_{ij} is the true visibility of the source on the $i-j$ baseline, \mathcal{G}_{ij} is the baseline-based complex gain, and ϵ_{ij} is the thermal noise on the baseline. Most data corruption occurs before the signal pairs are correlated, so that the baseline-based complex gain \mathcal{G}_{ij} can be approximated by the product of the two associated antenna-based complex gains \mathcal{G}_i and \mathcal{G}_j ,

$$\mathcal{G}_{ij}(\nu, t) = \mathcal{G}_i(\nu, t)\mathcal{G}_j^*(\nu, t) = a_i(\nu, t)a_j(\nu, t)e^{i(\phi_i(\nu, t) - \phi_j(\nu, t))}, \quad (2.19)$$

where $a_i(\nu, t)$ is an antenna-based amplitude correction and $\phi_i(\nu, t)$ is the antenna-based phase correction. Then, equation (2.18) can be rewritten as:

$$V_{ij}(\nu, t) = \mathcal{G}_i(\nu, t)\mathcal{G}_j^*(\nu, t)V'_{ij}(\nu, t) + \epsilon_{ij}. \quad (2.20)$$

For the amplitude calibration, the phase terms of the antenna gains can be omitted. The thermal noise term can be ignored after proper averaging of the data in the scan, because it is usually small. Then, to calibrate the observed visibility, we can use equation (2.20), and obtain

$$S_{ij}(\nu, t) = \frac{A_{ij}(\nu, t)}{a_j(\nu, t)a_i(\nu, t)}, \quad (2.21)$$

where A_{ij} represents the observed visibility amplitude, and is usually the raw correlation coefficient from the correlator. Here we have equated the amplitude of the true visibility V'_{ij} with the calibrated, correlated flux density S_{ij} . At a certain frequency and time, the equation (2.21) can be rewritten in terms of practical calibration parameters as:

$$S_{ij} = A_{ij}b\sqrt{\frac{T_{s_i}T_{s_j}}{K_iK_j}}, \quad (2.22)$$

where b is the correlator dependent factor that accounts for digitization losses, K_i and K_j are the antenna gains measured in K/Jy, and T_{s_i} and T_{s_j} are the antenna system temperatures in Kelvin. The antenna gains are measured systematically; the system temperatures are logged for every experiment. The b -factors are determined for each correlator individually. For a strong source, the antenna temperatures T_a can be measured and used for the amplitude calibration, in place of the antenna gains: $K_i = T_a/S_{\text{tot}}$. The calibration formula in this case is:

$$S_{ij} = A_{ij}bS_{\text{tot}}\sqrt{\frac{T_{s_i}T_{s_j}}{T_{a_i}T_{a_j}}}, \quad (2.23)$$

where S_{tot} is the total source flux density.

More extensive discussions of the calibration procedures can be found in Walker (1989) and Moran & Dhawan (1995).

2.3 Imaging

The interferometric array produces images of the celestial radio source only indirectly. An image is constructed and refined in the steps: Fourier inversion, deconvolution, and self-calibration. In this section, those three steps are reviewed

2.3.1 Fourier inversion

After the phases and delays of the interferometer have been calculated, and the visibilities have been calibrated, the relation (2.9) can be formally inverted via a Fourier transform for finding the true intensity distribution

$$I_\nu(l, m) = \int \int V_\nu(l, m) e^{2\pi i(ul+vm)} dudv. \quad (2.24)$$

In practice, the spatial coherence function V_ν is sampled at particular places on the uv -plane, so it is not known everywhere. To describe the sampling, we can introduce a sampling function $S(u, v)$ (also called the *uv-coverage*):

$$S(u, v) = \sum_k \delta(u - u_k) \delta(v - v_k). \quad (2.25)$$

The sampling function can be used to rewrite the equation (2.24):

$$I_\nu^D(l, m) = \int \int V_\nu(u, v) S(u, v) e^{2\pi i(ul+vm)} dudv. \quad (2.26)$$

I_ν^D is known as the *dirty image* which is related to the true intensity distribution I_ν by the Fourier convolution theorem:

$$I_\nu^D(l, m) = B(l, m) * [I_\nu(l, m) + N(l, m)], \quad (2.27)$$

where $*$ represents convolution, $N(l, m)$ describes the noise in the image, and B (called the *point spread function* or *synthesized beam*) is the two-dimensional Fourier transform of the sampling function $S(u, v)$

$$B(l, m) = \int \int S(u, v) e^{2\pi i(ul+vm)} dudv. \quad (2.28)$$

The shape of the *synthesized beam* can be controlled by introducing weighting functions T_k and D_k in the sampling function $S(u, v)$:

$$S(u, v) = \sum_k T_k D_k \delta(u - u_k) \delta(v - v_k), \quad (2.29)$$

where T_k is the *tapering function* used to downweight the data at the outer edge of the uv -plane (e.g. a Gaussian taper; $T(r_k) = \exp(-r^2/2\sigma^2)$, $r_k \equiv \sqrt{u_k^2 + v_k^2}$), and D_k is the *density weighting function* used to offset the high concentration of the uv tracks near the center and lessen the side-lobes caused by gaps in the coverage. There are two choices for the density weighting function: $D_k = 1$ for *natural weighting* and $D_k = 1/\rho(k)$ for *uniform weighting*, where $\rho(k)$ is the local density of the sample. Since natural weighting gives the best signal-to-noise ratio for detecting weak sources, it is used for the VLBI survey data presented in this dissertation. Uniform weighting is satisfactory for images of bright objects because the uniform weighting scheme minimizes the rms side-lobes of the dirty beam.

2.3.2 Deconvolution

Since the VLBI sampling functions are finite and poorly defined in practice, $I(l, m)$ itself cannot be recovered directly using the simple Fourier inversion. So, non-linear deconvolution methods and self-calibration techniques are used in order to refine the *primary solution* I^D . The two deconvolution methods widely used in radio interferometry are the *Maximum Entropy Method* (MEM) and the “CLEAN” algorithm. Reviews of the MEM technique can be found in Narayan & Nityananda (1986) and Cornwell et al. (1999).

The “CLEAN” algorithm was introduced by Högbom (1974), and modified later by Clark (1980) and Schwab & Cotton (1983). The DIFMAP implementation of “CLEAN” (Shepherd et al. 1994) was used for producing all of the images presented in this dissertation. The “CLEAN” method and its modifications provide a solution to the convolution equation (2.27) by representing the true intensity distribution by a number of point sources (δ -functions). The field of view outside the area selected for the source search is assumed to be empty. A simple iterative approach is used to find the positions and strengths of these point sources. The final deconvolved image (“CLEAN” image) is the sum of the point components convolved with an artificial “CLEAN” beam. Detailed discussions of the “CLEAN” algorithm can be found in Wilkinson (1989), Cornwell et al. (1999), and Cornwell (1995).

Figure 2.3 gives an example of sampling function, point spread function, dirty beam, and clean image. All pictures are produced from the VLBI data for 3C 84 observed on October 24 2002 at 86 GHz.

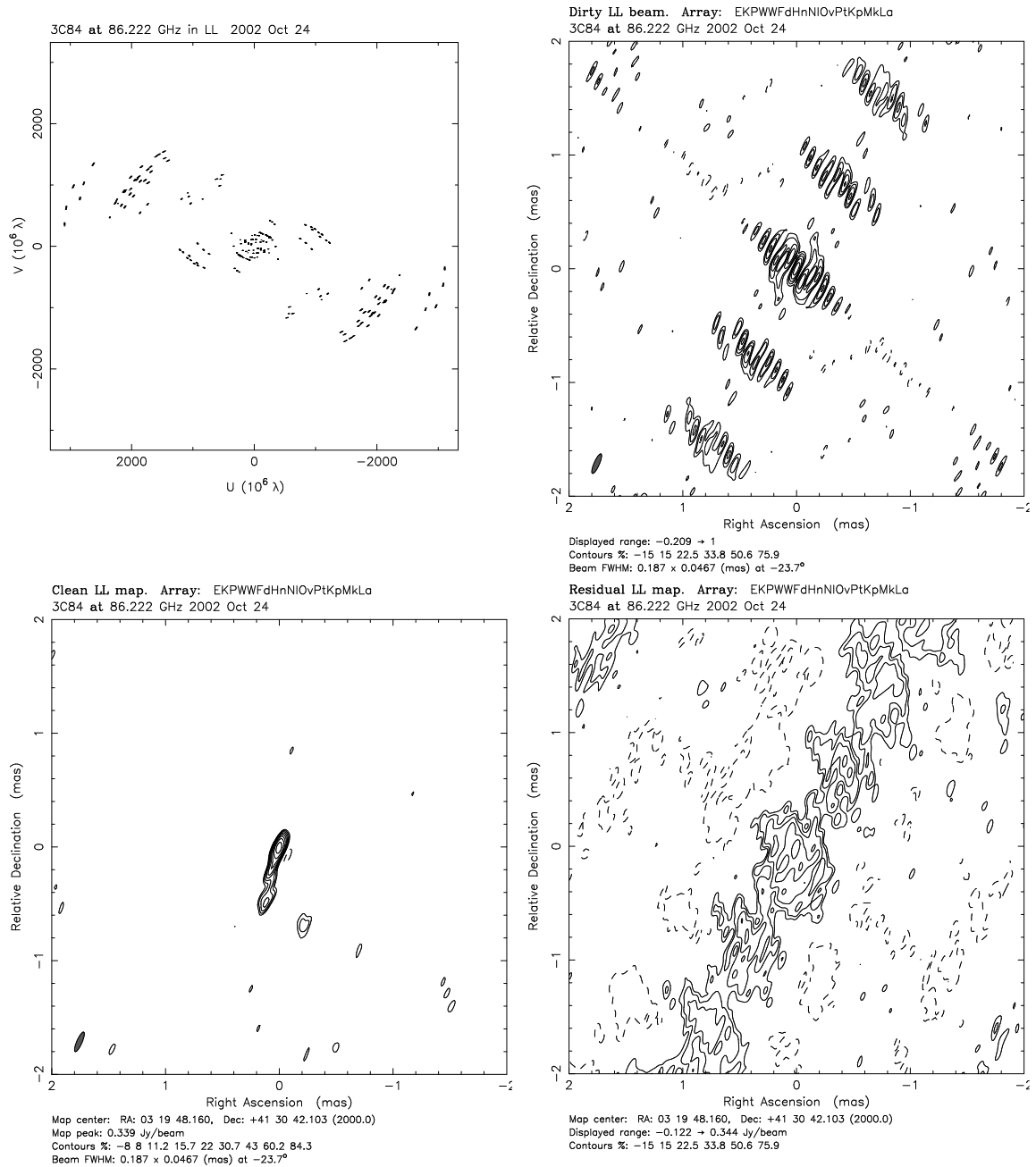


Figure 2.3: Clockwise from the upper left panel: the uv -coverage (sampling function), the synthesized beam, the dirty beam, and the “CLEAN” map for the observation of 3C 84 made on October 24 2002 at 86 GHz with the global mm-VLBI array.

2.3.3 Closure quantities

In the equation (2.18), if the complex gain factors $\mathcal{G}_{ij}(\nu, t)$ are varying faster than they can be measured, it is impossible to recover the true visibility of the source, V'_{ij} , from the measurements. When more than two antennas are used simultaneously, however, the concepts of *closure quantities* make it possible to recover the true visibility of the source. Using the explicit expression for the complex gain factor in (2.19), we can rewrite (2.20) for the visibility observed on the $i - j$ baseline as:

$$V_{ij} = a_i a_j e^{i(\phi_i - \phi_j)} V'_{ij} + \epsilon_{ij}. \quad (2.30)$$

Time and frequency dependences of all terms are regarded as implicit.

Ignoring the noise terms ϵ_{ij} , the phases of any three antennas, and amplitudes of any four antennas can be related to be free of antenna dependent terms (Jennison 1958; Twiss et al. 1960; Readhead et al. 1980). We assume that the relation

$$V'_{ij} = A_{ij} e^{i\psi_{ij}} \quad (2.31)$$

represents the ideal complex correlation coefficient corresponding to one spatial frequency. Then, from (2.30), the *closure phase* is given by

$$\begin{aligned} C_{ijk} &= (\psi_{ij} + \phi_i - \phi_j) + (\psi_{jk} + \phi_j - \phi_k) + (\psi_{ki} + \phi_k - \phi_i) \\ &= \psi_{ij} + \psi_{jk} + \psi_{ki} \\ &= C'_{ijk}. \end{aligned} \quad (2.32)$$

In the sum represented by (2.32) all antenna-based phase errors cancel. This is true for any closed loop of baselines, not just a triangle. Thus the observed closure phase is uncorrupted by antenna-based phase errors. The closure phase is the argument of the *bispectrum* of the sky brightness distribution, given by the triple product of the complex visibilities on a closed triangle of baselines:

$$\mathcal{B} = V(u, v) V(u', v') V(-u - u', -v - v'), \quad (2.33)$$

which indicates that the closure phase is a function of four variables (two positions in the uv -plane). Due to the poor sampling of the uv -plane the information preserved by the closure phase relation can be ambiguous. The ambiguity can be overcome with increasing the number of antennas, since the fraction of the visibility information available from the closure phase is $(N - 2)/N$, where N is the number of antennas (Pearson 1995).

Another observable closure quantity is the *closure amplitude*, Γ_{klmn} , with the four antennas k, l, m, n . It is possible to form ratios of the visibility amplitudes that are independent of the antenna gain factors:

$$\Gamma_{klmn} = \frac{|V_{kl}| |V_{mn}|}{|V_{km}| |V_{ln}|} = \frac{A_{kl} A_{mn}}{A_{km} A_{ln}}. \quad (2.34)$$

The closure amplitude, therefore, is a function of six variables (three positions in the uv -plane). If all six interferometer pairs formed by the four antennas are correlated, three different closure amplitudes can be calculated ($\Gamma_{klmn}, \Gamma_{klnm}, \Gamma_{knml}$), but only two of these are independent. Therefore, the fraction of information that can be recovered from the closure amplitude is related to the number of antennas as $(N - 3)/(N - 1)$. The ratio, and also that of the closure phase, show the rewards to be given by increasing the number of antennas in the array; with only 4 antennas, 50 % of the phase information and 33 % of the amplitude information is available, while for 12 antennas (for the VLBI survey presented in the dissertation), these ratios increase to 83 % and 82 %, respectively.

The closure quantities have the property that the observed and true values are identical with the noise being ignored and so they are the useful constraints during the restoration of the true intensity distribution, although it is not possible to recover the true intensity distribution with only the closure quantities. If only the closure phases and closure amplitudes are measured, knowledge of both the absolute strength and the absolute position of the source is lost. In VLBI experiments, the *self-calibration* method is used for calibrating visibility phase and amplitude using the closure quantities, so the absolute information of the source can be recovered.

2.3.4 Self-calibration

Self-calibration is an iterative process of producing an optimal model, \hat{I} such that its Fourier transform

$$\hat{V}_{ij}(u, v) = \int \int \hat{I}_{ij}(l, m) e^{-2\pi i(ul + vm)} dl dm \quad (2.35)$$

reproduces the observed visibilities $V_{ij}(u, v)$ to within the noise level. One reliable method to achieve such agreement is to minimize a certain function \mathcal{S} which is the sum of the squares of the residuals:

$$\mathcal{S} = \sum_k \sum_{i,j;i \neq j} w_{ij}(t_k) \left| V_{ij}(t_k) - \mathcal{G}_i(t_k) \mathcal{G}_j^*(t_k) \hat{V}_{ij}(t_k) \right|^2 \quad (2.36)$$

(Schwab 1980), where w_{ij} are the weights reflecting the signal-to-noise ratio of the corresponding visibility and $\mathcal{G}_i(t_k)$ are the complex antenna gains. Minimization of \mathcal{S} produces solutions for the complex antenna gains, and allows for corrections of the phase and amplitude errors to be incorporated into the observed visibilities. The corrected visibility is:

$$V_{ij,corr}(t) = \frac{V_{ij}(t)}{\mathcal{G}_i(t) \mathcal{G}_j^*(t)}. \quad (2.37)$$

A new model can be formed by deconvolution of the corrected data, and used in the next iteration of self-calibration unless one is satisfied with the current model. Self-calibration has been shown to converge to a unique solution, for most of the VLBI observations with a large number of antennas, good *a priori* calibration, and a fairly simple source structure. More detailed discussions on the topic of self-calibration are given in Cornwell & Fomalont (1999), and Cornwell (1995).

2.4 Model fitting

The fitting of brightness models (*model fitting*) to measured visibility data was used widely in early radio interferometry, specially when the phase information was poorly calibrated or the number of data points were not sufficient to conduct proper imaging processes such as Fourier transformation, deconvolution, and self-calibration. For certain types of sources the radio emission can be specified with reasonable accuracy in terms of a physical model that involves only a small number of parameters. The parameters of the physical model can then best be determined by fitting the model visibility function directly to the observed values.

2.4.1 Imaging as an inverse process

Model fitting is a technique which is generally used for solving the *inverse problems* in which the true distribution of a certain variable needs to be recovered from the measured distribution. In its application to VLBI, model fitting produces a parametric model of the sky brightness distribution and calculates the expected measurements. These calculated measurements are compared with the actual measurements, and the model is adjusted using the discrepancies between measurements and model predictions unless the model is satisfactory. For model fitting VLBI data, the *least squares* implementation of the *maximum likelihood* method is used. The *likelihood* of the model is the probability of obtaining the data, which is given by

$$P \propto \prod_{i=1}^N \left\{ \exp \left[-\frac{1}{2} \left(\frac{V(u_i, v_i) - F(u_i, v_i; a_1, \dots, a_M)}{\sigma_i} \right)^2 \right] \right\}, \quad (2.38)$$

where V and F are the observed and predicted distributions, σ_i is a standard deviation, N is the number of data points and a_1, \dots, a_M are the model parameters. The fitting is being achieved by maximizing P , which is equivalent to minimizing the following sum:

$$\chi^2 \equiv \sum_{i=1}^N \left(\frac{V(u_i, v_i) - F(u_i, v_i; a_1, \dots, a_M)}{\sigma_i} \right)^2, \quad (2.39)$$

which, thus, is the weighted sum of squares of the deviations between the measurements and the model. It should be noted that this is strictly applicable only if the measurements have Gaussian errors. If the errors are Gaussian, the quality of the optimized model is judged by the *reduced chi-square* $\chi^2/(N - M)$ which should be close to 1 for a good fit. Large values of the reduced chi-square indicate that the model is far away from the measurement and so the fit is bad, whereas much smaller values than 1 show that the errors σ_i might be overestimated and so the fit is too good to be true.

There are two simple and commonly-used methods for the model fitting: the “grid search” (Bevington & Robinson 1992) and the “gradient search” (see Press et al. 1992b, for the Levenberg–Marquardt method). A more detailed discussion of model fitting is given in Pearson (1995).

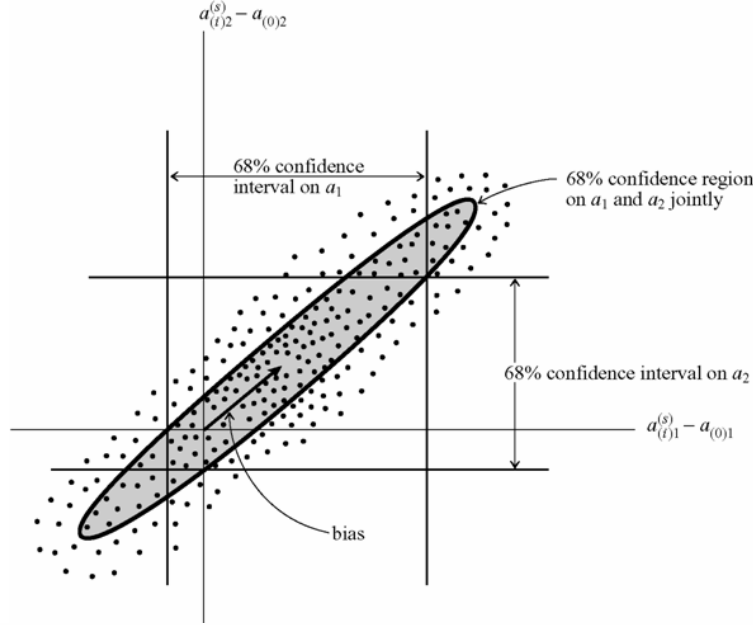


Figure 2.4: Confidence intervals in dimensions of parameter 1 and 2. The same fraction of measured points (here 68 %) lies (i) between the two vertical lines, (ii) between the two horizontal lines, (iii) within the ellipse (taken from Press et al. (1992b), sec. 14.5).

2.4.2 Error estimation

The observed visibilities are subject to additive noise from the sky, receivers, ground pick-up, etc. To a very good approximation, the noise is Gaussian with equal variance in the real and imaginary parts of the visibility. The Fourier inversion of the observed visibility function (2.9) has the desirable property that the noise in the dirty image is also Gaussian, with known covariance. However, if the image is deconvolved with the non-linear techniques (e.g., CLEAN, MEM, etc), the noise properties of the resulting image will be poorly understood and it may be difficult to estimate the uncertainty in a measurement (e.g., of flux density, size, etc.) of a component in the image. For quantitative analysis of uncertainties, it is often better to work directly with the visibilities. To determine the uncertainties or confidence limits on the estimated model parameters, it is best to calculate contours of constant χ^2 (taken at a desired confidence level) around the minimum in the multi-dimensional space of all parameters (Figure 2.4). It is important to remember that these theoretical confidence limits will not apply if the data are not Gaussian or not independent.

Here we assume that the brightness distribution of the sources can be approximated by elliptical Gaussian components. The uncertainties of the parameters for the Gaussian components are related to the signal-to-noise ratio (SNR) of detection of a given model fit component, being based on an analytical (first order) approximation. The general fit parameters of a component in VLBI images of radio sources are S_{tot} - total flux density, S_{peak} - peak flux density, σ_{rms} - post-fit rms, d - size, r - radial distance (for jet components), θ - position angle (for jet components). And then the uncertainties of the fit parameters can be estimated from approximations given by Fomalont (1999):

$$\sigma_{\text{peak}} = \sigma_{\text{rms}} \left(1 + \frac{S_{\text{peak}}}{\sigma_{\text{rms}}} \right)^{1/2}, \quad (2.40)$$

$$\sigma_{\text{tot}} = \sigma_{\text{peak}} \left(1 + \frac{S_{\text{tot}}^2}{S_{\text{peak}}^2} \right)^{1/2}, \quad (2.41)$$

$$\sigma_d = d \frac{\sigma_{\text{peak}}}{S_{\text{peak}}}, \quad (2.42)$$

$$\sigma_r = \frac{1}{2}\sigma_d, \quad (2.43)$$

and

$$\sigma_\theta = \text{atan}\left(\frac{\sigma_r}{r}\right), \quad (2.44)$$

where σ_{peak} , σ_{tot} , σ_d , σ_r , and σ_θ are the uncertainties of total flux density, peak flux density, post-fit rms, size, and radial distance of a component, respectively.

When the size, d , of a component was determined, the resolution limits (Lobanov 2005) should be taken into account. So, the minimum resolvable size of a component in an image is given by

$$d_{\text{min}} = 2^{1+\beta/2} \left(\frac{ab \ln 2}{\pi} \ln \frac{\text{SNR}}{\text{SNR} - 1} \right)^{1/2}, \quad (2.45)$$

where a and b are the axes of the restoring beam, SNR is the signal-to-noise ratio, and β is the weighting function, which is 0 for natural weighting or 2 for uniform-weighting. When $d < d_{\text{min}}$, the uncertainties should be estimated with $d = d_{\text{min}}$.

2.4.3 Estimating the brightness temperature from VLBI data

The spectral distribution of the radiation of a black body is given by the *Planck Law*:

$$I_\nu(T) = \frac{2h\nu^3}{c^2} \frac{1}{e^{h\nu/k_B T} - 1}, \quad (2.46)$$

where I_ν is the specific intensity, T the temperature, ν the frequency, c the speed of light, h the Planck constant, and k_B the Boltzmann constant. When $h\nu \ll k_B T$ (e.g. in the radio regime), a Taylor expansion of the exponential in (2.46):

$$e^{h\nu/k_B T} \cong 1 + \frac{h\nu}{k_B T} + \dots, \quad (2.47)$$

results in:

$$I_\nu(T) = \frac{2\nu^2}{c^2} k_B T, \quad (2.48)$$

which is referred to as the *Rayleigh-Jeans Law*. So, brightness temperature T_b is defined as:

$$T_b = \frac{c^2}{2k_B} \frac{1}{\nu^2} I_\nu = \frac{\lambda^2}{2k_B} I_\nu, \quad (2.49)$$

where λ is the wavelength. It is important that equation (2.49) holds for black body radiators. Historically the term, *brightness temperature*, has been used also for non black body sources, hence for nonthermal sources with a spectral index α ($S_\nu \propto \nu^\alpha$). It corresponds to the temperature that the source should have as if it was a black body to radiate the specific intensity I_ν . For a source with flux density, S_ν , and solid angle, Ω , the brightness temperature is given by:

$$T_b = \frac{1}{2k_B} \frac{S_\nu \lambda^2}{\Omega}, \quad (2.50)$$

where we have taken $I_\nu = S_\nu/\Omega$. If the source can be modeled as a circular Gaussian with a full width at half-maximum θ_{FWHM} , then the solid angle of the source is:

$$\Omega = \frac{\pi}{4 \ln 2} \theta_{\text{FWHM}}^2, \quad (2.51)$$

and (2.50) can be re-cast as:

$$T_b = \frac{2 \ln 2}{\pi k_B} \frac{S_\nu \lambda^2}{\theta_{\text{FWHM}}^2}. \quad (2.52)$$

From (2.52), the brightness temperature of the emission region represented by a Gaussian component with the total flux density S_{tot} and the angular size d ($\equiv \theta_{\text{FWHM}}$), is given by:

$$T_b = \frac{2 \ln 2}{\pi k_B} \frac{S_{\text{tot}} \lambda^2}{d^2}. \quad (2.53)$$

For a source observed at redshift z , the brightness temperature at the source rest frame $T_{b,s}$ is given as:

$$T_{b,s} = \frac{2 \ln 2}{\pi k_B} \frac{S_{\text{tot}} \lambda^2}{d^2} (1+z), \quad (2.54)$$

where λ is the wavelength at the observer's frame. The factor $1+z$ in (2.54) reflects the cosmological effect on the observed brightness temperature. Practically, the brightness temperature can be calculated by simplifying (2.54):

$$T_{b,s} = 1.22 \times 10^{12} \frac{S_{\text{tot}}}{d^2 \nu^2} (1+z) \text{ K}, \quad (2.55)$$

where the total flux density S_{tot} is measured in Jy, the size of the circular Gaussian component d in mas, and the observing frequency ν in GHz. If $d < d_{\text{min}}$, then the lower limit of T_b is obtained with $d = d_{\text{min}}$.

Doppler boosting correction

Assuming the emission region to be relativistically moving towards the observer, the radiation can be amplified, or Doppler boosted. Doppler boosting of the brightness temperature in distant sources is given by the *Doppler factor* $\delta = \gamma^{-1}(1 - \beta \cos \theta)^{-1}$, which depends on the Lorentz factor ($\gamma = 1/\sqrt{1 - \beta^2}$) and flow speed ($\beta = v/c$), where v is the velocity of the source moving at an angle θ to the line of sight. Taking into account the K-correction to the source at redshift z , the Doppler factor is often replaced by the factor $\mathcal{D} = \delta/(1+z)$. The relativistic Doppler effect on the source intrinsic flux density (and hence intrinsic brightness temperature) depends on the geometry of the emission region, hence the jet models. Here, the Doppler boosting correction on the observed flux $S_\nu(\nu)$ is briefly discussed in the cases of two jet models; a spherical blob and a continuous jet. For the spherical jet model, the Doppler boosting correction to the observed brightness temperature is also discussed. Most of the discussion follows Lind & Blandford (1985) and Hughes (1991) where more details can be found.

The simplest jet model is the optically thick spherical blob (or the optically thin ‘‘plasmoid’’) moving uniformly at an angle θ to the line of sight. If a single blob in the jet emits isotropically in the rest frame of the *jet* (Σ'), the observed frequency and intensity will be Lorentz-transformed according to the Doppler factor δ , which relates the rest frame of the source Σ' and the observer's frame Σ :

$$\nu = \delta \nu', \quad (2.56)$$

$$S_\nu = \delta^3 S'_{\nu'}. \quad (2.57)$$

Assume that the spectral index α ($S_\nu = k\nu^\alpha$) is constant over the entire range of $\nu (= \delta\nu')$, then $S'_{\nu'} = k'\nu'^\alpha$, where k' is constant in the rest frame (Σ'). We can obtain the flux density in the rest frame, at the observing frequency ν :

$$S'_{\nu'} = k'\nu' = k'\nu/\delta^\alpha = \delta^{-\alpha} S'_\nu, \quad (2.58)$$

and then (2.57) can be rewritten as:

$$S_\nu = \delta^{3-\alpha} S'_\nu. \quad (2.59)$$

Since the size of a sphere would not be affected by the *aberration effect*, the angular size of the spherical blob in the observer's frame should not change:

$$d = d'. \quad (2.60)$$

From the equations (2.52), (2.56), (2.59), and (2.60), the brightness temperature in the observer's frame is given by

$$\begin{aligned} T_b &= \mathcal{C} \frac{S_\nu}{\nu^2 d^2} \\ &= \mathcal{C} \frac{\delta^{3-\alpha} S'_\nu}{(\delta\nu')^2 d'^2} \\ &= \delta^{1-\alpha} T'_b, \end{aligned} \quad (2.61)$$

where \mathcal{C} is constant. Therefore, the Doppler boosting correction, $\delta^{1-\alpha}$, should be taken into account in the case of a single blob jet.

In this simplistic jet model, the jet is considered as a discrete feature (one blob). In a more realistic model, it is assumed that we are seeing several blobs (or plasmoids) in emission region. The blobs are

merged together to form a continuous jet, and a stationary pattern is seen by the observer. So, the continuous jet could be a steady stream of isotropically emitting optically thin material or a series of optically thick spheres. In the observer's frame Σ , the lifetime of one emitting particle is smaller than that in Σ' by a factor of δ . Accounting for the relativistic time dialation, equation (2.59) gives:

$$S_\nu = \delta^{2-\alpha} S'_\nu. \quad (2.62)$$

Therefore in the continuous jet, the intrinsic brightness temeprature will be Doppler boosted by a factor of $\delta^{2-\alpha}$.

Chapter 3

Physics of Compact Radio Sources

3.1 Compact radio sources

Compact radio sources are generally defined as radio sources whose flux at an intermediate radio frequency, e.g., ~ 1 GHz, is dominated by the contribution of a single bright component smaller than ~ 1 kpc in size. Compact radio sources usually have flat radio spectra and exhibit pronounced radio variability. In addition, the ratio of optical to radio flux tends to be higher in these objects than in steep-spectrum sources, making their identification easier (Blandford & Königl 1979).

The radio emission from parsec-scale jets in compact radio sources is partially optically thin synchrotron emission with characteristic spectral and polarization properties, as well as significant inverse-Compton emission (see Marscher 1990; Hughes & Miller 1991). The flat spectra of the radio emission is generally interpreted as the superposition of the incoherent synchrotron radiation from a non-thermal distribution of relativistic electrons located in several distinct components (Kellermann & Pauliny-Toth 1969; Marscher 1995). The individual components form the compact structure, the compact base of the jet, and the bright regions within the jet flow. The physical processes of the formation of “inner jets” that connect the nucleus to the observed radio jet, their acceleration to the relativistic speed (near the speed of light), and the strong collimation of the jets up to large scales (pc to kpc) are extensively investigated but remain poorly understood (e.g., Marscher 2006; Lobanov & Zensus 2006; Lobanov 2007).

Physical aspects of compact radio sources are discussed in this chapter. First, an introductory review of synchrotron radiation is presented including a brief discussion of synchrotron self-absorption. Then, the limits of the brightness temperature are discussed in detail. Relativistic jets as compact radio sources are discussed, and finally applications of VLBI observations for investigate the compact radio sources are summarized.

3.2 Synchrotron Radiation

When charged particles, in particular electrons or positrons, are forced to move in a curved path, photons are emitted. At relativistic velocities, i.e. when the particles are moving at a velocity very close to the speed of light, these photons are emitted in a narrow cone in the forward direction, at a tangent to the orbit. For high energy electrons or positrons spiraling through magnetic fields in space, these photons are emitted with a wide range of energies. This radiation is called *Synchrotron Radiation*. It was first proposed as a concept by Schwinger (1949) and soon suggested as the source of radio emission from the newly discovered cosmic radio sources by Alfvén & Herlofson (1950). Synchrotron radiation has a number of unique properties:

1. Synchrotron radiation is extremely intense and highly collimated.
2. Synchrotron radiation is emitted with a wide range of energies, allowing a beam of any energy to be produced.
3. Synchrotron radiation is highly polarized.
4. It is emitted in very short pulses, typically less than a nano-second (a billionth of a second).

The synchrotron radio emission can be observed in many classes of astrophysical objects such as:

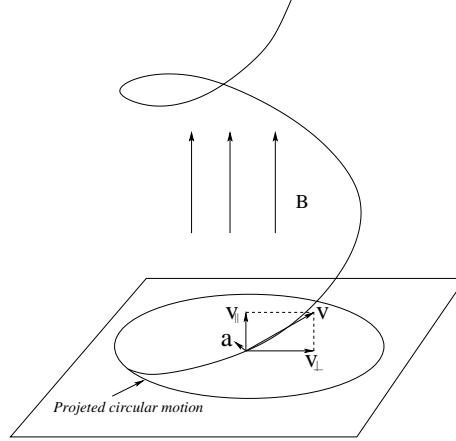


Figure 3.1: A schematic for helical motion of a particle in a uniform magnetic field.

1. jets of compact radio sources
2. supernova and supernova remnants
3. stars (non-thermal radiation)
4. galaxy and cluster halos.

In the following section, we derive the power radiated by a single charged particle moving relativistically in a homogeneous magnetic field. The spectrum it emits is discussed in section 3.2.2. The associated properties of the synchrotron radiation is reviewed in section 3.2.3. We follow closely the mathematical argumentation of Rybicki & Lightman (1979). A detailed and thorough discussion on the physics of synchrotron radiation can be found in Jackson (1975) and Shu (1991).

3.2.1 Total radiated power

A particle of mass m and charge q in a magnetic field \mathbf{B} is moving with a velocity \mathbf{v} . The motion of the particle can be found by using the representation of the Lorentz force equations;

$$\frac{d}{dt}(\gamma m \mathbf{v}) = \frac{q}{c} \mathbf{v} \times \mathbf{B} \quad (3.1)$$

$$\frac{d}{dt}(\gamma m c^2) = q \mathbf{v} \cdot \mathbf{E} = 0, \quad (3.2)$$

where $\gamma = (1 - v^2/c^2)^{-1/2}$. Since (3.2) indicates that $\gamma = \text{constant}$ or that $|\mathbf{v}| = \text{constant}$, (3.1) can be rewritten as

$$m \gamma \frac{d\mathbf{v}}{dt} = \frac{q}{c} \mathbf{v} \times \mathbf{B}. \quad (3.3)$$

If the velocity \mathbf{v} is divided into two components along the field, \mathbf{v}_{\parallel} , and in a plane normal to the field \mathbf{v}_{\perp} , from (3.3) we have

$$\begin{aligned} \frac{d\mathbf{v}_{\parallel}}{dt} &= 0, \\ \frac{d\mathbf{v}_{\perp}}{dt} &= \frac{q}{\gamma m c} \mathbf{v}_{\perp} \times \mathbf{B}. \end{aligned} \quad (3.4)$$

From (3.4) it follows that $\mathbf{v}_{\parallel} = \text{constant}$, and since the total $|\mathbf{v}| = \text{constant}$, also $|\mathbf{v}_{\perp}| = \text{constant}$. The constant \mathbf{v}_{\perp} and the acceleration normal to the velocity imply a uniform circular motion of the projected motion. These motions imply that the particle produces a *helical* motion in a uniform magnetic field \mathbf{B} (Figure 3.1).

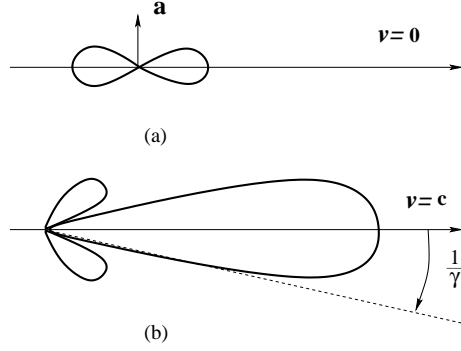


Figure 3.2: Radiation patterns: (a) Dipole radiation pattern for particle at rest, and (b) Angular distribution of radiation emitted by a particle with perpendicular acceleration and velocity.

The emission from a single accelerated charge q is given by the *Larmor's formula*:

$$P = \frac{2q^2}{3c^3} \mathbf{a}' \cdot \mathbf{a}', \quad (3.5)$$

where \mathbf{a}' is the acceleration in the rest frame of a particle. Since the acceleration in the rest frame of the particle \mathbf{a}' is related to the observer's frame \mathbf{a} as

$$a'_{\parallel} = \gamma^3 a_{\parallel}, \quad (3.6)$$

$$a'_{\perp} = \gamma^2 a_{\perp}, \quad (3.7)$$

(3.5) can be rewritten as

$$P = \frac{2q^2}{3c^3} (a'_{\parallel}{}^2 + a'_{\perp}{}^2) = \frac{2q^2}{3c^3} \gamma^4 \left(\frac{qB}{\gamma mc} \right)^2 v_{\perp}^2. \quad (3.8)$$

Here we have taken the acceleration perpendicular to the velocity as $a_{\perp} = \omega_B v_{\perp}$, where $\omega_B = \frac{qB}{\gamma mc}$, the frequency of the rotation. Taking into account an isotropic distribution of velocities, the total emitted radiation is given by

$$P = \frac{4}{3} \sigma_T c \beta^2 \gamma^2 U_B, \quad (3.9)$$

where $\sigma_T = 8\pi r_0^2/3$ is the Thompson cross section, $\beta = v/c$, and U_B is the magnetic energy density, $U_B = B^2/8\pi$.

3.2.2 Spectrum of synchrotron radiation

The spectrum of synchrotron radiation must be related to the detailed variation of the electric field as seen by an observer. Because of the *beaming* effect the emitted radiation field appears to be concentrated in a narrow set of directions about the particle's velocity. In the case of the synchrotron radiation, the velocity and acceleration are perpendicular, so the appropriate scheme is like the one in Figure 3.2 (panel (b)). The observer will see a pulse of radiation confined to a time interval much smaller than the period of the projected circular motion. The spectrum will thus be spread over a much broader region than one of order $\omega_B/2\pi$. This is an essential feature of synchrotron radiation.

For the highly relativistic case ($\beta \approx 1$), the power per unit frequency emitted by each electron is given by

$$P(\omega) = \frac{\sqrt{3}}{2\pi} \frac{q^3 B \sin \theta}{mc^2} F \left(\frac{\omega}{\omega_c} \right), \quad (3.10)$$

where θ is the angle between field and velocity (*pitch angle*), $\omega_c = \frac{3\gamma^2 qB \sin \theta}{2mc}$ and F is a dimensionless function.

In the equation (3.10), there is no factor of γ except for the one in the term of ω_c . With this, we are able to derive a very important result related to synchrotron spectra. In astronomy, it is usual for the spectrum to be approximated by a power law over a limited range of frequency as

$$P(\omega) \propto \omega^\alpha, \quad (3.11)$$

where α is called the *spectral index*. The spectral index of astronomical radiation is often constant over a fairly wide range of frequencies (e.g. $\alpha = 2$ for Rayleigh-Jeans portion of the blackbody law).

The power law is also applicable to the particle distribution of relativistic electrons. The number density of particles with energies between E and $E + dE$ (or γ and $\gamma + d\gamma$) can be approximately expressed as

$$N(E)dE = CE^{-s}dE, \quad E_1 < E < E_2, \quad (3.12)$$

or

$$N(\gamma)d\gamma = C\gamma^{-s}d\gamma, \quad \gamma_1 < \gamma < \gamma_2, \quad (3.13)$$

where the quantity C can vary with pitch angle and the like. The total power radiated per unit volume per unit frequency by such a distribution is given by

$$P_{\text{tot}}(\omega) = C \int_{\gamma_1}^{\gamma_2} P(\omega)\gamma^{-s}d\gamma \propto \int_{\gamma_1}^{\gamma_2} F\left(\frac{\omega}{\omega_c}\right)\gamma^{-s}d\gamma. \quad (3.14)$$

Here we have taken the integral of $N(\gamma)d\gamma$ times the single particle radiation formula over all γ . By changing variables of integration to $x \equiv \omega/\omega_c$ and considering $\omega_c \propto \gamma^2$, (3.14) can be rewritten as

$$P_{\text{tot}}(\omega) \propto \omega^{(1-s)/2} \int_{x_1}^{x_2} F(x)x^{(s-3)/2}dx, \quad (3.15)$$

where the limits $x_{1,2}$ correspond to the limits $\gamma_{1,2}$ and depend on ω . If the energy limits are sufficiently wide we can approximate $x_1 \approx 0$, $x_2 \approx \infty$, so that the integral is approximately constant. If this is the case, (3.15) can be simplified as

$$P_{\text{tot}}(\omega) \propto \omega^{(1-s)/2} \quad (3.16)$$

so that the spectral index α is related to the particle distribution index s by

$$\alpha = \frac{1-s}{2}. \quad (3.17)$$

3.2.3 Synchrotron self-absorption

Synchrotron emission from compact radio sources is accompanied by absorption, in which a photon interacts with a charged particle (e.g. electron) in a magnetic field and is absorbed, giving up its energy to the particle. Another process that can occur is stimulated emission, in which a particle is induced to emit more strongly into a direction and at a frequency where photons already are present. In order to find out the spectrum of synchrotron self-absorption, Longair (1981) gives some physical arguments. Here we largely follow their arguments to obtain the spectrum of synchrotron self-absorbed sources.

If a source has the same physical size at all frequencies, its brightness temperature is, considering (3.11),

$$T_b = \left(\frac{\lambda^2}{2k}\right) \left(\frac{S_\nu}{\Omega}\right) \propto \nu^{\alpha-2}, \quad (3.18)$$

where S_ν is the flux density of the source and Ω is its solid angle. Therefore, at low frequencies, the self-absorption effects become important since the brightness temperature of the radiation may approach the kinetic temperature of the radiating particles.

The synchrotron radiation spectrum has been derived assuming a power-law energy distribution of relativistic electrons in (3.12). Although this energy spectrum is not a thermal equilibrium spectrum, the argument with temperature can still be valid for two reasons;

1. The spectrum of the radiation emitted by particles of energy E is peaked about the critical frequency $\nu \approx \nu_c \approx \gamma^2\nu_g$, where $\gamma = E/m_e c^2 \gg 1$ and $\nu_g = eB/2\pi m_e$ is the non-relativistic gyrofrequency. Thus, the emission and absorption processes at frequency ν are associated with electrons of roughly the same energy.

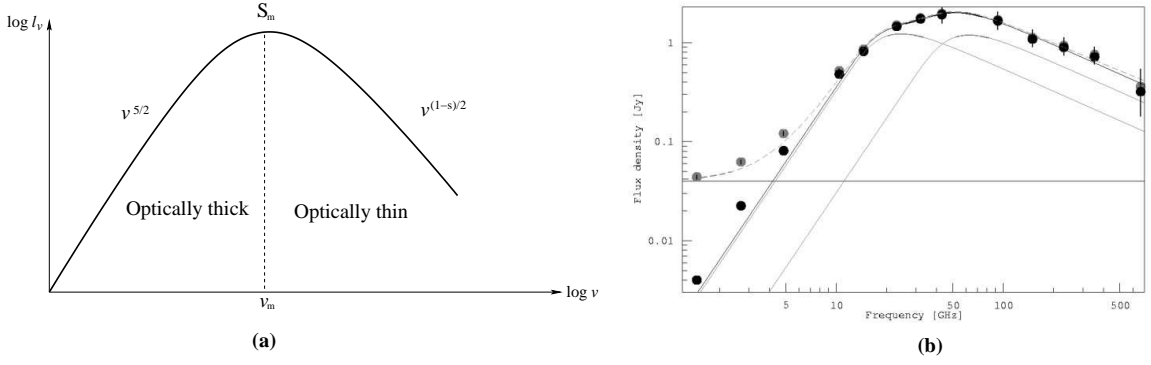


Figure 3.3: (a) Synchrotron spectrum from a power-law distribution of electrons. The dashed line divides the spectrum into two parts for optically thick and thin regions. (b) Synchrotron self-absorbed spectrum of III Zw 2, taken from Falcke et al. (1999). After subtraction of a constant background (grey points), the resulting data (black points) can be well reproduced with a superposition of two self-absorbed synchrotron spectra with spectral indices $\alpha = 2.5$ in the optically thick and $\alpha = -0.75$ in the optically thin region.

2. The timescale for the relativistic electron gas to be in an equilibrium condition is very long, because the electron number densities are very low. Therefore, a temperature T_e can be associated with electrons of a given energy through the relativistic formula which relates particle energy to temperature: $\gamma m_e c^2 = 3kT_e$.

Thus, the temperature T_e of the electrons becomes a function of their energy:

$$T_e \approx \left(\frac{m_e c^2}{3k} \right) \left(\frac{\nu}{\nu_g} \right)^2. \quad (3.19)$$

Here we have considered $\gamma \approx (\nu/\nu_g)^{1/2}$ and T_e is called the *effective temperature* or the kinetic temperature of the electrons. For a self-absorbed source, the brightness temperature of the radiation must be equal to the kinetic temperature of the emitting particles, $T_b = T_e$, yielding in the Rayleigh-Jeans limit

$$S_\nu = \frac{2kT_e}{\lambda^2} \Omega = \frac{2m_e c^2}{3} \frac{c^2}{\lambda^2} \left(\frac{\nu}{\nu_g} \right)^{1/2} \Omega. \quad (3.20)$$

If we assume that the physical size of the source is the same at all frequencies and the magnetic field is constant, then $\Omega = \text{constant}$ and $\nu_g = \text{constant}$. From (3.20) the spectrum of synchrotron self-absorption is given as:

$$S_\nu \propto \nu^{5/2}. \quad (3.21)$$

It is of interest that the spectrum is a power law with an index $\frac{5}{2}$, independent of the value of the particle distribution index s . It should be particularly noted that this index is not equal to 2, the Rayleigh-Jeans value, because the emission is non-thermal.

For optically thin synchrotron emission, the observed intensity is proportional to the source function. Since the emission and source functions for a non-thermal power law electron distribution are proportional to $\nu^{(1-s)/2}$ and $\nu^{5/2}$, respectively, [see equations (3.16) and (3.21)], we see that the optically thick region occurs at low frequencies and produces a low frequency cutoff of the spectrum (Figure 3.3). For a uniform source of angular size θ , a redshift z , magnetic field B , and for a power law distribution of particle energy given by (3.13), the frequency ν_m (*turnover frequency*), where the flux density reaches a maximum value S_m , is given approximately by Kellermann & Pauliny-Toth (1981):

$$\nu_m \sim f(s) \left(\frac{B}{1 \text{ G}} \right)^{1/5} \left(\frac{S_m}{1 \text{ Jy}} \right)^{2/5} \left(\frac{\theta}{1 \text{ mas}} \right)^{-4/5} (1+z)^{1/5} \text{ GHz}. \quad (3.22)$$

The function $f(s)$ only weakly depends on s , and for $s = 2$, $f(s) \sim 8$.

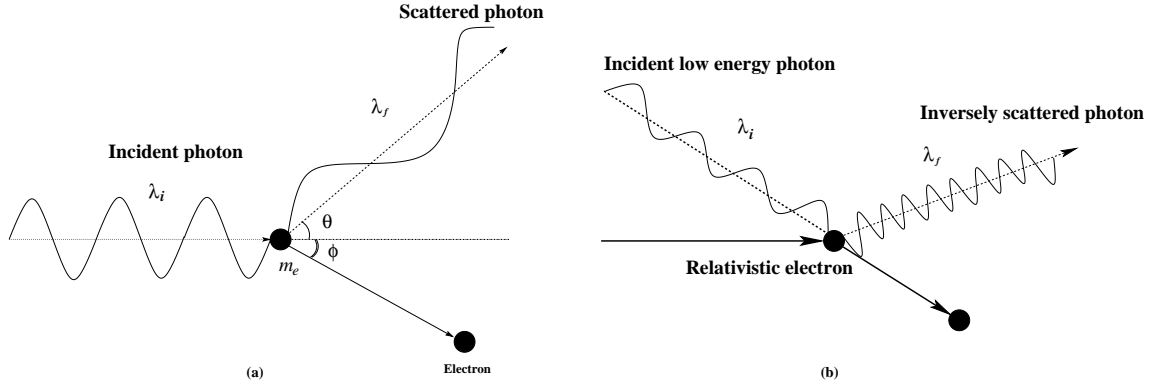


Figure 3.4: (a) The Compton effect: The scattering of a photon by a free electron. (b) The inverse Compton effect: The scattering of a low energy photon by a relativistically moving electron.

3.3 Brightness temperature (T_b) limits

3.3.1 Inverse Compton scattering

When a beam of radiation is scattered by a stationary electron, the scattering can be described by *Thomson scattering*, introducing the *Thomson cross-section*,

$$\sigma_T = \frac{8\pi}{3} r_e^2, \quad (3.23)$$

where r_e is the classical electron radius. The scattering is symmetric with respect to the scattering angle α and the scattered radiation is polarized, even if the incident beam of radiation is unpolarized. In the case of Thomson scattering, there is no change in the frequency of the radiation. In general, as long as the energy of the photon is less than the rest mass energy of the electron, $\hbar\omega \ll m_e c^2$, in the center of the momentum frame of reference, the scattering may be accurately treated as Thomson scattering. In the case of compact radio sources, however, the frequency change associated with the collision between the electron and the photon is important, since there are relativistic electrons and high energy photons interacting with each other in the compact radio sources.

When the incoming high energy photons collide with electrons at rest and increase the energy and momentum of the electrons by transferring some of their energy, the photons, as a result, have less energy and momentum than before. The loss of the energy of the photon corresponds to an increase in its wavelength, since the energy and momentum are proportional to the frequency of the radiation, $E = \hbar\nu$ and $p = \hbar\nu/c$. The final wavelength of the photon, λ_f , is greater than its initial wavelength, λ_i , by the amount,

$$\Delta\lambda = \lambda_f - \lambda_i = \frac{h}{m_e c} (1 - \cos\theta), \quad (3.24)$$

where m_e is the mass of the electron and θ is the angle by which the photon is scattered (Figure 3.4a). This change in wavelength is known as the *Compton effect*. The term $h/m_e c$ in (3.24), called the *Compton wavelength* ($\equiv \lambda_C$), is the characteristic change in the wavelength of the scattered photon.

Whenever the energy of the moving electron is sufficiently comparable to the photon energy, then there is a transfer of energy from the electron to the photon, in contrast to the situation of Compton scattering. In such a case the scattering process is called *inverse Compton* (Figure 3.4b). The net power lost by the electron, and thereby converted into increased radiation is,

$$P_{\text{compt}} = \frac{dE_{\text{rad}}}{dt} = \frac{4}{3} \sigma_T c \gamma^2 \beta^2 U_{\text{ph}}. \quad (3.25)$$

Using (3.9), we obtain the interesting result:

$$\frac{P_{\text{synch}}}{P_{\text{compt}}} = \frac{U_B}{U_{\text{ph}}}, \quad (3.26)$$

which implies that the radiation losses due to synchrotron emission and the inverse Compton effect have the same ratio as the magnetic field energy density and photon energy density. It should be noted that this result does not depend on the value of the electron's velocity, β , but on the validity of Thomson scattering in the rest frame so that $\gamma\epsilon \ll mv^2$.

From (3.25) for the inverse Compton power for a single scattering, we can calculate the total Compton power, per unit volume, from a homogeneous and isotropic medium of relativistic electrons. Assuming the number of electrons per unit volume with γ in the range γ to $\gamma + d\gamma$ is given by $N(\gamma)d\gamma$ with

$$N(\gamma) = \begin{cases} C\gamma^{-p}, & \text{if } \gamma_{\min} \leq \gamma \leq \gamma_{\max} \\ 0, & \text{otherwise,} \end{cases} \quad (3.27)$$

then, with $\beta \sim 1$, we obtain

$$\begin{aligned} P_{\text{tot}}(\text{erg s}^{-1} \text{ cm}^{-3}) &= \int P_{\text{compt}} N(\gamma) d\gamma \\ &= \frac{4}{3} \sigma_T c U_{\text{ph}} C (3-p)^{-1} (\gamma_{\max}^{3-p} - \gamma_{\min}^{3-p}). \end{aligned} \quad (3.28)$$

In the case of a thermal distribution of nonrelativistic electrons of a number density n_e , we can also compute the total power as,

$$P_{\text{tot}}(\text{erg s}^{-1} \text{ cm}^{-3}) = \left(\frac{4kT}{mc^2} \right) \sigma_T c n_e U_{\text{ph}}. \quad (3.29)$$

Here we took $\gamma \approx 1$ and $\langle \beta^2 \rangle = \langle v^2/c^2 \rangle = 3kT/mc^2$.

3.3.2 Inverse Compton limits of T_b

Kellermann & Pauliny-Toth (1969) presented the inverse Compton cooling arguments in terms of the peak brightness temperature, T_b , which could be directly related to observation. They showed that the ratio of inverse Compton radiation to incoherent synchrotron radiation, L_{IC}/L_S , is the ratio of the energy density in the radiation field to that in the magnetic field, u_γ/u_B , which is simply a function of T_b :

$$\frac{L_{\text{IC}}}{L_S} = \frac{u_\gamma}{u_B} \sim \frac{1}{2} \left(\frac{T_b}{10^{12}} \right)^5 \nu_c \left[1 + \frac{1}{2} \left(\frac{T_b}{10^{12}} \right)^5 \nu_c \right], \quad (3.30)$$

where ν_c is the upper cutoff frequency of the radio spectrum in MHz. The first and the second term in (3.30) represent the effect of the first-order and the second-order scattering respectively. If $T_b \geq 10^{12}$ K, the ratio is dominated by the second term - hence $L_{\text{IC}}/L_S \sim (T_b/10^{11})^{10}$ for $\nu_c \sim 10^5$ MHz. Therefore, whenever the brightness temperature is greater than 10^{12} K, inverse Compton scattering of the radio photons dominates, and most of the energy will be radiated away in X-rays in a short time scale (e.g. a day). The relationship (3.30) was re-derived as equations (1a) and (1b) in Readhead (1994), taking into account the spectral properties of the emission region. For a typical powerful extragalactic radio source at $z = 1$, with spectral index $\alpha = -0.75$ ($S \propto \nu^\alpha$), the observed frequency of the peak in the spectrum $\nu_{\text{op}} = 3.5$ GHz, and the upper cutoff frequency of the radio spectrum $\nu_{\text{high}} = 100$ GHz, the relationship can be simplified as

$$\frac{L_{\text{IC}}}{L_S} = \left(\frac{T_b}{10^{11.45}} \right)^5 \left[1 + \left(\frac{T_b}{10^{11.45}} \right)^5 \right], \quad (3.31)$$

Although this result also explains well the inverse Compton catastrophe for $T_b \sim 10^{12}$ K, Readhead (1994) found a more realistic limit of T_b with the study of the radiative cooling timescale. The timescale for radiative cooling by combined synchrotron and inverse Compton radiation can be written as

$$\tau_{\text{IC+S}} = 6\nu_{\text{op}}^{-2} f_3(\alpha)^{-3} \left(\frac{T_b}{10^{11}} \right)^3 \left(1 + \frac{L_{\text{IC}}}{L_S} \right)^{-1} \text{ yr}, \quad (3.32)$$

where $f_3(\alpha)$ is given by equation (15c) of Scheuer & Williams (1968). Readhead (1994) found that the maximum values of the radiative loss timescales for radio sources which have spectral turnovers, caused by synchrotron self-absorption, at frequencies from 62.5 MHz to 16 GHz, occur around 3×10^{11} K, which is a more plausible limit of T_b than the one from Kellermann & Pauliny-Toth (1969). It should be noted that the inverse Compton limit of T_b , $T_{b,\text{max}}$, reported in Kellermann & Pauliny-Toth (1969) is in the range of 10^{11-12} K instead of the upper value of the range, 10^{12} K (Kellermann 2003), whereas Readhead (1994) estimated the exact value of 3×10^{11} K for $T_{b,\text{max}}$.

3.3.3 Equipartition limits of T_b

Readhead (1994) found that there is an alternative limit to the brightness temperature, T_b , for synchrotron self-absorption dominated radio sources (between parsec and kiloparsec, observed at frequencies less than 1 GHz). This limit is based on the assumption that the fractions of energy density in relativistic particles (e.g. electrons) and magnetic fields are in equipartition (Burbidge & Burbidge 1957). He suggested that perhaps parsec-scale jets are in equipartition as well. Following his argument, the *equipartition brightness temperature* is defined as,

$$T_{\text{eq}} = \left(\frac{2c^2}{\pi k_B} \right) \left(\frac{S}{\theta_{\text{eq}}^2} \right) \nu^{-2}, \quad (3.33)$$

where θ_{eq} is the equipartition angular size (radius) of the radio source. It should be noted that T_{eq} depends only weakly on the observed peak frequency and flux density. Assuming that we observe a radio source at the peak frequency (e.g. 3.5 GHz) of the synchrotron self-absorption spectrum with $\alpha = -0.75$ ($S \propto \nu^\alpha$), and the flux density of the source at $z = 1$ is 1 Jy, the equipartition brightness temperature of the source in the rest frame is given by

$$T_{\text{eq}} = 5 \times 10^{10} h^{-\frac{1}{8.5}} \delta^{\frac{11.5}{17}} \text{ K}, \quad (3.34)$$

where δ is the Doppler factor. We assume here an Einstein-de Sitter universe with $H_0 = 100h$ km/s/Mpc. It is noted that the radio sources may radiate at an equipartition brightness temperature around 5×10^{10} K in most circumstances. In fact, if the sources are in rough equipartition between particle energy and magnetic energy the inverse Compton limit (3×10^{11} K) cannot be reached.

3.3.4 Relaxation of the limits of T_b

The real brightness temperatures of many compact radio sources may reach a much higher value, violating the equipartition limit of 5×10^{10} K or the inverse Compton limit of $1 - 10 \times 10^{11}$ K. The violation of the brightness temperature limits can be explained by Doppler boosting, transient non-equilibrium events, coherent emission, emission by relativistic protons, or a combination of these effects (e.g., Kardashev 2000; Kellermann 2003).

1. Doppler boosting

If the emission region in the compact radio sources are relativistically moving toward the observer, the radiation from the region can be amplified, or Doppler boosted, causing the observed brightness temperature to be apparently in excess of the limits of brightness temperature (*Doppler boosting*). Doppler boosting of the brightness temperature in distant sources due to their redshift z is given by the cosmologically corrected *Doppler factor*, \mathcal{D} (Lind & Blandford 1985),

$$\mathcal{D} = \frac{\delta}{1+z}, \quad (3.35)$$

where $\delta = \gamma^{-1}(1 - \beta \cos \theta)^{-1}$, $\gamma = (1 - \beta^2)^{-1/2}$, $\beta = v/c$, and v is the velocity of a source moving at an angle θ to the line of sight. \mathcal{D} is the ratio of the brightness temperature in the observer's frame to the temperature at the rest frame where the synchrotron emission is isotropic. The flux density in the observer's frame is boosted by $\mathcal{D}^{p-\alpha}$, where α is the spectral index ($S_\nu \propto \nu^\alpha$), $p = 2$ for a continuous jet and $p = 3$ for discrete features because of the relativistic time dilation of the features' finite synchrotron-emitting lifetime. A more detailed discussion can be found in section 2.4.3.

2. Non-stationary sources

Extremely high brightness temperatures can be achieved in non-stationary sources either by injecting electrons at high energy, or by balancing their cooling against a powerful acceleration mechanism (Slysh 1992). In order to explain the excess of limits of brightness temperature, Slysh (1992) introduced a model for a monoenergetic electron distribution in a strongly absorbed source. Two scenarios were considered; (1) a time-dependent case in which electrons were injected at high Lorentz factor and then cooled, and (2) another case in which a strong continuous re-acceleration of the electron resulted in a high brightness temperature equilibrium. In the first scenario in which high energy particles are injected into the source, a brightness temperature of $T_b > 5 \times 10^{15}$ K can be sustained over 1 day at a frequency of 1 GHz. In the second, a powerful acceleration balances inverse Compton losses to provide a brightness temperature of 10^{14} K at 1 GHz.

3. Coherent emission

The Compton limit of brightness temperature applies only to incoherent synchrotron radiation. Coherent emission mechanisms can be invoked for the compact radio sources to overcome the violation of the inverse Compton limit of brightness temperature. Colgate (1967) proposed a specific plasma emission model for coherent emission mechanism for compact radio sources. In his model, the observed emission could be due to photons with twice the plasma frequency (ω_p) in the nonlinear interactions of plasma waves. These photons are subsequently scattered by the plasma waves and shifted in frequency by $\pm\omega_p$ in each event. By this mechanism, photons escape with high energies when their mean free path is comparable with the size of the source. Weatherall & Benford (1991) found that for the inhomogeneous beam of electrons, the radiation by beam scattering on turbulent electrostatic fields becomes partially coherent and that a specific model for beam density fluctuation statistics yields a power-law radiation spectrum greatly exceeding synchrotron emission. Although more suggestions for a coherent emission from compact radio sources are given by Lesch & Pohl (1992), Krishan & Wiita (1994), and Benford & Lesch (1998), the arguments against coherent emission point out that existing models for coherent emission in compact radio sources have not taken into account how the microphysics is related to macroscopic model (Melrose 2002), including the source of the free energy, the emission mechanism itself, and the escape of the radiation.

4. Relativistic protons

The synchrotron emission by relativistic protons can have a higher brightness temperature than by relativistic electrons. In Jukes (1967) the proton synchrotron emission was first considered to explain the radio emission from the central regions of compact radio sources, and an analogous mechanism for the emission from pulsars was discussed in Pacini & Rees (1970). Since the limit of the brightness temperature T_b scales with the mass of the particle as $T_b \propto m^{9/7}$ (Kardashev 2000), the ratio of the mass of the proton to the mass of the electron gives a factor of $(m_p/m_e)^{9/7} = 1.6 \times 10^4$, changing the limit of 10^{12} K into 1.6×10^{16} K. This model requires that the source be optically thick to proton synchrotron emission and optically thin to electron synchrotron emission, preventing synchrotron absorption by relativistic electrons from reducing the brightness temperature to the self-absorption limit for electrons, which is 10^{12} K.

3.4 Relativistic jets as compact radio sources

3.4.1 Relativistic outflows

Relativistic outflow (or jet) is a common phenomenon in GRB (Gamma-Ray Burst), AGN (Active Galactic Nucleus), and XRB (X-Ray Binary or “microquasar”) sources. GRBs evidently involve ultra-relativistic ($\gamma_\infty \sim 10^2 - 10^3$), highly collimated ($\theta_j \sim 2^\circ - 20^\circ$) outflows of typical kinetic energy $E_K \sim 10^{51}$ ergs (Kulkarni et al. 1999; Greiner et al. 2003). They are likely powered by extraction of rotational energy from a newly formed stellar-mass black hole or rapidly rotating neutron star, or from a surrounding debris disk (see Piran 2005). Magnetic fields provide the most plausible means of extracting the energy on the burst timescale (Meszaros & Rees 1997; Di Matteo et al. 2002). They can also guide, collimate, and accelerate the flow (Vlahakis & Königl 2003).

Relativistic outflows in the powerful AGN have apparent “superluminal” motions (see section 3.5.1) of the apparent velocities β_{app} as high as $\sim 45c$ (e.g., Jorstad et al. 2005) in the radio regime and rapid flux and polarization variability of a relativistic outflow component on scales ≤ 1 pc. Although the jets may also contain nonrelativistic components, there is evidence that the relativistic component persists to large scales from kpc to Mpc (e.g., Walker et al. 2001). While the matter content of the relativistic outflow remains uncertain, there are indications that protons dominate the mass flux even as electron-positron pairs dominate the particle flux in relativistic AGN jets (Sikora & Madejski 2000). Magnetic fields are considered the most likely driving mechanism in this scale as well (Blandford & Znajek 1977; Blandford & Payne 1982).

Relativistic outflow in Galactic X-Ray binary sources (or microquasars) was first discovered by Mirabel & Rodríguez (1994) and was secondly reported in another source from radio observations by Tingay et al. (1995). The discovery makes it possible to explore the mechanisms by which accreting black holes and neutron stars produce highly collimated outflows with velocities close to the speed of light c (Mirabel & Rodríguez 1998). Although the measured apparent superluminal motions in XRB sources ($\beta_{app} \sim 2 - 5c$) appear to be lower than in AGN (Mirabel & Rodríguez 1999), a value of $\geq 15c$ has already been measured in Cir X-1 (Fender et al. 2004a), and it has been argued that the jet Lorentz factors might be comparable

to those of AGN (Miller-Jones et al. 2006). The distinct X-ray states (e.g., low/hard and high/soft states) and the well-defined differences in outflow properties demonstrate that the relativistic outflow is intimately connected with the central engine (e.g., Fender et al. 2004b).

Since the relativistic jet is the ubiquitous phenomenon in the most prominent astronomical objects, including AGN, we can obtain powerful insights into the processes governing the creation, physics, and behavior of relativistic jets by studying, comparing, and contrasting the different properties of these objects. In order to facilitate this endeavor, the relativistic jets in AGN as compact radio sources have been extensively studied with both theoretical and observational approaches by thousands of astronomers and astrophysicists. However, in an attempt to get astrophysical insights into the parsec-scale region of the relativistic jets, where the radio emission at mm wavelengths in VLBI observation is dominated, this short section of “relativistic jets” concentrates on the aspects of the relativistic jets in AGN that appear to relate most closely to the parsec-scale region: innermost region of relativistic jets, accelerating and decelerating jet models, and composition of the relativistic jet in AGN.

3.4.2 Innermost region of relativistic jets

Jet formation

Relativistic jets in AGN are formed in the immediate vicinity of the central black hole, and they interact with every major constituent of AGN (see Lobanov & Zensus 2006). The relativistic jets are currently known to be driven from either the inner accretion disk (Hujeirat et al. 2003) or the ergosphere of a rotating black hole (Koide et al. 2002; Semenov et al. 2004; Komissarov 2005). The origin of the jet, however, is not directly imaged with the existing astronomical facilities. The most upstream feature in the radio jet (the core) in VLBI observation does not represent the origin of the jet. The core is *generally* believed to represent a section of the jet where the optical depth at the observing frequency is unity (Königl 1981; Lobanov 1998b; Lobanov & Zensus 1999). Through the region between the origin and the radio core of the jet, the energy from the origin is transferred to the core by a disturbance passing through it (Marscher & Gear 1985). The jet is known to be collimated and accelerated by a twisted, most likely a poloidal magnetic field (e.g., Meier et al. 2001), which could be perturbed and generate the disturbance, and to be structured with an extremely relativistic “spine” surrounded by a slower, funnel-shaped “sheath” (see, e.g., Punsly 1996; Meier 2003; McKinney 2005). In this model, the spine structure probably consists of electron-positron pairs and the sheath contains normal matter (electrons and protons).

Ultracompact jet

The physical conditions in the immediate vicinity of the central black hole, where the jets are formed, determine many aspects of the jet evolution at larger scales. The scale of this “ultracompact” region of the jet is estimated to be $\sim 0.1 - 10$ pc (Lobanov 1998b; Lobanov & Zensus 2006). While the jet seems roughly self-similar on parsec scales (Marscher 1995), it is not likely that the jet will remain so all the way down to its origin (or the launching site) adjacent to the central engine. This changing point is indicated by the frequency ν_m at which the spectrum of the source starts to be steep. Beyond this point the jet emission is optically thin. Impey & Neugebauer (1988) found that the frequency ν_m of compact radio sources is in the range of tens to > 1000 GHz. The angular size of the core at this point can be estimated by the value at 43 GHz (Marscher 2006), $R_{\text{cor},\nu_m} \sim R_{\text{cor},43}(43 \text{ GHz}/\nu_m)$, where $R_{\text{cor},43} \sim 50 \mu\text{as}$. For a source with a redshift of order 0.5 and $\nu_m \sim 86$ GHz, the size translates to ~ 0.15 pc, and if the source has the frequency $\nu_m \sim 1000$ GHz then it is 0.013 pc (a few 10^{16} cm), which is small but still hundreds of gravitational radii even for $M_{\text{BH}} \sim 10^9 M_{\odot}$.

The ultracompact jet becomes visible in the radio regime and is accessible to high-resolution VLBI observations (Junor et al. 1999; Krichbaum et al. 2006a). In many VLBI observations, the ultracompact jets observed on sub-parsec scales show strongly variable but weakly polarized emission, and in many cases, the emission is optically thick.

These characteristics of ultracompact jets as well as the fact that the core is usually the brightest component in the jet, can be explained by smooth changes in particle density of the flowing plasma (Lobanov & Zensus 1999). The acceleration of the flow is gradual, so that the greatest Doppler beaming occurs some distance from the central engine (see, e.g., Vlahakis & Königl 2004). Furthermore, the flow should start out very broad and become more collimated as it accelerates downstream. The acceleration and collimation of relativistic jets are observed with VLBI observations (Junor et al. 1999; Bach et al. 2005; Krichbaum et al. 2006a)

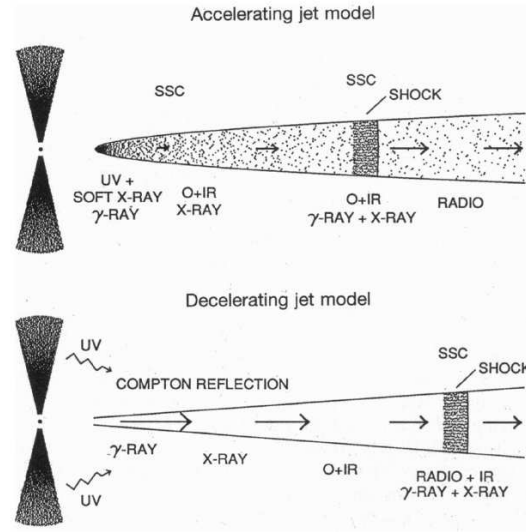


Figure 3.5: Sketch of accelerating jet model and decelerating jet model (taken from Marscher 1995).

There are other explanations for the ultracompact jets. One of them is that the core is a conical “re-collimation” shock that accelerates particles and amplifies the component of the magnetic field that is parallel to the shock front without decelerating the flow too severely (Daly & Marscher 1988; Gomez et al. 1995; Bogovalov & Tsinganos 2005). The expectation of this simplified model is quite comparable with VLBI observations (see Cawthorne 2006). According to this model the ultracompact jets would then be the first conical shock if it could be imaged at $\nu = \nu_m$. However, at lower frequencies the secondary standing shocks would be seen, which are indeed revealed in VLBI images (Jorstad et al. 2001; Kellermann et al. 2004).

3.4.3 Accelerating and decelerating jet models

There are at present two main models accounting for the observations of the relativistic jets. In the accelerating jet model (Blandford & Rees 1974; Maraschi et al. 1992) an external pressure (hydrostatic and/or magnetohydrodynamic) that decreases along the jet axis acts as a collimating agent. The internal energy of the plasma is converted to bulk kinetic energy and the jet is accelerated and focused. The electrons interact with a predominately random magnetic field and cool through synchrotron radiation and adiabatic expansion. In this model the synchrotron emission at UV, optical and IR frequencies is confined to the region closest to the central engine, opaque to the radio emission. The radio emission is produced outside this region, with the maximum intensity occurring where the Lorentz factor Γ is highest. Following this model, self-Compton scattered γ - and X-rays are produced in coincidence with the synchrotron emission in the UV, optical and IR bands closest to the central engine and in the radio core as well. Moreover, inverse Compton reflection of optical and UV photons produced by the accretion disk would take place in the vicinity of the central engine, again producing X- and γ -ray emission.

In a model considering a decelerating flow of relativistic positrons and electrons (Melia & Königl 1989), the jets are assumed to be accelerated to super-relativistic Lorentz factors by hydrodynamic and electromagnetic processes close to the black hole, and are Compton-dragged to $\Gamma_\infty \leq 10$. In this model the UV photons produced by the accretion disk are up-scattered to X- and γ -ray energies. Radio and infrared synchrotron emission (plus self-Compton scattered X- and γ -ray emission) is produced where the Lorentz factor decreases down to a value of ~ 10 .

As is shown in Figure 3.5 for the accelerating jet and decelerating jet models, the relative position of the emission region at each wavelength is quite model dependent. Both models connect the emission in the different wavelengths, and the location along the jet where the emission takes place, so in principle it

should be possible to discriminate between models and have some insight to the nature of the inner jets in compact radio sources by means of multifrequency observations. In particular, the careful measurement of the time lags, during outbursts, between various wavebands, principally the high and low energy bands, and the measurement of the relative amplitude of variability in the high and low energy bands can distinguish the two models. Another way to test these jet models is discussed in section 3.5.3.

3.4.4 Matter content of jets

One of the most important issues about the relativistic jets of compact radio sources is their nature and composition: *Are they made up of a normal (electron–proton) plasma, a pair (electron–positron) plasma, or a combination of the two?* Answering this question or constraining these possibilities is crucial for understanding the physical processes occurring within the relativistic jets. However, with the 40-years study of the relativistic jets, the question has been poorly answered. Arguments and evidence in favor of each composition are actively being advanced, but they are conflicting each other.

1. Electron–proton plasma: Heavy jets

The radio observations tell us that the relativistic electrons and the accompanying magnetic field must exist in the relativistic jet to produce the synchrotron emission. There is presumably another charged particle species carried outward with the electrons and magnetic field that provides charge neutrality, but its nature has remained generally obscure and observationally inaccessible. Hence, indirect arguments have been put forward to favor various candidates, such as positrons, protons, and possibly other species.

Celotti & Fabian (1993) advanced arguments in favor of electron–proton jets. Using synchrotron self-Compton constraints from radio-core observations and information about the energetics of jets from radio-lobe studies, they showed that in the case of pure electron-positron jets, the required number of electron-positron (e^+e^-) pairs is too high to be delivered from the central engine.

From X-ray observations of blazars associated with optically violent variable quasars, Sikora & Madejski (2000) place constraints on the pair content of the radio-loud quasar jets. They exclude both pure light jets, as these over-predict the soft X-ray flux, and pure heavy jets as these predict too weak non-thermal X-ray emission. Although the pair number density is larger than the proton number density, the jets would be dynamically dominated by the protons.

2. Electron–positron plasma: Light jets

Dunn et al. (2006) found that low power radio sources, such as M87 and Perseus (3C 84), are predominantly composed of an electron-positron pair plasma, while jets associated with powerful sources are energetically dominated by a proton component. They have, however, no robust explanation of such a discrepancy between results supporting electron-proton dominated jets and their work.

Circular and linear polarization observations of jets can be used to constrain the low-energy particle distribution, the magnetic field strength and the particle content. Depending on whether this is intrinsic to the synchrotron emission or produced by "Faraday conversion" of linear polarization to circular, different limits can be set on the low-energy particle distribution (e.g, Homan 2005).

Wardle et al. (1998) measured circular polarization from 3C 279 and, considering that most likely this results from Faraday conversion, set an upper limit $\gamma_{\min} < 20$, which would be evidence for electron-positron jets in this source. Further observations of PKS 0528+134, 3C 273 and even 3C 84, detected circular polarization, but no limits on γ_{\min} have been determined (Homan & Wardle 1999, 2004). In any case, more recently Ruszkowski & Begelman (2002) showed that the observations of 3C 279 could be consistent with both types of jet, by arguing that the linear and circular polarizations observed could, depending on the field configuration, be consistent with different plasma compositions. Therefore, no strong conclusion can (yet) be drawn on such measurements.

3.5 VLBI observations as a tool to investigate relativistic jets

The underlying physics of jets in compact radio sources can be revealed by high angular resolution VLBI observations, since many of the compact radio sources are so bright and highly variable, and emit over several decades in wavelengths. For about 40 years, many attempts using the VLBI technique to reveal the nature

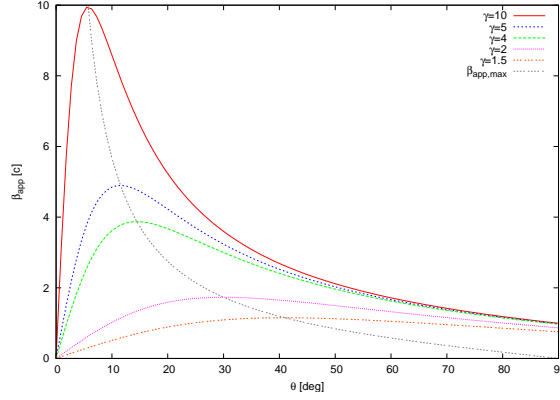


Figure 3.6: Apparent superluminal velocity as a function of the viewing angle θ for $\gamma=1.5, 2, 4, 5, 10$. The black dotted line shows the maximum velocity $\beta_{\text{app,max}} (= \beta\gamma)$ at the angle θ_{max} ($\cos\theta_{\text{max}} = \beta$).

of the compact radio sources have been made. As the VLBI technique is developed the attempts are largely stratified into four categories: multi-epoch observation, multi-frequency observation, polarization observation, and survey observation. For one particular source, it is natural to make a large observational campaign, including all of the first three categories for investigating the kinematics, spectral evolution, and polarization of the source. For statistical studies of many (e.g., > 100) sources or a pre-survey to support frontier projects (e.g. mm-VLBI or space-VLBI observation), a large survey should be made with a large (sometimes complete) sample. Here, we discuss the observable features of the compact radio sources through VLBI observations in the categories defined above except for polarization observation and in particular suggest the way to investigate the relativistic jet models with VLBI survey observations.

3.5.1 Multi-epoch VLBI observations

Since many of the compact radio sources are highly variable at radio frequencies, observing them in a very short time interval should give rise to very interesting results for possible structural changes. In the early 1970s, VLBI observation (Whitney et al. 1971) discovered an interesting phenomenon: the apparently faster-than-light expansion between components in the milliarcsecond-scale structure, referred to as *superluminal motion*, which had been predicted by Rees (1966). Since the first discovery, the phenomenon has been observed in many other compact radio sources (see Zensus & Pearson 1987). The apparently faster-than-light velocity β_{app} (in light speed units) is derived from a simple geometry that an emission region at a cosmological distance moves with a relativistic speed v at an angle θ to the line of sight, taking into account *time dilation* due to the relativistic Doppler effect:

$$\beta_{\text{app}} = \frac{\beta \sin \theta}{1 - \beta \cos \theta}, \quad (3.36)$$

where $\beta = v/c$ and c is the speed of light. When $\beta \rightarrow 1$ ($\gamma \gg 1$) the apparent velocity is very sensitive to the intrinsic velocity β and the viewing angle θ as shown in Figure 3.6. The maximum apparent velocity $\beta_{\text{app,max}}$ is obtained by solving $\frac{\partial \beta_{\text{app}}}{\partial \theta} = 0$:

$$\beta_{\text{app,max}} = \beta\gamma, \quad (3.37)$$

at the viewing angle $\theta_{\text{max}} = \cos^{-1} \beta$. The apparent velocity is also related with observational values such as redshift z , the dimensionless Hubble constant h (assuming that $H_0 = 100h$ km/s/Mpc), the cosmological density parameter of matter Ω_m , and the measured angular proper motion μ (in mas/year):

$$\beta_{\text{app}} = 94.9 \mu \frac{\Omega_m z + (\Omega_m - 2)(\sqrt{1 + \Omega_m z} - 1)}{h \Omega_m^2}. \quad (3.38)$$

Here we have taken $\beta_{\text{app}} = \mu D_L / c$, where D_L is the luminosity distance, given by:

$$D_L = \frac{2c}{H_0} \frac{[\Omega_m z + (\Omega_m - 2)(\sqrt{1 + \Omega_m z} - 1)]}{\Omega_m^2}. \quad (3.39)$$

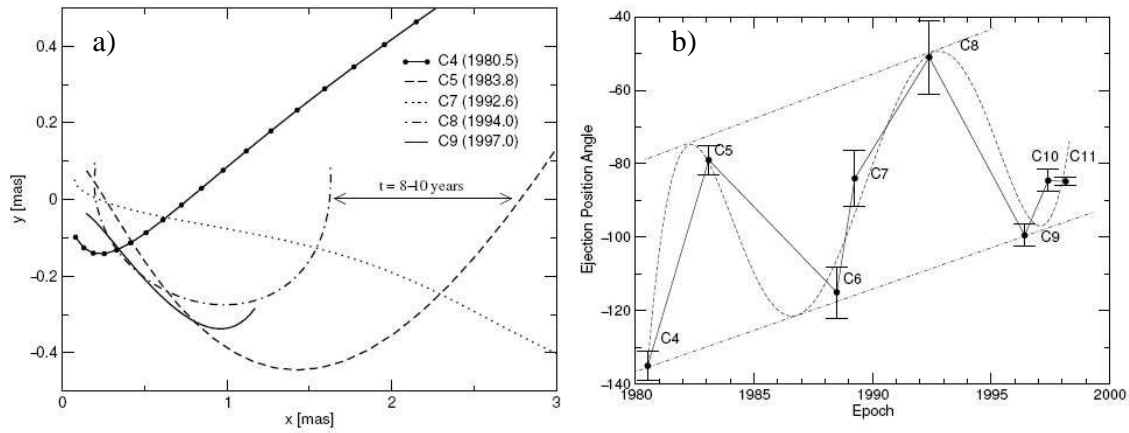


Figure 3.7: (a) Component tracks near the core of 3C345 and (b) position angle of the ejection point of the different components (they are referred to as C1,C2,C3,...etc) (taken from Klare et al. 2005).

Since for objects at $z \sim 1$ a superluminal motion at a velocity of $10c$ can be obtained from measuring a proper motion of a few tenths of a mas/year, one has to keep monitoring over many years for measuring velocities of $1c$ or even less.

Detailed long-term monitoring of 3C 345 for 20 years has shown that many jet components have been ejected and apparently speeded up to superluminal velocities (Unwin et al. 1983; Zensus et al. 1995a; Lobanov 1996; Ros et al. 2000; Klare et al. 2005). The speeds and paths of successive components are different and in particular the trajectories of successive components are strongly curved. The different paths and position angles of the different components are shown in Figure 3.7. The superluminal motion is known to be observed when the relativistic jets move with high Lorentz factor (e.g., $\gamma \sim 10$) at a very small angle to the line of sight. If the viewing angle θ is $\sim 1/\gamma$, the maximum apparent velocities $\beta_{app,max}$ of γc can be observed. In this case the small change in the true jet angle can be magnified and then produce the apparent velocity and angle changes. The detailed analysis of the long-term monitoring of the highly variable compact radio sources suggests a possible precession of the axis of the ejection (e.g., Klare et al. 2005; Agudo et al. 2005).

3.5.2 Multi-frequency VLBI observations

In the radio regime, the compact radio sources emit over several decades in wavelength. In order to investigate the physics of the compact radio sources, especially of the milliarcsecond-scale (or parsec-scale) jets, VLBI observations at several radio frequencies should be carried out. The compact “core” seen in the VLBI map at each frequency is to be understood as a region near the base of the jet where radio emission is first seen, at the transition point where its optical depth is turning over from optically thin to optically thick towards the origin of the jet. It was suggested and confirmed by VLBI observations that the core is closer to the jet base at higher frequencies, with a frequency dependence of roughly ν^{-1} (Lobanov 1998b). Figure 3.8 shows the frequency-dependency of a core position. Taking into account the core shift, multifrequency VLBI monitoring made it possible to study the spectral evolution of the parsec-scale jet in the quasar 3C 345 (Lobanov 1996, 1998a; Lobanov & Zensus 1999). The combined data at different frequencies can be used to derive the basic properties of synchrotron spectra of the VLBI core and the jet components: the spectral index distribution, the turnover frequency, the turnover flux density, and the deduced magnetic field strength across the core-jet structure. The distribution of the turnover frequencies of the parsec-scale jet in 3C 345 is shown in Figure (3.9).

3.5.3 VLBI surveys

Throughout much of the electromagnetic spectrum, surveys as an observational area have been used effectively to study the nature and environments of the compact radio sources, because of their complex structure

and various emission mechanisms. The data from the Spitzer surveys (Fadda et al. 2004) in the far-infrared regime have already yielded a fundamental result on obscuration in compact radio sources (AGN) (Urry & Treister 2005). The optical data from deep surveys such as the ongoing SDSS survey (York et al. 2000) have addressed the structure and demographics of AGN (Heckman et al. 2004), and the AGN-SMBH co-evolution (Urry & Treister 2005). The extensively large databases from many other surveys like ROSAT, IRAS, ISO, SIRTF, FIRST and NVSS, and deep observations with the HST, XMM, and Chandra have triggered the activity of AGN research.

Since VLBI makes it possible to observe the close vicinity of the central engine of the compact radio sources, a number of ground and space VLBI surveys have also been undertaken to study the nature of jets in the compact radio sources. In the centimeter regime the first VLBI imaging survey with a sample of 65 powerful compact radio sources has been carried out by Pearson & Readhead (1988) (referred to as the Pearson-Readhead survey or PR survey)¹, who found out the fundamental morphology of the compact radio sources: asymmetric core-jet structures, compact symmetric structures, etc. The asymmetric core-jet structure can be explained by *Doppler favoritism*. Objects with jets oriented close to the line of sight have their flux density strongly Doppler boosted, and so they are preferentially found in flux-limited samples of sources chosen at centimeter wavelengths (e.g., Vermeulen & Cohen 1994). Later on the series of the Caltech-Jodrell Bank VLBI surveys¹, CJ1 (Polatidis et al. 1995; Thakkar et al. 1995; Xu et al. 1995) and CJ2 (Taylor et al. 1994; Henstock et al. 1995), have been undertaken, increasing the number of sources imaged up to 200 and lowering the flux density limit to $S \geq 0.35$ Jy. The large sample of CJ1 and 2 made it possible to study cosmological evolution of the compact radio sources and misalignment between pc- and kpc-scale structures. The data of nearly 300 sources in the Caltech-Jodrell Bank Flat-spectrum (CJF) survey (Taylor et al. 1996) have provided a homogeneous complete sample integrated from the PR, CJ1 and CJ2 surveys.

At a higher frequency (15 GHz), but still in the centimeter regime, the VLBA 2 cm Survey² has made use of the Very Long Baseline Array (VLBA), which is a dedicated VLBI instrument with an array of ten antennas, to yield 171 sources imaged at multi-epochs and 250 sources analyzed with visibility data (Kellermann et al. 1998; Zensus et al. 2002; Kellermann et al. 2004; Kovalev et al. 2005). This survey has revealed a wealth of information about morphology, kinematics and evolution of radio-emitting material in the nuclear regions and relativistic outflows in AGN on sub-parsec scales. Statistical study of the kinematics showed that the jets are moving always outwards from the core and most likely the jet flow seems to follow a continuous path. The distribution of the apparent speeds showed that the very high Lorentz factors ($\gamma > 25$) are quite rare in the relativistic jets of the compact radio sources. The visibility analysis showed that the brightness temperature estimates and lower limits for the VLBI core components typically range between 10^{11} and 10^{13} K, but they extend up to 5×10^{13} K, apparently in excess of the equipartition brightness temperature or the inverse Compton limit for stationary synchrotron sources. At low frequencies (e.g., < 20 GHz) what is seen as the core in VLBI images should be the section of the jet where the optical depth is roughly unity at the frequency of observation. In that case, the measured brightness temperature will indicate the ratio of relativistic electron to magnetic energy density, following the formula for the ratio of the relativistic electron u_{re} to magnetic energy density u_{mag} as shown in Readhead (1994):

$$\frac{u_{re}}{u_{mag}} \propto T'_b{}^{8.5} S_m^{-0.5}, \quad (3.40)$$

where T'_b is the rest frame brightness temperature and S_m is the flux density at the self-absorption turnover frequency ν_m . Homan et al. (2006) have analyzed the dataset of the brightness temperatures from the visibility analysis (Kovalev et al. 2005), finding that cores are typically near equipartition ($T'_b \approx 3 \times 10^{10}$ K). It should be noted that the “core” seen at 15 GHz does not represent the base of the jet, since the turnover frequency, below which the synchrotron self-absorption is dominated, is usually at short millimeter or even sub-millimeter wavelengths (see Impey & Neugebauer 1988).

The VLBA 2 cm Survey was followed by a long-term, systematic, full-Stokes imaging survey of a large complete sample in which the selection effects are well-understood: the Monitoring Of Jets in AGN with VLBA Experiments (MOJAVE) program³ (Lister 2003a; Lister & Homan 2005; Homan & Lister 2006). There are many other ground-based VLBI surveys in the centimeter regimes for various purposes: VIPS (Taylor et al. 2005), VCS (Beasley et al. 2002; Fomalont et al. 2003; Petrov et al. 2005, 2006; Kovalev et al. 2007), RRFID (Fey et al. 1996; Fey & Charlot 1997, 2000) and VLBApls (Fomalont et al. 2000).

¹Pearson-Readhead and Caltech-Jodrell Bank surveys: www.astro.caltech.edu/~tjp/cj/

²VLBA 2 cm Survey: www.cv.nrao.edu/2cmsurvey/

³Monitoring Of Jets in AGN with VLBA Experiments (MOJAVE): www.physics.purdue.edu/astro/MOJAVE/

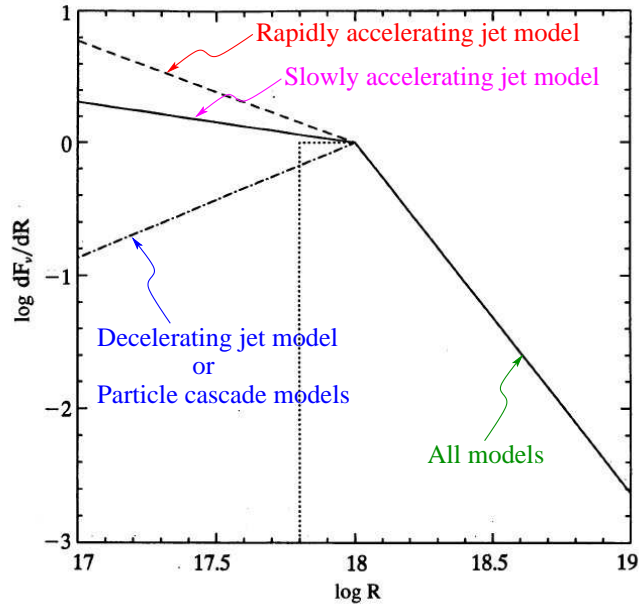


Figure 3.10: Prediction for flux density per unit length of relativistic jets by various jet models. (Marscher 1995, taken from).

Since the resolution of VLBI imaging is proportional to λ/B , where λ is the wavelength and B is the length of the baseline, higher resolutions can be achieved by extending the baseline as long as possible, or by going to the higher frequencies. One way to achieve the higher resolution is using the VLBI array with antennas distributed over the world (global VLBI) or more extreme way, putting an antenna above the Earth (space-ground VLBI). The extreme idea had come true and been devoted to study the compact radio sources. A space VLBI survey has been conducted, being led by the VSOP (VLBI-Space Observatory Program) mission (Fomalont et al. 2000; Hirabayashi et al. 2000; Horiuchi et al. 2004; Lovell et al. 2004; Scott et al. 2004). An 8-m telescope shipped on the dedicated satellite named HALCA⁴ has provided the longest baseline to ground based telescopes, yielding high angular resolutions of up to 3 times greater than with ground arrays at the same frequency. The VSOP survey enabled us to study the sub-milliarcsecond structure of a flux density-limited sample of compact radio sources and to obtain higher brightness temperature measurements well above the inverse Compton limit, confirming the Doppler boosting effect to the brightness temperatures.

Another way to achieve higher resolution is to go down to short wavelengths (e.g., 86 GHz). Although the large atmospheric phase and amplitude errors make the fidelity of “mm-VLBI” imaging worse, four major mm-VLBI surveys have been carefully carried out (Beasley et al. 1997; Lonsdale et al. 1998; Rantakyro et al. 1998; Lobanov et al. 2000), yielding a total of 24 bright sources imaged out of 124 sources observed. Comparing with the surveys in the centimeter regime the total number of sources imaged in the millimeter regime is too small to conduct the statistical analysis comparable to that done at centimeter wavelengths. Since the turnover frequency, however, is usually at mm or sub-mm wavelengths, mm-VLBI survey can be used to investigate the innermost region of compact jets and to test observationally the inner jet models (see section 3.4.3 and 3.4.4). The prediction (see Figure 3.10) from the jet models (see section 3.4.3) led to the fact that the flux density per unit length of a relativistic jet, dS_ν/dR , along the distance from the origin, R , shows a slope of -2.8 in an outer region ($R > R_c$) of the jet and the varying slopes of -1 to 1 in the inner region ($R < R_c$) depending on the models (Marscher 1995). The spectrum of the unit section of the jet peaks at a progressively higher frequency as one considers the section closer to the origin of the jet. Since VLBI observations generally show that the size (θ) of a component should be inversely proportional to the peak frequency (ν_m) of its spectrum, the factor $\nu^2\Omega$ in (2.55) is constant and $dS_\nu/dR \propto T'_{\text{int}}$. Therefore, it is implied that $T'_b \propto \nu^\xi$ with $\xi = 2.8$ below a critical frequency ν_c , which is corresponding to the peak frequency of the spectrum of the section R_c , and with $-1 < \xi < 1$ beyond ν_c , depending on the jet models. By measuring the intrinsic brightness temperature at several frequencies (e.g., 15 GHz,

⁴Highly Advanced Laboratory for Communication and Astronomy.

43 GHz, and 86 GHz), which should be around ν_c , we would be able to constrain the physical conditions (e.g., composition and dynamics) of the innermost region of compact sources.

Data from the VLBI surveys have also been used effectively for addressing the physical questions for the compact radio sources, including AGN evolution (Shaver et al. 1996) and population modeling (Lister & Smith 2000; Lister 2003b; Homan et al. 2006), jet formation (Lobanov et al. 2000), fundamental astrophysical emission processes (Lister & Marscher 1999; Kellermann 2002), and cosmology (Gurvits et al. 1999).

Chapter 4

A Global 3 mm-VLBI Survey

4.1 Introduction

Very long baseline interferometry (VLBI) at millimeter wavelengths offers the best tool for imaging compact radio structures on scales of several dozens of micro-arcseconds. The first detection of single-baseline interference fringes by 89 GHz (3.4 mm) VLBI observation was reported by Readhead et al. (1983), demonstrating the feasibility of 3 mm-VLBI. After that, many VLBI observations at 86 GHz have been made, probing the most compact regions in active galactic nuclei (AGN). However, the number of objects detected and imaged at 86 GHz has remained small, compared with the number of objects imaged with VLBI at lower frequencies.

Sensitive VLBI observations at 86 GHz have been made for several sources, including 3C 111 (Doeleman & Claussen 1997), 3C 454.3 (Krichbaum et al. 1995, 1999; Pagels et al. 2004), NRAO 150 (Agudo et al. 2005), NRAO 530 (Bower et al. 1997), M87 (Krichbaum et al. 2006b), 3C 273 and 3C 279 (Attridge 2001). In order to increase the number of objects imaged at 86 GHz, four detection and imaging surveys were conducted during the 1990s, with a total of 124 extragalactic radio sources observed (see Beasley et al. 1997; Lonsdale et al. 1998; Rantakyrö et al. 1998; Lobanov et al. 2000). In these surveys fringes were detected in 44 objects, and only 24 radio sources have been successfully imaged. Table 4.1 gives an overview of these surveys. The low detection and imaging rates of previous 86 GHz surveys were caused by the relatively poor baseline sensitivities, small numbers of telescopes and short observing times.

In October 2001, a large global 86 GHz VLBI survey of compact radio sources started. The survey was conducted during three sessions of the global millimeter VLBI array, which are in the transition period of the Coordinated Millimeter VLBI Array (CMVA) (Rogers et al. 1995) and the Global Millimeter VLBI Array (GMVA)¹. The main aim of this VLBI survey is to increase the total number of objects accessible for future 3 mm-VLBI imaging by factors of 3-5. In the following section, we describe briefly the survey observations. The data reduction procedure of the survey is discussed in detail in section 4.3 and the imaging technique for the 3 mm-VLBI survey data is summarized in section 4.4. In section 4.5, we present the results of the survey, including the maps of all the imaged sources, all parameters of each image, and statistical properties of the survey sample. This chapter is summarized in section 4.7.

4.2 Survey observations

4.2.1 Source selection

The source selection is based on the results from the VLBI surveys at 22 GHz (Moellenbrock et al. 1996) and 15 GHz (Kellermann et al. 1998), and on source fluxes obtained from the multi-frequency monitoring data from Metsähovi at 22, 37, and 86 GHz (Teräsanta et al. 1998) and from Pico Veleta at 90, 150, and 230 GHz (Ungerechts, priv. comm.). Using these databases, we selected the sources with an expected flux density above 0.3 Jy at 86 GHz. We excluded some of the brightest sources already imaged at 86 GHz, and focused on those sources which had not been detected or imaged in the previous surveys. Sources at higher northern declinations ($\delta \geq -40^\circ$) were preferred, in order to optimize the uv -coverage of the survey data.

¹GMVA: www.mpifr-bonn.mpg.de/div/vlbi/globalmm/index.html

Table 4.1: VLBI surveys at 86 GHz

Ref.	N_{ant}	ΔS	ΔI_{m}	D_{img}	N_{obs}	N_{det}	N_{img}
(1)	(2)	(3)	(4)	(5)	(6)	(7)	(8)
1	3	~ 0.5	45	12	...
2	2–5	~ 0.7	79	14	...
3	6–9	~ 0.5	~ 30	70	67	16	12
4	3–5	~ 0.4	~ 20	100	28	26	17
Total number of unique objects:					124	44	24
Properties described in this thesis							
	12	~ 0.2	≤ 10	50	127	121	109

Notes: Columns: 1 - references; 2 - number of participating antennae; 3 - average baseline sensitivity [Jy]; 4 - average image sensitivity [mJy/beam]; 5 - typical dynamic range of images; 6 - number of sources observed; 7 - number of objects detected; 8 - number of objects imaged. **References:** 1 - Beasley et al. (1997); 2 - Lonsdale et al. (1998); 3 - Rantakyrö et al. (1998); 4 - Lobanov et al. (2000).

According to the aforementioned selection criteria, a total of 127 compact radio sources was selected and observed, consisting of 88 quasars, 25 BL Lac objects, 11 radio galaxies, 1 X-ray binary star (Cyg X-3), and 2 unidentified sources. The general information about the observed sources is summarized in Table 4.2. In Figure 4.1, the sky-distribution of the observed sources is shown.

4.2.2 Snapshot observations with GMVA

The survey observations have been conducted during three sessions of the global millimeter VLBI array (GMVA) on October 2001, April 2002 and October 2002. The log of the survey observations is summarized in Table 4.3. It should be noted that several sources are observed in more than one epoch. In Table 4.4, the technical information of the participating antennae is described. The participation of large, sensitive European antennas (like the 100-m radio telescope at Effelsberg, the 30-m millimeter radio telescope at Pico Veleta, the 6×15 -m IRAM interferometer on Plateau de Bure) and the 8 VLBA¹ antennas available at 86 GHz provides a single baseline sensitivity of ~ 0.1 Jy, and an image sensitivity of better than 10 mJy/beam.

Every source in the survey was observed for 3-4 scans of 7-minute duration (*snapshot* mode). Although the uv -coverage of such an experiment in snapshot mode limits the dynamic range and structural sensitivity of images, the large number of the participating antennas gives a global uv -coverage for the sources at both low and high declinations (Figure 4.2). The data were recorded either with a 128 MHz bandwidth (epoch A and B) or a 64 MHz bandwidth (epoch C), using the MKIV VLBI system in a sampling mode either of 1-bit (epoch A and B) or 2-bit (epoch C). The observations were made in the left-hand circular polarization (LCP). We recorded 3-4 scans per hour, using the time between VLBI scans for focus checks, pointing and calibration. The data were correlated at the Mark IV (MKIV hereafter) correlator at the Max-Planck-Institut für Radioastronomie (MPIfR), Bonn with an integration time of 1 sec.

4.3 Data reduction

In this section, we describe the post-correlation processing of the 3 mm-VLBI survey dataset. Before loading the data from correlator into AIPS (Astronomical Image Processing System) a post-processing is needed. By using the HOPS (Haystack Observatory Postprocessing System) and a modified AIPS task **MK4IN** (Alef et al. 2000), we are able to export a correlator output into AIPS. Moreover a precise determination of phase-residuals out of the correlation is essential for 3 mm-VLBI observations since the coherence time is short (e.g., 10 s – 30 s), the sensitivity is low, and the fringe fit results have to be inspected scan by scan in order to determine whether the fringes have been detected. We needed a more precise determination technique in order to detect the fringes on weaker sources for this survey. We used the fringe-fitting program - *fourfit* -

¹The VLBA is an instrument of the National Radio Astronomy Observatory, which is a facility of the National Science Foundation operated under cooperative agreement by Associated Universities, Inc.

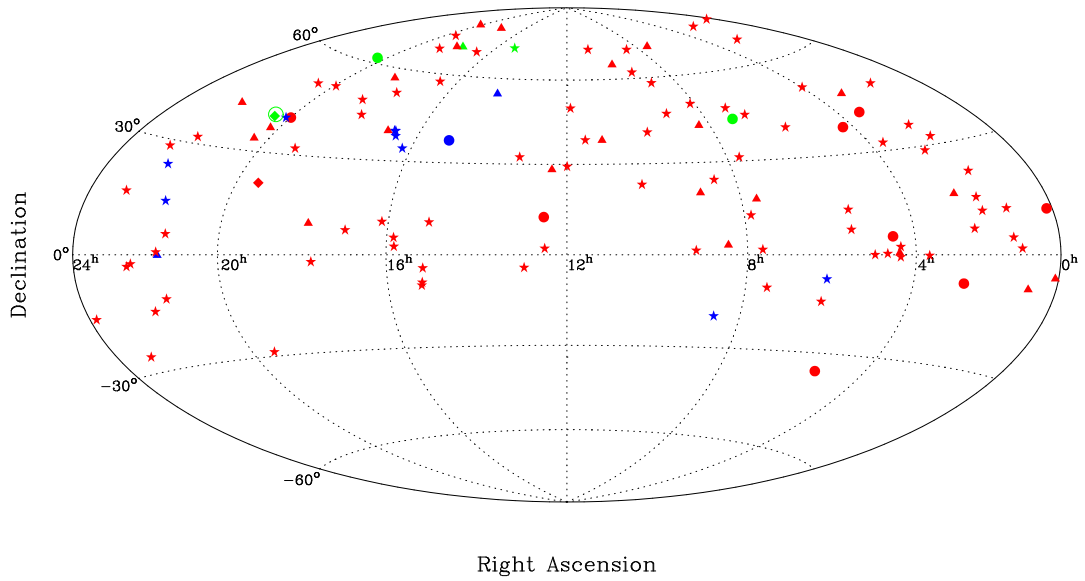


Figure 4.1: The sky-distribution of 86 GHz VLBI sources: 109 detected and imaged sources (red), 12 detected and non-imaged sources (blue) and 6 non-detected sources (green). Symbols: stars are quasars (Q), triangles are BL Lac objects (B), circles are galaxies (G), diamonds are unidentified sources (U) and a single open star represents a star, Cyg X-3 (S).

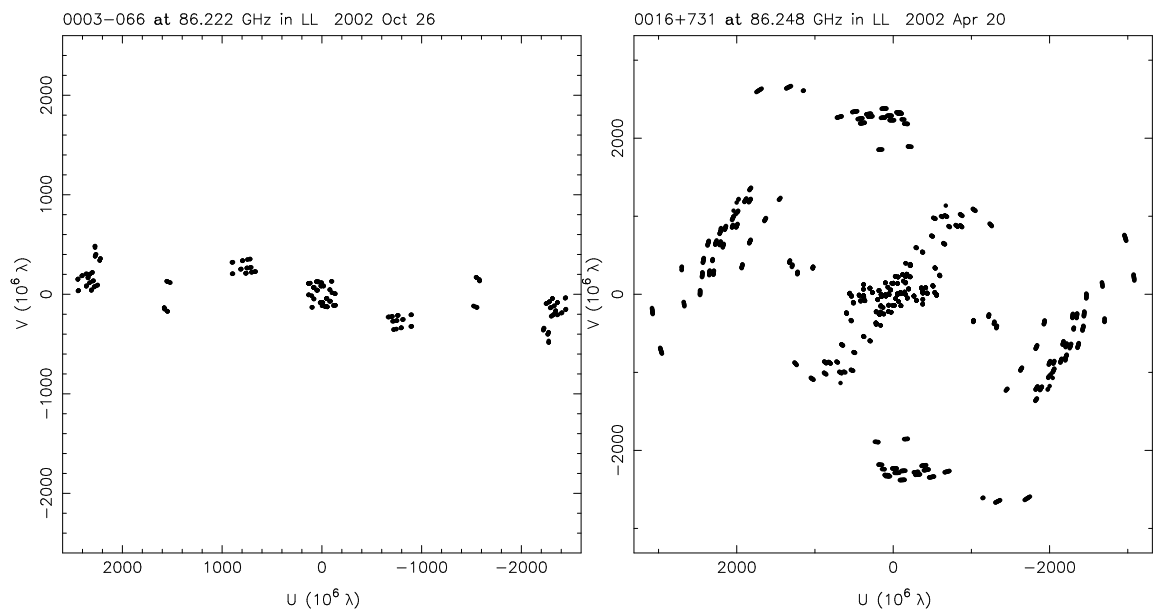


Figure 4.2: uv -plots of 0003-066 and 0016+731 at low and high declinations of -06 and 73 degrees, respectively.

Table 4.2: Source list

Name	Obs.	α_{2000}	δ_{2000}	Status	z	Type	m_v	$S_{86 \text{ GHz}}$	
	(1)	(2)	(3)	(4)	(5)	(6)	(7)	(8)	
0003-066	NRAO005	C	00 06 13.89289	-06 23 35.3356	++	0.347	B	19.5	2.16
0007+106	III Zw2	C	00 10 31.00587	+10 58 29.5038	++	0.089	G	15.4	0.60
0016+731		B	00 19 45.78642	+73 27 30.0174	++	1.781	Q	18.0	0.84
0048-097		C	00 50 41.31739	-09 29 05.2103	++	...	B	17.4	0.60
0106+013	4C01.02	A	01 08 38.77104	+01 35 00.3232	++	2.107	Q	18.3	1.36
0119+041		C	01 21 56.86169	+04 22 24.7343	++	0.637	Q	19.5	0.68
0119+115		C	01 21 41.59504	+11 49 50.4131	++	0.570	Q	19.5	0.68
0133+476		A,B	01 36 58.59481	+47 51 29.1001	++	0.859	Q	18.0	4.25 [†]
0149+218		A,C	01 52 18.05900	+22 07 07.6997	++	1.32	Q	20.8	0.98 [†]
0201+113		C	02 03 46.65706	+11 34 45.4096	++	3.61	Q	20.0	0.39
0202+149	4C15.05	A	02 04 50.41402	+15 14 11.0453	++	0.405	Q	22.1	...
0202+319		C	02 05 04.92537	+32 12 30.0956	++	1.466	Q	18.2	1.01
0212+735		A,B	02 17 30.81336	+73 49 32.6218	++	2.367	Q	19.0	0.78 [†]
0218+357		C	02 21 05.47330	+35 56 13.7910	++	0.944	Q	20.0	0.58
0221+067		C	02 24 28.42819	+06 59 23.3416	++	0.511	Q	19.0	0.59
0224+671	4C67.05	B	02 28 50.05146	+67 21 03.0292	++	0.523	Q	19.5	1.34
0234+285	4C28.07	A,B,C	02 37 52.40568	+28 48 08.9901	++	1.207	Q	18.9	3.11 [†]
0235+164		A	02 38 38.93006	+16 36 59.2789	++	0.940	B	19.0	1.62
0238-084	NGC1052	B,C	02 41 04.79852	-08 15 20.7518	++	0.005	G	12.1	0.63
0300+470		B	03 03 35.24222	+47 16 16.2754	++	...	B	17.2	3.11
0316+413	3C84	A,B,C	03 19 48.16010	+41 30 42.1030	++	0.017	G	12.6	4.71 [†]
0333+321	NRAO140	A	03 36 30.10760	+32 18 29.3430	++	1.263	Q	17.5	1.77
0336-019	CTA26	A	03 39 30.93771	-01 46 35.8040	++	0.852	Q	18.4	2.11
0355+508	NRAO150	A,C	03 59 29.74726	+50 57 50.1615	++	...	Q	...	7.18 [†]
0415+379	3C111	B,C	04 18 21.27700	+38 01 35.9000	++	0.049	G	18.0	2.37 [†]
0420+022		C	04 22 52.21464	+02 19 26.9319	++	2.277	Q	19.5	0.48
0420-014		B	04 23 15.80072	-01 20 33.0653	++	0.915	Q	17.8	5.83
0422+004		B	04 24 46.84205	+00 36 06.3298	++	0.310	B	17.0	1.46
0430+052	3C120	B,C	04 33 11.09553	+05 21 15.6194	++	0.033	G	14.2	3.19 [†]
0440-003	NRAO190	C	04 42 38.66076	-00 17 43.4191	++	0.844	Q	19.2	0.88
0458-020	4C-02.19	B	05 01 12.80988	-01 59 14.2562	++	2.291	Q	18.4	1.12
0521-365		C	05 22 57.98463	-36 27 30.8516	++	0.055	G	14.5	...
0528+134		A	05 30 56.41665	+13 31 55.1484	++	2.07	Q	20.0	2.02
0529+075		A	05 32 39.02004	+07 32 43.3466	++	1.254	Q	19.0	1.13
0552+398	DA193	A	05 55 30.80564	+39 48 49.1654	++	2.363	Q	18.0	1.34
0605-085		A	06 07 59.69905	-08 34 49.9798	+m	0.872	Q	18.5	1.28
0607-157		B	06 09 40.94953	-15 42 40.6726	++	0.324	Q	17.0	...
0642+449		B	06 46 32.02598	+44 51 16.5901	++	3.408	Q	18.5	1.67
0707+476		C	07 10 46.10490	+47 32 11.1426	++	1.292	Q	18.2	0.27
0710+439		C	07 13 38.16412	+43 49 17.2069	-	0.518	G	19.7	0.22
0716+714		B,C	07 21 53.44846	+71 20 36.3633	++	...	B	15.5	3.67 [†]
0727-115		B	07 30 19.11247	-11 41 12.6004	++	1.591	Q	22.5	...
0735+178		B	07 38 07.39374	+17 42 18.9982	++	0.424	B	14.9	1.23
0736+017		A	07 39 18.03380	+01 37 04.6180	++	0.191	Q	16.5	2.24
0738+313		C	07 41 10.70330	+31 12 00.2286	++	0.630	Q	16.7	0.47

Table 4.2: Source list (*continued*)

Name	Obs.	α_{2000}	δ_{2000}	Status	z	Type	m_v	$S_{86 \text{ GHz}}$	
	(1)	(2)	(3)	(4)	(5)	(6)	(7)	(8)	
0748+126	B	07 50 52.04573	+12 31 04.8281	++	0.889	Q	17.8	1.80	
0804+499	C	08 08 39.66627	+49 50 36.5304	++	1.432	Q	19.1	0.38	
0814+425	C	08 18 15.99961	+42 22 45.4149	++	0.530	B	18.5	0.50	
0823+033	A	08 25 50.33800	+03 09 24.5100	++	0.506	B	18.5	1.02	
0827+243	B	08 30 52.08619	+24 10 59.8204	++	0.941	Q	17.3	2.16	
0834-201	C	08 36 39.21522	-20 16 59.5038	+ <i>m</i>	2.752	Q	19.4	...	
0836+710	4C71.07	C	08 41 24.36528	+70 53 42.1730	++	2.218	Q	16.5	1.16
0850+581	C	08 54 41.99638	+57 57 29.9392	++	1.322	Q	18.2	0.26	
0851+202	OJ287	B	08 54 48.87492	+20 06 30.6408	++	0.306	B	14.0	2.71
0859+470	OJ499	C	09 03 03.99010	+46 51 04.1375	++	1.462	Q	19.4	0.42
0906+015	B	09 09 10.09159	+01 21 35.6176	++	1.018	Q	17.3	2.43	
0917+624	A	09 21 36.23053	+62 15 52.1763	++	1.446	Q	19.5	1.01	
0945+408	4C40.24	A	09 48 55.33817	+40 39 44.5872	++	1.252	Q	17.9	0.95
0954+658	A	09 58 47.24428	+65 33 54.8108	++	0.367	B	16.7	1.16	
1012+232	B	10 14 47.06544	+23 01 16.5709	++	0.565	Q	17.5	1.01	
1044+719	B	10 48 27.61991	+71 43 35.9382	++	1.150	Q	19.0	0.87	
1101+384	Mk421	C	11 04 27.31394	+38 12 31.7991	++	0.031	B	13.3	0.58
1128+385	C	11 30 53.28261	+38 15 18.5470	++	1.733	Q	18.6	0.97	
1150+497	4C49.22	C	11 53 24.46664	+49 31 08.8301	++	0.334	Q	17.4	1.02
1156+295	4C29.45	A	11 59 31.83390	+29 14 43.8295	++	0.729	Q	17.0	4.42
1219+285	C	12 21 31.69051	+28 13 58.5002	++	0.102	B	16.5	0.36	
1226+023	3C273B	A	12 29 06.69973	+02 03 08.5982	++	0.158	Q	12.9	10.81
1228+126	3C274	A	12 30 49.42338	+12 23 28.0439	++	0.004	G	9.6	4.16
1253-055	3C279	C	12 56 11.16656	-05 47 21.5246	++	0.538	Q	17.8	16.90
1308+326	A	13 10 28.66372	+32 20 43.7818	++	0.997	Q	19.0	1.44	
1418+546	C	14 19 46.59741	+54 23 14.7872	+	0.152	B	15.9	0.93	
1458+718	3C309.1	C	14 59 07.58386	+71 40 19.8677	-	0.904	Q	16.8	0.65
1502+106	C	15 04 24.97978	+10 29 39.1986	++	1.833	Q	18.6	0.82	
1504+377	C	15 06 09.52995	+37 30 51.1324	+	0.674	G	21.2	0.51	
1508-055	C	15 10 53.59143	-05 43 07.4171	++	1.191	Q	17.2	...	
1510-089	C	15 12 50.53292	-09 05 59.8296	++	0.360	Q	16.5	2.10	
1511-100	C	15 13 44.89341	-10 12 00.2646	++	1.513	Q	18.5	0.81	
1546+027	C	15 49 29.43683	+02 37 01.1632	++	0.412	Q	17.3	1.04	
1548+056	C	15 50 35.26924	+05 27 10.4482	++	1.422	Q	17.7	1.71	
1606+106	C	16 08 46.20318	+10 29 07.7758	++	1.226	Q	18.5	1.26	
1611+343	A	16 13 41.06416	+34 12 47.9093	+ <i>m</i>	1.401	Q	17.5	1.83	
1633+382	4C38.41	A	16 35 15.49297	+38 08 04.5006	+ <i>m</i>	1.807	Q	17.7	5.81
1637+574	C	16 38 13.45630	+57 20 23.9790	++	0.751	Q	17.0	1.70	
1638+398	NRAO512	C	16 40 29.63277	+39 46 46.0285	+	1.666	Q	18.5	0.50
1641+399	3C345	A	16 42 58.80995	+39 48 36.9939	+ <i>m</i>	0.594	Q	16.6	6.33
1642+690	C	16 42 07.84853	+68 56 39.7564	++	0.751	Q	19.2	1.36	
1652+398	DA426	A	16 53 52.22700	+39 45 36.4500	++	0.033	B	14.2	...
1655+077	C	16 58 09.01145	+07 41 27.5407	++	0.621	Q	20.8	1.00	
1739+522	C	17 40 36.97785	+52 11 43.4074	++	1.379	Q	18.5	1.45	
1741-038	C	17 43 58.85614	-03 50 04.6168	++	1.057	Q	18.6	4.16	

Table 4.2: Source list (*continued*)

Name	Obs.	α_{2000}	δ_{2000}	Status	z	Type	m_v	$S_{86\text{ GHz}}$	
	(1)	(2)	(3)	(4)	(5)	(6)	(7)	(8)	
1749+701	4C09.57	A	17 48 32.84008	+70 05 50.7705	—	0.770	B	17.0	...
1749+096		C	17 51 32.81857	+09 39 00.7285	++	0.320	B	16.8	4.03
1800+440		B	18 01 32.31485	+44 04 21.9003	++	0.663	Q	17.5	1.07
1803+784		A,C	18 00 45.68364	+78 28 04.0206	++	0.680	B	17.0	1.48
1807+698	3C371	A	18 06 50.68063	+69 49 28.1087	++	0.050	B	14.4	1.54
1823+568	4C56.27	A	18 24 07.06809	+56 51 01.4939	++	0.663	B	18.4	1.30
1828+487	3C380	A	18 29 31.72483	+48 44 46.9515	++	0.692	Q	16.8	1.96
1842+681		A	18 42 33.64129	+68 09 25.2314	++	0.475	Q	17.9	0.74
1901+319	3C395	C	19 02 55.93886	+31 59 41.7020	++	0.635	Q	17.5	0.59
1921–293		A	19 24 51.05590	–29 14 30.1210	++	0.352	Q	17.0	...
1923+210		B	19 25 59.60537	+21 06 26.1621	++	...	U	16.1	1.73
1928+738		A,C	19 28 00.00000	+73 00 00.0000	++	0.303	Q	16.5	2.52 [†]
1954+513		C	19 55 42.73827	+51 31 48.5462	++	1.223	Q	18.5	0.66
1957+405	CygA	C	19 59 28.35400	+40 44 02.1200	++	0.056	G	17.0	...
2005+403		A	20 07 44.94499	+40 29 48.6113	+ <i>m</i>	1.736	Q	19.5	1.25
2007+777		A	20 05 30.99883	+77 52 43.2493	++	0.342	B	16.5	0.92
2013+370		B	20 15 28.71260	+37 10 59.6940	++	...	B	21.6	2.89
2021+614		C	20 22 06.68167	+61 36 58.8047	—	0.227	G	19.5	0.58
2023+336		B	20 25 10.84209	+33 43 00.2145	++	0.219	B	...	1.77
2030+407	CygX-3	A,B	20 32 25.76740	+40 57 28.2794	—	...	S
2031+405	MWC349	A	20 30 56.85000	+40 29 20.2000	—	...	U	...	1.17
2037+511	3C418	B	20 38 37.03475	+51 19 12.6626	++	1.687	Q	20.0	1.44
2121+053		A	21 23 44.51727	+05 35 22.0971	++	1.941	Q	17.5	...
2128–123		A	21 31 35.26150	–12 07 04.7980	++	0.501	Q	15.5	...
2131–021		C	21 34 10.30961	–01 53 17.2393	+	1.285	B	18.7	1.15
2134+004	DA553	A	21 36 38.58615	+00 41 54.2195	++	1.932	Q	17.1	2.03
2136+141		C	21 39 01.30926	+14 23 35.9921	+ <i>m</i>	2.427	Q	18.5	1.03
2155–152		B	21 58 06.28190	–15 01 09.3280	++	0.672	Q	17.5	...
2200+420	BLLac	A	22 02 43.29138	+42 16 39.9899	++	0.069	B	14.5	3.57
2201+315	4C31.63	A	22 03 14.97564	+31 45 38.2749	++	0.298	Q	15.5	2.97
2209+236		C	22 12 05.96631	+23 55 40.5438	+ <i>m</i>	1.125	Q	19.0	0.68
2216–038		B	22 18 52.03772	–03 35 36.8794	++	0.901	Q	16.5	0.97
2223–052	3C446	B	22 25 47.25929	–04 57 01.3907	++	1.404	Q	17.2	3.90
2234+282		A	22 36 22.47100	+28 28 57.4200	++	0.795	Q	19.1	1.03
2251+158	3C454.3	A	22 53 57.74786	+16 08 53.5655	++	0.859	Q	16.1	5.97
2255–282		A,B	22 58 05.96289	–27 58 21.2568	++	0.927	Q	16.8	...
2345–167		B	23 48 02.60851	–16 31 12.0220	++	0.576	Q	17.5	...

Notes: Column designation: 1 - observing epochs: **A** - October 2001; **B** - April 2002; **C** - October 2002; 2, 3 - source coordinates; 4 - status: “—” - not detected; “+” - detected; “+*m*” - detected and only model fitted; “++” - detected and imaged; 5 - redshift; 6 - optical class: **Q** - quasar; **B** - BL Lac object; **G** - radio galaxy; **S** - star; **U** - unidentified; 7 - optical magnitude; 5, 6 - information obtained from Véron-Cetty & Véron (2006); 7 - information obtained from NASA/IPAC Extragalactic Database, <http://nedwww.ipac.caltech.edu>; 8 - total flux density [Jy] (obtained from pointing and calibration scan measurements made at Pico Veleta); †: mean value of measurements on multiple epochs.

Table 4.3: Log of survey observations

Date	Epoch	Bit Rate	Frequency	Sampling	Bandwidth	Sources	Telescopes
(1)	(2)	(3)	(4)	(5)	(6)	(7)	(8)
2001 October 26-29	A	256	16	1	128	48	VLBA + (Eb,PV,On,Mh,HA)
2002 April 20-23	B	256	16	1	128	35	VLBA + (Eb,PV,On,HA)
2002 October 24-27	C	256	8	2	64	60	VLBA + (Eb,PV,PdB,HA)

Notes: Column designation: 1 - observation Epoch; 2 - code of each epoch; 3 - total recorded bit rate in Mega-bits per second; 4 - number of baseband channels; 5 - sampling mode [bit]; 6 - total observing bandwidth; 7 - number of sources observed (12 of the 127 observed sources were observed during more than one session); 8 - telescopes participating: **VLBA** - Fort Davis, Hancock, North Liberty, Owens Valley, Pie Town, Mauna Kea, Los Alamos, Kitt Peak; **Eb** - Effelsberg; **PV** - Pico Veleta; **On** - Onsala ; **Mh** - Metsähovi; **PdB** - Plateau de Bure ; **HA** - Haystack.

Table 4.4: Participating telescopes

Name	code	D	G	T_{sys}	η_A	$SEFD$	$\Delta S^{256,30s}$	Threshold
(1)	(2)	(3)	(4)	(5)	(6)	(7)	(8)	(9)
Effelsberg	Eb	100	0.140	130	0.07	929	20	143
Haystack	HA	37	0.058	200	0.15	3448	39	273
Plateau de Bure	PdB	31	0.180	120	0.65	667	17	121
Pico Veleta	PV	30	0.140	120	0.55	857
Onsala	On	20	0.053	250	0.45	4717	45	321
Metsähovi	Mh	14	0.017	300	0.30	17647	89	621
Fort Davis	Fd	25	0.034	120	0.17	3529	40	278
Hancock	Hn	25	0.035	120	0.17	3429	39	274
North Liberty	Nl	25	0.055	270	0.17	4909	47	328
Owens Valley	Ov	25	0.020	100	0.17	5000	47	331
Pietown	Pt	25	0.024	100	0.17	4167	43	302
Kitt Peak	Kp	25	0.025	110	0.17	4400	44	310
Los Alamos	La	25	0.051	160	0.17	3137	37	262
Mauna Kia	Mk	25	0.023	100	0.17	4348	44	308

Notes: column designation: 1 - name of the participating telescope; 2 - abbreviation of the telescope name; 3 - diameter [m]; 4 - typical zenith gain [K/Jy]; 5 - system temperature [K]; 6 - aperture efficiency; 7 - typical zenith SEFD [K] obtained from the formula, $SEFD = T_{\text{sys}}/G$; 8 - baseline sensitivity [mJy] on baseline to Pico Veleta, assuming a recording rate of 256 Mbps and a fringe-fit interval of 30 seconds; 9 - 7σ detection threshold [mJy].

of the HOPS package and *FRING* in AIPS. In the following sections, we describe the procedure of such an essential post-correlation processing for the 3 mm-VLBI survey presented in this dissertation.

4.3.1 Fringe-fitting: *fourfit* and *FRING*

1. Loading the output from correlator

When we loaded the output from the correlator, it consisted of as many directories as the number of scans observed. Each directory contains three kinds of files; *ROOT* file (type 0 file, ASCII, one per scan), correlated data file (type 1 file, binary, one per baseline including autocorrelation), station file (type 3 file) (Alef et al. 2000). We construct *A-format* file for summarizing correlator data files, using a task *alist* in HOPS package. With the A-file, one can investigate, sort and edit the correlated or fringe-fitted data.

2. Fringe-fitting with *fourfit*

Using the fringe-fitting program, *fourfit*, we monitored the quality of the correlated data and determined precisely the residuals of the fringe-rate and delay remaining after the correlation. The specific procedure for the fringe-fitting consists of three steps:

- to run the first *fourfit* with a wide search window (e.g. a width of 1 μ sec for singleband delay, 2 μ sec for multiband delay and 500 psec/sec for delay rate) centered at zero point,
- to calculate a mean value and rms, σ , of the determined (or detected) residuals on each baseline, and run the second *fourfit* with an σ - search window, which has a width of 2σ with an offset of the mean value,
- and using the residuals determined for the detected scans, to interpolate the offset of the singleband delay for non-detected scans, and then, run the final *fourfit* with a *interpolated* search window with a width of 0.02 μ sec for singleband delay, centered at the offset interpolated.

Since the probability of false detection for fringes could be reduced, i.e. the signal-to-noise ratio (SNR) threshold for detection is lowered from 7 to 5, by narrowing the search window of fringe fit, more weaker sources are detected (see section 4.3.2). These residuals should be exported to AIPS, since *fourfit* gives a more precise estimate of the detection threshold than the *FRING* in AIPS.

3. Exporting data to AIPS with **MK4IN**

Since all MKIV correlators are lag based, which implies that the correlated data are complex numbers in delay-space, whereas AIPS expects data in the cross-spectral domain, one requires an interface program in order to export the raw data from the MKIV correlator into AIPS. A program, called **MK4IN**, was written by Alef & Graham (2002), which uses the raw data in the cross-spectral domain written by *fourfit* as an input. Using **MK4IN**, the data are exported into AIPS following the steps below;

- **Selecting data**

The final data-set is selected, using the HOPS tasks **aedit** and **linkdata**. Once we are satisfied with the fringe fitted data by *fourfit*, we sort the data in the order of the observed date, time and baseline served, using **aedit**. For a more sophisticated selection such as removing duplicate data by getting rid of bad data with extraordinarily short integration times (which makes data looking good with high SNR) and choosing good data with $\text{SNR} > 6$, we used a script, called *best52mk4*, written at the MPIfR. Based on the A-file of summarizing the fringe fitted, sorted and edited data, we created a *mirror* data directory with the task **linkdata**. This *mirror* data directory serves **MK4IN** as an input.

- **Reading data**

MK4IN in AIPS reads the ovex-file (Alef et al. 2000), sets up the AIPS header and creates the AN, SU, and FQ tables, which contain the information about participating antennas, observed sources and observing frequencies, respectively. The cross-spectra, the *fourfit* solutions, and the correlator model are read, reformatted and written to a UV-file, the BS table, and the CL table, respectively. The BS table contains the baseline delay, rate and phase solutions. The CL table is a table for the calibration parameters. The input parameters for **MK4IN** are 32 lags (NCHAN), 0.05 minutes of CL table increment (CLINT), 0.5 of weight threshold (WTTHRESH), 7.2 of SNR threshold.

- **Sorting and indexing data**

The AIPS data files created by **MK4IN** are in an arbitrary order. They are sorted in time-baseline order using the AIPS task **UVSRT**. The AIPS task **INDXR** creates an index (NX) table and indexes the UV-file.

- **Running BLAPP**

The baseline-based residuals from the BS table generated by **MK4IN** are used to derive the antenna-based residuals and create a first solution (SN) table with a slightly modified version of **BLAPP**.

4. Fringe fitting with *FRING*

Once the data are correlated and fringe-fitted with *fourfit* and exported into AIPS with **MK4IN**, they are in principle ready to be calibrated and then imaged. Since *fourfit* makes use of manual phase-cals, one can define the necessary phase corrections with *fourfit*. However, there are residual phase errors such as a gradient in phase between IFs (due to the *multi-band* delay) and also small gradients within each IF (caused by the *single-band* delay). These phase errors are mainly caused by the unavoidable correlator model errors for each station, that is errors in the geometrical time delays for each station, arising from propagation effects through the troposphere (severe in mm-wavelength) and ionosphere, inaccurate Earth geometry, etc. So, it is assumed that the *single-band* delay is the same in each IF; therefore the difference between the *multi-band* and *single-band* delays should be constant for a single telescope during the observation. In addition to these frequency dependent phase errors, the phase also suffers from the time-variable phase variations, *phase rates*, which is equivalent to the residual fringe rate.

It is one of the main purposes of fringe-fitting with the task **FRING** (antenna-based fringe fitting) of AIPS, to correct these frequency- and time-dependent phase errors for each antenna. And the other purpose of this step is to detect fringes for weaker sources based on the *global* fringe-fitting (Schwab & Cotton 1983). Although the fringes for weaker sources have already been fitted to each baseline with *fourfit* (baseline-based fringe fitting), it is necessary to fringe fit the data with **FRING** again with lower SNR threshold and narrow search window in order to yield the detections of *non-detected* sources or baselines. For achieving these goals, the procedure of fringe fitting with **FRING** in AIPS is as follows;

- **Applying *fourfit* solution**

Apply the phase solution of the *fourfit*-**MK4IN**-**BLAPP** run to the data in order to start the calibration with baseline-based fringe fit solutions.

- **Reference antenna and solution interval**

Select the appropriate reference antenna and the optimal solution interval for the subsequent fringe fits. Since “Pico Veleta” is the most sensitive antenna among the rest (see Table 4.4), it serves the fringe fits as the reference antenna for the data observed with European and VLBA antennas. In case of sources observed only with VLBA, “Fort Davis” is selected as the reference antenna. Due to the tropospheric effect over each antenna, the phase of each baseline varies in time with a time scale of 10 ~ 20 sec at 86 GHz. However, the solution interval for fringe fit should exceed the time scale, *coherence time*, in order to achieve a higher SNR for a true fringe search of weak sources. The full length of a single scan (7 minutes) is selected as the solution interval for the subsequent fringe fits.

- **Manual phase calibration**

Select a single scan on a strong source or other source that gives high-SNR fringe solutions (the residuals; single-band delay, multi-band delay and rate) over all antennas. In case that such a scan does not exist, select another scan which has good solutions for the missing antennas (including the reference antenna) and combine fringe fit solutions from those scans into a single solution table. Fringe fit on the data with relatively high SNR threshold (e.g. > 7), since the source is quite strong and core-dominant. Apply the fringe fit solutions to the other sources.

- **Global Fringe fit on the whole data**

After applying the manual fringe fit solution, *Global* fringe fit the whole data using one baseline for *coarse* searching. Assuming that single-band delays in each IF are the same, during a *Global* fringe fit, the difference between model phases and measured phases is minimized by solving

for the antenna-based instrumental phase, rate, and delay difference between single- and multi-band delays for each antenna. In order to avoid false detections, fringe fit the data with the SNR threshold of 5 and the searching-window widths of 100 nano-second for delay and 300 mHz for rate, and then fringe fit the data again with 4.5, 100 nano-second and 200 mHz for SNR threshold, delay-window width and rate-window width, respectively. After each fringe fit, the solutions detected from strong sources are applied to the adjacent weaker sources by linear interpolation.

4.3.2 Fringe detection

Fringes were first searched for each baseline. With the gradually-narrowing search window of the single band delay, the total number of fringe detections for the survey data increased by up to 20%. Figure 4.3 shows the number of fringe detections for each baseline before and after applying the window-controlling to the baseline-based fringe fitting (*fourfit*). During the fringe fitting, *fourfit* finds the signal within the search windows with widths of Π_{sbd} , Π_{mbd} and Π_{dr} for the single band delay, the multi band delay and the delay rate, respectively, and calculates the SNR of the signal. To judge the quality of the detection, the probability of false detection (**PFD**) is estimated, which is given by

$$\text{PFD} = 1 - [1 - e^{-\text{SNR}^2/2}]^n \simeq ne^{-\text{SNR}^2/2}, \quad (4.1)$$

where n is the number of independent points in the three-dimensional search over single band delay, multi band delay and delay rate, and so, $n \propto \Pi_{\text{sbd}}\Pi_{\text{mbd}}\Pi_{\text{dr}}$. If there is a *true* fringe signal which has a $\text{SNR} \geq 6$ and *well-behaved* residuals (e.g. single band delay) along the stream of residuals in time, the signal should be detected with a narrow search window. Figure 4.4 shows how a true fringe signal with SNR of 6.3 could be found by narrowing the search window. With wide search windows and so high **PFD** of 2.1×10^{-03} , we could not find the fringe signal of 2209+236 for the baseline of Haystack-Pico Veleta (*upper panel*), while with narrow windows and so low **PFD** of 9.3×10^{-06} , the fringe signal was found with the *Fringe quality* of 9 (*lower panel*). The *Fringe quality* of the *fourfit* program is judged by several criteria, ranging between 0 to 9, where **0** means non-detection of the signal and **1** to **9** mean, in principle, detection. Among those criteria, the most crucial one is **PFD**. If **PFD** $< 10^{-4}$, then 0 is given, whereas if **PFD** $\geq 10^{-4}$, 1 to 9 would be given with a few indication letters of error according to the rest of the criteria.

With the fringe fit of *fourfit*, 121 out of 127 observed sources have yielded fringe detections with $\text{SNR} \geq 6$. Figure 4.5 shows the fringe SNR distribution in the whole survey data. Only 6 sources (0710+439, 1458+718 (3C 309.1), 1749+701 (4C 09.57), 2021+614, 2030+407 (Cyg X-3), 2031+405 (MWC 349)) are not detected. The highest SNRs are 425 on the ‘‘Pico Veleta–Plateau de Bure’’ baseline of 1741-038 and 425 on the ‘‘Effelsberg-Pico Veleta’’ baseline of 1633+382.

4.3.3 Amplitude calibration

The fringe fitted data were amplitude calibrated using regular measurements of the system temperatures and antenna gains and the weather information for each station during the observations. Where possible, time-dependent factors in the antenna power gains were accounted for by applying atmospheric opacity corrections. The AIPS task APCAL is used to calibrate the amplitude. As a check for the accuracy and consistency of the amplitude calibration, we have investigated (independently for each of the detected sources) the calibrated visibility amplitudes using the best fit Gaussian component models obtained from the data (the corresponding models are given in Table 4.6). For each of the sources, the antenna gains were allowed to be scaled by a constant factor so as to optimize the fit by the Gaussian model.

The obtained corrections are within 20% for most of sources, which is also reflected in the average correction factors listed in Table 4.5. On the average, the gain factors for Pico Veleta, Onsala, North Liberty, Owens Valley, and Los Alamos remain within 10% during the whole observations. The average gains for Effelsberg do not change much except for the session C. Fort Davis and Mauna kia yield larger average corrections by more than 20%. Time-dependent errors may still be present in the calibrated data. Therefore we expect overall calibration accuracy of 20~30%

4.4 Imaging

With the phase- and amplitude-calibrated data, the images are made using the DIFMAP software (Shepherd et al. 1994). The *uv*-data are averaged over 30 seconds. Some bad data are flagged. After averaging and

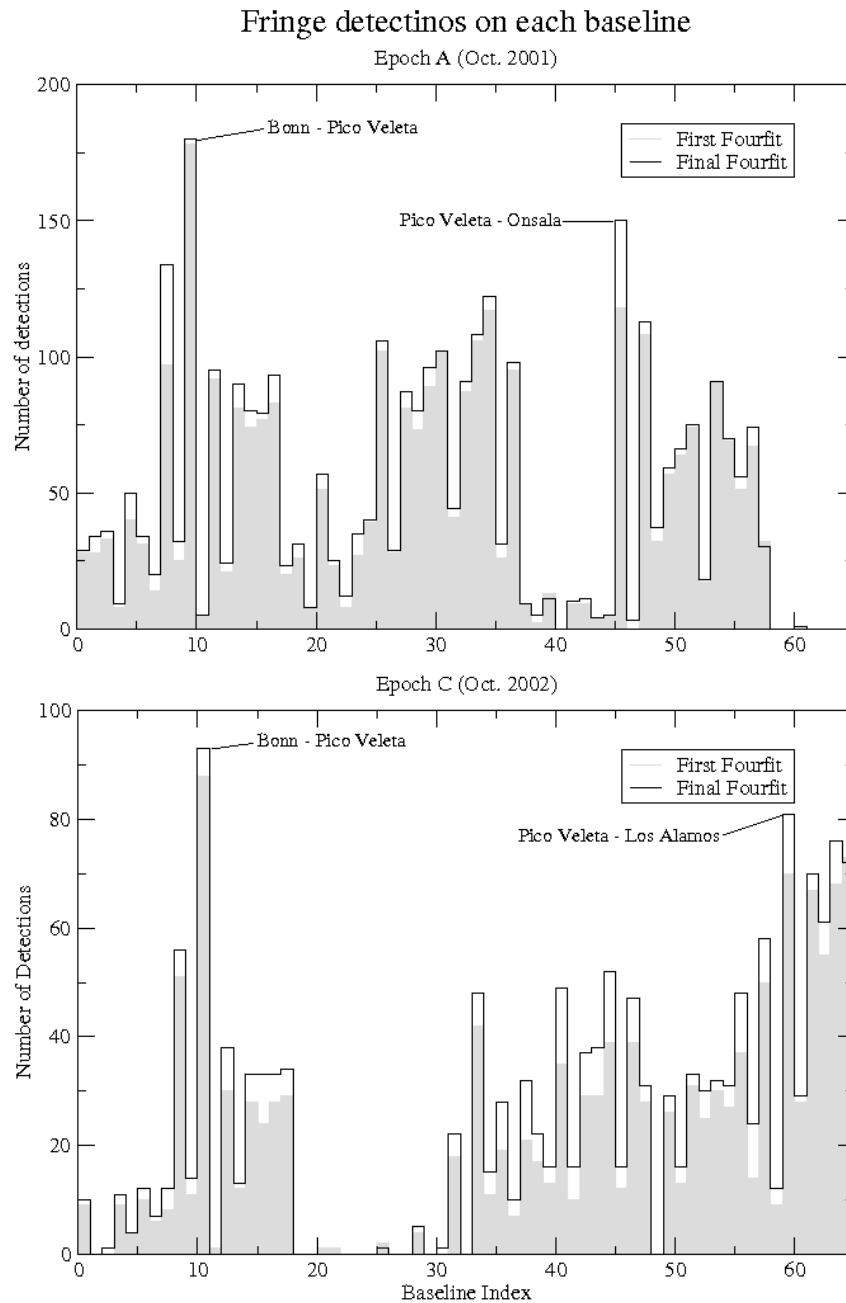


Figure 4.3: Fringe detections on each baseline for epoch A (Oct. 2001) and epoch C (Oct. 2002). The grey-filled and the black-outlined histograms are for the fringe detections before (the first *fourfit* run) and after (the final *fourfit* run) applying the window-controlling of single band delay, respectively.

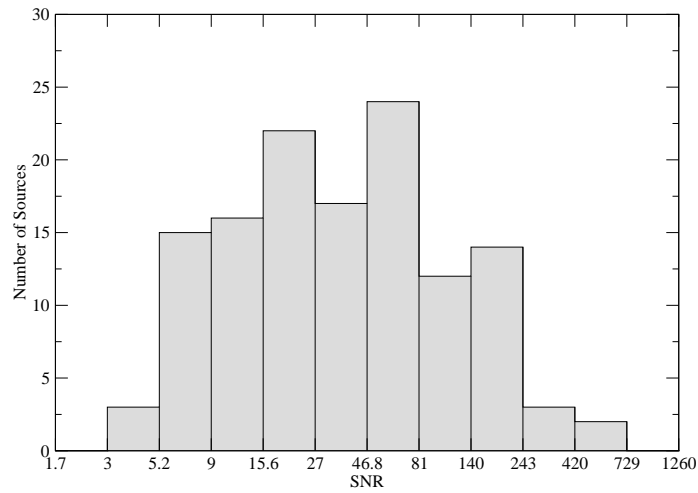


Figure 4.5: Distribution of fringe detection SNR of the sources. The highest SNRs are 425 on the baseline with Pico Veleta - Plateau de Bure of 1741-038 and 425 with Effelsberg - Pico Veleta of 1633+382. X-axis is in logarithmic scale of $\sqrt{3}$. The labels in the axis are corresponding to $\sqrt{3}^1, \sqrt{3}^2, \dots, \sqrt{3}^{13}$.

Table 4.5: Average antenna gain corrections

Telescope	Session A	Session B	Session C
(1)	(2)	(3)	(4)
Eb	0.998 ± 0.129	1.079 ± 0.183	1.354 ± 0.555
HA	1.160 ± 0.179	1.155 ± 0.315	1.180 ± 0.350
PdB	0.964 ± 0.150
PV	0.971 ± 0.157	0.938 ± 0.156	0.952 ± 0.192
On	1.033 ± 0.110	0.956 ± 0.121	...
Mh
Fd	1.215 ± 0.216	1.213 ± 0.298	1.080 ± 0.321
Hn	1.055 ± 0.235
Nl	0.996 ± 0.136	1.003 ± 0.116	1.002 ± 0.231
Ov	1.053 ± 0.158	1.107 ± 0.181	1.079 ± 0.221
Pt	1.139 ± 0.286	1.131 ± 0.284	1.046 ± 0.183
Kp	1.104 ± 0.172	1.059 ± 0.150	1.123 ± 0.259
La	1.009 ± 0.163	1.058 ± 0.266	1.076 ± 0.182
Mk	1.191 ± 0.240	1.543 ± 0.499	1.241 ± 0.268

Notes: Column designation: 1 - abbreviation for the name of telescopes; 2 - average and rms of antenna gains for observing session A; 3 - average and rms of antenna gains for observing session B; 4 - average and rms of antenna gains for observing session C.

flagging, the visibility data for each object detected are model fitted with a single-component Gaussian model instead of a point source model. In case that the data are not well fitted with a single-component Gaussian model, we model fit the uv -data with multiple Gaussian components. The satisfactory Gaussian models are subsequently used as starting models for hybrid mapping. We apply the self-calibration method (Cornwell 1995) to the visibility phase, in order to reveal the source structure in detail. A natural weighting is applied to the visibility data during the imaging, in order to improve the sensitivity of the image. In the following sections, the standard procedure for imaging the survey data is summarized in detail.

4.4.1 Model fitting

Model fitting is a technique which is generally used for solving the *inverse problem* in which the true distribution of a certain variable needs to be recovered from the measured distribution (Lobanov 1996). In VLBI experiments, this technique has been used to recover the true sky brightness from the observed visibility data, by describing the source brightness distribution in terms of Gaussian components. Through the model fitting, these Gaussian components are obtained by minimizing the agreement factor, χ^2 , between the observed visibility and the calculated values from the model components. Detailed discussions on this issue are found in Chapter 2.

Since model fitting is very useful for interpreting sparse or poorly calibrated data, and for quantitative analysis, we employ the model fitting technique in order to reveal the source brightness distribution and estimate the astronomical quantities (e.g. the size of core or jet components, the position of secondary and tertiary jet components, and the uncertainties in the measurement) for the survey data with the snapshot observation.

In the first step of the model fitting, we fit the visibility data with a single circular Gaussian component using the DIFMAP program. Since most of the sources observed at 86 GHz are expected to be described with a one- or two-component model, a single Gaussian component is a good starting point for the model fitting. Moreover the speed of the fitting should be increased by the single Gaussian model rather than a point-source model which is frequently used for a starting model.

In case that the respective single-component model does not represent the data satisfactorily, we apply a multi-component model to the data. In order to assess the image quality or the reliability of the final multi-component model, we make use of the agreement factor, the smoothness of residual flux, and noise in the final image. At first, we monitor the changes of the agreement factors with increasing number of Gaussian components in the model. The modeling is stopped whenever the introduction of an additional Gaussian component does not lead to a sensible improvement of the fit (expressed quantitatively by the reduced χ^2 -agreement factors). Secondly, we check the smoothness of the residual flux, which should be distributed smoothly, with a nearly zero mean and comparable positive and negative amplitudes. Thirdly, we check the noise in the final image, which should have a Gaussian distribution and is expressed quantitatively by the quality (ξ_r) of the residual noise. Suppose that a residual image has an rms σ_r and the maximum absolute flux density $|s_r|$. For Gaussian noise with a zero mean, the expectation of s_r is

$$|s_{r,\text{exp}}| = \sigma_r \left[\sqrt{2} \ln \left(\frac{N_{\text{pix}}}{\sqrt{2\pi}\sigma_r} \right) \right]^{1/2}, \quad (4.2)$$

where N_{pix} is the total number of pixels in the image. The quality of the residual noise is given by $\xi_r = s_r/s_{r,\text{exp}}$. When the residual noise approaches Gaussian noise, $\xi_r \rightarrow 1$. If $\xi_r > 1$, not all the structure has been adequately recovered, and if $\xi_r < 1$, the image model has an excessively large number of degrees of freedom (Lobanov et al. 2006). The values of ξ_r for the images in the survey are presented in Table 4.6 and the distribution of them is shown in Figure 4.6, implying that the images adequately represent the structure detected in the visibility data.

4.4.2 Hybrid mapping

Hybrid mapping is a process of making an image of a source that is strong enough to be detected in a coherence time, but has poorly calibrated initial phases, and involves an iterative procedure in which both the source structure and the antenna calibrations are determined. This procedure is now usually just called *self-calibration*, since the self-calibration method is predominantly employed for this procedure. Detailed discussions on this self-calibration method are found in Cornwell & Fomalont (1999) and Cornwell (1995).

The satisfactory Gaussian models are subsequently used as starting models for hybrid mapping with DIFMAP, so we could obtain the most reliable models for the observed uv -data quickly. We apply the

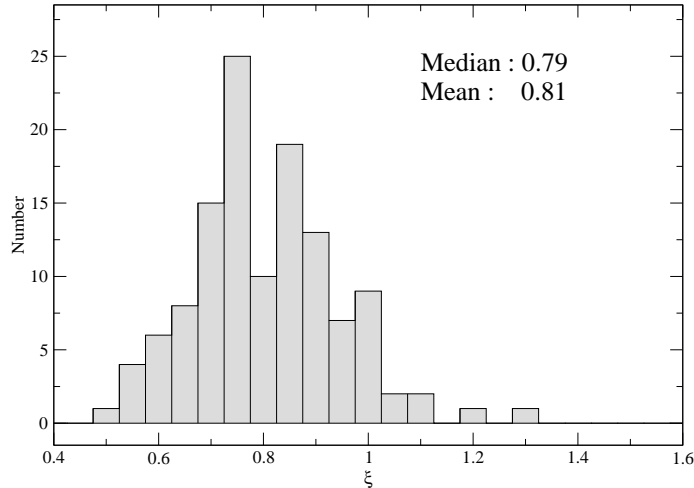


Figure 4.6: Distribution of the image quality factor ξ_r . The median and mean of the distribution are presented.

self-calibration method to the visibility phase, in order to reveal the source structure in detail. We start with locating a tight CLEAN window around the brightest emission region, which is largely central. A couple of CLEANs with ten iterations and a gain factor of 0.1 Jy, are applied until the first negative flux is obtained. Then the obtained δ -components model is used for self-calibration. If any distinctively bright emission around the CLEAN window appears in a residual map, another CLEAN window is put around the emission region. Since the second bright emission is usually not as bright as the brightest emission in the center of the map, a CLEAN with 100 (or 200) iterations and a gain factor of 0.01~0.05 Jy is run until the first appearance of negative flux. The resulting δ -components are used for another self-calibration. If there is no longer distinctively bright emission region, in an attempt to find a detail source structure, a few more tight CLEAN windows slightly overlapped each other, are located around and a few CLEAN with 200 iterations and a gain factor of 0.01 Jy are conducted. The series of self-calibration stops as soon as the residual flux is smoothly distributed with a nearly zero mean and comparable positive and negative amplitude. The reliability of the resulting models is judged by the quality of the residual noise, ξ_r .

We do not modify the visibility amplitudes, except for introducing an overall, time-constant gain correction factor wherever it is required for improving the agreement between the CLEAN model and the data. Addition to the check for the antenna gain corrections described in section 4.3.3, we investigated the changes of the visibility amplitudes with and without introducing the time-constant gain correction factor, by using the correlated flux densities S_S , S_L at the shortest and longest baselines B_S , B_L (presented in Columns 4–7 in Table 4.6), for each of the sources. The correlated flux densities $S_{S,L}$ with introducing the antenna gain corrections are compared with the flux densities S'_S and S'_L before the gain corrections. As shown in Figure 4.7 for the distributions of the ratios $R_S = S_S/S'_S$ and $R_L = S_L/S'_L$, the visibility amplitudes at the shortest and longest baselines for each of the sources were not changed for most of the sources during the hybrid mapping. For exceptional sources, the ratios of the visibility amplitudes fall within a range of 0.75–1.25. This investigation shows again that the amplitude calibration error of this survey observations is 20%–30%.

We introduce a zero-baseline flux to recover a faint structure in the extended region by adding a fake visibility at the origin of the uv plane. Since the shortest baseline of this survey observations is about 50–100 M λ , no value is added to the pixel at the origin of the uv plane grid. For the faint structure in the extended region of the sources, this may result in the faint structures of the extended regions appearing to be negative because the flux in every pixel of the map is offset by a small negative amount. The effect may be countered to some extent by adding the fake visibility at the origin of the uv plane. The measured total flux density of each source S_{86} (listed Column 3 in Table 4.6) is used as the zero-baseline flux.

4.4.3 Measuring image parameters

In order to extract physical quantities out of the images, the final uv -data are fitted by Gaussian-component model, and then image parameters are measured: total and peak flux densities, positions, and sizes of each component are obtained from the fit. Uncertainties in the models are estimated. The fluxes of core and jet

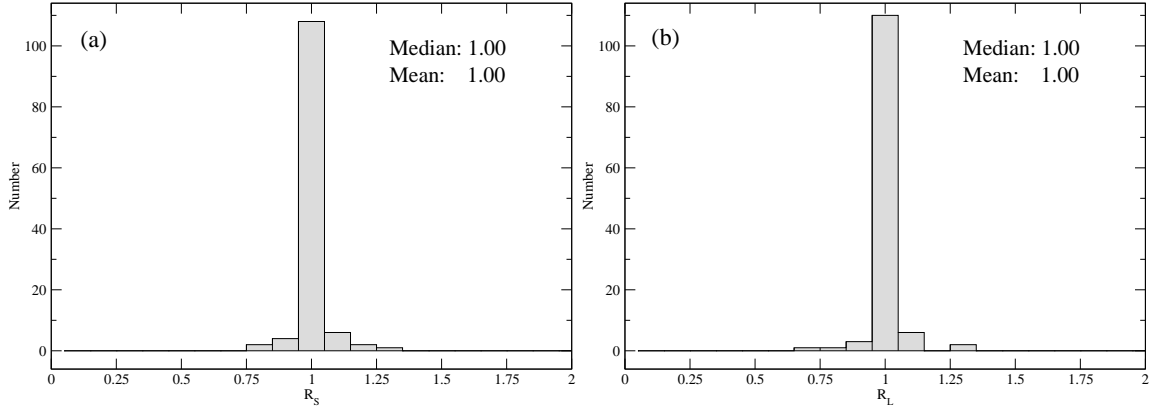


Figure 4.7: Distributions of the correlated flux density ratios (a) $R_S (= S_S/S'_S)$ and (b) $R_L (= S_L/S'_L)$. The means and medians for the distributions are presented in each panel. The correlated flux densities $S_{S,L}$ are listed in Table 4.6.

components are measured by removing each component out of the fitted image and investigating the residual map whose distribution is reflecting the Gaussian component. The off-source rms noise is measured from the statistical information of pixels within the whole residual map. As expected, the overall noise in the images are less than 10 mJy/beam. The measured parameters of the images are presented in section 4.5. The uncertainties of the fit parameters are obtained using the set of equations (2.40)-(2.44).

4.5 Results of the survey

In this section, we present the graphical results of the global 86 GHz VLBI survey of compact radio sources. Out of 127 sources, 109 sources are imaged and investigated in order to estimate physical parameters. This survey made the first 3 mm-VLBI maps for 90 sources, increasing the number of sources ever imaged with 3 mm-VLBI observations up to 110. All images are shown with the plots of the corresponding visibility amplitudes against uv -radius and of the uv -sampling distribution. The image parameters and modelfit parameters are also summarized here, which are obtained from the procedure explained in section 2.4.2. The interesting properties of the sample are also discussed.

4.5.1 Images

In Figure 4.8, we present two plots and one contour map for each source at each epoch. In the left panel, the plot of the visibility amplitudes against uv -radius is shown. The corresponding uv -sampling distribution is given in the inset. The X-axis of the plot of the visibility amplitude represents the uv -radius which is the length of the baseline used to obtain the corresponding visibility point. The uv -radius is given in the units of $10^6 \lambda$, where λ is the wavelength of the observing emission. The Y-axis of the plot shows the amplitude of each visibility point (i.e., correlated flux density) in units of Jy. The uv -sampling distribution in the inset of the left panel describes the overall distribution of the visibility in the uv -plane, whose maximum scale equals to that of uv -radius. In the right panel, the contour map of each source is shown with the X- and Y-axis in the units of milliarcsecond. The name and observing date of the source are put in the upper left corner of the map. The lowest contour level is also presented in the lower right corner of the map. The shaded ellipse represents the FWHM of the restoring beam in the image. In all of the images, the contours are drawn at $-1, 1, 1.4, \dots, 1.4^n$ of the lowest flux density level shown in each map of Figure 4.8.

For 12 sources (0133+476, 0149+218, 0212+735, 0234+285, 0238-084, 0316+413, 0355+508, 0415+379, 0430+052, 0716+714, 1928+738, 2255-282), multi-epoch images are presented in turn. Most sources are centered on the brightest component (VLBI core), but for a few sources with a larger structure, we have shifted the center to fit the image in the box.

In Table 4.6, the parameters of the images shown in Figure 4.8 are summarized. For sources imaged at multi epochs, the source name only at the first epoch, whenever it is, is presented, and for the rest of the epochs, the name is not shown. For each image, Table 4.6 lists the source name, the observing epoch, the

total flux density, S_{86} (Jy), obtained from pointing and calibration measurements during the observation, the correlated flux densities, $S_{S,L}$ (Jy), measured on the shortest and longest baselines, $B_{S,L}$ ($10^6\lambda$), the parameters of restoring beam (the size of the major axis, B_a (μas), and the minor axis, B_b (μas), and the position angle of the beam, B_{PA} ($^\circ$)), the total flux, S_t (mJy), the peak flux density, S_p (mJy/beam), the off-source RMS, σ (mJy/beam), and the quality of the residual noise in the image (see section 4.4.1).

Table 4.6 lists all of the parameters of each model-fit component; the total flux, S_{tot} (mJy), peak flux density, S_{peak} (mJy/beam), size, d (μas), minimum resolvable size, d_{min} (μas), radius, r (μas) (only for jet components), position angle, θ ($^\circ$) (only for jet components), and measured brightness temperature, T_b (10^{10} K). For sources with multiple components, parameters of core component are followed by those of jet components in turn. Sources observed at multiple epochs are listed with the indices of epochs. The uncertainties estimated by the procedure in section 4.4.3 are given next to each parameter. The upper limits of size, d and the lower limits of brightness temperature, T_b , are in italic with brackets (e.g. $<$ for upper limit and $>$ for lower limit).

Table 4.6: Image parameters

Name	Obs	S_{86}	S_S	B_S	S_L	B_L	B_a	B_b	B_{PA}	S_t	S_p	σ	ξ_r
(1)	(2)	(3)	(4)	(5)	(6)	(7)	(8)	(9)	(10)	(11)	(12)	(13)	(14)
0003-066	C	2.16	0.71 ± 0.30	60	0.29 ± 0.16	2450	461	49	-6.2	613	209	17	0.86
0007+106	C	0.60	0.59 ± 0.00	10	0.35 ± 0.06	2470	457	54	-2.7	372	181	9	1.00
0016+731	B	0.84	0.48 ± 0.13	60	0.25 ± 0.08	3130	75	51	-11.6	434	181	8	0.91
0048-097	C	0.60	0.43 ± 0.13	60	0.11 ± 0.06	2440	466	42	-3.3	486	163	6	0.75
0106+013	A	1.36	0.49 ± 0.06	100	0.24 ± 0.05	2390	900	45	-8.6	447	354	15	0.62
0119+041	C	0.68	0.20 ± 0.06	70	0.20 ± 0.09	2390	602	79	-9.9	233	227	9	0.77
0119+115	C	0.68	0.34 ± 0.12	60	0.16 ± 0.06	2390	400	44	-7.1	232	176	10	0.63
0133+476	A	3.96	1.99 ± 0.86	60	0.09 ± 0.03	3140	170	51	-16.4	2148	675	17	0.80
	B	4.53	0.70 ± 0.39	30	1.36 ± 0.54	2430	206	43	5.1	4164	881	20	0.79
0149+218	A	0.96	0.38 ± 0.14	130	0.07 ± 0.04	2450	266	39	-7.1	425	230	12	0.68
	C	0.99	0.41 ± 0.12	50	0.06 ± 0.03	2420	262	50	-5.4	529	278	10	0.77
0201+113	C	0.39	0.27 ± 0.10	60	0.16 ± 0.05	2470	455	47	-2.6	212	159	8	0.66
0202+149	A	...	0.32 ± 0.08	140	0.21 ± 0.04	2470	381	44	-6.0	370	193	9	0.81
0202+319	C	1.01	0.59 ± 0.16	60	0.10 ± 0.05	3140	230	44	-15.3	684	263	8	0.84
0212+735	A	0.77	0.16 ± 0.06	60	0.11 ± 0.03	2960	109	48	-44.5	174	136	4	0.87
	B	0.79	0.33 ± 0.14	230	0.20 ± 0.07	670	1354	151	-65.3	430	229	11	0.49
0218+357	C	0.58	0.14 ± 0.04	60	0.11 ± 0.03	3140	229	43	-17.2	182	109	4	0.90
0221+067	C	0.59	0.42 ± 0.06	110	0.11 ± 0.02	2470	582	68	-0.2	357	272	25	0.59
0224+671	B	1.34	0.27 ± 0.10	40	0.29 ± 0.06	2380	183	50	38.5	362	209	9	1.04
0234+285	A	2.98	2.07 ± 0.30	210	0.13 ± 0.07	2380	215	37	-3.3	2110	549	12	0.95
	B	3.24	2.44 ± 0.48	210	0.17 ± 0.06	2310	218	42	2.9	2691	1073	25	0.74
	C	...	1.47 ± 0.20	60	0.24 ± 0.04	2460	466	53	-6.4	1662	931	38	0.75
0235+164	A	1.62	0.99 ± 0.30	410	0.45 ± 0.06	2470	298	37	2.1	966	482	22	0.73
0238-084	B	...	0.27 ± 0.06	250	0.08 ± 0.02	2420	425	35	-6.2	246	155	8	0.74
	C	0.63	0.33 ± 0.11	60	0.12 ± 0.00	2430	1001	51	-4.7	307	247	9	0.67
0300+470	B	3.11	0.91 ± 0.15	240	0.13 ± 0.05	2460	178	36	-9.5	953	377	4	0.99
0316+413	A	4.76	1.84 ± 0.28	60	0.21 ± 0.07	2470	203	43	-15.6	2849	426	20	1.20
	B	4.80	1.23 ± 0.51	30	0.22 ± 0.09	2380	353	61	-1.1	1530	419	12	0.76
	C	4.56	0.90 ± 0.20	60	0.17 ± 0.06	3140	187	47	-23.7	1347	339	8	0.94
0333+321	A	1.77	0.42 ± 0.16	210	0.34 ± 0.07	2440	211	42	-2.6	624	273	16	0.98
0336-019	A	2.11	1.09 ± 0.60	300	0.22 ± 0.03	2280	368	52	-3.4	1971	461	14	0.69
0355+508	A	6.76	3.86 ± 0.79	60	0.27 ± 0.06	3140	150	47	-28.6	4198	653	47	0.82
	C	7.59	4.03 ± 0.40	70	1.36 ± 0.54	1470	697	90	-31.3	4140	2487	95	1.01
0415+379	B	2.17	0.56 ± 0.26	90	0.18 ± 0.06	2460	203	44	-7.9	2696	508	24	0.77
	C	2.57	1.53 ± 0.23	60	0.13 ± 0.07	3120	220	42	-16.7	1445	375	30	0.69
0420+022	C	0.48	0.33 ± 0.15	60	0.10 ± 0.04	2470	684	51	-0.7	234	161	7	0.76
0420-014	B	5.83	1.42 ± 0.89	50	0.48 ± 0.12	2470	445	48	-5.8	1866	879	43	0.84
0422+004	B	1.46	0.62 ± 0.25	60	0.37 ± 0.09	2460	438	48	-5.3	667	409	12	0.92
0430+052	B	4.05	0.14 ± 0.08	100	0.20 ± 0.05	2460	359	43	-5.7	3585	555	26	0.71
	C	2.32	0.87 ± 0.12	60	0.39 ± 0.07	2460	594	56	-0.8	1523	542	16	0.77
0440-003	C	0.88	0.37 ± 0.12	70	0.31 ± 0.06	2470	497	56	-2.4	481	337	12	0.87
0458-020	B	1.12	0.50 ± 0.18	50	0.17 ± 0.04	2460	433	49	-5.4	501	357	9	0.77
0521-365	C	...	0.43 ± 0.17	40	0.22 ± 0.09	1400	1196	150	-13.5	330	297	18	0.53
0528+134	A	2.02	0.54 ± 0.06	140	0.29 ± 0.05	2410	336	50	-1.3	1051	391	6	0.82
0529+075	A	1.13	0.29 ± 0.07	270	0.25 ± 0.07	2250	840	52	2.9	267	260	20	0.68
0552+398	A	1.34	0.72 ± 0.12	60	0.15 ± 0.03	2470	248	41	-9.9	778	348	11	0.77
0607-157	B	...	1.00 ± 0.40	60	0.41 ± 0.14	1350	718	127	-23.9	1188	798	16	0.84
0642+449	B	1.67	1.16 ± 0.11	60	0.18 ± 0.05	2470	214	43	-6.1	1295	486	7	0.73

Table 4.5: Image parameters (continued)

Name	Obs	S_{86}	S_S	B_S	S_L	B_L	B_a	B_b	B_{PA}	S_t	S_D	σ	ξ_r
(1)	(2)	(3)	(4)	(5)	(6)	(7)	(8)	(9)	(10)	(11)	(12)	(13)	(14)
0707+476	C	0.27	0.08 ± 0.02	330	0.08 ± 0.02	2470	255	37	-4.9	75	72	3	0.67
0716+714	B	1.16	0.51 ± 0.10	50	0.29 ± 0.04	2470	141	49	3.5	565	369	12	0.92
	C	2.51	0.61 ± 0.43	100	0.61 ± 0.06	3120	122	40	-15.9	1020	865	29	0.89
0727-115	B	...	0.65 ± 0.24	70	0.45 ± 0.15	620	928	265	-21.8	675	545	25	0.69
0735+178	B	1.23	0.30 ± 0.11	50	0.12 ± 0.05	2390	315	42	-0.5	629	141	5	0.71
0736+017	A	2.24	1.36 ± 0.48	320	0.24 ± 0.09	2400	341	49	-1.9	1990	577	18	0.79
0738+313	C	0.47	0.41 ± 0.08	30	0.08 ± 0.04	2320	303	51	6.1	439	254	8	0.81
0748+126	B	1.80	0.52 ± 0.20	270	0.33 ± 0.09	2400	333	42	-2.0	1628	506	14	0.84
0804+499	C	0.38	0.20 ± 0.07	40	0.10 ± 0.04	2360	213	40	0.0	175	113	4	0.71
0814+425	C	0.50	0.39 ± 0.10	40	0.05 ± 0.01	2380	232	43	2.8	409	178	7	0.74
0823+033	A	1.02	0.59 ± 0.09	60	0.15 ± 0.05	2400	348	39	-3.6	590	239	8	0.71
0827+243	B	2.16	0.55 ± 0.16	70	0.50 ± 0.06	2380	314	54	-19.7	720	535	13	1.02
0836+710	C	1.16	0.39 ± 0.11	90	0.16 ± 0.09	3000	156	62	21.1	451	361	14	0.85
0850+581	C	0.26	0.14 ± 0.01	50	0.09 ± 0.03	2470	247	37	-13.8	165	72	4	0.83
0851+202	B	2.71	0.60 ± 0.20	60	0.29 ± 0.12	3140	366	52	-12.0	901	505	19	0.83
0859+470	C	0.42	0.33 ± 0.09	40	0.14 ± 0.03	2330	230	43	10.5	306	174	8	0.88
0906+015	B	2.43	0.73 ± 0.29	60	0.36 ± 0.09	2470	452	46	-5.1	649	488	16	0.86
0917+624	A	1.01	0.27 ± 0.12	50	0.07 ± 0.04	2350	154	44	-16.8	142	116	6	0.92
0945+408	A	0.95	0.11 ± 0.06	170	0.22 ± 0.07	2890	180	46	-16.8	798	229	13	0.93
0954+658	A	1.16	0.43 ± 0.12	50	0.27 ± 0.02	3040	144	45	-4.0	784	336	8	0.95
1012+232	B	1.01	0.77 ± 0.11	60	0.09 ± 0.05	3110	345	41	-12.4	693	191	7	0.99
1044+719	B	0.87	0.26 ± 0.14	60	0.30 ± 0.06	2470	218	49	-30.2	204	181	8	0.92
1101+384	C	0.58	0.33 ± 0.09	90	0.12 ± 0.03	2470	220	44	-6.8	407	169	5	0.84
1128+385	C	0.97	0.44 ± 0.19	170	0.10 ± 0.03	3140	213	43	-2.0	482	258	10	0.74
1150+497	C	1.02	0.46 ± 0.14	160	0.33 ± 0.14	2390	284	48	13.1	616	392	11	0.92
1156+295	A	4.42	2.97 ± 0.62	220	0.93 ± 0.21	2470	188	37	-8.5	3006	1176	28	0.97
1219+285	C	0.36	0.23 ± 0.06	50	0.09 ± 0.01	2470	343	38	-5.3	179	104	3	0.75
1226+023	A	10.81	2.05 ± 0.33	100	0.32 ± 0.17	2440	439	54	-5.5	2160	630	27	0.65
1228+126	A	4.16	0.94 ± 0.16	180	0.16 ± 0.07	1590	198	78	-4.8	897	568	35	0.61
1253-055	C	16.90	2.32 ± 0.83	70	3.04 ± 0.54	2460	440	56	-4.3	8653	4286	158	1.29
1308+326	A	1.44	0.45 ± 0.07	150	0.44 ± 0.05	2330	215	46	1.4	734	466	12	0.76
1502+106	C	0.82	0.45 ± 0.12	150	0.28 ± 0.02	2450	440	47	-2.3	564	298	11	0.76
1508-055	C	...	0.49 ± 0.15	130	0.16 ± 0.07	2310	469	45	-0.3	1192	285	16	0.62
1510-089	C	2.10	0.67 ± 0.24	130	0.66 ± 0.10	2350	400	42	-4.7	1864	576	46	0.69
1511-100	C	0.81	0.64 ± 0.15	120	0.18 ± 0.03	2440	580	40	-1.3	598	264	16	0.67
1546+027	C	1.04	0.50 ± 0.26	140	0.28 ± 0.07	2470	407	44	-4.0	436	220	19	0.74
1548+056	C	1.71	0.63 ± 0.16	260	0.18 ± 0.07	2470	464	44	-2.8	551	248	12	0.84
1606+106	C	1.26	0.37 ± 0.10	70	0.53 ± 0.11	3140	401	52	-10.1	397	344	16	0.98
1637+574	C	1.70	1.13 ± 0.37	110	0.61 ± 0.08	3130	118	36	-58.1	1186	741	12	1.10
1642+690	C	1.36	0.50 ± 0.11	60	0.23 ± 0.09	3140	107	43	-59.9	512	360	12	1.11
1652+398	A	...	0.24 ± 0.09	230	0.10 ± 0.05	720	805	145	78.7	245	159	10	0.57
1655+077	C	1.00	0.49 ± 0.22	130	0.27 ± 0.08	2470	381	44	-7.4	569	330	11	0.85
1739+522	C	1.45	1.12 ± 0.11	320	0.45 ± 0.08	3140	115	35	-46.6	1030	693	8	0.96
1741-038	C	4.16	3.73 ± 0.58	160	0.34 ± 0.13	2470	448	38	-4.7	3210	1293	41	0.87
1749+096	C	4.03	2.37 ± 0.50	70	1.47 ± 0.14	2470	390	46	-7.6	2388	1978	26	0.89
1800+440	B	1.07	0.71 ± 0.11	60	0.18 ± 0.07	3140	170	49	-18.8	508	357	11	1.00
1803+784	C	1.48	1.00 ± 0.19	240	0.21 ± 0.06	3140	85	38	-39.4	996	382	5	0.89
1807+698	A	1.54	0.25 ± 0.05	200	0.22 ± 0.07	2360	181	49	84.7	231	225	7	0.75
1823+568	A	1.30	0.21 ± 0.08	100	0.29 ± 0.09	3080	130	50	24.5	1000	332	14	0.91
1828+487	A	1.96	0.87 ± 0.45	220	0.18 ± 0.04	2940	182	65	-47.2	1995	587	19	0.76

Table 4.5: Image parameters (*continued*)

Name	Obs	S_{86}	S_S	B_S	S_L	B_L	B_a	B_b	B_{PA}	S_t	S_p	σ	ξ_r
(1)	(2)	(3)	(4)	(5)	(6)	(7)	(8)	(9)	(10)	(11)	(12)	(13)	(14)
1842+681	A	0.74	0.24 ± 0.03	120	0.10 ± 0.02	3110	162	50	24.1	259	159	7	0.79
1901+319	C	0.59	0.27 ± 0.06	50	0.12 ± 0.05	2370	312	94	-12.3	248	185	6	0.70
1921-293	A	...	2.78 ± 0.41	60	0.22 ± 0.11	1770	727	102	-24.0	2896	1477	44	0.67
1923+210	B	1.73	1.22 ± 0.17	60	0.23 ± 0.04	2470	280	46	-10.1	919	443	13	0.93
1928+738	A	2.60	0.62 ± 0.18	60	0.14 ± 0.03	3130	106	57	41.1	487	294	9	0.86
	C	2.43	0.75 ± 0.33	60	0.27 ± 0.07	3120	132	43	-9.6	1383	325	24	0.85
1954+513	C	0.66	0.35 ± 0.13	70	0.25 ± 0.05	3110	137	49	-44.4	354	276	13	1.06
1957+405	C	...	0.17 ± 0.08	480	0.13 ± 0.04	2080	175	58	-45.5	192	133	22	0.57
2007+777	A	0.92	0.37 ± 0.13	250	0.21 ± 0.06	3130	108	39	64.8	352	215	6	1.00
2013+370	B	2.89	2.07 ± 0.21	60	0.29 ± 0.10	3070	206	47	-13.0	2083	958	26	0.89
2023+336	B	1.77	0.98 ± 0.27	60	0.18 ± 0.12	2920	227	48	-13.7	825	402	19	0.82
2037+511	B	1.44	0.74 ± 0.14	180	0.31 ± 0.06	3130	146	46	-37.3	596	317	16	0.87
2121+053	A	...	0.39 ± 0.10	350	0.11 ± 0.02	2350	296	42	-4.7	391	247	14	0.62
2128-123	A	...	0.31 ± 0.13	70	0.17 ± 0.05	480	772	335	-17.8	338	212	10	0.72
2134+004	A	2.03	0.28 ± 0.10	140	0.25 ± 0.08	2350	346	44	-5.3	186	187	18	0.68
2155-152	B	...	0.38 ± 0.10	190	0.16 ± 0.09	1280	476	119	-14.7	369	224	7	0.74
2200+420	A	3.57	1.41 ± 0.11	110	0.96 ± 0.09	2400	326	48	-20.5	1495	1137	17	0.67
2201+315	A	2.97	1.02 ± 0.31	220	0.60 ± 0.19	710	287	169	75.3	1098	783	30	0.78
2216-038	B	0.97	0.50 ± 0.08	100	0.31 ± 0.11	480	722	294	-35.9	444	391	11	0.54
2223-052	B	3.90	1.29 ± 0.15	80	0.19 ± 0.07	2460	399	48	-4.7	1556	382	17	0.76
2234+282	A	1.03	0.66 ± 0.00	70	0.13 ± 0.03	2320	242	58	-22.5	365	271	13	0.77
2251+158	A	5.97	1.67 ± 0.17	110	0.92 ± 0.11	2430	292	55	-10.8	4084	865	18	0.86
2255-282	A	...	1.56 ± 0.40	30	0.84 ± 0.26	600	2856	207	-31.1	1861	1475	45	0.69
	B	...	0.73 ± 0.24	90	0.53 ± 0.13	1280	666	129	-23.3	1007	981	51	0.70
2345-167	B	...	0.33 ± 0.14	70	0.24 ± 0.00	340	1077	500	4.0	349	281	16	0.58

Notes: Column designation: 1 - source name; 2 - observing epochs: **A** - October 2001; **B** - April 2002; **C** - October 2002; 3 - total flux density [Jy] (obtained from pointing and calibration scan measurements made at Pico Veleta); 4,6 - correlated flux density [Jy] measured on baselines 5,7 [M λ]; 8-10 - restoring beam: 8 - major axis [μ as]; 9 - minor axis [μ as]; 10 - position angle of the major axis [$^\circ$]; 11 - total CLEAN flux density [mJy]; 12 - peak flux density [mJy/beam]; 13 - off-source RMS in the image [mJy/beam]; 14 - quality of the residual noise in the image (see section 4.4.1).

Table 4.6: Model fit parameters of sources

Name	Obs	S_{tot}	S_{peak}	d	d_{min}	r	θ	T_{b}
(1)	(2)	(3)	(4)	(5)	(6)	(7)	(8)	(9)
0003-066	C	203±84	213±61	< 42	42	> 2.6
		181±161	136±97	179±127	73	579±64	-3.3± 6.3	0.13±0.18
0007+106	C	185±93	196±67	< 53	53	> 1.2
		48±63	65±51	< 155	155	461±60	-138.3± 7.4	> 0.036
0016+731	B	312±293	197±157	< 28	28	> 18
		51±51	56±38	65±44	41	115±22	114.6±10.8	0.55±0.77
0048-097	C	268±73	179±41	42±10	20	2.5±1.1
		63±32	53±20	< 42	42	266±8	6.3± 1.7	> 0.6
		76±77	44±38	127±111	64	760±55	7.7± 4.2	0.077±0.14
0106+013	A	431±125	351±79	36±8	34	17±7.7
0119+041	C	217±98	228±71	< 65	65	> 1.4
0119+115	C	201±72	184±48	< 30	30	> 5.9
0133+476	A	971±180	689±104	47±7	9	13±4.1
		284±86	194±48	51±13	15	97±6	-70.2± 3.7	3.3±1.7
		464±336	154±106	212±146	20	822±73	-10.7± 5.1	0.32±0.43
0133+476	B	1771±725	1060±372	47±16	18	24±17
		670±581	179±150	206±172	20	1247±86	-1.9± 4.0	0.48±0.81
		267±236	171±127	194±144	41	1807±72	-14.3± 2.3	0.22±0.33
		301±313	95±94	317±314	27	2803±157	-26.1± 3.2	0.091±0.18
		208±190	138±105	498±380	43	3776±190	-29.9± 2.9	0.026±0.039
0149+218	A	427±149	184±59	66±21	13	3.7±2.4
0149+218	C	494±209	303±109	61±22	23	5.1±3.6
0201+113	C	183±74	157±48	< 36	36	> 11
0202+149	A	246±119	183±71	< 34	34	> 4.8
		132±66	57±26	81±37	24	78±19	-93.6±13.4	0.46±0.43
0202+319	C	614±389	321±180	56±31	27	7.9±8.9
0212+735	A	162±20	137±13	29±3	5	11±2
		164±98	184±73	< 184	184	> 0.27
0218+357	C	359±345	77±72	457±429	85	668±214	113.5±17.8	0.095±0.18
		154±94	118±57	< 34	34	> 4.3
		355±89	299±57	48±9	30	3.8±1.5
0224+671	B	287±178	219±108	< 33	33	> 6.6
0234+285	A	1250±504	368±142	65±25	10	11±8.3
		80±84	69±55	< 55	55	84±22	128.1±14.6	> 0.96
		611±318	217±106	61±30	14	139±15	20.3± 6.1	6±5.8
		423±384	101±89	83±73	17	150±37	-161.5±13.7	2.2±3.9
0234+285	B	1312±349	604±146	66±16	10	11±5.3
		672±350	260±126	86±42	17	76±21	12.2±15.4	3.3±3.2
		505±303	302±155	61±31	27	121±16	-170.9± 7.4	4.9±5.1
0234+285	C	986±207	799±131	39±6	19	24±7.7
		485±50	392±31	42±3	9	240±2	-32.2± 0.4	10±1.6
		218±24	172±15	45±4	10	838±2	-17.8± 0.1	3.9±0.67
0235+164	A	385±74	388±52	< 13	13	> 69
		678±401	158±91	83±48	13	68±24	-89.6±19.4	3.1±3.6
0238-084	B	267±86	142±40	47±13	17	2±1.1
0238-084	C	292±100	252±65	< 47	47	> 2.2
0300+470	B	924±277	259±75	72±21	6	2.9±1.7
0316+413	A	724±167	431±86	51±10	10	4.7±1.9
		247±109	192±67	41±14	23	161±7	140.3± 2.5	2.5±1.7
		813±383	198±91	238±109	10	438±55	175.9± 7.1	0.24±0.22
		305±173	122±64	119±63	18	1043±31	-149.7± 1.7	0.36±0.38
		476±425	91±80	387±339	15	1412±170	-160.1± 6.8	0.053±0.093

Table 4.6: Model fit parameters of sources (*continued*)

Name	Obs	S_{tot}	S_{peak}	d	d_{min}	r	θ	T_{b}
(1)	(2)	(3)	(4)	(5)	(6)	(7)	(8)	(9)
0316+413	B	474±59	394±38	46±4	11	3.7±0.72
		224±109	188±70	62±23	42	390±12	-177.4± 1.7	0.97±0.73
		272±130	152±63	275±114	32	853±57	-161.6± 3.8	0.06±0.05
		362±289	128±96	579±435	36	2729±218	-165.9± 4.6	0.018±0.027
0316+413	C	599±129	351±65	62±12	10	2.6±0.97
		138±40	125±27	28±6	17	250±3	160.4± 0.7	2.9±1.3
		207±111	90±44	144±71	19	505±35	168.7± 4.0	0.17±0.16
		44±44	51±33	< 64	64	749±21	-159.4± 1.6	> 0.18
		51±48	55±35	< 58	58	1052±19	-143.3± 1.0	> 0.25
0333+321	A	384±135	282±80	32±9	18	14±7.9
		208±169	88±66	56±42	27	72±21	-75.5±16.2	2.5±3.7
		147±153	58±56	72±70	33	144±35	-89.2±13.6	1.1±2
0336-019	A	832±138	499±71	67±10	11	5.6±1.6
		477±141	308±77	59±15	21	199±7	89.8± 2.1	4.2±2.1
		706±177	281±65	130±30	12	1011±15	58.9± 0.9	1.3±0.59
0355+508	A	1184±776	637±368	82±47	24	2.9±3.4
		239±251	277±190	< 60	60	152±21	66.3± 7.7	> 1.1
		415±236	440±172	< 32	32	248±6	136.4± 1.4	> 6.8
		209±251	249±192	< 70	70	363±27	49.1± 4.3	> 0.7
0355+508	C	2953±831	2557±544	63±13	43	12±5.2
		1064±629	769±368	173±83	80	370±41	89.8± 6.4	0.58±0.56
0415+379	B	1307±922	556±361	65±42	24	5.3±6.9
		374±264	198±123	87±54	29	272±27	74.3± 5.7	0.85±1.1
		147±205	161±152	119±112	91	1652±56	52.3± 1.9	0.18±0.36
0415+379	C	1104±741	455±282	68±42	23	4.1±5.1
		425±159	229±75	62±20	16	93±10	78.8± 6.3	1.9±1.3
0420+022	C	230±68	173±41	43±10	31	6.7±3.2
0420-014	B	1332±493	902±276	47±14	28	19±12
		156±137	177±103	< 86	86	799±25	-167.9± 1.8	> 0.66
0422+004	B	629±416	426±233	< 49	49	> 5.6
0430+052	B	1107±365	575±168	59±17	18	5.4±3.2
		912±407	370±153	80±33	19	232±17	-105.8± 4.1	2.4±2
		1270±770	278±165	249±147	15	880±74	-114.4± 4.8	0.35±0.41
0430+052	C	668±157	566±101	34±6	26	9.8±3.5
		331±137	224±77	91±31	39	67±16	-116.8±13.1	0.68±0.47
		96±87	113±66	< 113	113	664±33	-108.7± 2.9	> 0.13
		148±71	109±42	100±38	48	1374±19	-118.0± 0.8	0.25±0.19
0440-003	C	77±85	106±68	148±96	147	2645±48	-121.6± 1.0	0.06±0.083
		364±162	330±109	< 46	46	> 5.2
		62±54	70±40	< 98	98	309±28	-175.5± 5.2	> 0.2
0458-020	B	501±85	370±50	47±6	14	12±3.3
0521-365	C	331±27	303±18	79±5	22	0.92±0.11
0528+134	A	510±219	405±136	< 32	32	> 25
		268±103	160±53	58±19	24	98±10	120.5± 5.6	4±2.7
		85±23	87±16	< 23	23	217±2	70.0± 0.6	> 8
0529+075	A	114±69	73±37	69±35	39	815±18	35.7± 1.2	1.2±1.2
		259±51	260±36	< 27	27	> 13
0552+398	A	480±52	362±31	35±3	6	22±3.7
		128±37	102±23	26±6	17	48±3	68.9± 3.5	10±4.7
		127±80	57±33	85±49	24	224±25	112.0± 6.2	0.97±1.1
0607-157	B	965±137	814±88	85±9	26	2.9±0.63
		132±39	117±26	56±13	56	340±6	-53.1± 1.1	0.92±0.41
		42±49	65±41	< 270	270	399±85	72.6±12.0	> 0.013

Table 4.6: Model fit parameters of sources (*continued*)

Name	Obs	S_{tot}	S_{peak}	d	d_{min}	r	θ	T_{b}
(1)	(2)	(3)	(4)	(5)	(6)	(7)	(8)	(9)
0642+449	B	590±95	352±49	52±7	7	16±4.4
		585±180	164±49	290±86	7	173±43	98.4±13.9	0.5±0.3
		119±69	57±30	154±80	22	1197±40	87.6±1.9	0.36±0.38
0707+476	C	83±9	72±6	21±2	6	7.1±1.1
0716+714	B	545±276	398±163	34±14	23	7.7±6.4
0716+714	C	1048±304	872±195	22±5	12	36±16
0727-115	B	640±66	573±44	142±11	32	1.4±0.21
0735+178	B	395±192	184±81	62±27	22	2.4±2.1
		178±85	76±33	70±31	20	271±15	96.4±3.2	0.85±0.74
0736+017	A	832±352	589±203	40±14	29	10±7
		387±129	232±66	60±17	21	129±9	-94.6±3.8	2.1±1.2
		329±144	215±79	50±18	29	200±9	-92.2±2.6	2.6±1.9
		160±190	119±114	124±118	82	413±59	-67.2±8.2	0.2±0.4
0738+313	C	447±243	270±126	58±27	32	3.6±3.3
0748+126	B	679±244	480±141	36±11	23	16±9.6
		442±157	209±67	65±21	17	231±10	77.7±2.6	3.2±2.1
0804+499	C	140±38	113±24	30±6	15	6.2±2.6
0814+425	C	311±98	171±47	58±16	14	2.3±1.3
0823+033	A	374±161	211±79	43±16	23	5±3.8
		262±204	57±43	100±76	18	69±38	87.1±28.9	0.65±0.99
0827+243	B	598±222	557±151	< 30	30	> 21
0836+710	C	583±508	375±275	< 42	42	> 17
0850+581	C	104±30	77±18	35±8	15	3.2±1.5
0851+202	B	618±186	533±121	26±6	25	20±9
		150±118	116±72	144±89	60	1054±45	-118.5±2.4	0.16±0.2
0859+470	C	222±59	180±37	27±6	15	12±5.1
		91±47	42±19	64±30	20	652±15	9.4±1.3	0.9±0.84
0906+015	B	670±345	489±204	< 40	40	> 14
0917+624	A	135±68	114±44	37±14	25	4±3.1
0945+408	A	363±49	239±27	52±6	6	5±1.1
		246±175	139±86	118±73	29	852±36	159.2±2.4	0.65±0.81
0954+658	A	325±187	282±122	< 28	28	> 9.5
		223±134	174±82	32±15	27	96±8	-80.2±4.5	4.9±4.7
		96±70	69±41	78±46	31	665±23	-60.1±2.0	0.35±0.42
1012+232	B	309±47	195±25	45±6	9	3.9±1
		140±96	81±48	68±40	38	330±20	99.3±3.5	0.78±0.93
1044+719	B	204±96	180±63	< 30	30	> 8.3
1101+384	C	292±193	164±95	48±28	29	2.1±2.5
1128+385	C	504±266	273±127	53±25	22	8.1±7.5
		44±47	60±38	< 75	75	208±24	-156.9±6.5	> 0.35
1150+497	C	455±165	376±105	27±8	25	14±7.7
		69±36	76±26	< 41	41	135±7	-155.7±3.0	> 0.9
		78±52	63±33	79±41	45	651±21	-129.7±1.8	0.27±0.29
1156+295	A	1629±388	919±191	42±9	9	26±11
		1143±379	517±156	49±15	11	79±7	66.7±5.4	14±8.2
		177±143	191±105	< 45	45	88±12	11.1±7.9	> 2.5
1219+285	C	186±38	110±19	46±8	11	1.6±0.56
1226+023	A	828±435	584±251	43±18	43	8.5±7.4
		698±404	291±155	141±75	32	121±38	-92.2±17.3	0.67±0.71
		377±300	279±178	107±68	66	420±34	54.0±4.7	0.63±0.81
1228+126	A	1046±254	624±130	99±21	14	1.8±0.74
1253-055	C	5615±2493	4453±1549	< 40	40	> 89

Table 4.6: Model fit parameters of sources (*continued*)

Name	Obs	S_{tot}	S_{peak}	d	d_{min}	r	θ	T_{b}
(1)	(2)	(3)	(4)	(5)	(6)	(7)	(8)	(9)
1308+326	A	640±219	482±132	34±9	19	18±9.9
		106±41	86±26	36±11	23	336±5	-79.0± 0.9	2.7±1.6
1502+106	C	360±102	312±67	< 25	25	> 27
		77±25	61±15	43±11	27	519±5	127.2± 0.6	1.9±0.99
		92±57	52±28	148±81	41	1432±40	135.4± 1.6	0.2±0.21
1508-055	C	503±153	318±82	63±16	22	4.6±2.4
		270±201	207±122	67±40	60	776±20	88.6± 1.5	2.2±2.6
		199±171	154±105	80±54	69	1332±27	59.9± 1.2	1.1±1.5
1510-089	C	668±414	538±260	< 46	46	> 7
		483±141	239±63	64±17	16	695±8	-6.4± 0.7	2.6±1.4
1511-100	C	550±171	351±92	47±12	24	10±5.4
1546+027	C	306±246	228±147	< 58	58	> 2.1
		223±111	142±60	46±19	33	333±10	-176.7± 1.7	2.4±2.1
1548+056	C	367±177	270±105	< 38	38	> 10
		241±130	168±74	59±26	41	1201±13	1.9± 0.6	2.8±2.4
1606+106	C	342±103	345±73	< 29	29	> 15
1637+574	C	1145±323	777±181	32±7	10	32±15
		148±56	119±35	29±9	14	58±4	-123.3± 4.2	5.1±3
		53±51	66±39	< 43	43	142±13	-146.7± 5.2	> 0.81
1642+690	C	597±396	389±216	33±18	23	16±18
1652+398	A	283±50	152±24	188±30	27	0.14±0.043
1655+077	C	462±131	346±79	35±8	21	10±4.6
		20±31	39±27	< 211	211	210±73	-22.8±19.3	> 0.012
1739+522	C	847±211	596±121	29±6	8	39±16
		264±236	60±52	75±65	12	140±33	42.2±13.2	1.8±3.2
1741-038	C	2404±860	868±292	66±22	15	19±13
		656±550	218±173	92±73	32	210±37	-122.9± 9.9	2.6±4.2
1749+096	C	2375±510	1977±326	29±5	17	61±20
1800+440	B	432±84	376±55	26±4	11	17±5.2
		57±53	72±42	< 60	60	101±17	-88.4± 9.7	> 0.43
1803+784	C	785±306	324±117	52±19	8	8±5.8
		296±371	47±58	92±114	10	132±57	-135.3±23.3	0.97±2.4
1807+698	A	218±66	228±48	< 19	19	> 10
1823+568	A	485±202	380±124	31±10	19	14±9.1
		212±97	118±47	111±44	17	503±22	-157.2± 2.5	0.47±0.38
		334±181	121±62	189±96	14	1129±48	-168.4± 2.4	0.26±0.26
		295±159	116±58	141±71	15	1551±35	-171.2± 1.3	0.41±0.41
1828+487	A	1183±331	708±170	112±27	15	2.6±1.3
		232±127	225±89	51±20	38	963±10	-55.1± 0.6	2.5±2
		952±571	333±189	210±119	20	3982±59	-31.4± 0.9	0.6±0.68
1842+681	A	253±128	171±72	41±17	24	3.6±3.1
1901+319	C	212±63	188±42	42±9	32	3.2±1.4
		59±36	44±21	232±113	57	1164±57	114.2± 2.8	0.029±0.029
1921-293	A	2069±549	1594±335	108±23	41	3.9±1.7
		328±234	272±150	214±118	113	1030±59	-12.0± 3.3	0.16±0.18
		313±230	264±148	250±140	117	1088±70	-37.3± 3.7	0.11±0.13
1923+210	B	574±160	415±94	41±9	17	5.6±2.5
		387±181	176±75	150±64	20	186±32	-114.7± 9.7	0.28±0.24
1928+738	A	349±137	256±81	40±13	17	4.7±3
		149±48	106±28	46±12	13	56±6	-6.7± 6.1	1.5±0.79
1928+738	C	656±395	461±227	51±25	24	5.4±5.4
		618±554	264±218	166±137	24	1037±68	140.8± 3.8	0.48±0.79

Table 4.6: Model fit parameters of sources (continued)

Name	Obs	S_{tot}	S_{peak}	d	d_{min}	r	θ	T_{b}
(1)	(2)	(3)	(4)	(5)	(6)	(7)	(8)	(9)
1954+513	C	279±123	279±87	24±7	24	18±11
1957+405	C	178±65	144±41	33±9	22	2.8±1.6
2007+777	A	195±49	196±35	< 11	11	> 37
		108±85	48±34	76±54	19	71±27	-77.7±21.0	0.41±0.59
2013+370	B	1252±213	1005±133	34±5	10	18±4.7
		307±123	256±79	40±12	23	195±6	176.4± 1.8	3.2±1.9
2023+336	B	579±157	507±104	43±9	17	6.3±2.6
		176±87	154±57	89±33	31	294±17	-15.9± 3.2	0.44±0.33
2037+511	B	345±48	316±32	19±2	7	42±8.6
		116±88	90±54	69±41	34	152±21	-134.0± 7.7	1.1±1.3
2121+053	A	414±159	230±77	48±16	19	8.7±5.9
2128-123	A	237±23	212±15	158±11	31	0.23±0.034
		66±61	72±45	353±222	313	1210±111	26.9± 5.2	0.013±0.017
2134+004	A	220±147	184±94	< 48	48	> 4.6
2155-152	B	293±65	254±42	64±11	32	2±0.66
		104±33	66±18	168±46	38	720±23	35.1± 1.8	0.1±0.055
2200+420	A	1137±83	1136±58	< 6	6	> 550
		168±80	154±54	< 37	37	159±7	-138.8± 2.4	> 2.1
2201+315	A	817±349	700±227	59±19	57	5±3.3
		341±268	127±94	242±178	56	258±89	63.4±19.1	0.12±0.18
2216-038	B	458±72	407±48	157±19	45	0.58±0.14
2223-052	B	642±129	395±67	59±10	14	7.3±2.5
		283±87	205±51	47±12	23	347±6	146.6± 1.0	5.1±2.5
		183±75	111±39	65±23	27	480±11	146.8± 1.4	1.7±1.2
		139±80	66±34	72±37	32	736±19	91.2± 1.5	1.1±1.1
2234+282	A	405±179	278±101	52±19	28	4.4±3.2
2251+158	A	696±332	764±246	< 41	41	> 13
		138±145	189±117	< 97	97	105±30	-116.5±16.0	> 0.45
		238±159	267±119	< 57	57	247±13	-100.2± 2.9	> 2.2
		275±207	268±145	< 60	60	339±16	-105.2± 2.7	> 2.3
		124±167	172±135	< 131	131	618±52	-105.6± 4.8	> 0.22
		354±308	214±159	193±143	52	2323±72	-97.4± 1.8	0.29±0.43
2255-282	A	1868±330	1470±204	171±24	79	2±0.56
2255-282	B	993±403	981±283	< 77	77	> 5.3
2345-167	B	365±112	294±70	288±69	131	0.11±0.054
		59±57	79±46	< 512	512	1259±148	121.7± 6.7	> 0.0058

Notes: Column designation: 1 - source name; 2 - observing epoch: **A** - October 2001; **B** - April 2002; **C** - October 2002; 3 - model flux density of the component [mJy]; 4 - peak brightness of individual component measured in the image [mJy/beam]; 5 - size [μas]; 6 - minimum resolvable size [μas]; 7 - radius [μas]; 8 - position angle [$^{\circ}$]; 9 - measured brightness temperature [$\times 10^{10}$ K]; italic numbers indicate lower limits.

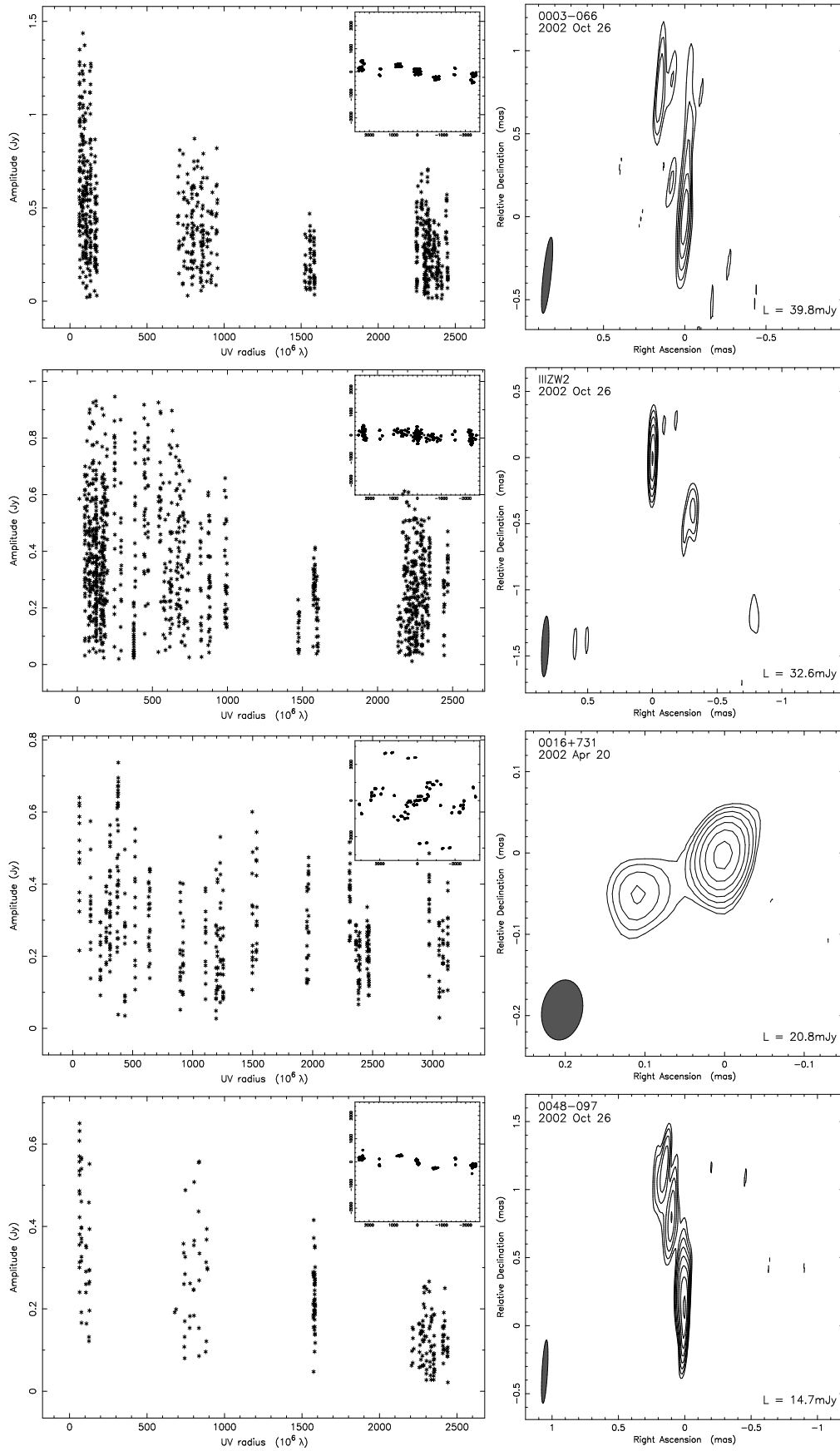


Figure 4.8: 123 contour maps of 109 sources with the distributions of the uv -sampling and of the visibility amplitude against uv -radius. In the left panel, X-axis represents the visibility amplitude (correlated flux density) in Jy, averaged over 30 seconds, and Y-axis shows the uv -distance in $10^6 \lambda$. The corresponding uv -sampling distribution is given in the inset. In the right panel, a contour map of the cleaned image is shown. The axes of the maps show the relative offset from the center of image in milliarcsecond. Minimum contour level is shown in the lower-right corner of each map. Image parameters of each image are summarized in Table 4.6.

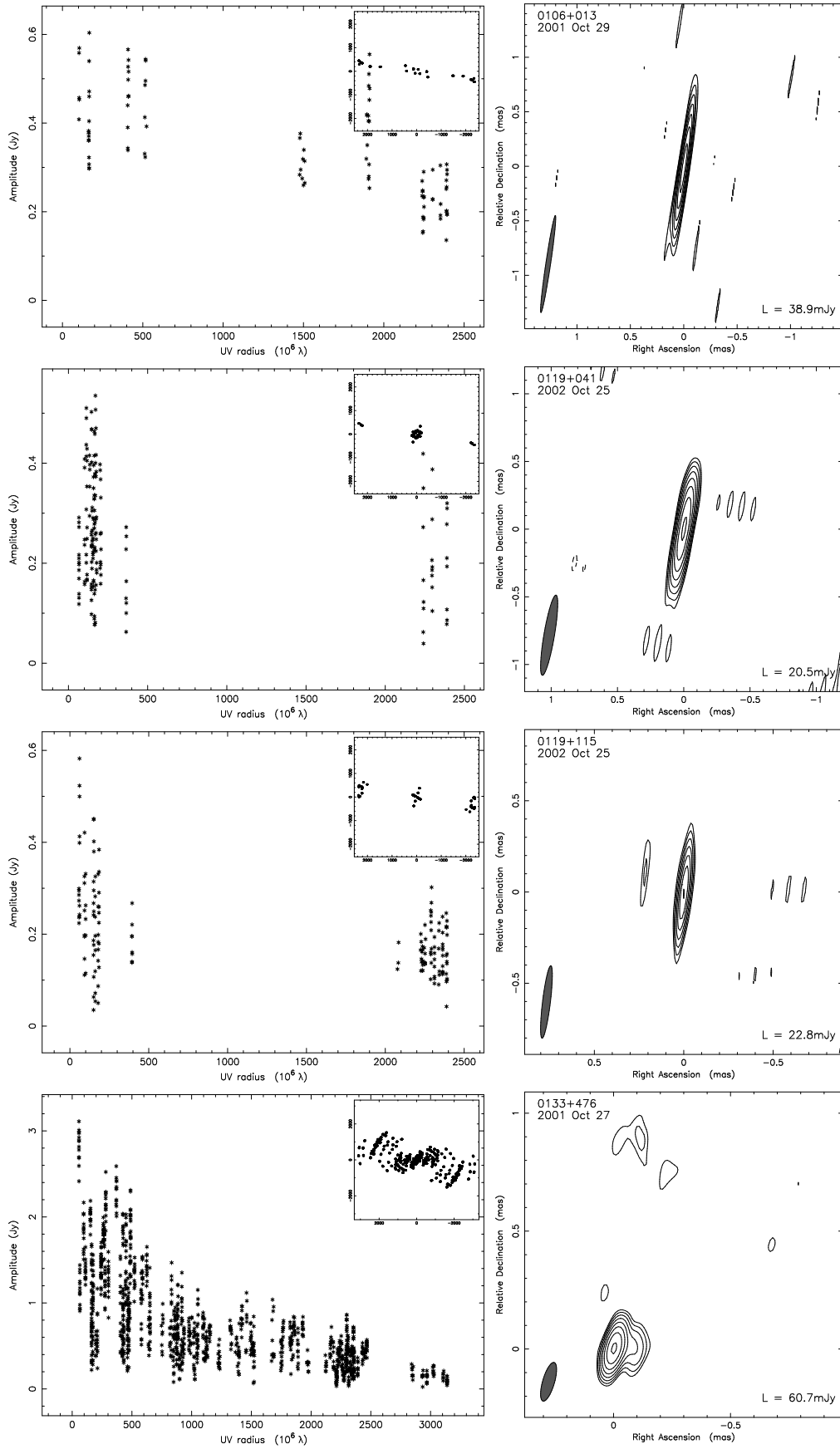


Figure 4.7: - continued.

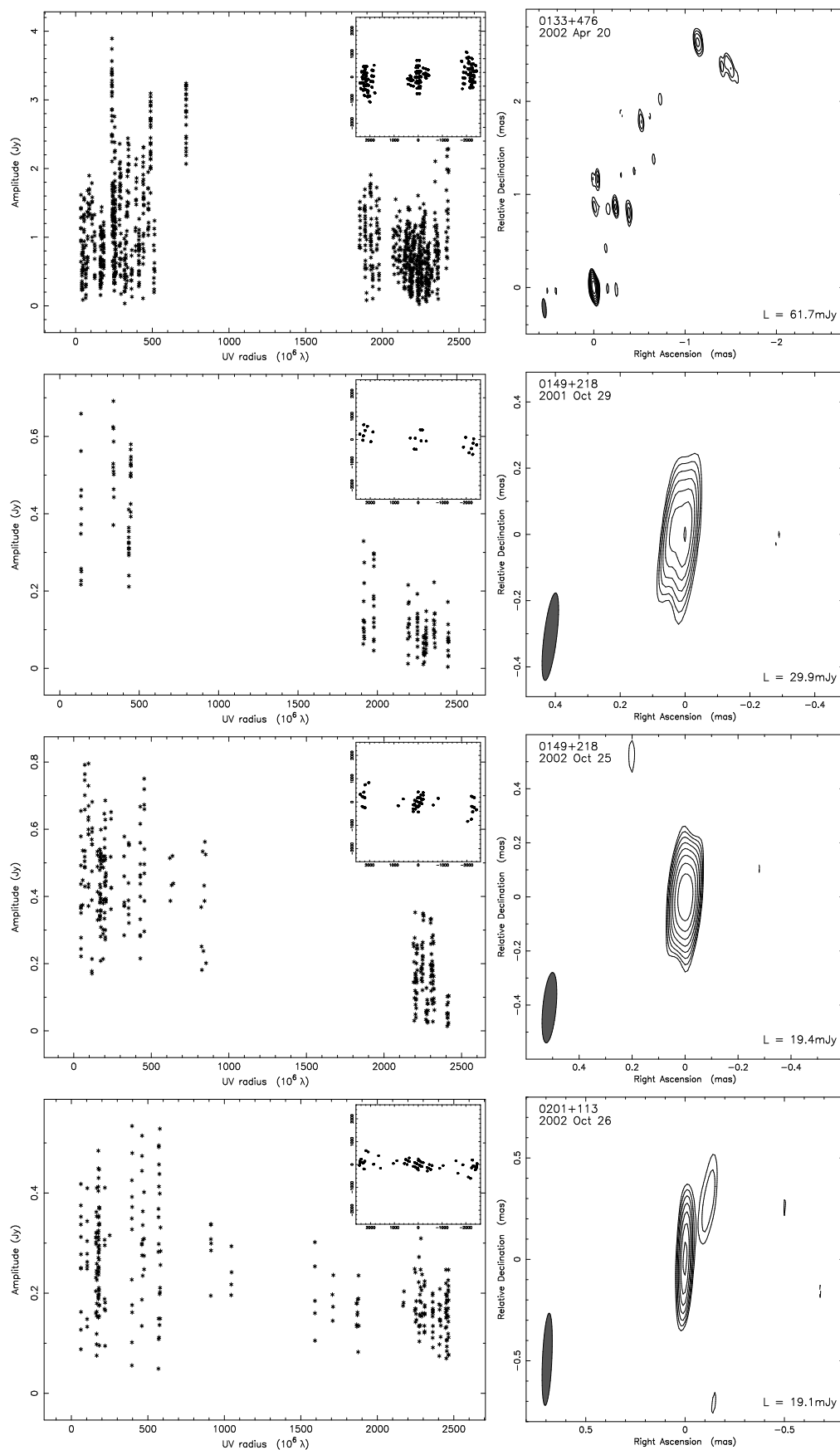


Figure 4.7: - continued.

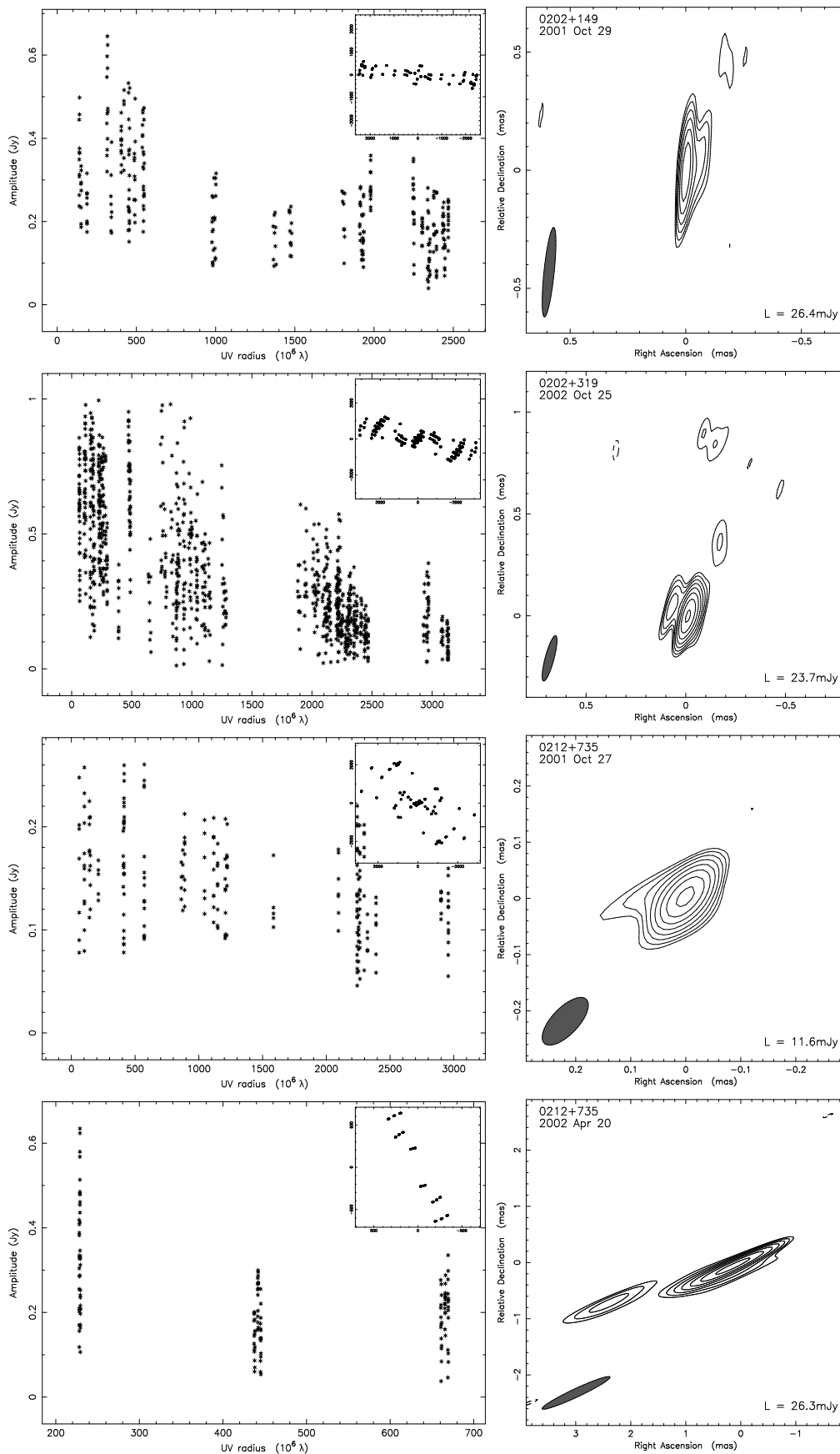


Figure 4.7: - continued.

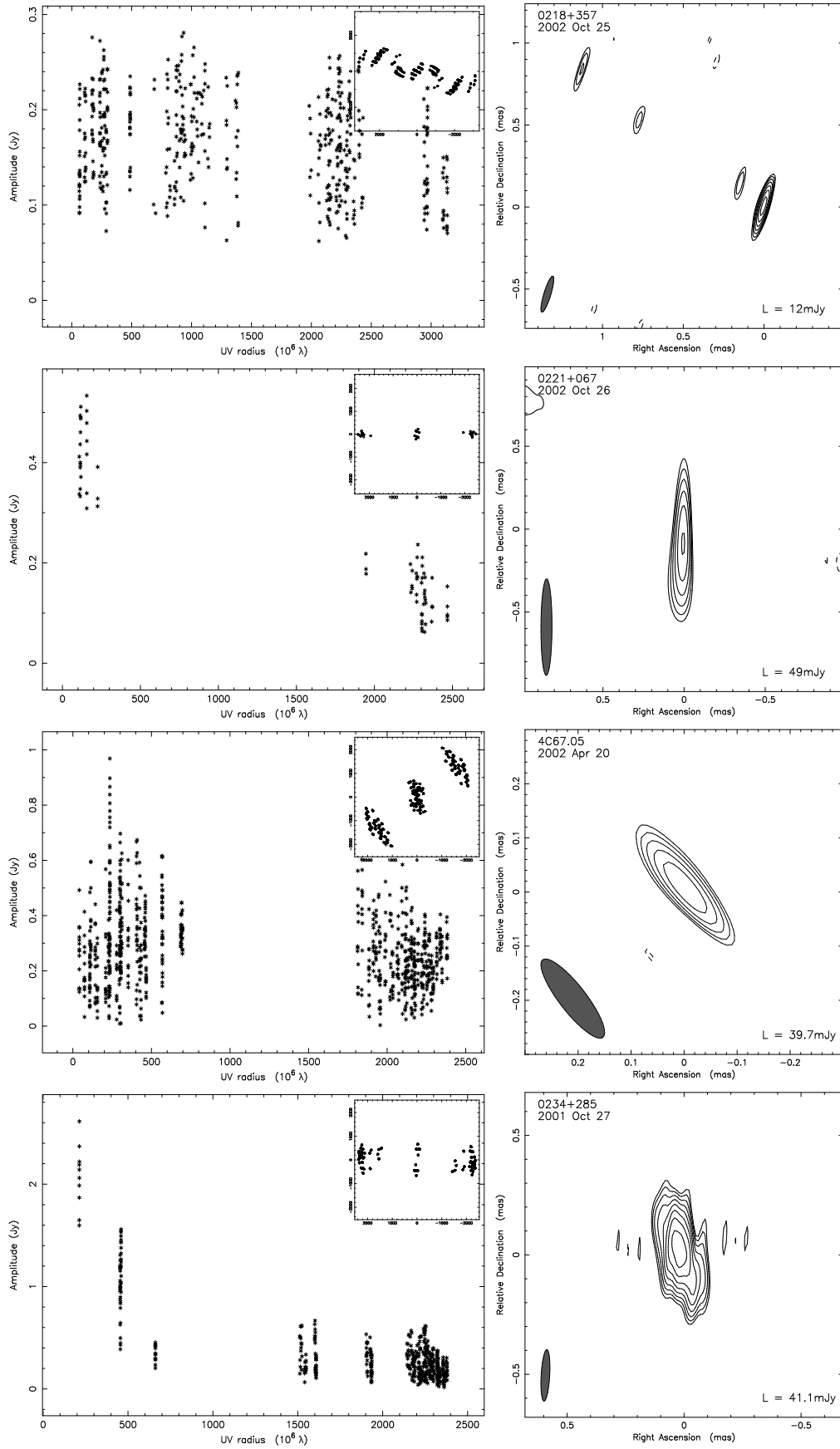


Figure 4.7: - continued.

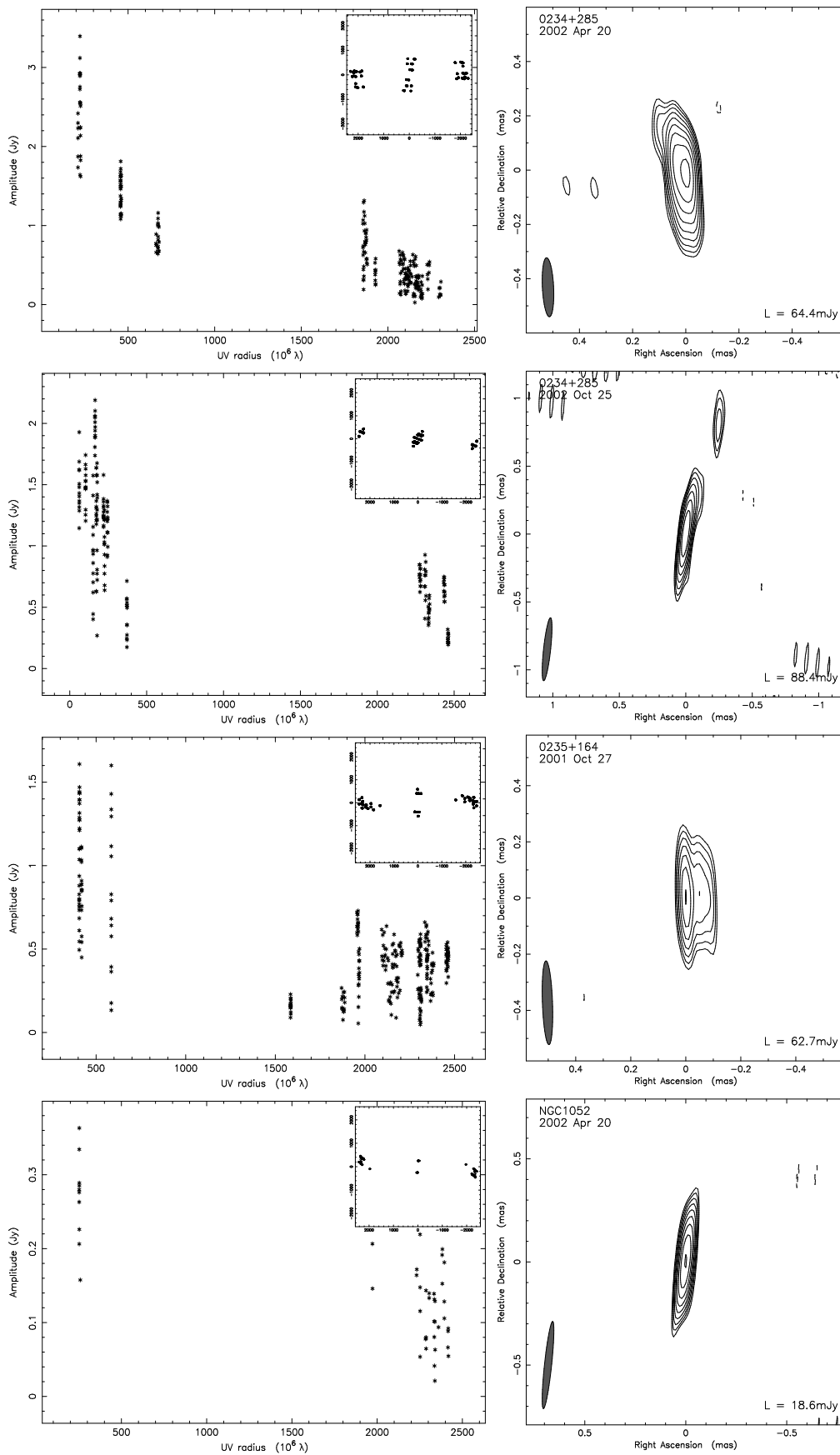


Figure 4.7: - continued.

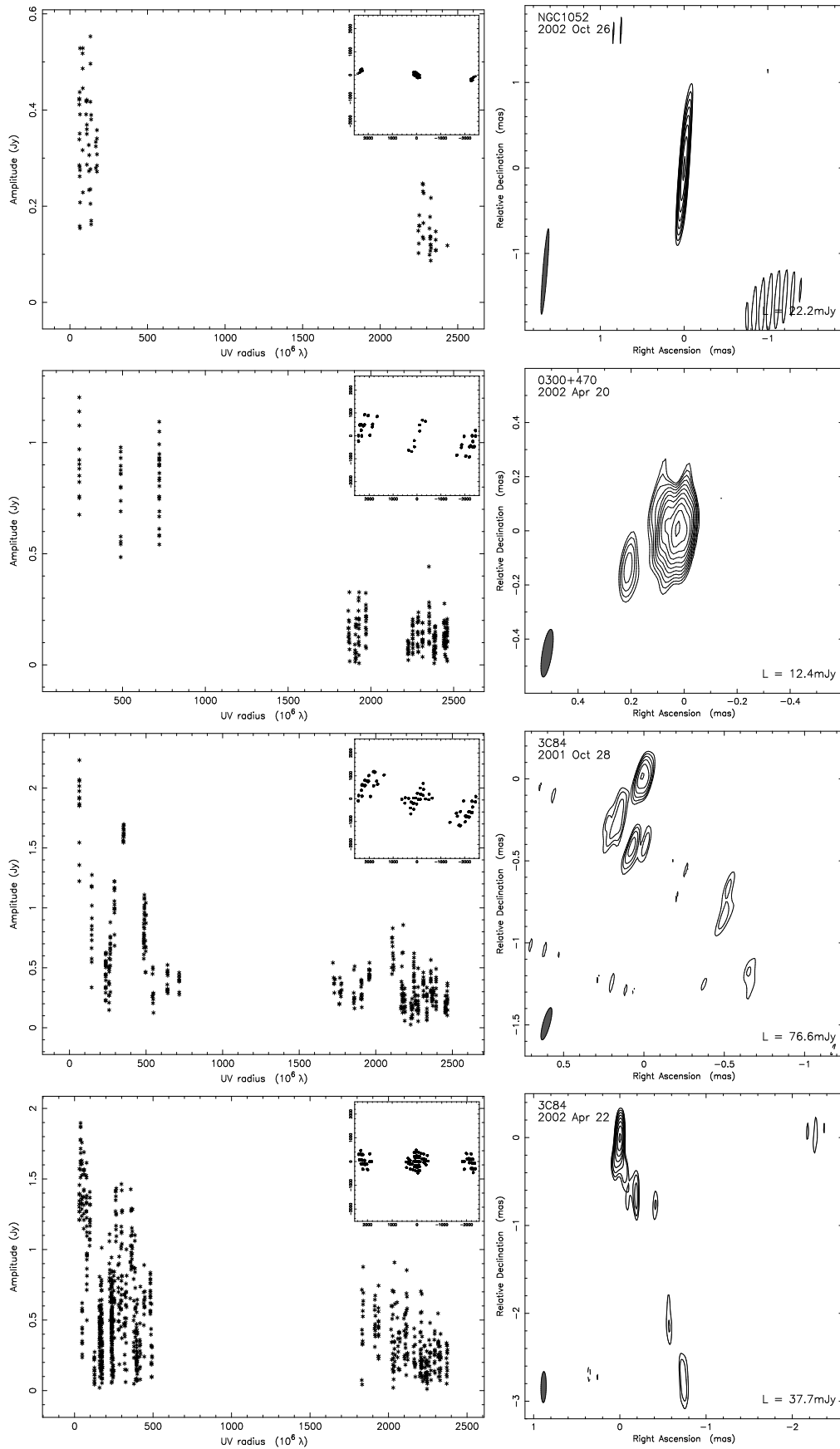


Figure 4.7: - continued.

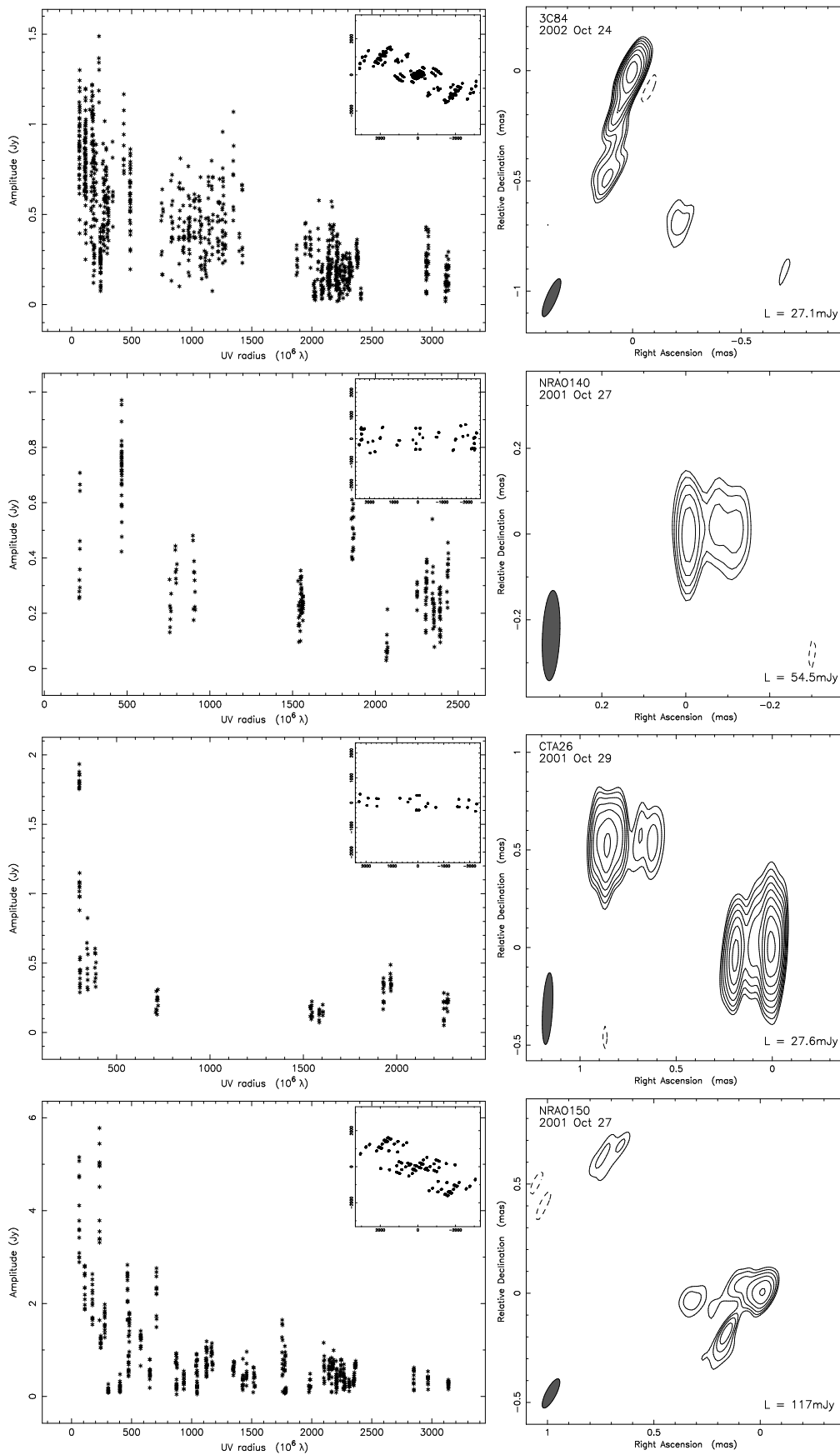


Figure 4.7: - continued.

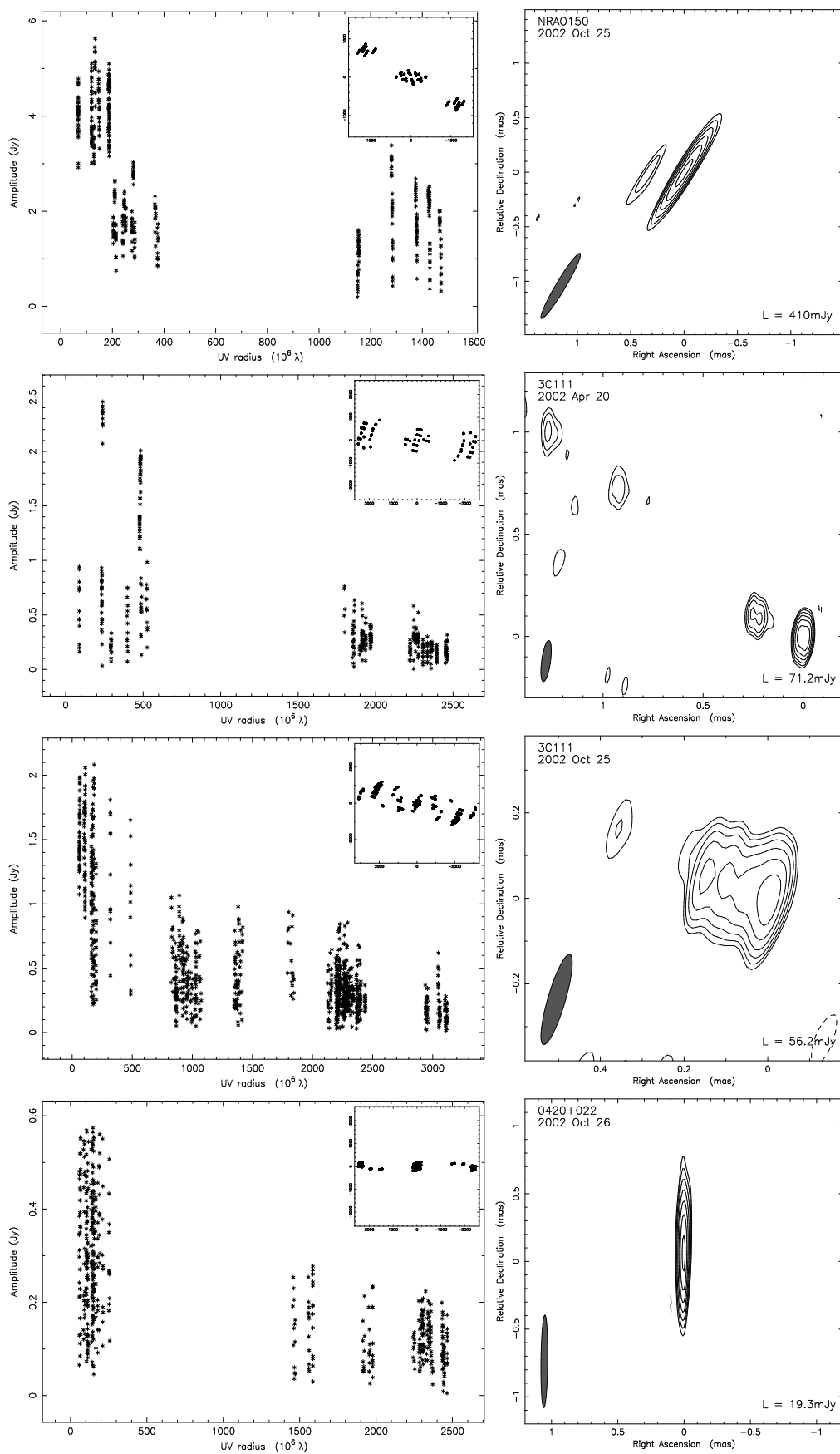


Figure 4.7: - continued.

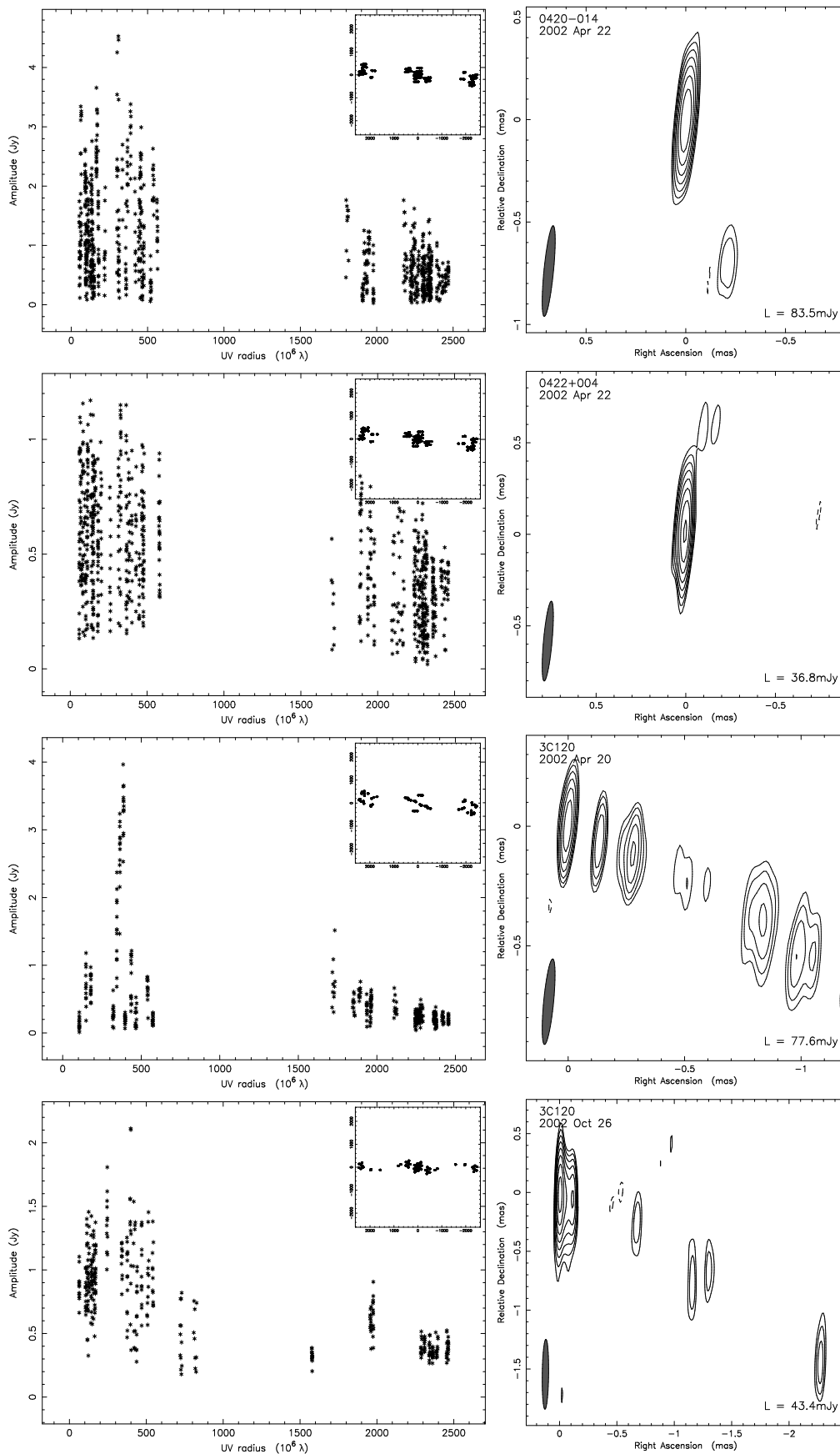


Figure 4.7: - continued.

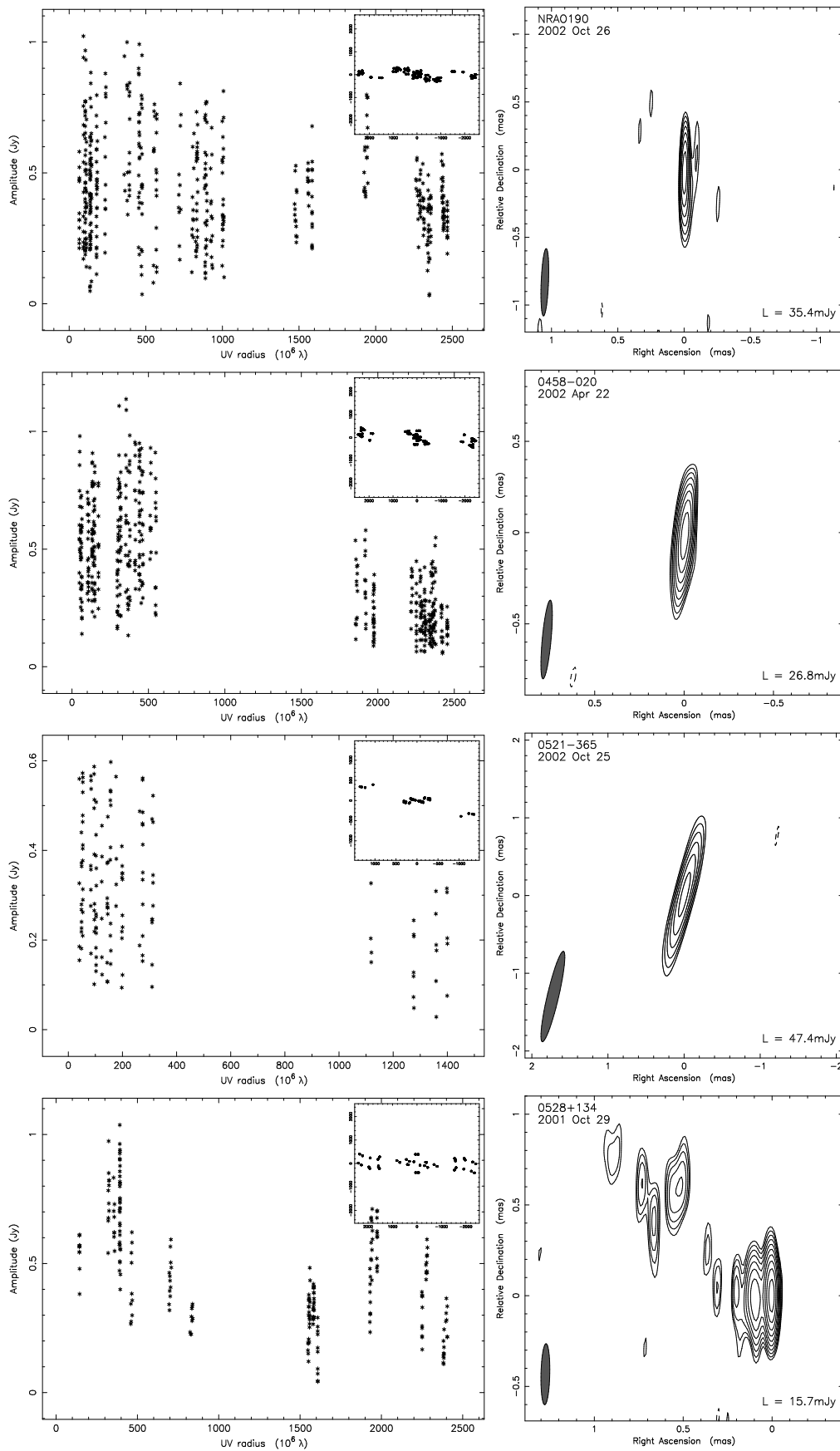


Figure 4.7: - continued.

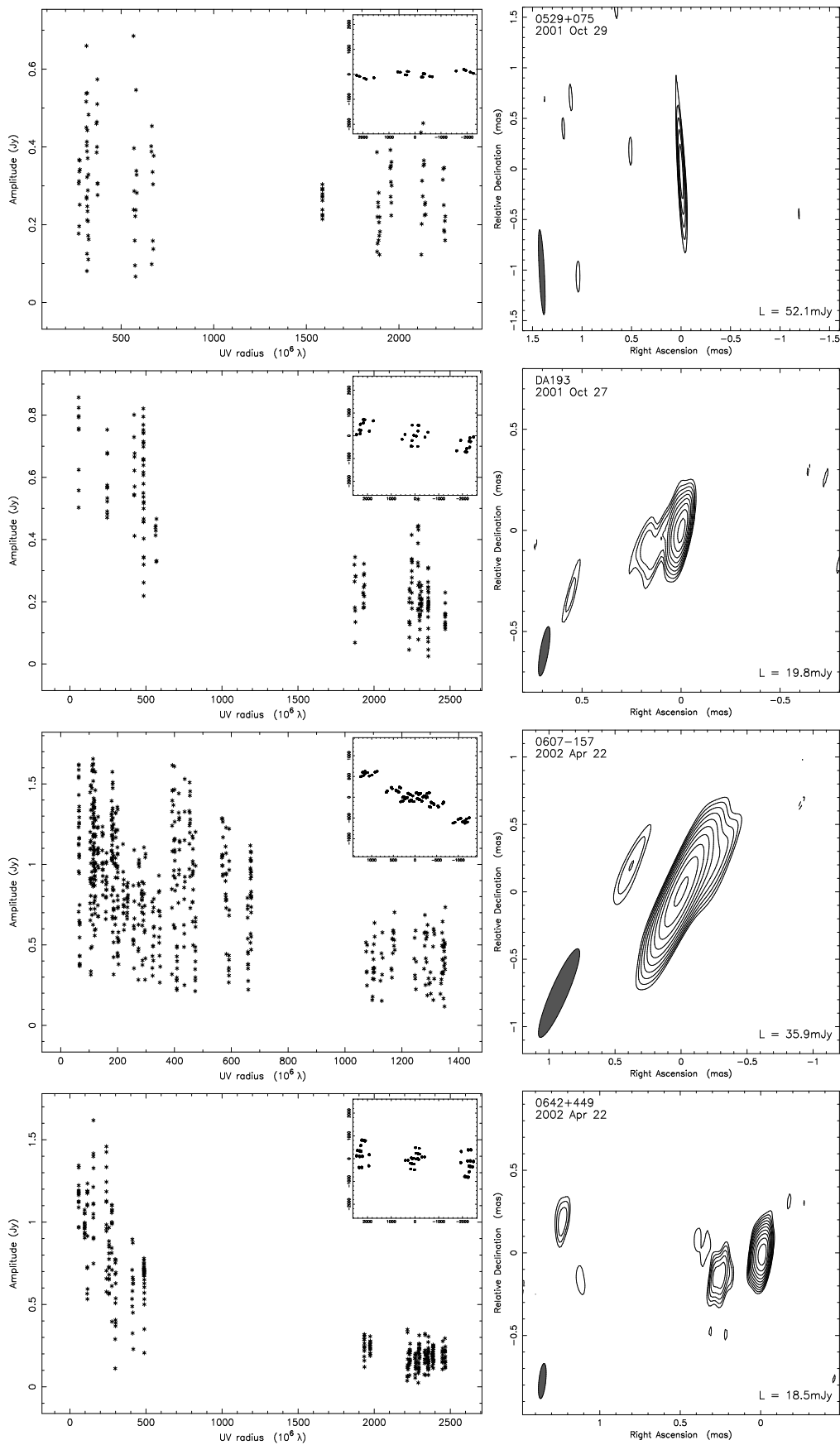


Figure 4.7: - continued.

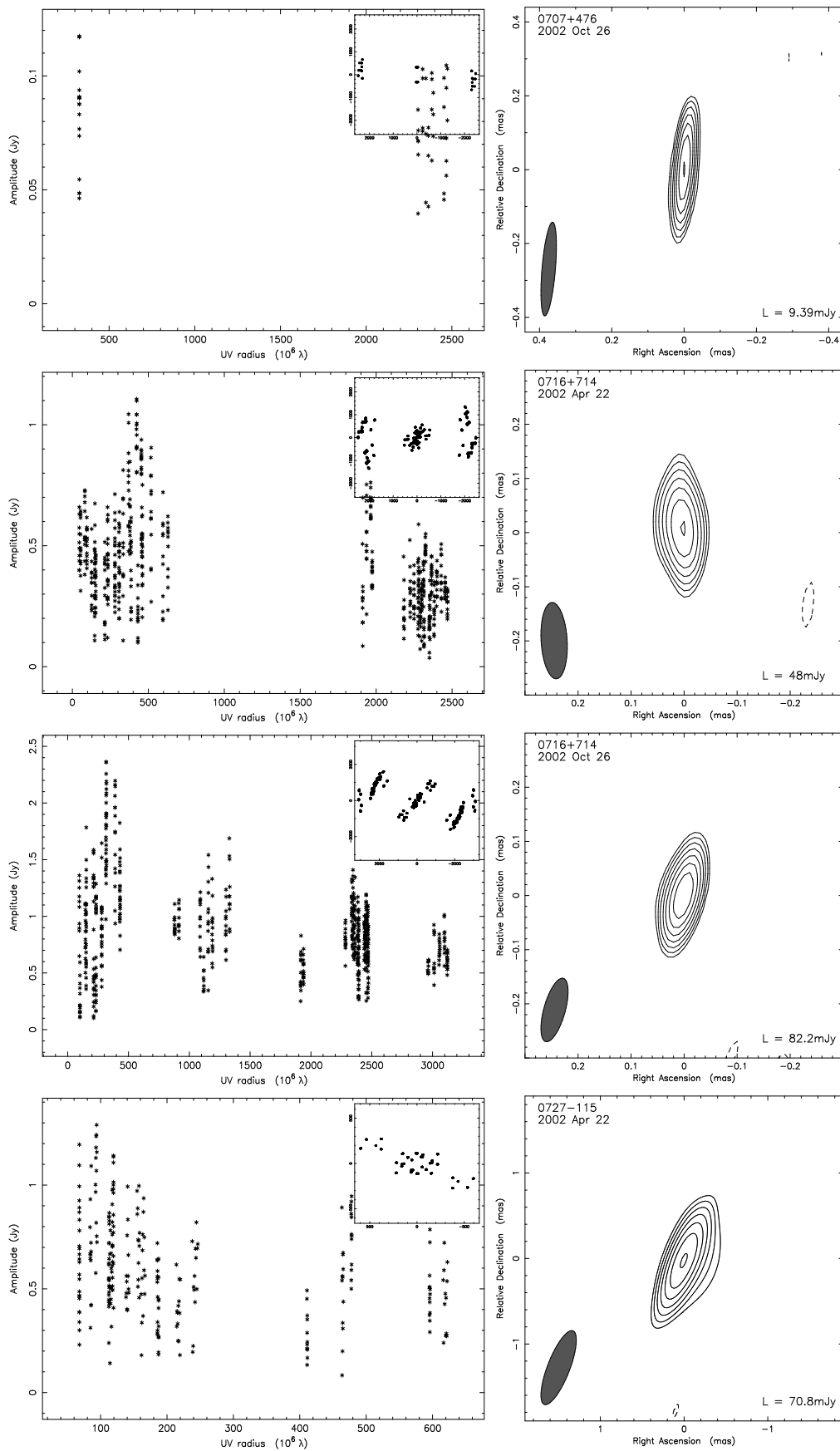


Figure 4.7: - continued.

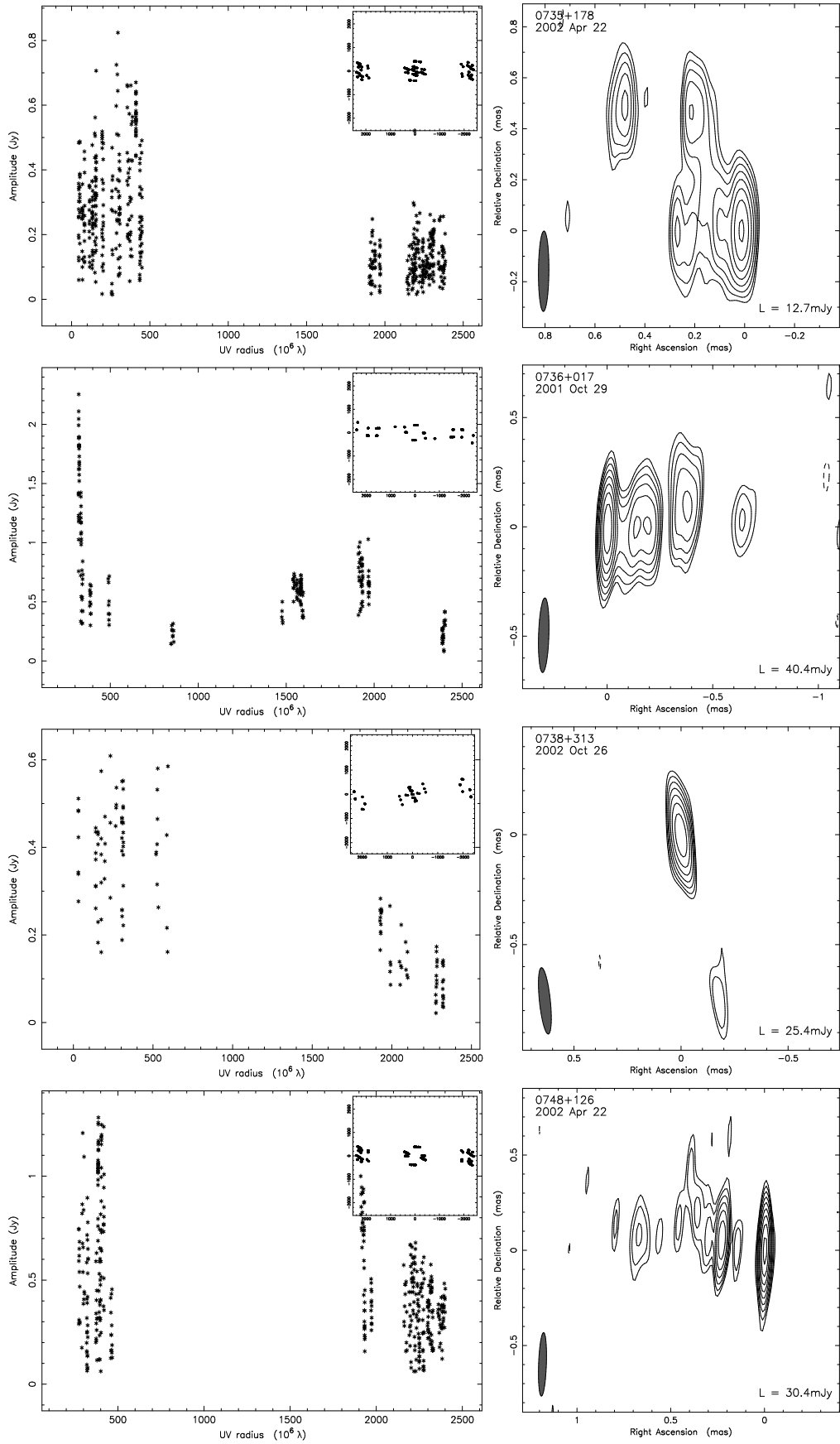


Figure 4.7: - continued.

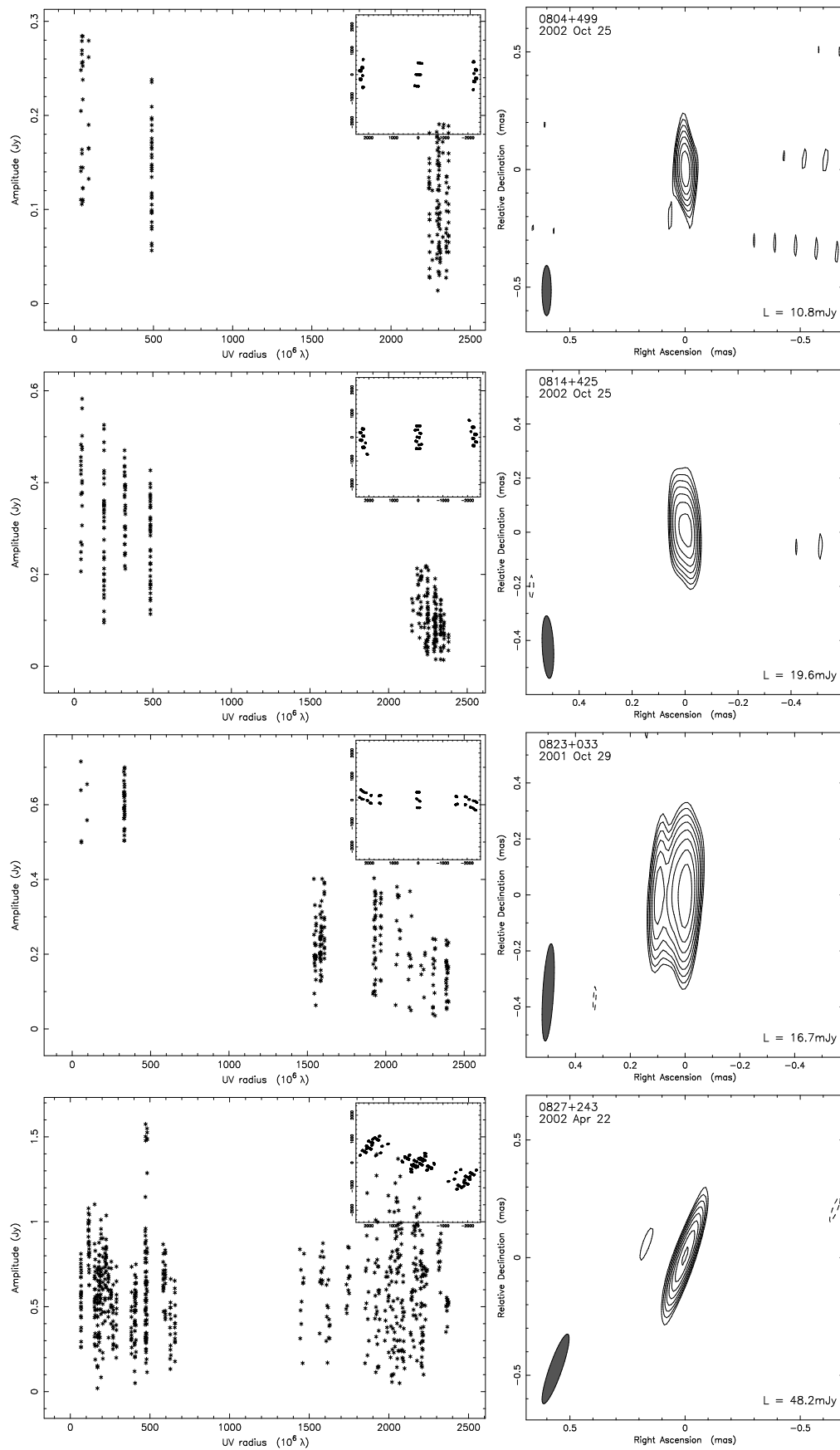


Figure 4.7: - continued.

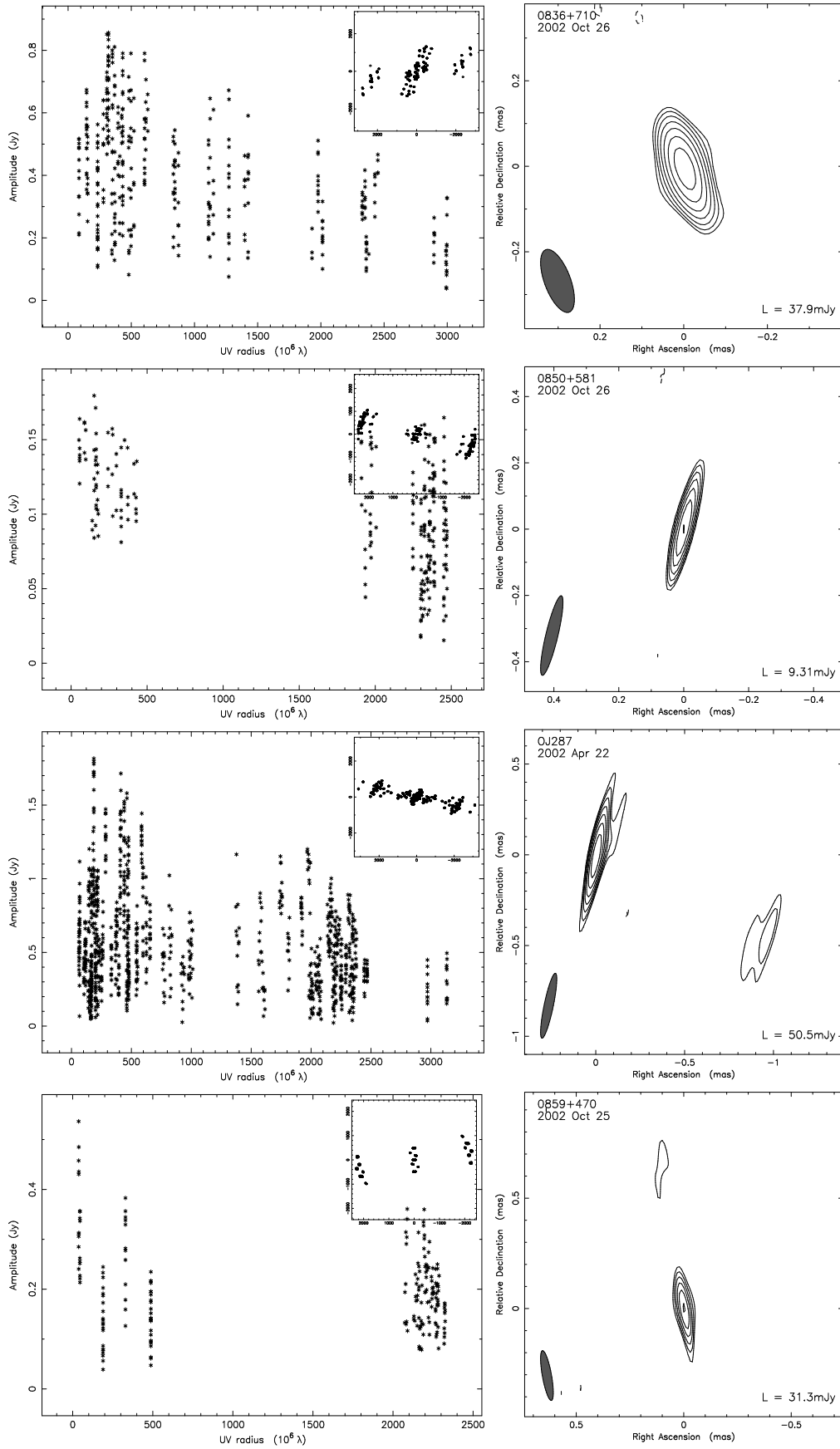


Figure 4.7: - continued.

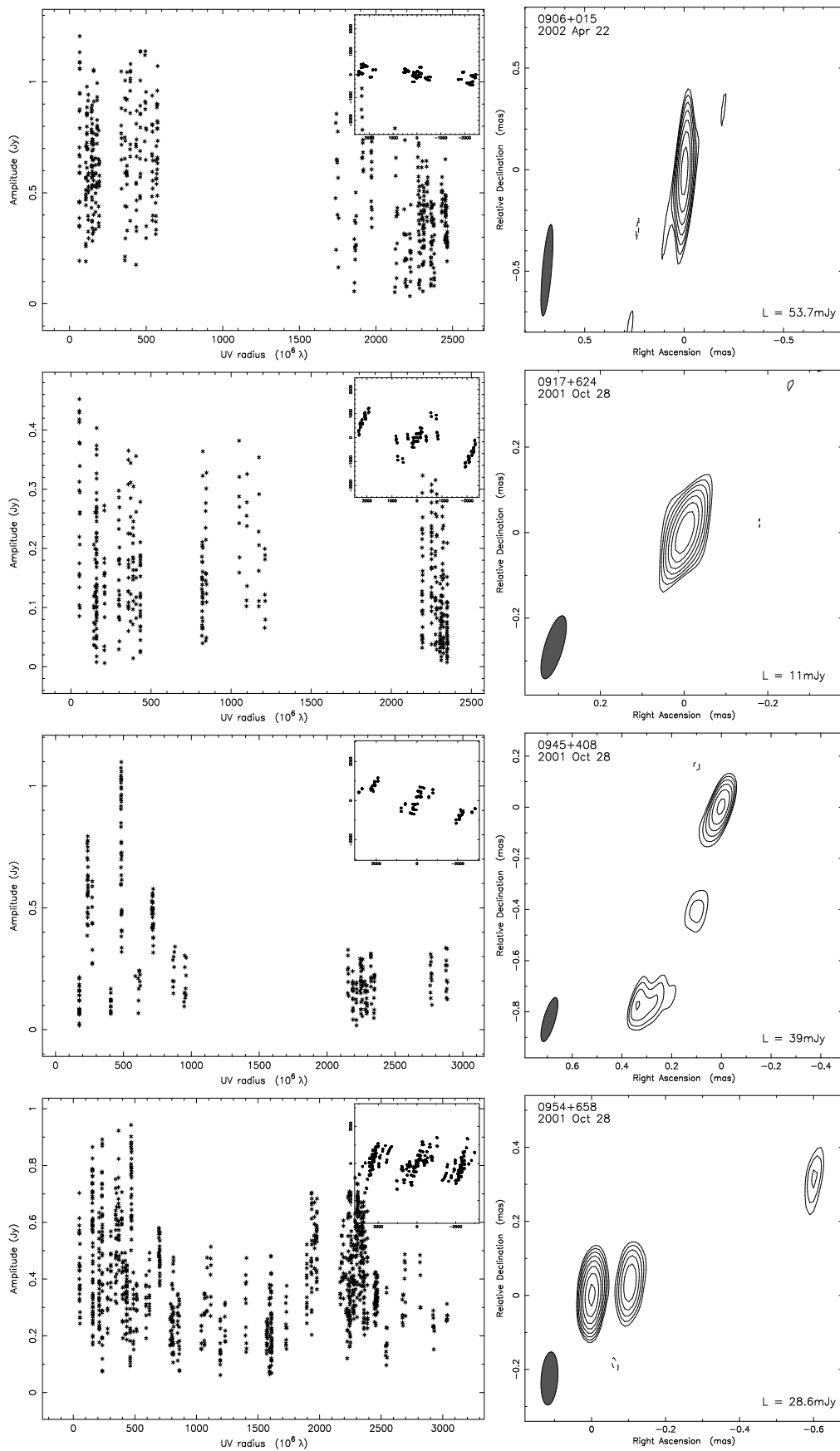


Figure 4.7: - continued.

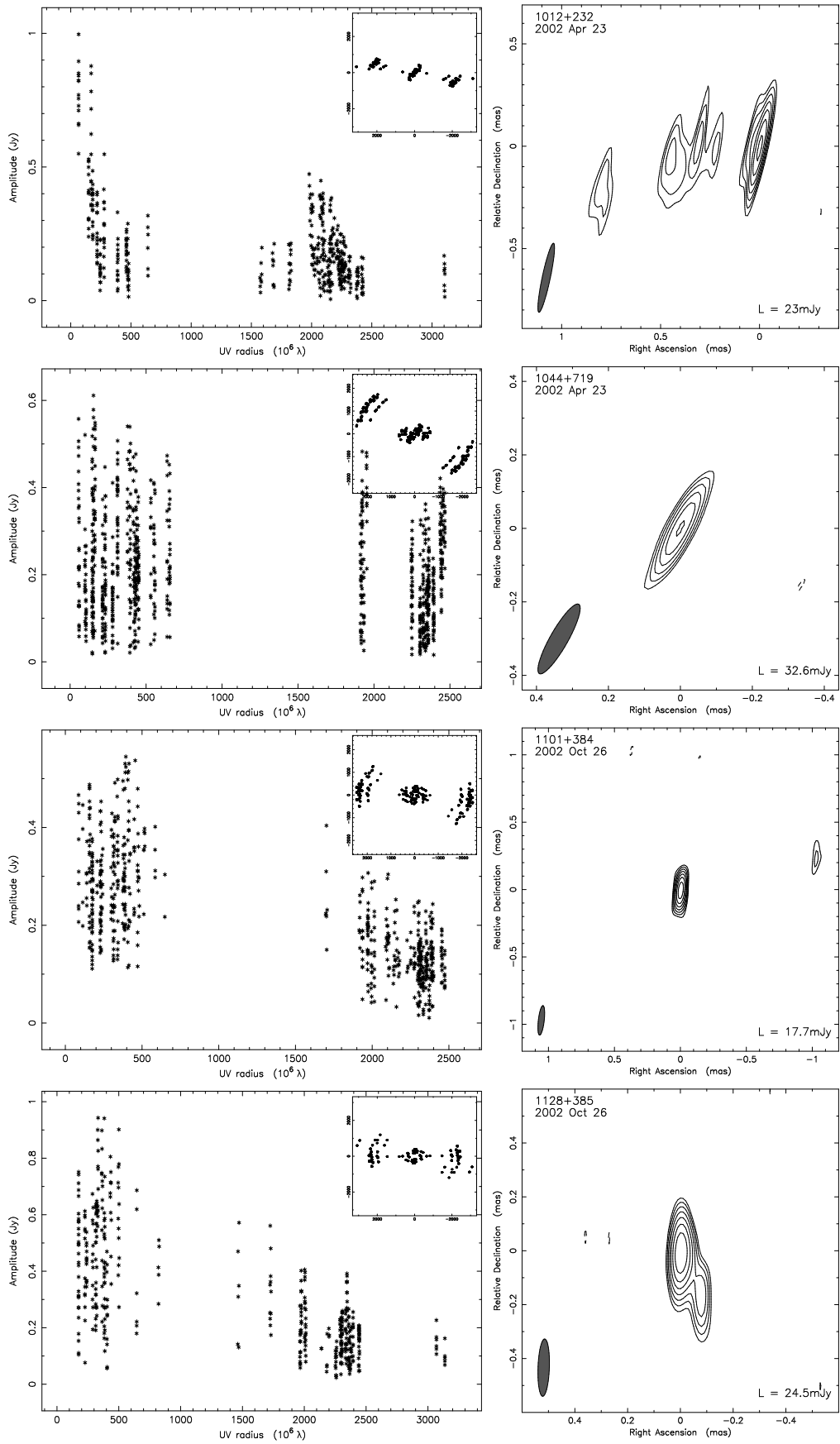


Figure 4.7: - continued.

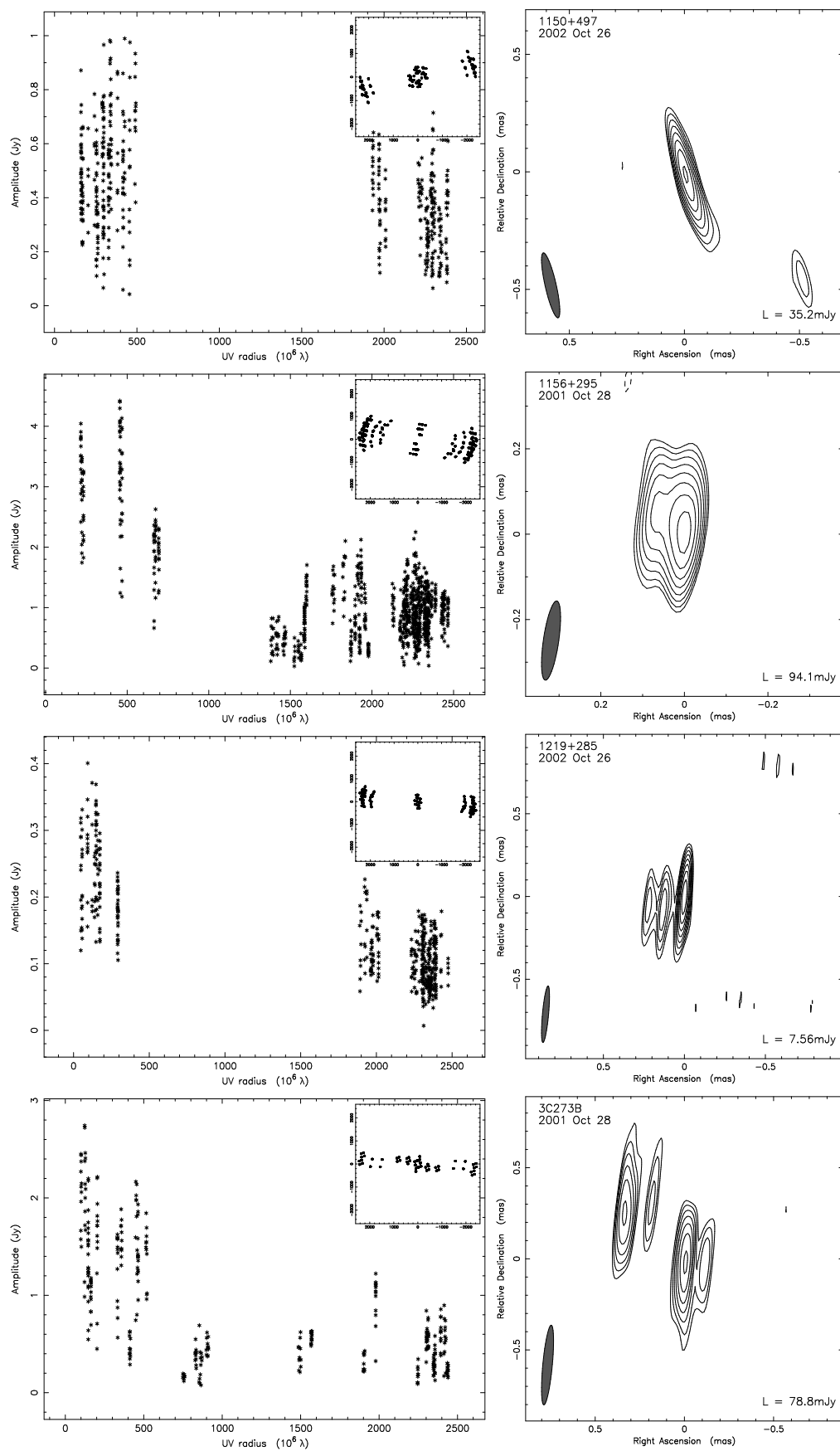


Figure 4.7: - continued.

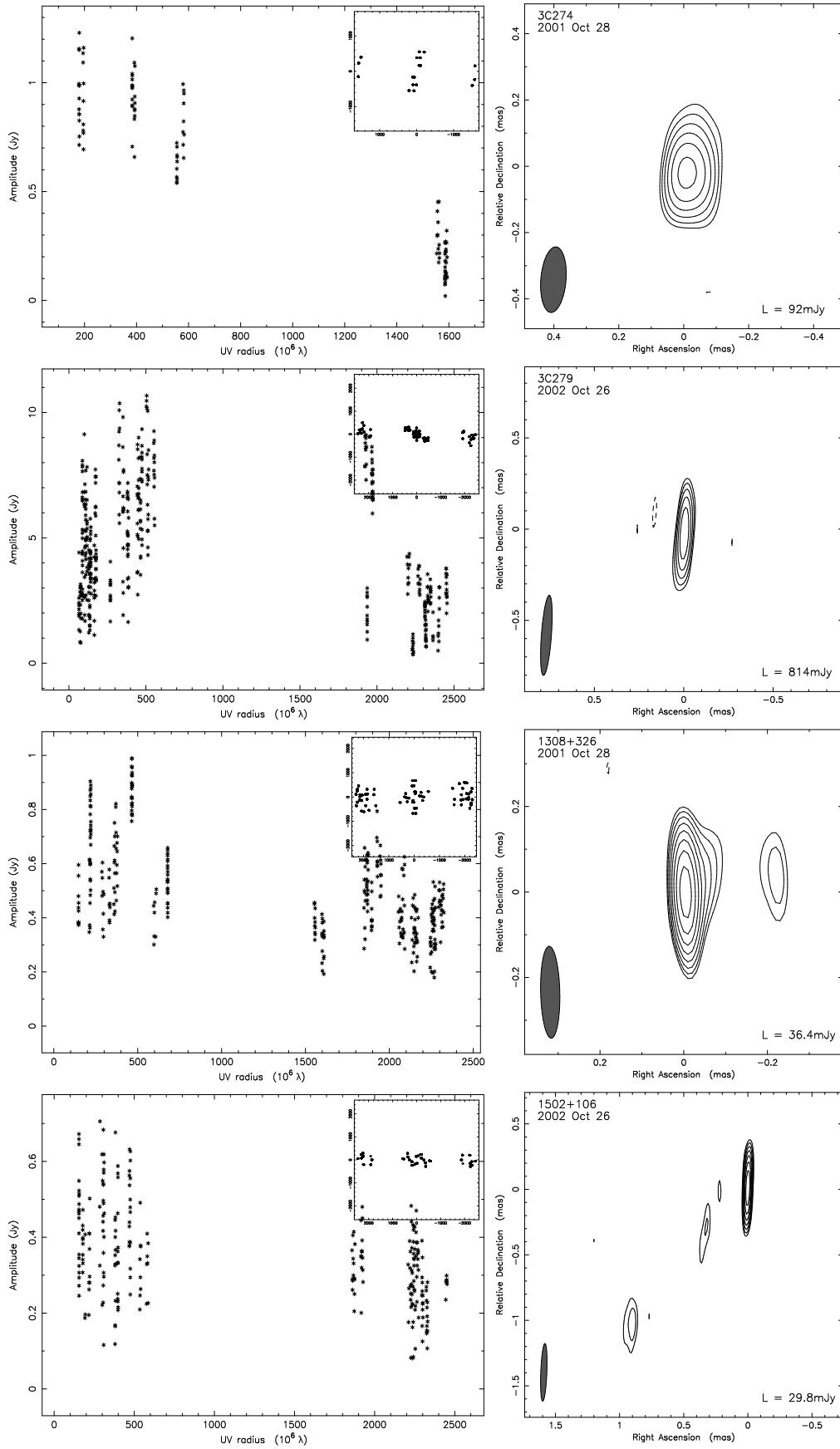


Figure 4.7: - continued.

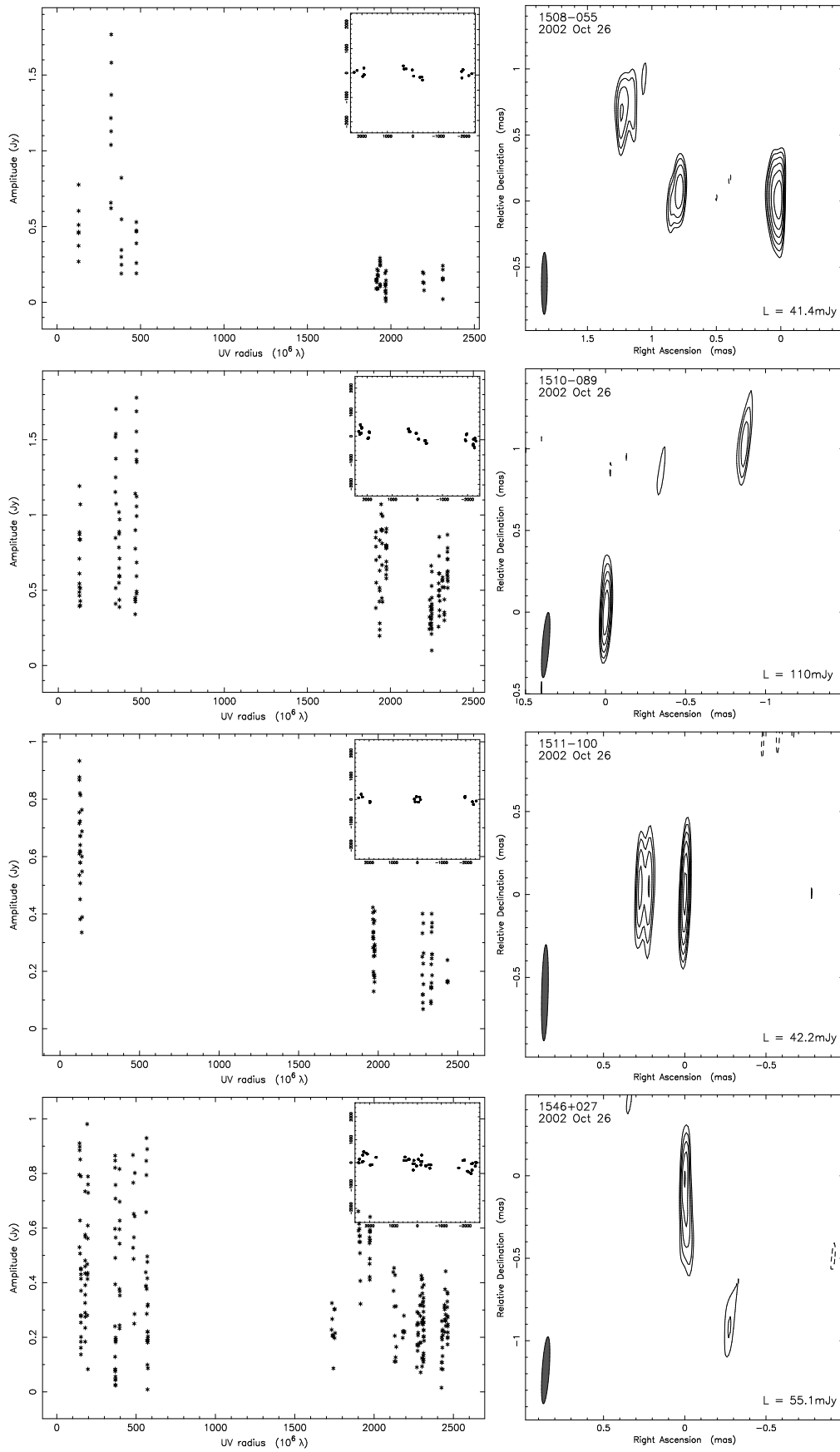


Figure 4.7: - continued.

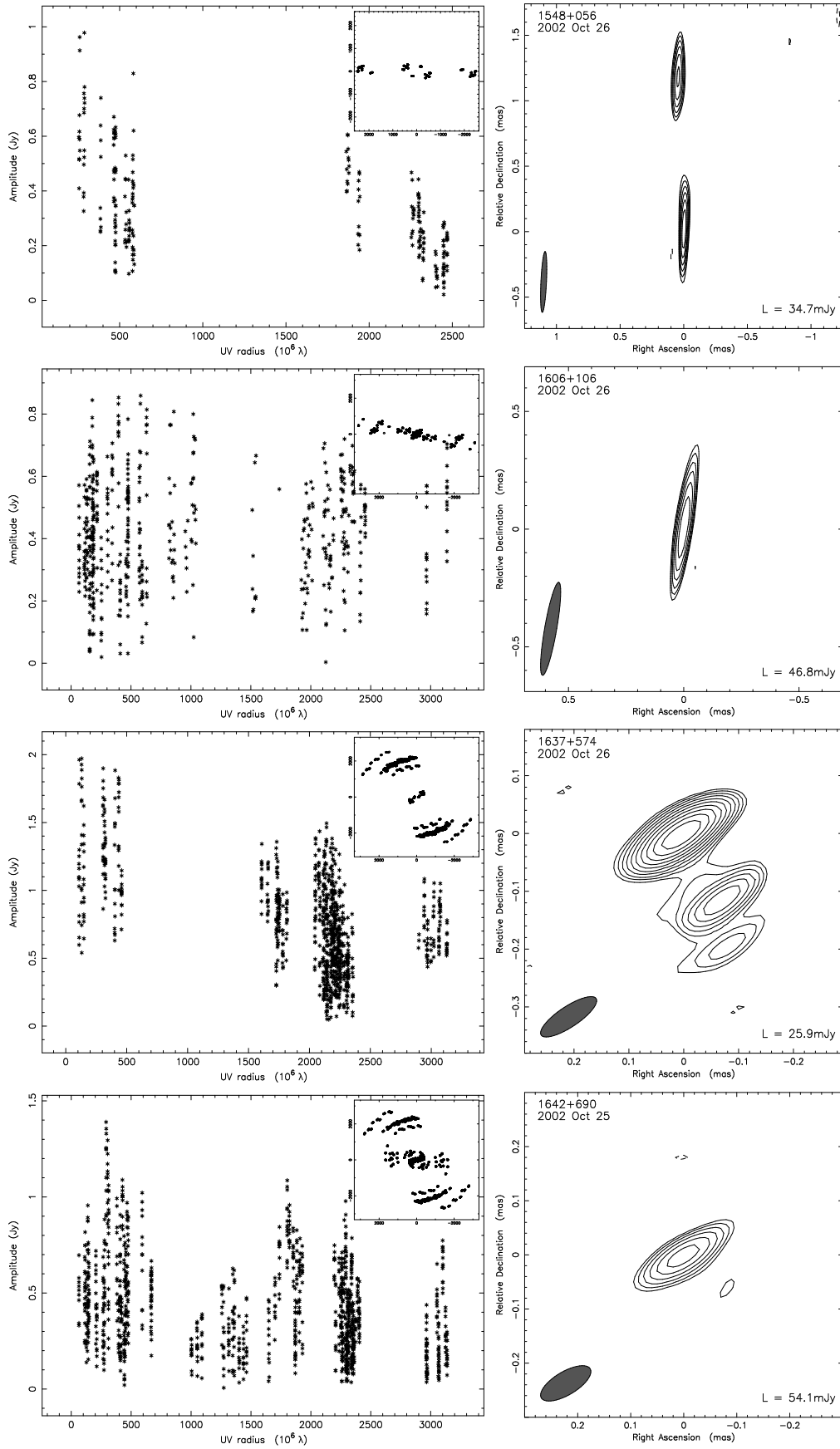


Figure 4.7: - continued.

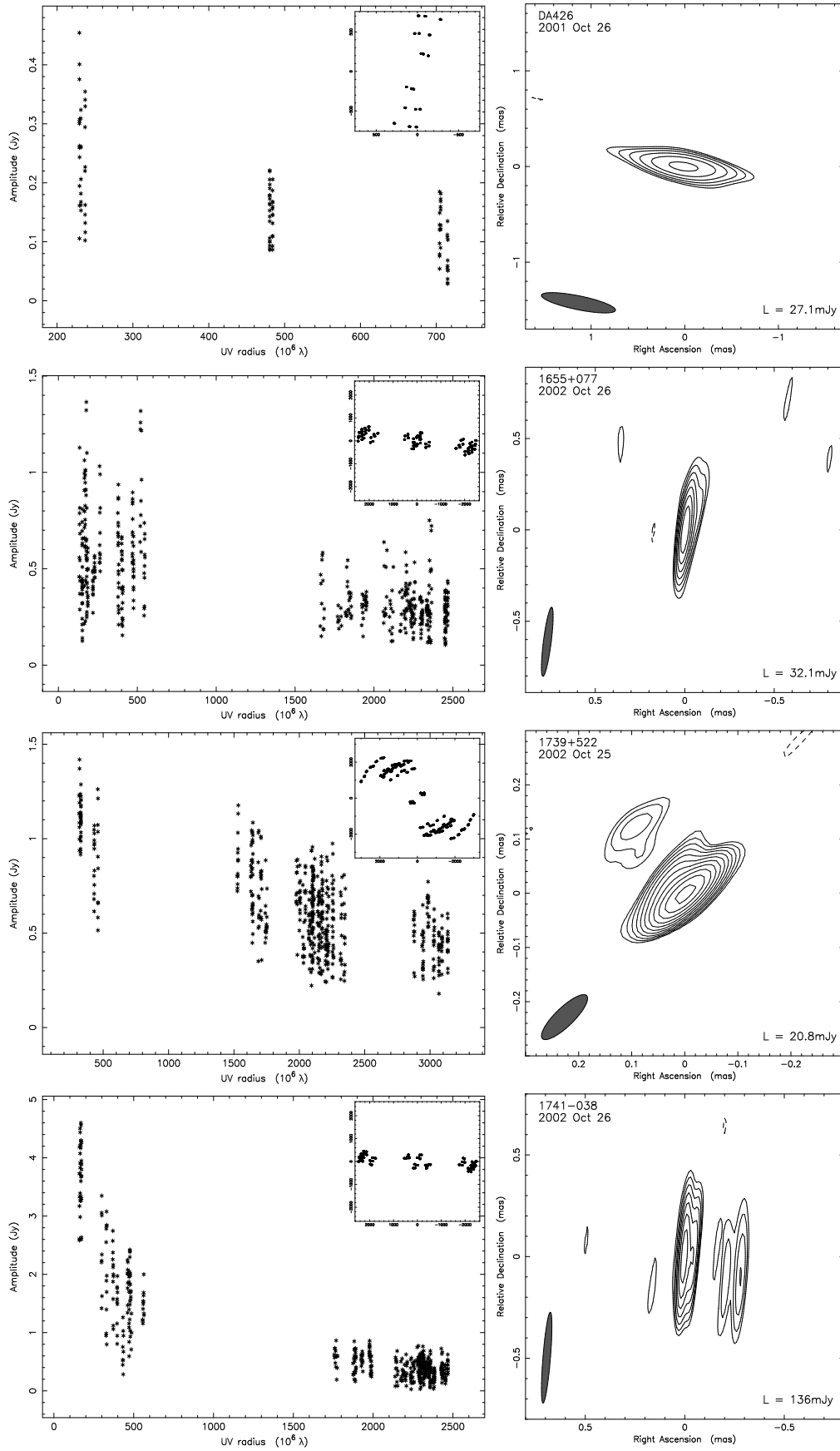


Figure 4.7: - continued.

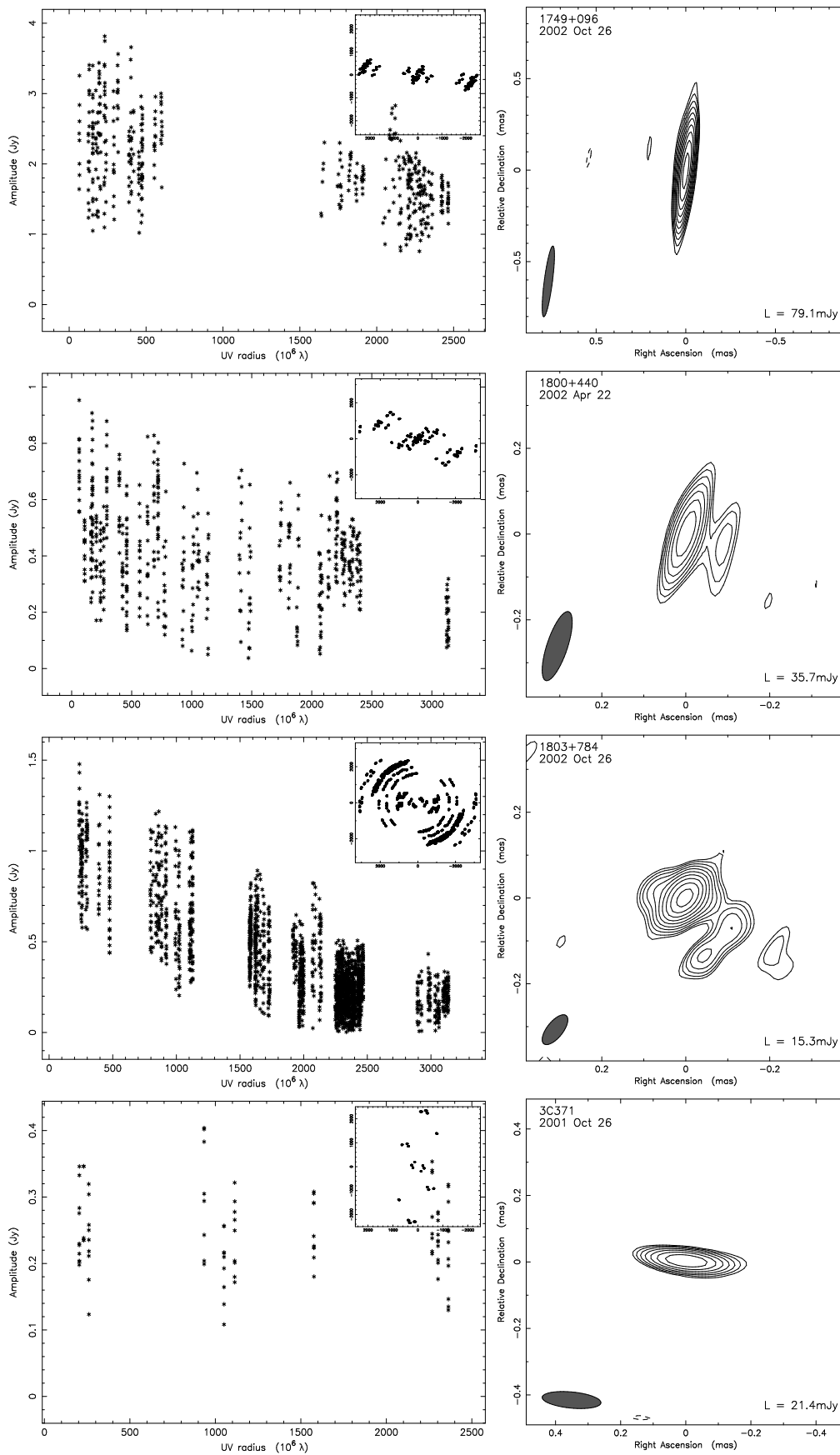


Figure 4.7: - continued.

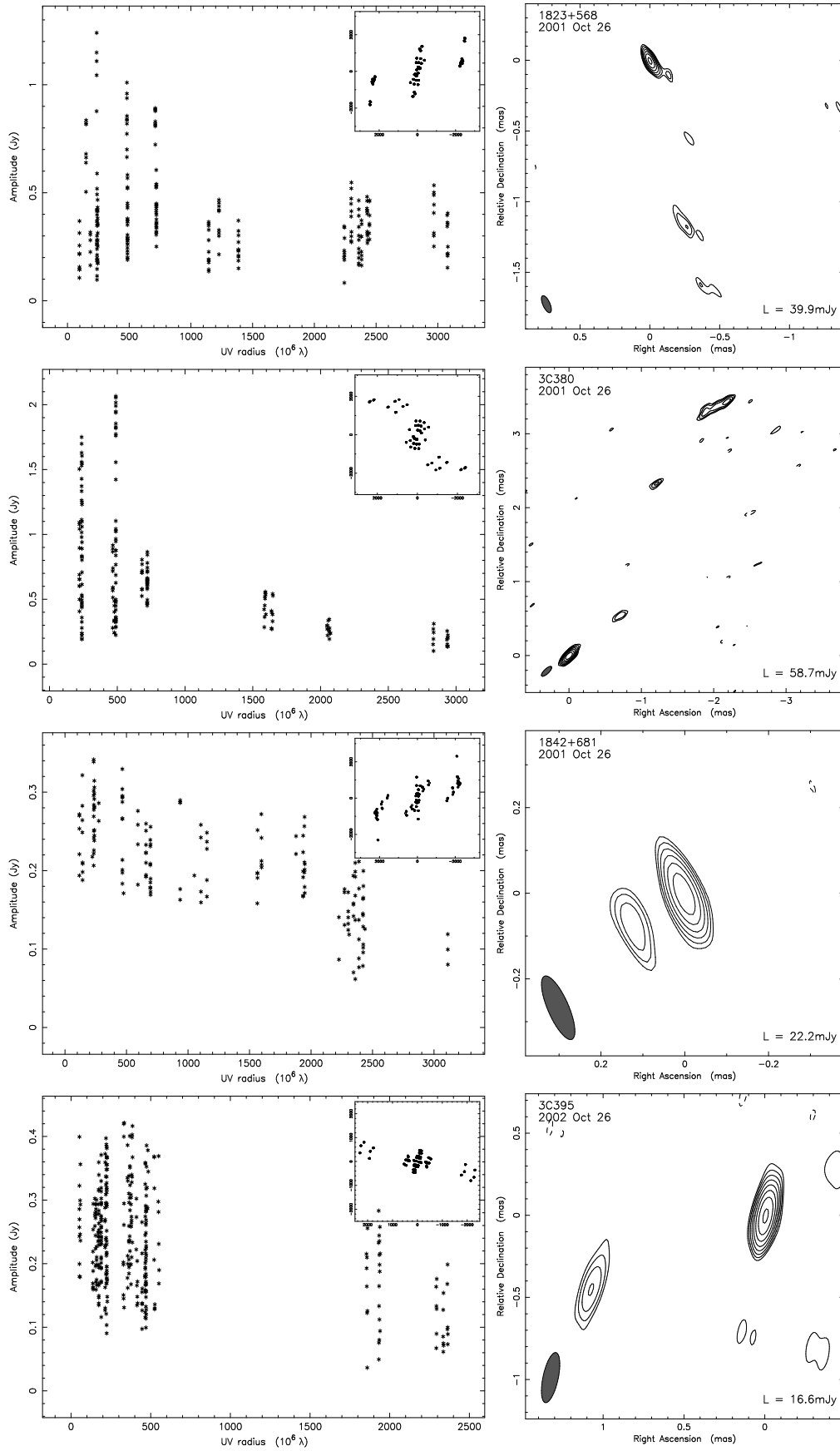


Figure 4.7: - continued.

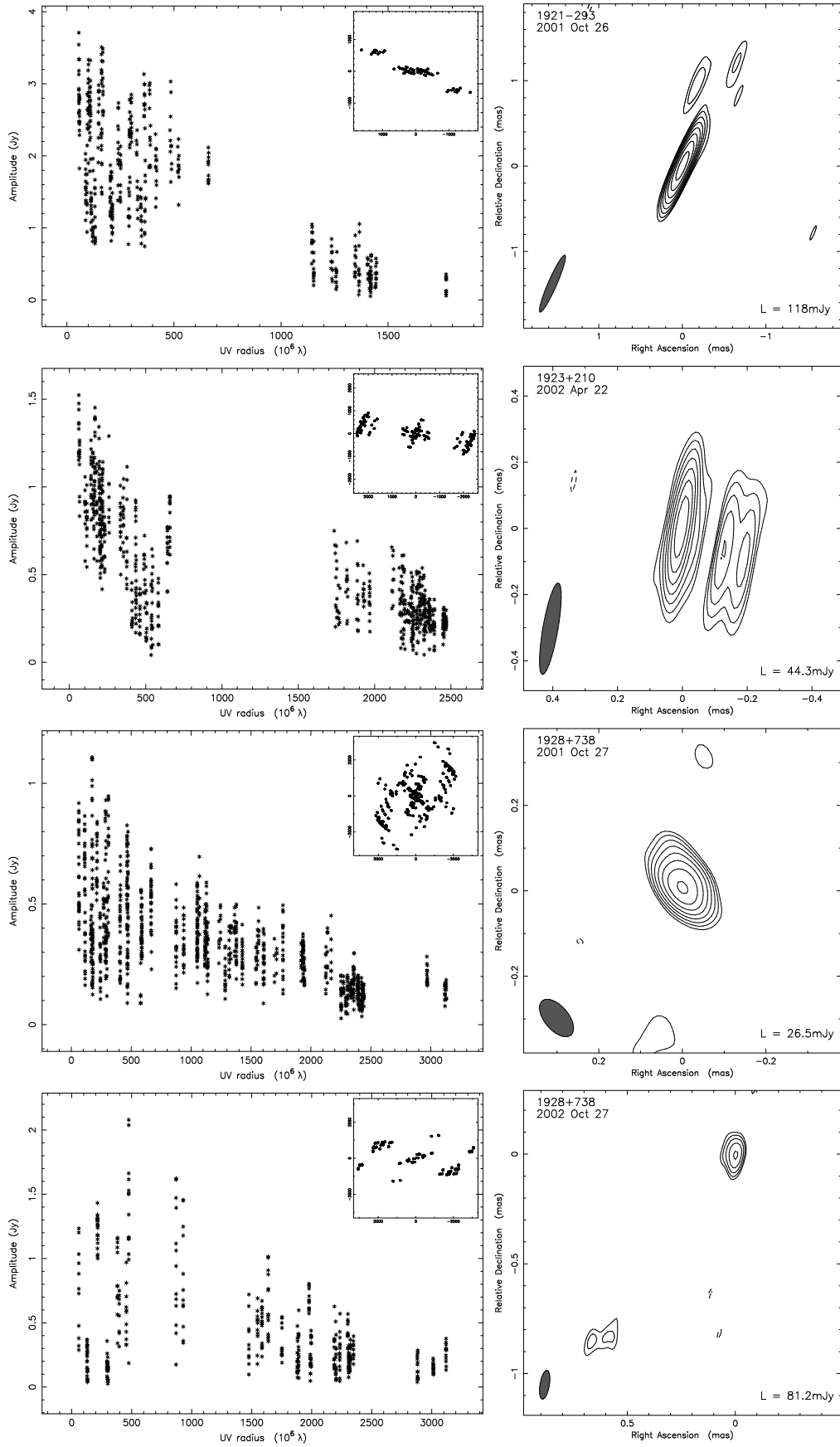


Figure 4.7: - continued.

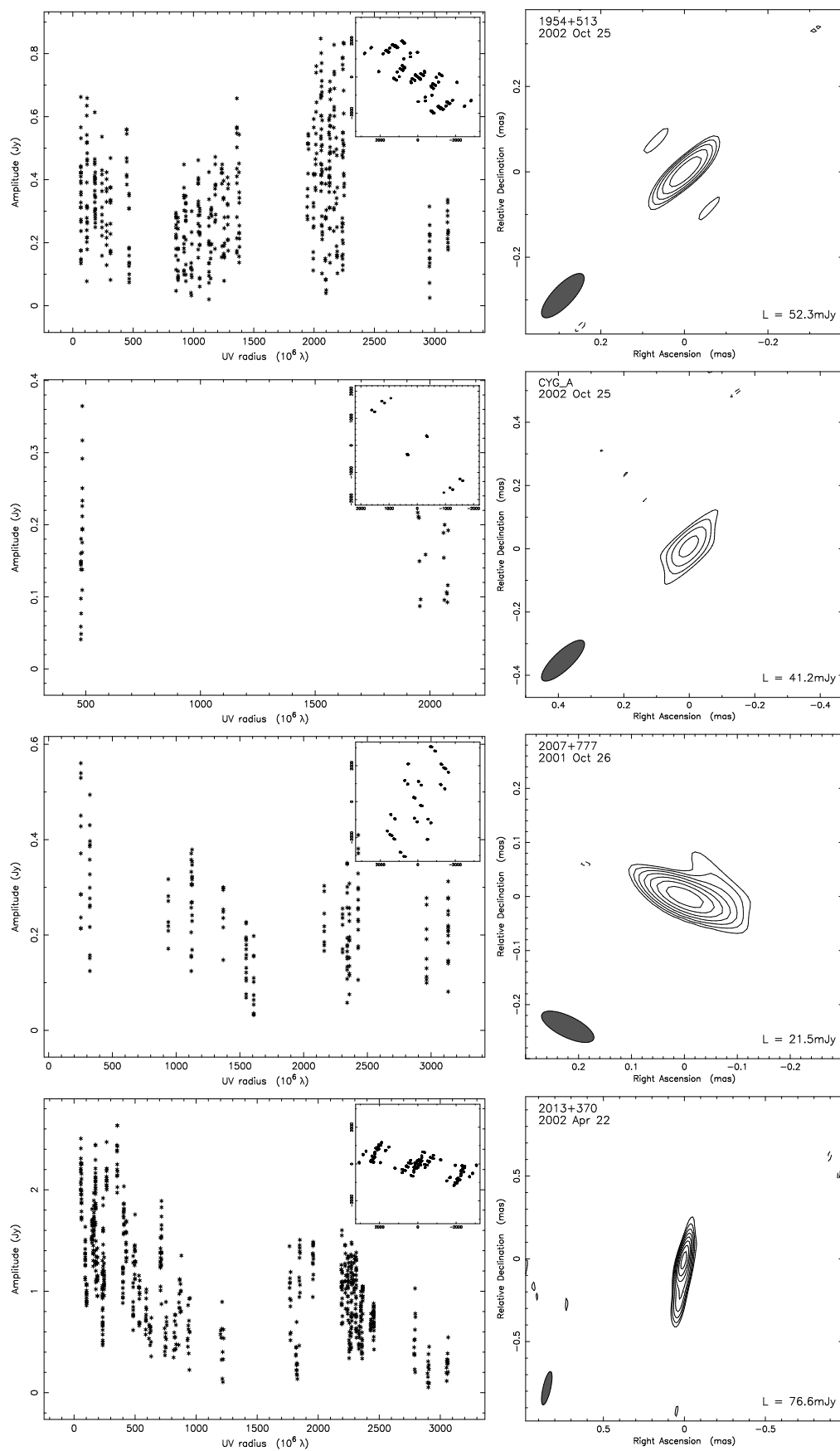


Figure 4.7: - continued.

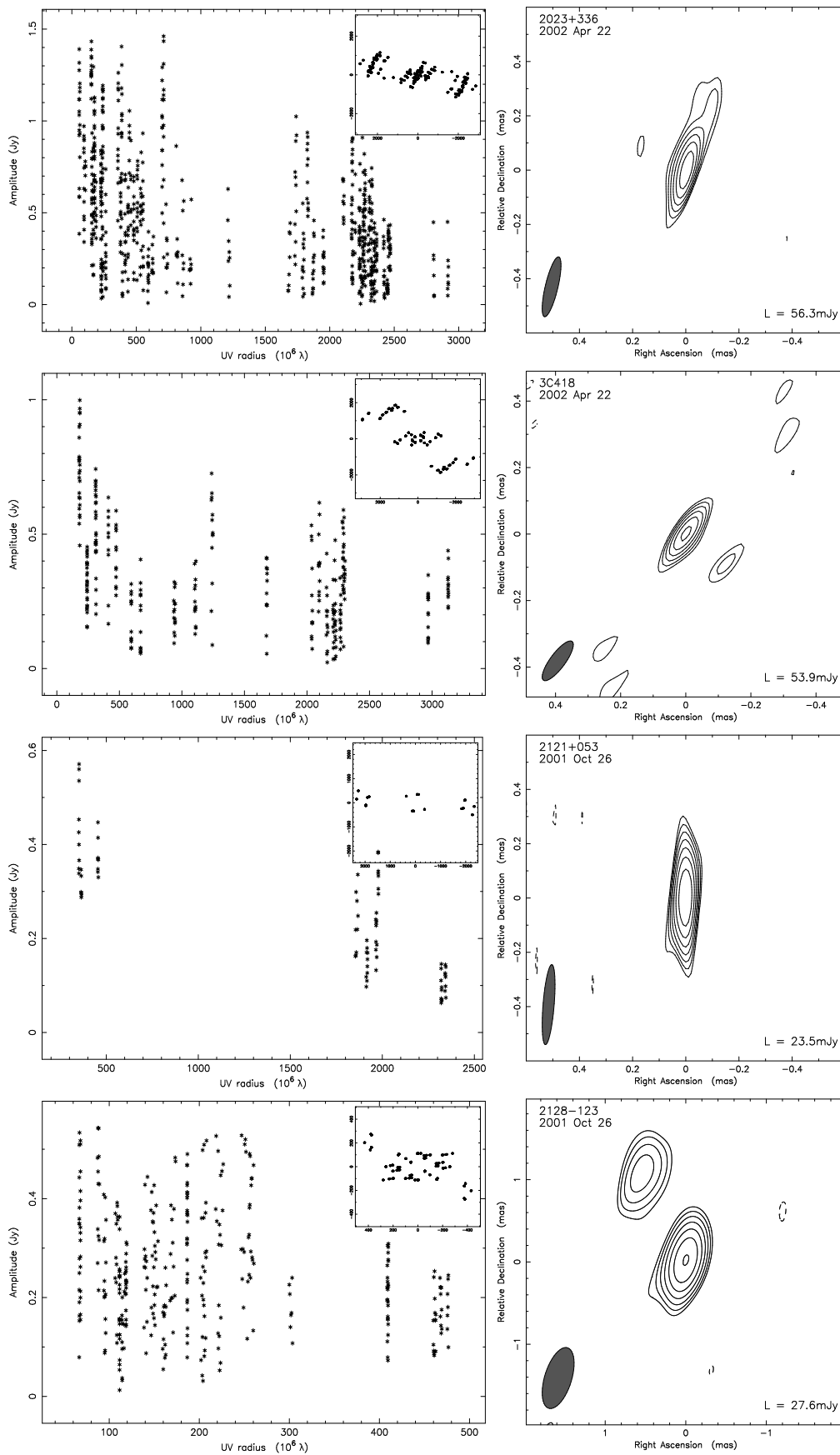


Figure 4.7: - continued.

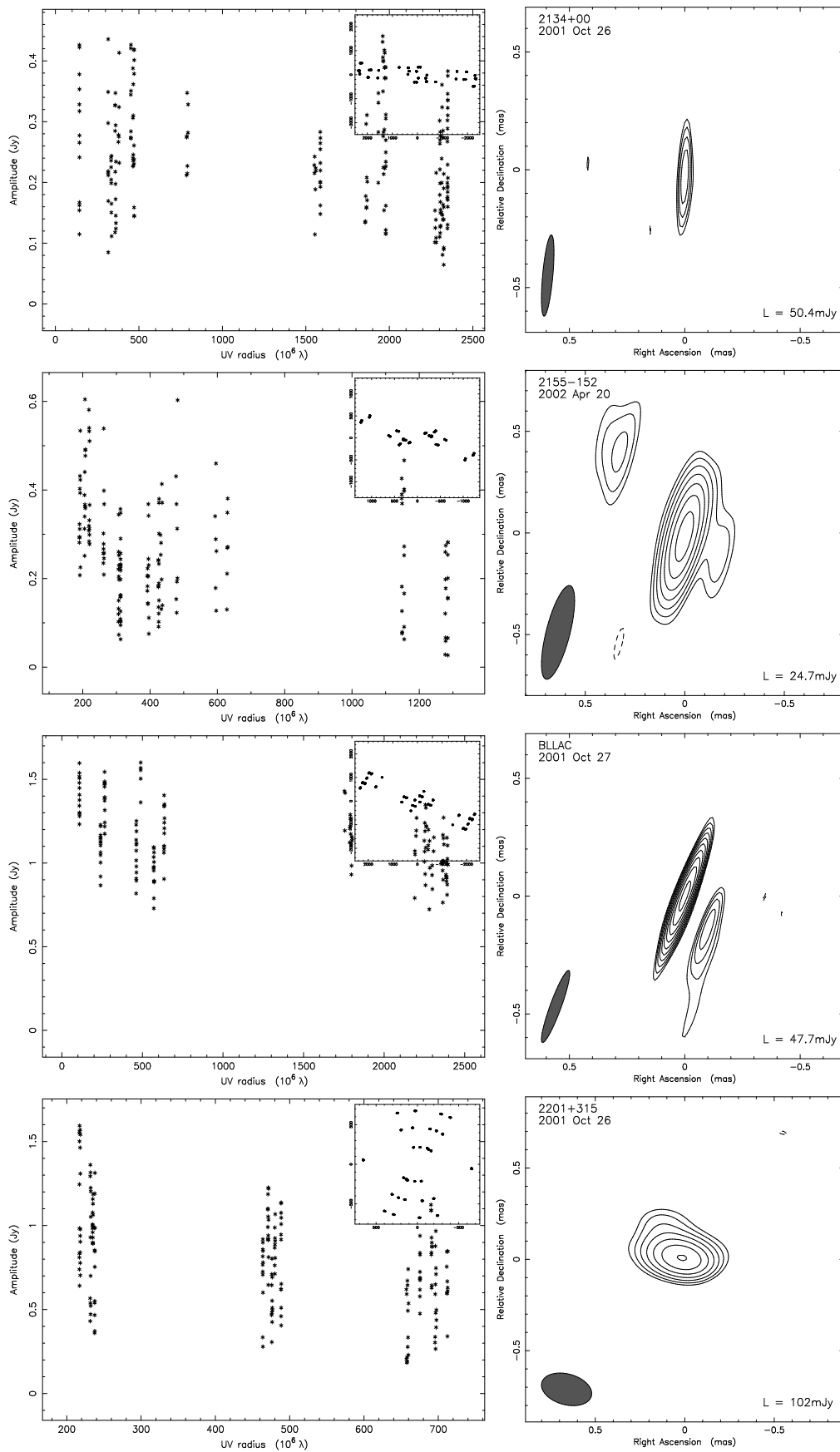


Figure 4.7: - continued.

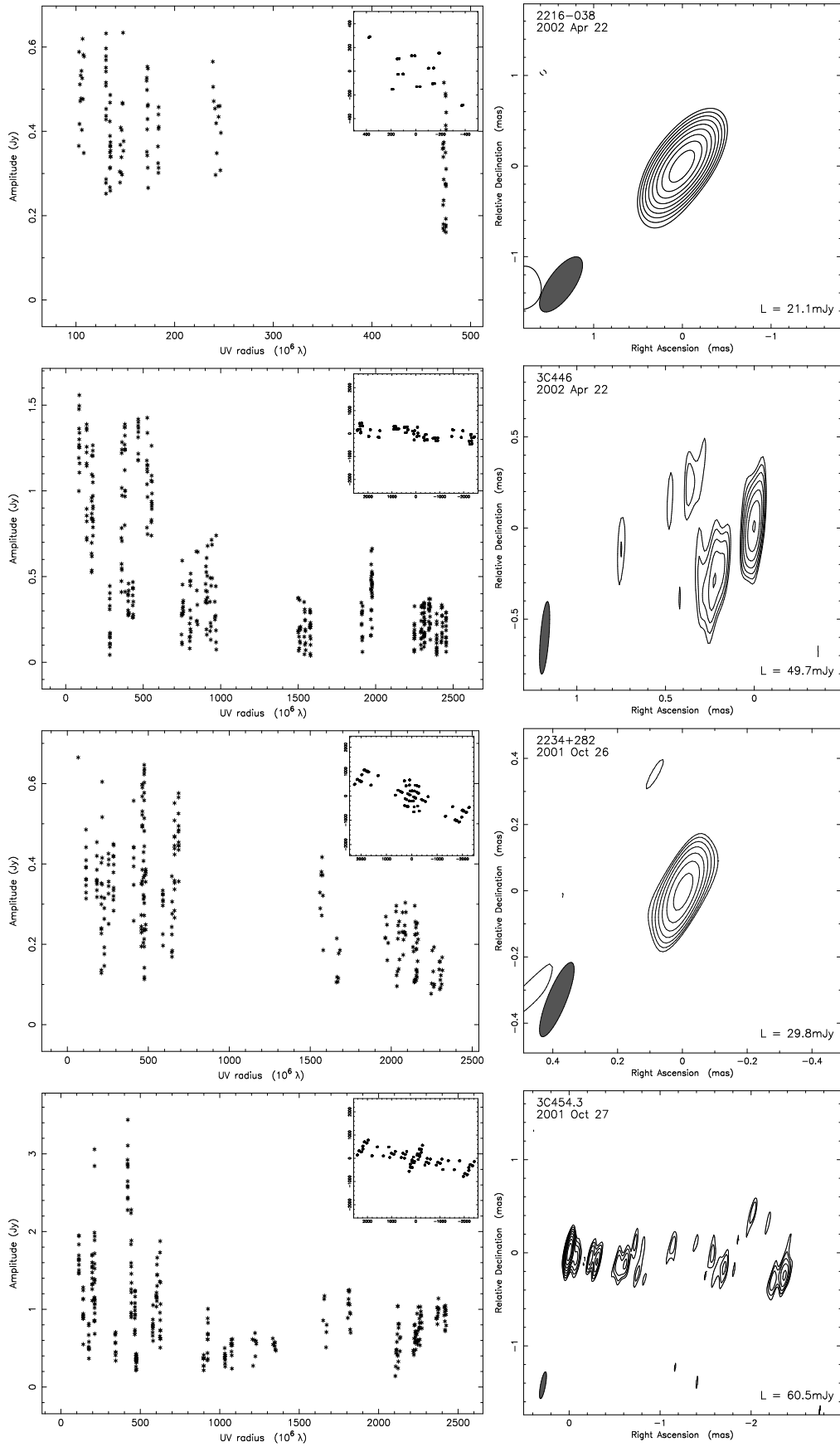


Figure 4.7: - continued.

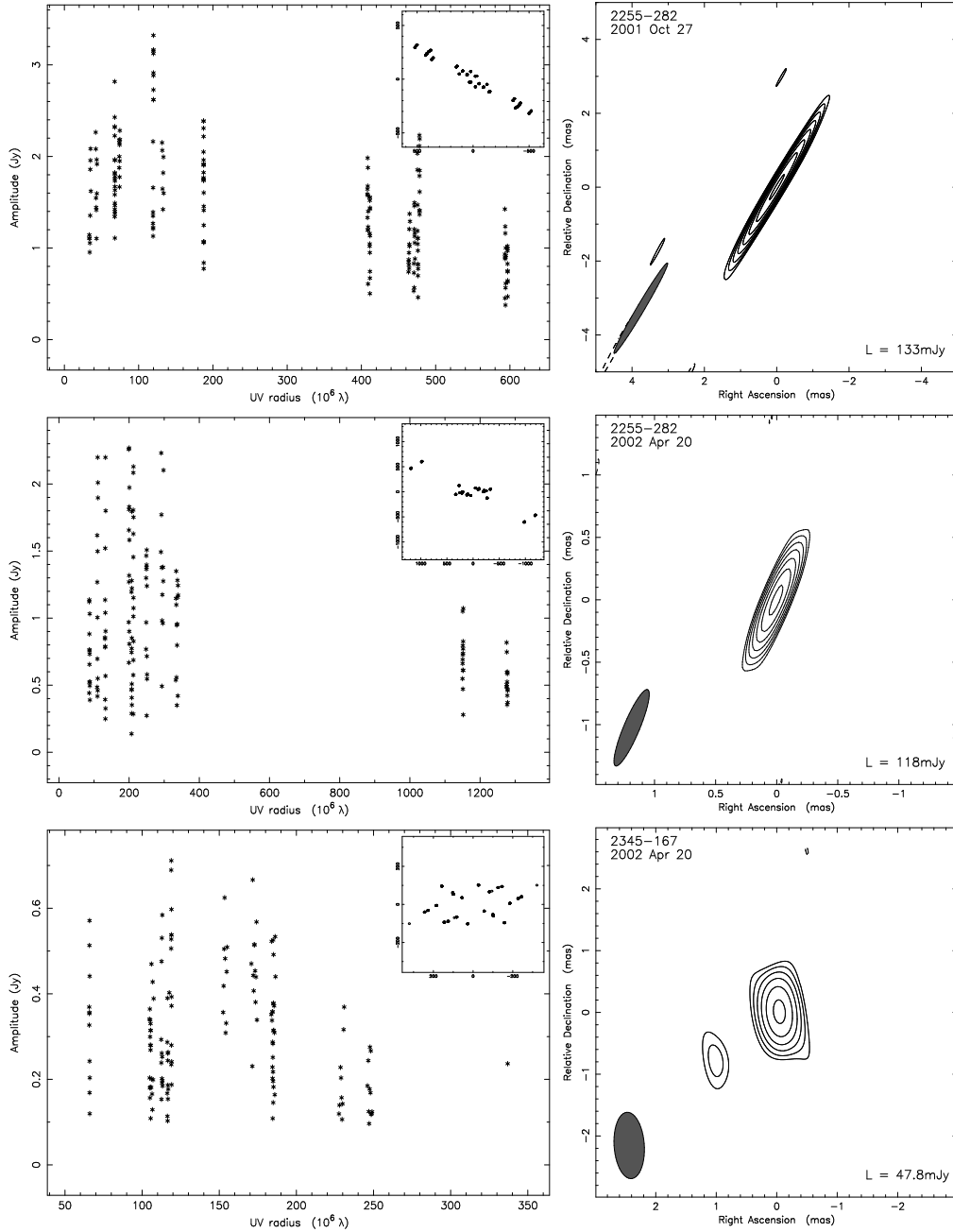


Figure 4.7: - continued.

4.6 Discussion

4.6.1 Source compactness

For imaged sources, we discuss here the source compactness, showing the distributions of the total flux density S_{86} , the CLEAN flux density S_{CLEAN} , and the correlated flux densities $S_{S,L}$ measured on the shortest and longest baselines, listed in Table 4.6. In Figure 4.8, we present the distributions of the flux densities and the indices of source compactness. The distribution of the total flux density S_{86} (*top left panel*) peaks at 1.3 Jy, and shows that almost all sources are brighter than 0.3 Jy, which is corresponding to the flux limit of our source selection. The median value of the CLEAN flux density S_{CLEAN} (*middle left panel*) is 0.6 Jy and the peak of the distribution is around 0.5 Jy, indicating that much of the emission at 86 GHz from the compact

radio sources are resolved out at milliarcsecond scales. The source compactness on milliarcsecond scales S_{CLEAN}/S_{86} is also shown in Figure 4.8 (*top right panel*). The median compactness on milliarcsecond scales of our sample is 0.51.

While the median correlated flux density at the longest baseline S_L is 0.22 Jy (*bottom left panel*), quite a many sources have considerable flux at the longest baselines (e.g., Pico Veleta and Kitt Peak). Among 95 sources whose correlated flux density at projected baselines longer than 2000 M λ is able to be measured, 82 sources have the correlated flux density greater than 0.1 Jy. From the distribution of the source compactness on sub-milliarcsecond scales S_L/S_S (*middle right panel*) we can see that most of the imaged sources are resolved. A few sources have slightly greater flux density on the longest baseline than on the shortest baseline, since they are very compact and faint, giving a large scatter of visibility points on the long baselines. Although most of the imaged sources are seen as resolved, they are highly core-dominated in flux (*bottom right panel*). Quite a number of single-component sources have a core dominance index $S_{\text{core}}/S_{\text{CLEAN}}$ higher than unity due to the uncertainty of model components.

The imaged sources consist of 78 quasars, 22 BL Lac objects, and 8 radio galaxies. Despite the significant difference in the number of sources between the optical classes, the dependence of sub-milliarcsecond scale compactness S_L/S_S on the optical class is apparent in the distribution. Quasars and BL Lacs have quite similar distributions (the average is 0.54 for quasars and 0.48 for BL Lacs, and the median is 0.48 for quasars and 0.42 for BL Lacs), and radio galaxies have a relatively different distribution (the average is 0.38 and the median is 0.41). The dependence is also evident in Figure 4.9, which shows the normalized mean visibility function in terms of uv -radius, averaged for Quasars, BL Lacs, and radio galaxies. The normalized mean visibility amplitudes for radio galaxies are, on average, lower than those for quasars and BL Lacs. At the long uv -radius ranging from 700 M λ to 2500 M λ , the amplitudes for the radio galaxies are quite distinct from the others, whereas for the quasars and BL Lacs no distinction is seen. Overall, the radio galaxies are less compact than the others, but BL Lacs and quasars are similar in compactness.

This dependence implies that *in our sample* quasars and BL Lacs are more compact than radio galaxies on sub-milliarcsecond scales. If we do the same work with a more *complete* sample in the future, the apparent compactness of the compact radio sources can be investigated. According to the unification paradigm of AGN (Urry & Padovani 1995), it is predictable that quasars and BL Lacs on sub-milliarcsecond scales are still more compact than radio galaxies since the former are seen at smaller viewing angle and so Doppler boosted. Our results from the 86 GHz VLBI survey are consistent with this.

4.6.2 Brightness temperature T_b

Figure 4.10 shows the distributions of flux density and angular size for the core components. Most of the cores are smaller than 0.1 mas in angular size. The cores for 77 sources are resolved and for 32 sources are unresolved. Most of the unresolved sources are quasars (23), and a few sources are BL Lacs (7) and radio galaxies (2).

Figure 4.11 shows the distributions of the measured core brightness temperature in the source frame. The median value of these brightness temperatures is 7×10^{10} K. The tail of the distribution extends up to 5×10^{12} K. Only about 1% of the imaged sources yield brightness temperatures greater than 1.0×10^{12} K, which is the maximum value of the inverse Compton limit (Kellermann & Pauliny-Toth 1969), and about 8% have higher brightness temperatures than 3.0×10^{11} K, which is corresponding to the equipartition limit (Readhead 1994). This distribution shows lower brightness temperatures by a factor of 10 than those derived from the VSOP survey at 5 GHz (see Horiuchi et al. 2004) and VLBA 2 cm Survey (see Kovalev et al. 2005). Higher brightness temperatures of compact radio sources can be explained by Doppler boosting, transient non-equilibrium events, coherent emission, emission by relativistic protons, or a combination of these effects (see Kardashev 2000; Kellermann 2003, and discussion in section 3.3.4). A more detailed discussion on the brightness temperature is presented in the next chapter.

4.6.3 Intraday variable sources

In order to identify intraday variable (IDV) sources in our sample, we used the list of IDV sources compiled in Kovalev et al. (2005, and see references therein). Almost all the imaged sources are clearly identified except 6 sources; 1044+719, 1150+497, 1842+681, 1923+210, 2013+370, and 2023+336. From the references in Kovalev et al. (2005), they are identified as “non-IDV” sources. In total, 26 sources are identified as “IDV” sources in our sample.

Table 4.7: Statistics of IDV and non-IDV selected sources

Sample	Number	S_L^a		S_L/S_S		S_{core}/S_{CLEAN}	
		Mean	Median	Mean	Median	Mean	Median
IDV	26	0.36±0.06	0.26	0.53±0.08	0.46	0.75±0.04	0.78
Non-IDV	83	0.31±0.04	0.21	0.51±0.04	0.44	0.76±0.03	0.75
Sample	Number	S_{core}^a		d_{core}^b		$\log(T_b)^c$	
		Mean	Median	Mean	Median	Mean	Median
IDV	26	0.70±0.11	0.42	0.039±0.004	0.035	11.1±0.1	11.1
Non-IDV	83	0.62±0.08	0.46	0.057±0.005	0.043	10.8±0.1	10.8

Notes: a - S_L and S_{core} are in Jy; b - d_{core} is in mas; c - T_b is in Kelvin. Each mean value is presented with its corresponding 1- σ error, assuming a normal distribution.

Figure 4.12 shows the distributions of the correlated flux density at the longest baseline S_L (*top left panel*), and the core flux density S_{core} (*top right panel*), as well as the distributions of the size d_{core} (*middle right panel*) and brightness temperature T_b (*bottom right panel*) of core component. The source compactness on sub-milliarcsecond scales S_L/S_S (*middle left panel*) and the core dominance S_{core}/S_{CLEAN} (*bottom left panel*) are also shown. The statistics of the distributions are summarized in Table 4.7 and the statistical significance of the difference between IDV and non-IDV selected sources with respect to these parameters are shown in Figure 4.13.

For the correlated flux density at the longest baseline S_L , the IDV and non-IDV sources have different mean values of 0.36 Jy and 0.31 Jy, and medians of 0.26 Jy and 0.21 Jy, respectively. A Kolmogorov-Smirnov (K-S) test (Press et al. 1992a) shows that there is a 17% chance that the IDV and non-IDV samples are derived from a common distribution. This is a somewhat inconclusive result due to a few points at higher flux densities in the non-IDV sample, which affects strongly the statistical results. If we exclude those outliers, then the mean of the non-IDV sample gets smaller than that of the IDV sample and the probability decreases to 15%. However, it is difficult to conclude that IDV sources have higher flux density S_L than non-IDV sources in our sample.

The distributions of the compactness index S_L/S_S for IDV and non-IDV sources have means of 0.53 and 0.51 with medians of 0.46 and 0.44. A K-S test shows that a common parent distribution for IDV and non-IDV sources is very much acceptable at the 100% level. In Figure 4.14, it is shown that the sub-milliarcsecond compactness S_L/S_S for the IDV sources is, on average, nearly identical to the non-IDV sources.

For the core dominance S_{core}/S_{CLEAN} , the IDV sources have a mean of 0.75 with a median of 0.78, and the non-IDV sources have a mean of 0.76 with a median of 0.75. The K-S comparison percentile plot (*bottom left panel* in Figure 4.13) shows quite similar distributions for IDV and non-IDV sources with the K-S probability at the 80% level, clearly indicating that both samples are from a common parent population. Therefore, it is clear that IDV sources are similar to non-IDV sources in core-dominance.

For the core parameters such as the core flux density, the core size, and the core brightness temperature, we found different results. The distributions of the core flux density S_{core} for IDV and non-IDV sources have means of 0.70 Jy and 0.62 Jy, with medians of 0.42 Jy and 0.46 Jy. They have a 34% probability of being derived from a common core flux density population. This is quite distinctive from the results for the rest parameters. The distributions of the core size d_{core} for IDV and non-IDV sources have means of 0.039 mas and 0.057 mas with medians of 0.035 mas and 0.043 mas. The cores of IDV sources are smaller in angular size than those of non-IDV sources. A K-S test also yields a probability of less than 4% that the core size has the same parent distribution for IDV and non-IDV sources. This result from the two parameters affect the distribution of the core brightness temperature, since the core brightness temperature strongly depends on the core flux density and the core size. Means of the core brightness temperature for IDV and non-IDV sources are $10^{11.1\pm0.1}$ K and $10^{10.8\pm0.1}$ K, and medians are $10^{11.1}$ K and $10^{10.8}$ K, respectively. A common parent population of the core brightness temperature for IDV and non-IDV sources are rejected at the 92% level. Although IDV sources have a similar core flux density to that of non-IDV sources, their brightness temperatures are higher than those of the non-IDV sources due to the smaller angular core size.

4.7 Summary

We have conducted the largest global 86 GHz VLBI survey of compact radio sources during three GMVA sessions of October 2001, April 2002, and October 2002. Due to the participation of many sensitive European and dedicated VLBA antennas, high baseline and image sensitivities are achieved as expected, and as a result 121 out of 127 observed sources are detected at least on one baseline and 109 sources imaged with a typical dynamic range of 50. The result of this survey, furthermore, extends the database of sources imaged at 86 GHz with VLBI observations by up to a factor of 5.

By fitting the visibilities of each source with a simple model of circular Gaussian components, we parameterize the physical characteristics of each component of the sources; flux density, size, radius, position angle, etc. With these results the source compactness and brightness temperatures are derived.

Almost all of the imaged sources are seen to be resolved and the cores of about 70% of the imaged sources are resolved. Radio galaxies are less compact than quasars and BL Lacs. BL Lacs are similar to quasars in the compactness at sub-milliarcsecond scales.

The distribution of the core brightness temperatures peak at $\sim 10^{11}$ K and only 1% have brightness temperatures higher than 10^{12} K. This shows apparently lower brightness temperatures than those derived from other VLBI surveys at lower frequencies (e.g., 5 GHz and 15 GHz).

IDV sources in our sample are similar to non-IDV sources in compactness at sub-milliarcseconds. The cores of IDV sources are smaller in angular size and so yield higher brightness temperature than non-IDV sources, since the core flux densities of both samples are similar to each other.

The overall amplitude calibration error investigated for the observations is 20%–30%, to which extent the results of the flux densities and brightness temperatures are accurate.

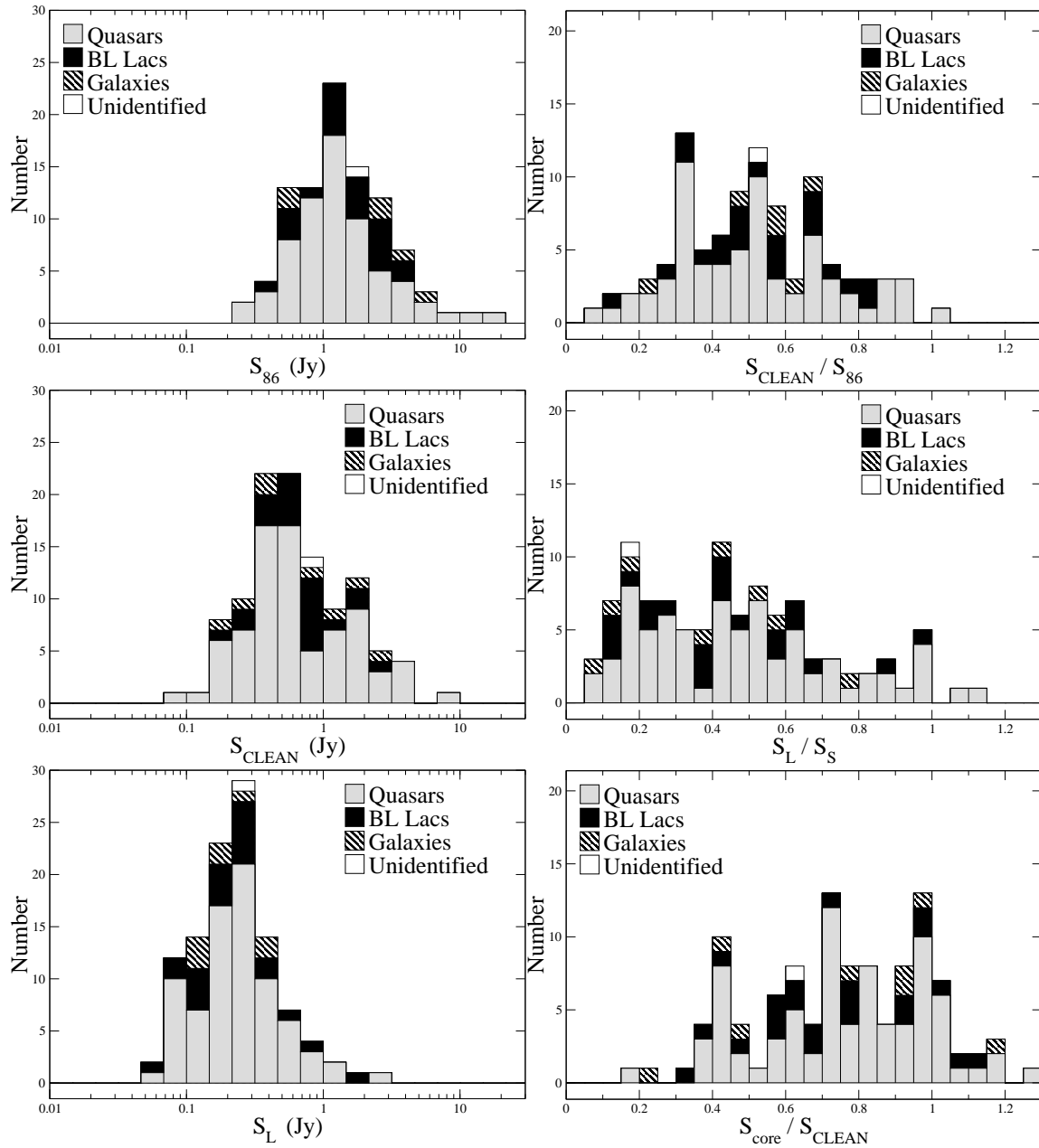


Figure 4.8: Distributions of the total flux density, S_{86} (top left), the CLEAN flux density, S_{CLEAN} (middle left), the correlated flux density on the longest baseline, S_L (bottom left), compactness indices on milliarcsecond scales S_{CLEAN}/S_{86} (top right) and sub-milliarcsecond scales S_L/S_S (middle right), and the core dominance $S_{\text{core}}/S_{\text{CLEAN}}$ of the imaged sources. In the top left panel, sources with the total flux density not available are excluded.

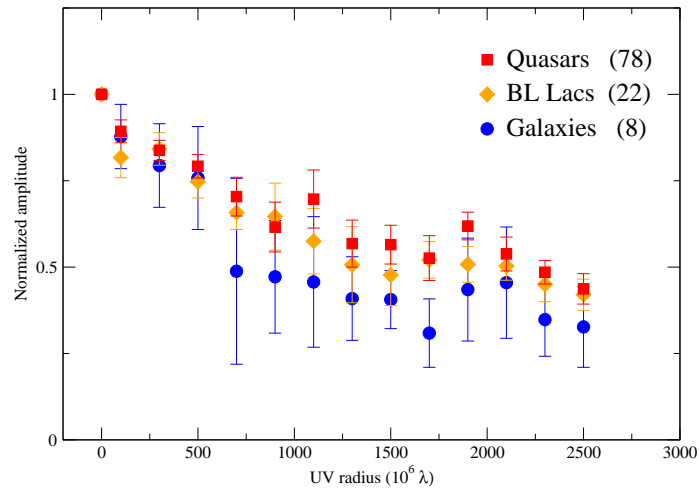


Figure 4.9: Normalized mean amplitude of the visibility function in terms of uv -radius for the survey sample. The visibility amplitude is normalized by the CLEAN flux density S_{CLEAN} for each source (which corresponds to points at $0 M\lambda$), binned with $200 M\lambda$ wide bins ranging from 0 to $2600 M\lambda$, and averaged. Not all bins are sampled for all sources.

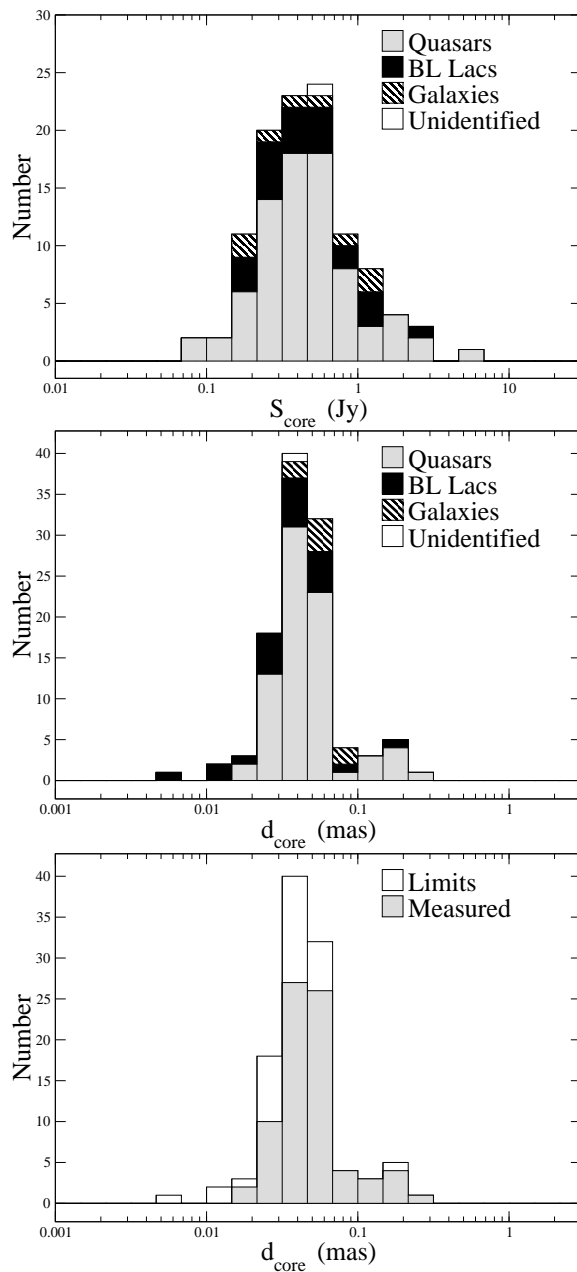


Figure 4.10: Distributions of the flux density (top panel) and the the angular size (middle and bottom panel) of the core components for the imaged sources.

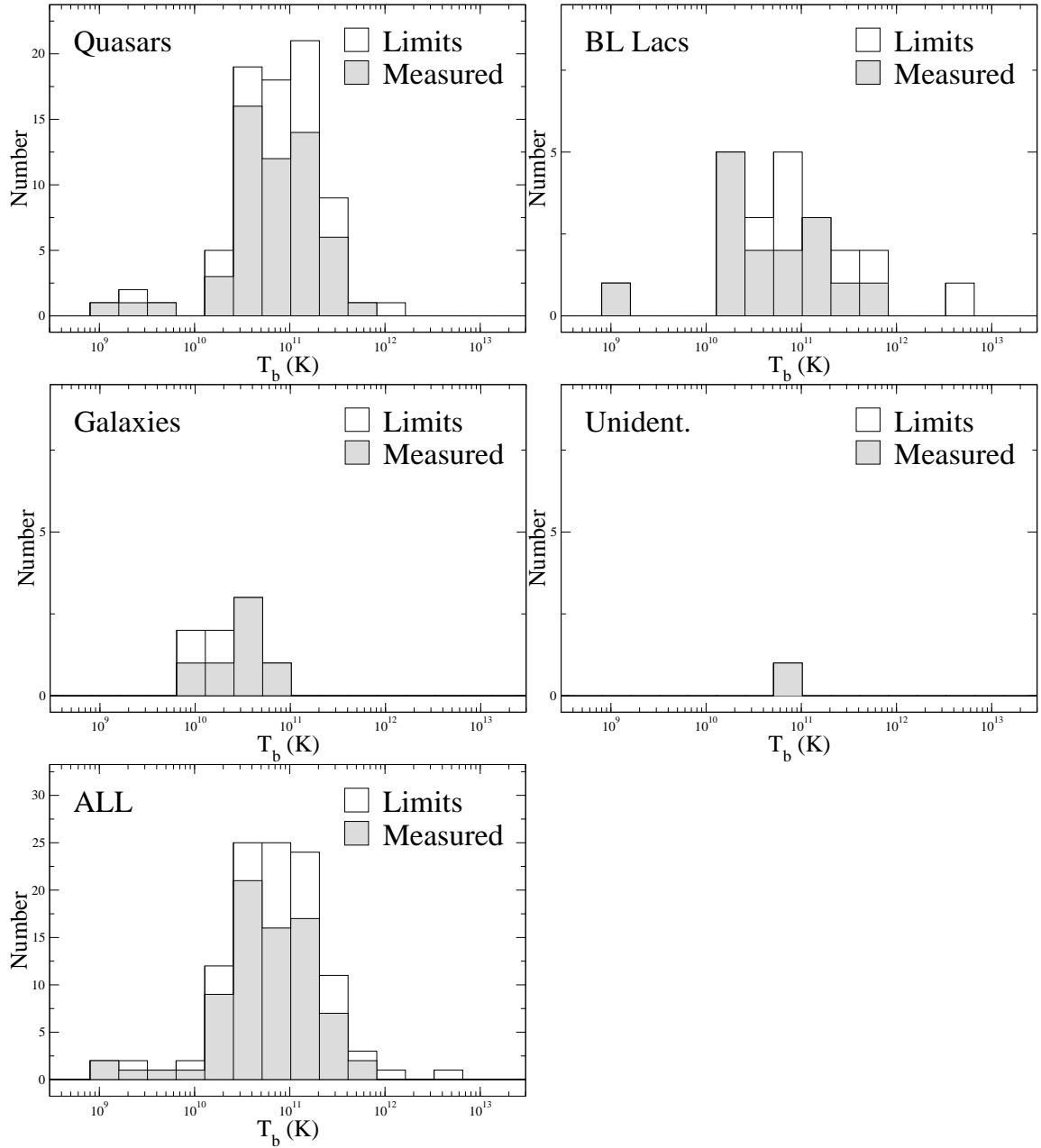


Figure 4.11: Distributions of the source frame brightness temperatures in the core components. The brightness temperatures are binned logarithmically, increasing by a factor of 2 from 1×10^8 K to a maximum value in each sample.

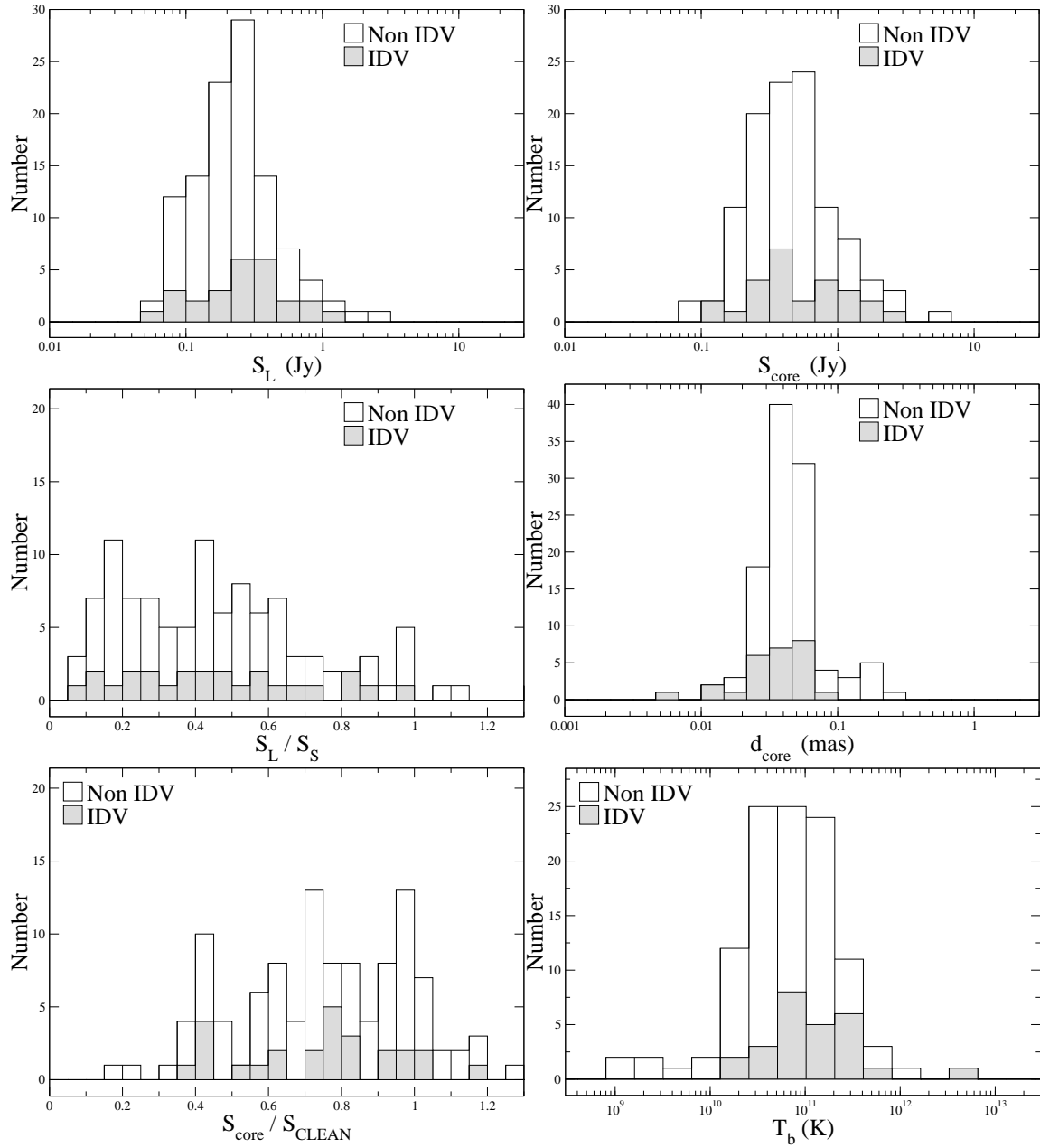


Figure 4.12: Distributions of the correlated flux density at the longest baseline S_L (top left), the compactness index S_L/S_S (middle left), the core dominance $S_{\text{core}}/S_{\text{CLEAN}}$ (bottom left), the core flux density S_{core} (top right), the size of core component d_{core} (middle right), and the brightness temperature T_b (bottom right) for IDV selected and non-IDV selected sources (see text for reference).

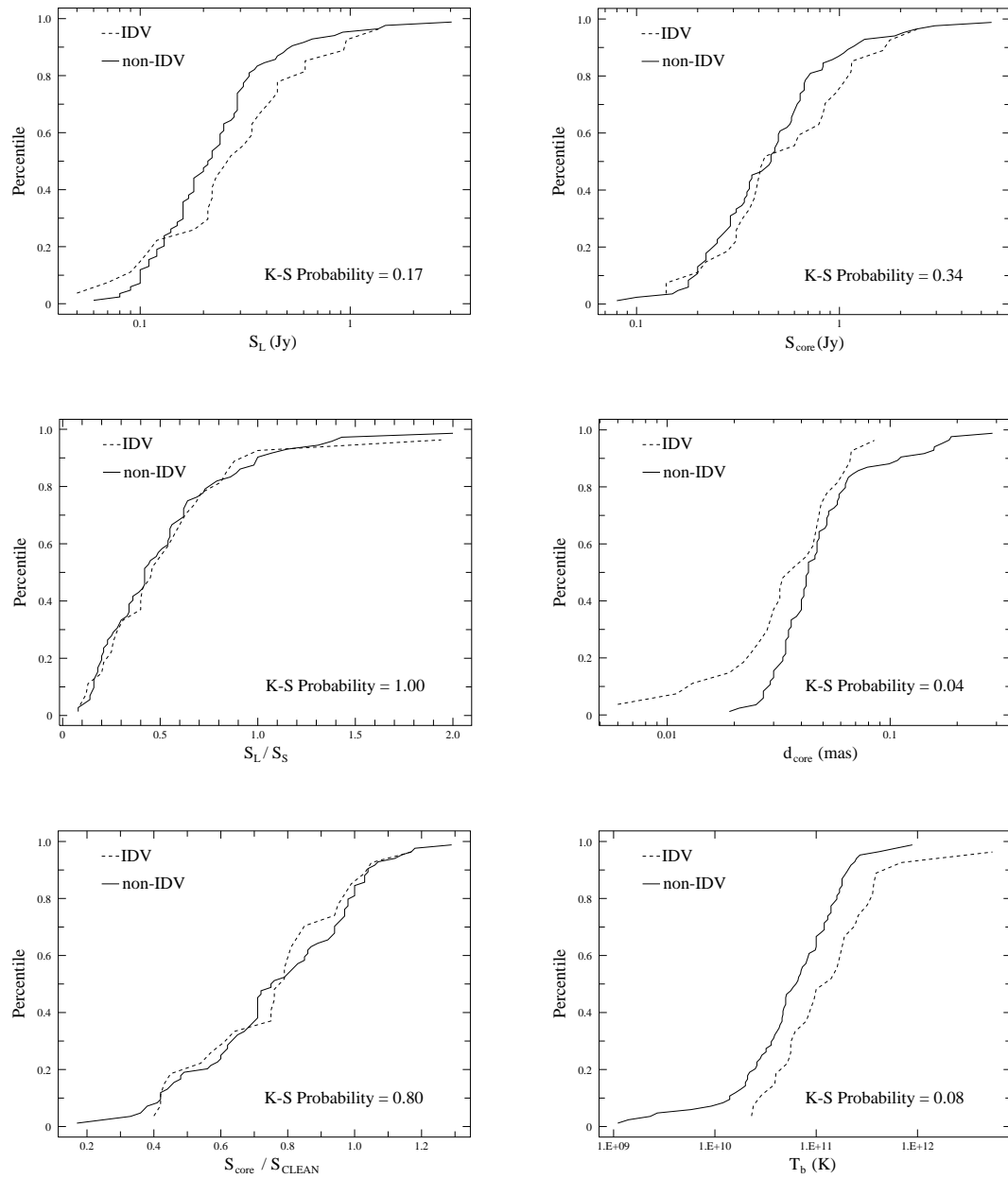


Figure 4.13: Comparison percentile plots of Kolmogorov-Smirnov (KS) test with the distributions shown in Figure 4.12 for IDV selected and non-IDV selected sources. K-S probability presented in each plot indicates probability that the samples for IDV and non-IDV selected sources have a common parent distribution with respect to each parameter.

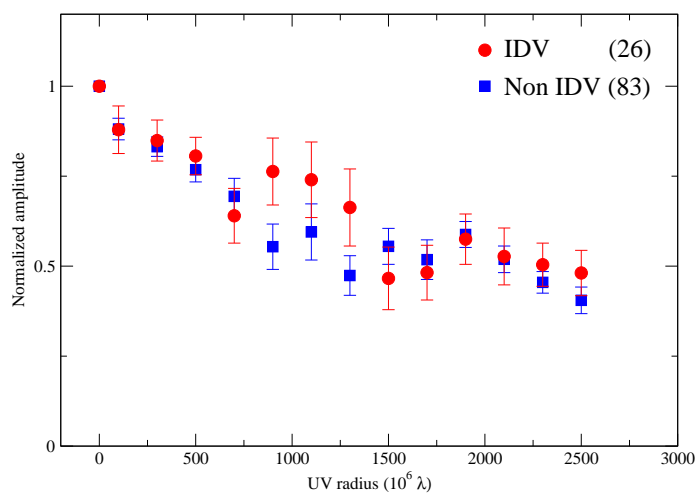


Figure 4.14: Normalized mean amplitude of the visibility function in terms of uv -radius for IDV and non-IDV sources (see text for details). The visibility amplitude is normalized by the CLEAN flux density S_{CLEAN} for each source (which corresponds to a point at $0 M\lambda$), binned with $200 M\lambda$ wide bins ranging from 0 to $2600 M\lambda$, and averaged. Not all bins are sampled for all sources.

Chapter 5

Intrinsic Properties of Compact Radio Sources

5.1 Introduction

It is very difficult to measure intrinsic properties of compact radio sources because the jets of compact radio sources are highly relativistic and therefore Doppler boosted. Observed brightness temperatures (T_b) can be used to study the intrinsic physical properties of the relativistic jets.

One application is to study the intrinsic brightness temperatures of VLBI “cores”, by using the observed brightness temperature T_b and the maximum jet speed β_{app} . The method from Homan et al. (2006) was applied to the 2 cm survey data (Kellermann et al. 2004) in order to study the intrinsic physical properties of prominent AGN (Cohen et al. 2007). The method could also be applied to our sample at 86 GHz with the maximum apparent jet speeds at 15 GHz taken from Kellermann et al. (2004), in order to constrain the intrinsic brightness temperature.

The intrinsic properties of relativistic jets depend on inner jet models (Marscher 1995). To test the accelerating and decelerating jet models, the comparison of the brightness temperatures measured at 86 GHz with those at lower frequencies (e.g., 2 – 43 GHz) can be used. Under the equipartition condition between jet particle and magnetic field energy densities, the position shift of the VLBI cores between two frequencies can be predicted (Lobanov 1998b). The brightness temperatures in the rest frame of sources and the predicted core shift should be able to test the inner jet models.

In this chapter, the intrinsic properties of compact radio sources are discussed. In section 5.2 the brightness temperatures at 86 GHz are compared with the maximum jet speeds at 15 GHz in order to constrain the intrinsic properties. The inner jet models are tested in section 5.3. The evolution of the brightness temperatures along the jet is discussed in section 5.4. In section 5.5, the main results of this chapter will be concluded.

5.2 Intrinsic brightness temperature

The highly relativistic jets are Doppler boosted to appear much brighter than their intrinsic brightness. Moreover, apparent proper motion of the relativistic jet as one of the observables is very dependant on the viewing angle of the jets, which is usually unknown. Therefore, it is very difficult to measure the intrinsic brightness temperature T_0 . However, the observed brightness temperature (T_b) and observed proper motion (hence jet speed β_{app}) can be used to constrain the intrinsic brightness temperature of a sample of the relativistic jets (Homan et al. 2006).

The physical aspects of the jet can be parameterized by the Lorentz factor γ_j , the intrinsic brightness temperature T_0 , and the angle to the line of sight θ_j . From these intrinsic physical properties, one can calculate the Doppler factor δ , the apparent jet speed β_{app} , and the observed brightness temperature T_b :

$$\delta = \frac{1}{\gamma_j(1 - \beta\cos\theta_j)}, \quad (5.1)$$

$$\beta_{\text{app}} = \frac{\beta\sin\theta_j}{1 - \beta\cos\theta_j}, \quad (5.2)$$

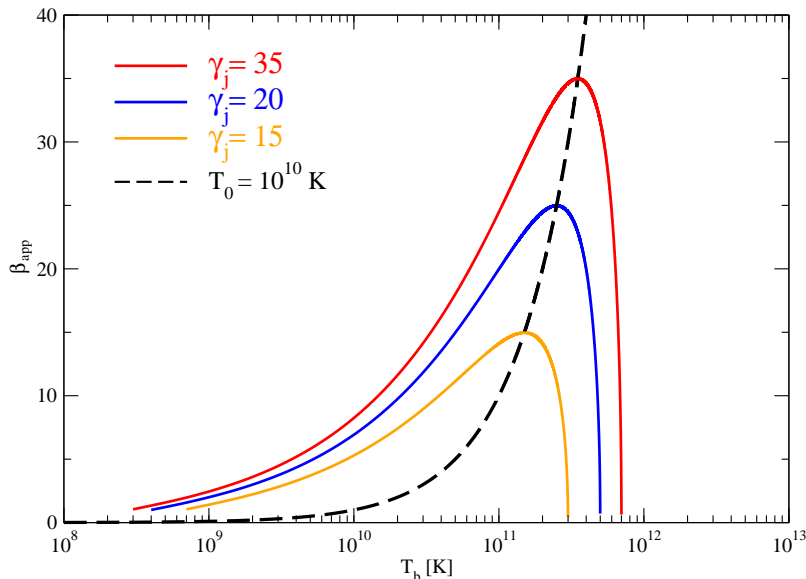


Figure 5.1: Plot of the apparent jet speed β_{app} with the observed brightness temperature T_b for a single intrinsic brightness temperature of $T_0 = 1 \times 10^{10}$ K and several values of Lorentz factors $\gamma_j = 15, 20,$ and 35 . The dashed line represents where sources observed at the critical angle would lie on this plot. The solid line represents the possible apparent speeds of a γ_j source with intrinsic brightness temperature given by T_0 .

$$T_b = T_0 \delta, \quad (5.3)$$

where $\beta = (1 - \gamma_j^{-2})^{1/2}$ is the speed of jet in the rest frame of the source (units of c).

Following Homan et al. (2006), we assume that a compact radio source contains an ideal relativistic jet, which is narrow and straight with no bends between the VLBI core and the jet components. It is clear that some jets are not straight and that θ_j is not the same in the core and in the moving jet components. The celebrated example of the jet bending is found in 3C 279 (Homan et al. 2003). However, as long as superluminal motion is found, the motion must be close to the line of sight, and any changes in angle will be strongly amplified by projection. An observed right-angle bend could correspond to an intrinsic bend of only a few degrees (Cohen et al. 2007).

In this case, we can also assume that the maximum speed of the jet component is the same as the speed of the jet flow through the jet core. The flow speed of the jet is usually different from the pattern speed of the jet in some low-luminosity sources. However, in those sources which are bright and straight, the pattern speeds are the same as the flow speeds. For simplicity, we make two further assumptions:

1. All jets have the same intrinsic brightness temperature T_0 , and
2. All sources have their viewing angles close to the critical value $\theta_c = \arccos \beta$ for the maximal apparent speed at a given β .

Under the assumptions above, one can relate the observed brightness temperature to the maximum jet speed:

$$\delta \simeq \beta_{\text{app}} \quad (5.4)$$

and

$$T_b \simeq \beta_{\text{app}} T_0. \quad (5.5)$$

This resultant simple relation between the observed brightness temperature and the apparent maximum jet speed is described as a solid line in Figure 5.1. From equations (5.1) and (5.2), one can also relate the apparent jet speed β_{app} to the Doppler factor δ and the Lorentz factor γ_j :

$$\beta_{\text{app}} = \sqrt{(\delta \gamma_j \beta)^2 - (\delta \gamma_j - 1)^2}, \quad (5.6)$$

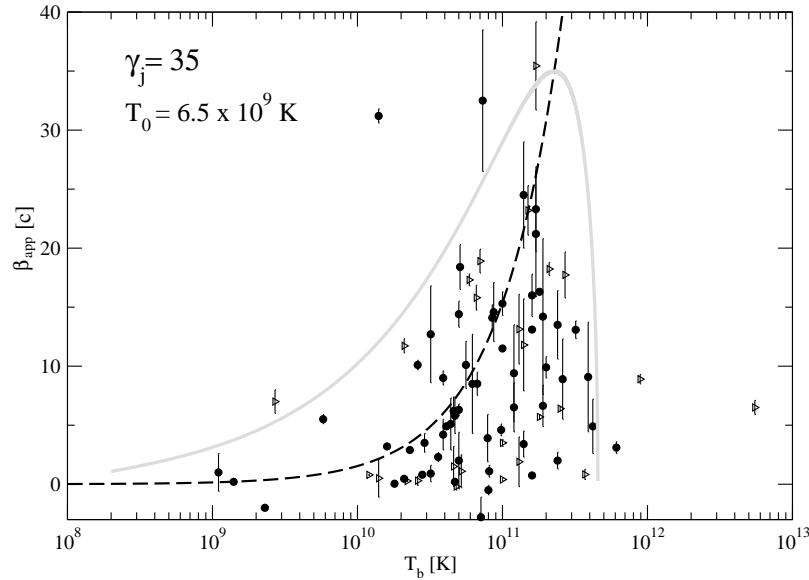


Figure 5.2: Plot of the apparent jet speed versus the observed brightness temperature for the sources in our sample. Lower limits of brightness temperatures are indicated by right triangle and solid circles represent measurements. The dashed line represents sources observed at the critical angle that have the intrinsic brightness temperature of $T_0 = 6.5 \times 10^9$ K. The solid grey line represents the possible apparent speeds of a $\gamma_j = 35$ source with intrinsic brightness temperature given by T_0 .

for the maximum and minimum possible Doppler factors $\delta_{\max} = 1/\gamma_j$ and $\delta_{\min} = 1/(\gamma_j - \sqrt{\gamma_j^2 - 1})$, as shown as the solid lines in Figure 5.1. The lines show actually the apparent speeds for jets with the maximum Lorentz factors of $\gamma_j = 15, 20,$ and 25 as functions of T_b , corresponding to a varying jet viewing angle. Homan et al. (2006) found that from the simulation of a relativistically beamed population of 1000 fictional compact radio sources with given T_0 and γ_j , approximately 75% of the sources fall below and to the right of the dashed line representing the critical angle. Those sources located to the right and below are indeed inside the critical angle, and they have large Doppler factors. Many of them are close enough to the line of sight to have small proper motions.

We use the observed brightness temperatures of VLBI cores at 86 GHz from this work and have taken the apparent jet speeds from the 2 cm VLBA survey (e.g., Kellermann et al. 2004). As described in the paper by Kellermann et al. (2004), we selected the fastest proper motion for each source, and we only considered those motions that are ranked as “excellent” (E) or “good” (G) by the criteria laid out in that paper. For some sources which are observed or do not yield any good measurements in Kellermann et al. (2004), we have taken the apparent speeds from the on-going MOJAVE project, assuming that the speeds are maximum values of individual sources. Figure 5.2 shows a plot of the maximum apparent speed β_{app} versus the observed brightness temperature T_b for 85 selected sources from our 3 mm-survey sample. The dashed line indicates sources at the critical angle which have $T_0 = 6.5 \times 10^9$ K, and the solid grey line was calculated using the same value for T_0 . The value of T_0 was chosen to have approximately 75% of the sources fall below and to the right of the dashed line, which is the same criterion for choosing the value of T_0 as in Homan et al. (2006). Since other choices for the simulation parameters described in Homan et al. (2006) are expected to give a roughly similar distribution of points and to yield fractions between 60% and 80% of sources within the critical angle, we take the corresponding values of $T_0 = 5.7 \times 10^{10}$ K for a 80% fraction and $T_0 = 8.6 \times 10^{10}$ K for a 60% fraction as the range of uncertainty for T_0 .

The intrinsic brightness temperature of $T_0 = 6.5 \times 10^9$ K is indeed less than the equipartition value of 5×10^{10} K (see section 3.3). This implies that the VLBI cores seen at 86 GHz may be representing a jet region where the magnetic field energy dominates the total energy in the jet. In this circumstance we could expect that the conversion of the magnetic field energy into the kinetic energy of particles in the jet and the intrinsic brightness temperature will increase as going down stream of the jet. Homan et al. (2006) actually found that AGN cores at 15 GHz are near equipartition in their median–low state, yielding the intrinsic brightness temperatures of $T_0 = 3 \times 10^{10}$ K for a 75% fraction and $T_0 = 4 \times 10^{10}$ K for a 60% fraction. Despite the

different sample of sources they used, the difference in the intrinsic temperatures T_0 deduced at 15 GHz and 86 GHz may imply that there will be only a small number of sources suitable for VLBI at higher frequencies (e.g., ≥ 215 GHz). The decrease of T_0 would also give a favorable argument to the decelerating jet model or particle cascade model as discussed by Marscher (1995). The kinematics of the innermost region of jet will be investigated in the following section by comparing the observed brightness temperatures at 86 GHz with those at lower frequencies.

5.3 Compact jets on sub-parsec scales

In an attempt to parameterize a relativistic jet, Blandford & Königl (1979) considered the idealized model of a steady radio jet. They assume a narrow conical jet of small opening angle ϕ whose axis makes an angle θ with the line of sight of the observer (the observed opening angle is $\phi_o = \phi \csc \theta$). The jet is assumed to be supersonic and free, and to have a constant speed β_j . The magnetic field in the jet B should vary as r^{-1} , where r is the distance from the apex of the jet (most likely the central engine). The flow of relativistic particles in the jet is accelerated by converting the internal relativistic particle energy γ_e to the bulk kinetic energy γ_k , and their particle energy distribution is $N(\gamma_e) = N_0 \gamma_e^{-s}$ for $\gamma_{\min}(r) < \gamma_e < \gamma_{\max}(r)$, where s is the particle energy spectral index. Those electrons radiate the inhomogeneous synchrotron radiation with a spectral index $\alpha = (1 - s)/2$. For a typical $\alpha = -0.5$, the corresponding particle energy distribution is $N(\gamma_e) = N_0 \gamma_e^{-2}$. Assuming the equipartition between the jet particle energy and the magnetic field energy, which is given by $k_e \Lambda B^2 / 8\pi$ ($k_e \leq 1$ and $\Lambda = \ln(\gamma_{\max}/\gamma_{\min})$), the total radiated synchrotron power from the emission region extending from r_{\min} to r_{\max} in the jet is

$$L_{\text{syn}} = \frac{1}{8} k_e \Delta \gamma_j \beta_j c B^2 r^2 \phi_o^2, \quad (5.7)$$

where $\Delta = \ln(r_{\max}/r_{\min})$.

The observed VLBI core at any given frequency is located at a region where the optical depth to synchrotron self-absorption is $\tau_s = 1$ in the jet. Assuming that the magnetic field and particle density decrease with r as $B = B_1 (r_1/r)^m$ and $N = N_1 (r_1/r)^n$, where B_1 , N_1 are the magnetic field and the electron density at $r_1 = 1$ pc, the corresponding τ_s is given by (see Rybicki & Lightman 1979):

$$\tau_s(r) = C_2(\alpha) N_1 \left(\frac{e B_1}{2\pi m_e} \right)^\epsilon \frac{\delta^\epsilon \phi_o}{r^{(\epsilon m + n - 1) \nu^{\epsilon+1}}}, \quad (5.8)$$

where e , m_e are the electron charge and mass, respectively, and δ , ϕ_o are the Doppler factor and the observed jet opening angle. Here $\epsilon = 3/2 - \alpha$, and $C_2(\alpha)$ is a constant at a given spectral index (Blumenthal & Gould 1970). For a typical $\alpha = -0.5$, $C_2(\alpha) = 8.4 \cdot 10^{10}$ in *cgs* units. The physical distance of the observed VLBI core from the central engine is obtained by equating the optical depth $\tau_s(r)$ to unity:

$$r = [\nu^{-1} (1+z)^{-1} B_1^{k_b} \{6.2 \cdot 10^{18} C_2(\alpha) \delta_j^\epsilon N_1 \phi_o\}^{1/(\epsilon+1)}]^{1/k_r} \text{ pc}, \quad (5.9)$$

where $k_r = ((3 - 2\alpha)m + 2n - 2)/(5 - 2\alpha)$ and $k_b = (3 - 2\alpha)/(5 - 2\alpha)$. Königl (1981) shows that it is most reasonable to use $m = 1$ and $m = 2$ to explain the observed X-ray and synchrotron emission from the ultra compact VLBI jets. In the case of $m = 1$, $n = 2$, the corresponding $k_r = 1$ does not depend on spectral index.

Assuming that we observe the equipartition region of the jet, the absolute position of the observed VLBI core r is related with the total radiated synchrotron luminosity L_{syn} as

$$r = \left[\xi C_r L_{\text{syn}} \{\nu(1+z)\}^{-1/k_r} \right]^{1/3} \text{ pc}, \quad (5.10)$$

with

$$\xi = 1.1 \cdot 10^{-37} \frac{8}{k_e \Delta} [6.2 \cdot 10^{18} C_2(\alpha)]^{1/k_r(\epsilon+1)} \quad (5.11)$$

and

$$C_r = \frac{[B_1^{k_b} (\delta_j^\epsilon N_1 \phi_o)^{1/(\epsilon+1)}]^{1/k_r}}{\gamma_j \beta_j c B^2 \phi_o^2}, \quad (5.12)$$

where L_{syn} is in erg/s and ν is in Hz.

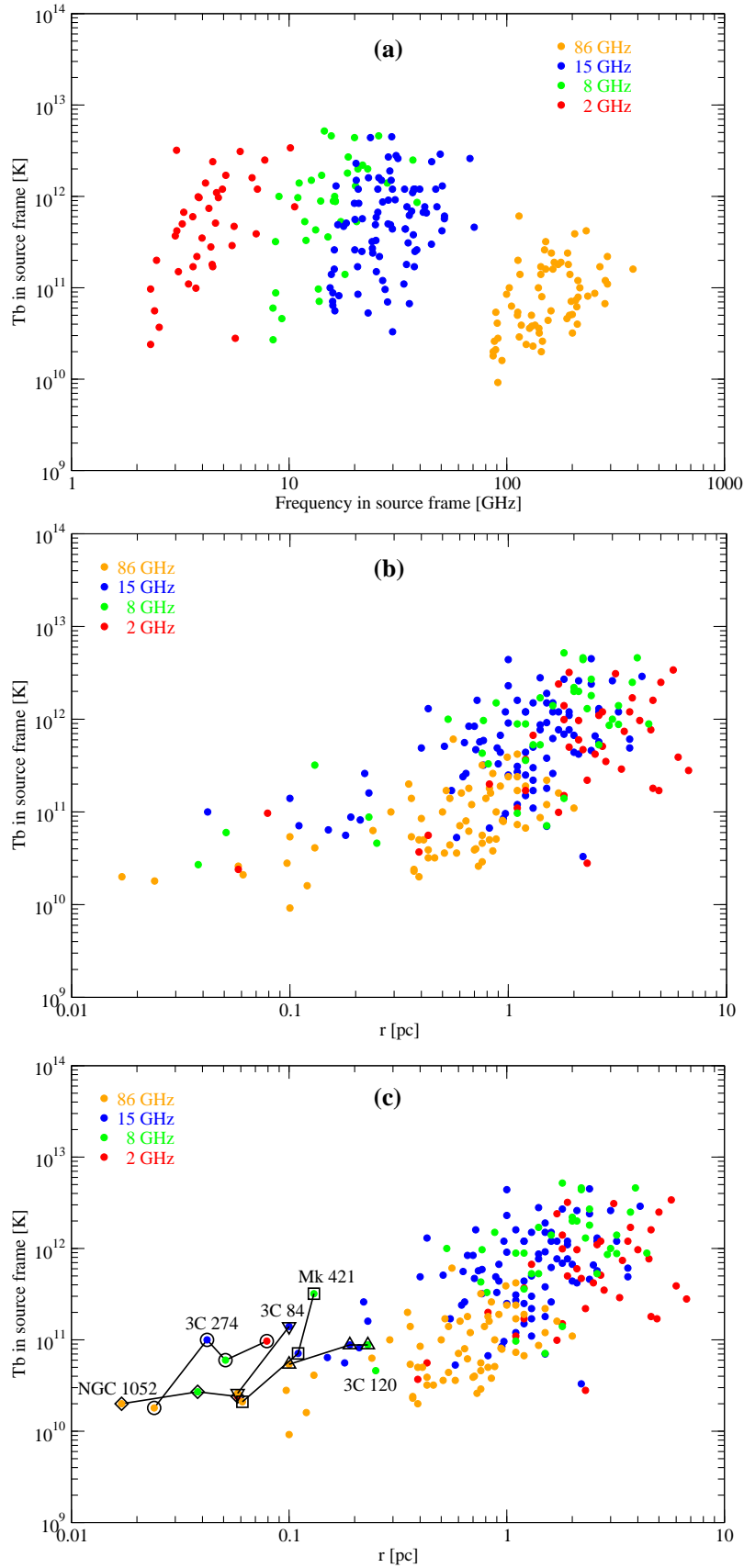


Figure 5.3: Brightness temperatures in source frame as a function of frequencies in source frame (a) and of absolute position of the VLBI core components (b,c). All available VLBI measurements (excluding lower limits) of core components at 2, 8, 15, and 86 GHz for the sources in the 3 mm-VLBI survey are used. Sources with only one measurement at one frequency and with large fitted size due to the lack of long baseline detections are excluded. The used parameters for the deduced position of the VLBI core are $\gamma_j = 10$, $\Phi_o = 1/\gamma_j^2$, $B = 1$ G, $N_1 = 5 \cdot 10^3 \text{ cm}^{-3}$, and $r_{\text{max}}/r_{\text{min}} = 100$. In panel (c), individual sources are indicated by solid lines with symbols: diamonds for NGC 1052, circles for 3C 274, triangles-down for 3C 84, triangles-up for 3C 120, and squares for Mk 421.

In order to investigate the physics of compact jets in sub-parsec scale regions, we used the VLBI core brightness temperatures at 86 GHz (this survey) and the collected brightness temperatures at lower frequencies: 2 GHz (A. B. Pushkarev & Y. Y. Kovalev, priv. comm.), 8 GHz (A. B. Pushkarev & Y. Y. Kovalev, priv. comm.), and 15 GHz (Kovalev et al. 2005). The core brightness temperatures were recalculated in the source frame, and the measurements for the lower limits were investigated to be excluded in the sample for this test. From the multi epoch measurements of the brightness temperatures at 15 GHz, we have taken the median value of them in order to take the near equipartition value (Homan et al. 2006).

Figure 5.3a shows the observed brightness temperatures in source frame T_b as a function of frequency in the rest frame of source, $\nu' = \nu_{\text{ob}}(1+z)$. One can see that in the rest frame of the source the brightness temperatures at lower frequencies between 2 and 10 GHz are increasing and start decreasing at 30 GHz. The brightness temperatures observed at 86 GHz are quite lower than those at lower frequencies (2, 8, and 15 GHz). Despite the uncertainties due to the amplitude calibration error of $20 \sim 30\%$ at 86 GHz and the source variability of a factor of ~ 2 , the brightness temperatures observed at 86 GHz are still relatively lower than those at the lower frequencies. From equation (5.9), the position of core is given as $r_{\text{core}} \propto \nu'^{-1/k_r}$. Since the reasonable choice of the combination $m = 1$, $n = 2$ gives $k_r = 1$, the position of the core is inversely proportional to the source rest frame frequency. Therefore, Figure 5.3a implies that the brightness temperature might be increasing from the innermost region ($\nu' = 400$ GHz) to the outer region ($\nu' = 10$ GHz) of the jet.

In Figure 5.3a, however, there is large scatter due mainly to the dependence of the absolute position of the core on the synchrotron luminosity of the source (see equation (5.10)). Since the particle energy and magnetic field energy densities at 1 pc, B_1 and N_1 , are different from source to source, and usually unknown, one cannot easily determine the absolute position of the core from equation (5.9) except for the case that the apparent shift of the core position at several frequencies is measured (Lobanov 1998b). Under the equipartition condition, the core position can be predicted with a known synchrotron luminosity L_{syn} by (5.10). The synchrotron luminosity can be calculated from the core flux measurements of each source over the range of rest frame frequencies, $\nu'_{\text{min}} \leq \nu' \leq \nu'_{\text{max}}$. Fitting the spectrum of the core gives the total flux of the source over the range of frequencies. Then, the synchrotron luminosity L_{syn} is given by:

$$L_{\text{syn}} = 4\pi D_L^2 F_t, \quad (5.13)$$

where D_L is luminosity distance. We use a Hubble constant $H_0 = 100 \text{ km s}^{-1} \text{ Mpc}^{-1}$ and a cosmological density parameter $\Omega_m = 0.3$. Table 5.1 lists the calculated synchrotron luminosity and the core flux density measurements at four frequencies.

Figure 5.3b shows the brightness temperatures as a function of the determined core position for all sources with core flux measurements at several frequencies. All sources are assumed to have the same Lorentz factor $\gamma_j = 10$, jet opening angle $\Phi_o = 1/\gamma_j$, and viewing angle $\theta = 1/\gamma_j$. The magnetic field in the jets are assumed to be constant $B = 1$ G, and the electron density at 1 pc is $N_1 = 5 \cdot 10^3 \text{ cm}^{-3}$. The synchrotron emission is emitting from the region with the scale factor of $r_{\text{max}}/r_{\text{min}} = 100$ at frequencies of $2 \text{ GHz} \leq \nu' \leq 400 \text{ GHz}$. As one can see in Figure 5.3c, the observed cores of sources at low redshifts are much closer to the central engine. It should be possible to investigate the formation and collimation of the jets and the environments of the central engine in those sources. We can actually see the jet collimation of 3C 274 with high frequency VLBI observations (Krichbaum et al. 2006b, 2007; Ly et al. 2007), and the evidence of the torus around the central engine in NGC 1052 (Kadler et al. 2004). As expected from Figure 5.3, the brightness temperatures are increasing from the inner region to the outer region of sub-parsec scales, which implies that the energy of the radiating particles is increasing as they are driven out from the central engine in the sub-parsec scale region of the jet.

In order to interpret the increase of the brightness temperatures along the jet, we modeled the jet with power-law functions. One single power-law does not explain the overall trend very well as shown in Figure 5.4a. Although there are few sources in the inner region $r < 0.4$ pc, the increasing pattern in the inner region looks a bit different from the one in the outer region $r \geq 0.4$ pc. Two power-law functions with restricted ranges of r can explain the trend with the improved goodness of fit as depicted in Figure 5.4b. With three power-law functions, the goodness of fit is further more improved by 50%, showing the slight decrease of the brightness temperatures in the third region $r > 2.3$ pc of the jets, as described in Figure 5.4c.

This picture matches very well with the magnetically driven, accelerating jet model by Vlahakis & Königl (2004). They argue that in the sub-parsec scale the mass flux is initially constant and then increasing, and in the outer region the mass flux gets constant again. The Lorentz factor also shows a similar trend such as being constant in the inner region and then increasing in the outer region. As the mass flux gets constant, the Lorentz factor also becomes constant in the outer region. Actually, the sub-parsec-scale accelerations of

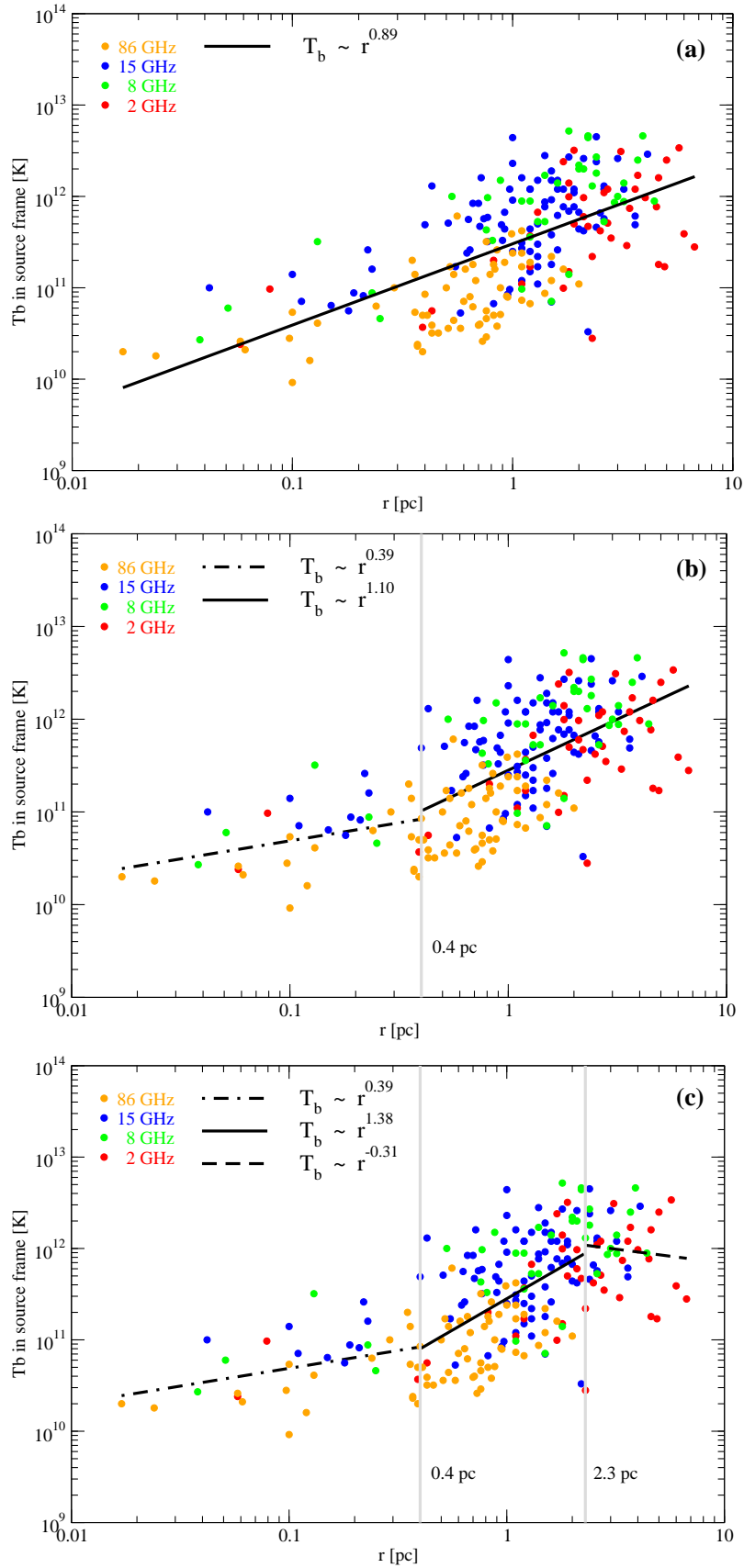


Figure 5.4: Brightness temperatures T_b as a function of core position r are fitted with one power-law function (a), two power-law functions (b), and three power-law functions (c). The power indices are shown in each panel. Grey solid lines indicate the restricted ranges of r for multiple power-law fitting.

Table 5.1: Synchrotron luminosity

Name	z	S_2 GHz (Jy)	S_8 GHz (Jy)	S_{15} GHz (Jy)	S_{86} GHz (Jy)	L_{syn} (erg s $^{-1}$)
(1)	(2)	(3)	(4)	(5)	(6)	(7)
0003-066	0.347	1.530	...	1.590	...	$9.8 \cdot 10^{44}$
0106+013	2.107	1.920	...	0.910	0.431	$1.8 \cdot 10^{46}$
0119+041	0.637	0.890	0.530	1.110	...	$2.5 \cdot 10^{45}$
0119+115	0.570	1.270	...	1.200	...	$1.9 \cdot 10^{45}$
0133+476	0.859	1.380	3.150	1.120	1.771	$9.6 \cdot 10^{45}$
0149+218	1.32	1.330	0.494	$7.6 \cdot 10^{45}$
0201+113	3.61	0.840	0.670	0.590	...	$5.4 \cdot 10^{46}$
0202+149	0.405	1.220	1.840	1.770	...	$1.2 \cdot 10^{45}$
0202+319	1.466	...	1.370	1.060	0.614	$1.0 \cdot 10^{46}$
0212+735	2.367	2.400	0.162	$1.3 \cdot 10^{47}$
0234+285	1.207	...	3.480	1.110	0.986	$1.3 \cdot 10^{46}$
0235+164	0.940	1.080	1.300	0.760	...	$1.2 \cdot 10^{45}$
0238-084	0.005	0.610	0.520	...	0.267	$2.5 \cdot 10^{40}$
0316+413	0.017	3.630	0.599	$9.1 \cdot 10^{41}$
0333+321	1.263	1.030	0.384	$5.2 \cdot 10^{45}$
0336-019	0.852	1.670	0.832	$3.8 \cdot 10^{45}$
0415+379	0.049	0.130	...	1.280	1.104	$1.0 \cdot 10^{43}$
0420+022	2.277	1.050	0.230	$2.4 \cdot 10^{46}$
0420-014	0.915	2.420	1.332	$7.0 \cdot 10^{45}$
0430+052	0.033	...	0.840	0.860	1.107	$5.6 \cdot 10^{42}$
0458-020	2.291	2.040	0.501	$4.7 \cdot 10^{46}$
0521-365	0.055	1.750	0.331	$5.1 \cdot 10^{42}$
0528+134	2.07	1.500	1.830	2.190	...	$8.2 \cdot 10^{46}$
0552+398	2.363	2.920	3.530	4.050	0.480	$5.1 \cdot 10^{46}$
0607-157	0.324	1.580	3.190	6.920	0.965	$5.4 \cdot 10^{44}$
0642+449	3.408	0.840	3.190	2.060	0.590	$1.0 \cdot 10^{47}$
0707+476	1.292	0.490	0.083	$2.3 \cdot 10^{45}$
0727-115	1.591	2.500	3.400	1.720	...	$9.7 \cdot 10^{45}$
0735+178	0.424	0.960	0.690	...	0.395	$3.5 \cdot 10^{44}$
0736+017	0.191	2.260	0.832	$1.3 \cdot 10^{44}$
0738+313	0.630	0.280	0.447	$1.0 \cdot 10^{45}$
0748+126	0.889	2.860	0.679	$5.1 \cdot 10^{45}$
0804+499	1.432	0.410	0.480	1.020	0.140	$3.3 \cdot 10^{45}$
0823+033	0.506	...	0.610	1.100	0.374	$4.7 \cdot 10^{44}$
0827+243	0.941	0.510	0.790	1.820	...	$2.8 \cdot 10^{46}$
0850+581	1.322	0.060	0.104	$1.0 \cdot 10^{45}$
0851+202	0.306	1.600	1.950	2.560	0.618	$2.7 \cdot 10^{44}$
0859+470	1.462	0.350	...	0.520	0.222	$3.6 \cdot 10^{45}$
0906+015	1.018	1.060	...	0.880	...	$4.6 \cdot 10^{45}$
0917+624	1.446	0.640	0.135	$4.1 \cdot 10^{45}$
0945+408	1.252	1.320	0.363	$6.0 \cdot 10^{45}$
1012+232	0.565	0.870	0.309	$6.0 \cdot 10^{44}$
1044+719	1.150	1.540	1.110	$5.3 \cdot 10^{45}$

Table 5.1: Synchrotron luminosity (*continued*)

Name	z	$S_{2\text{ GHz}}$ (Jy)	$S_{8\text{ GHz}}$ (Jy)	$S_{15\text{ GHz}}$ (Jy)	$S_{86\text{ GHz}}$ (Jy)	L_{syn} (erg s^{-1})
(1)	(2)	(3)	(4)	(5)	(6)	(7)
1101+384	0.031	...	0.290	0.380	0.292	$1.1 \cdot 10^{42}$
1128+385	1.733	...	0.760	0.750	0.504	$1.0 \cdot 10^{46}$
1156+295	0.729	1.220	2.420	1.790	1.629	$5.0 \cdot 10^{45}$
1219+285	0.102	0.180	0.160	0.230	0.186	$8.1 \cdot 10^{42}$
1226+023	0.158	11.78	0.828	$3.4 \cdot 10^{44}$
1228+126	0.004	1.420	1.290	1.720	1.046	$6.2 \cdot 10^{40}$
1308+326	0.997	1.140	...	3.830	0.640	$5.2 \cdot 10^{45}$
1508-055	1.191	0.620	0.503	$4.5 \cdot 10^{45}$
1511-100	1.513	0.590	0.550	$8.2 \cdot 10^{45}$
1606+106	1.226	1.900	2.460	1.040	...	$2.6 \cdot 10^{45}$
1637+574	0.751	1.740	1.145	$3.6 \cdot 10^{45}$
1642+690	0.751	0.360	0.597	$1.9 \cdot 10^{45}$
1655+077	0.621	0.580	0.780	1.170	0.462	$9.6 \cdot 10^{44}$
1739+522	1.379	0.430	0.520	1.740	0.847	$1.1 \cdot 10^{46}$
1741-038	1.057	3.010	3.960	3.580	2.404	$1.6 \cdot 10^{46}$
1749+096	0.320	1.700	...	3.210	2.375	$1.1 \cdot 10^{45}$
1800+440	0.663	0.890	0.432	$1.1 \cdot 10^{45}$
1803+784	0.680	1.270	1.510	1.130	0.785	$2.0 \cdot 10^{45}$
1823+568	0.663	0.400	0.750	2.140	0.485	$1.2 \cdot 10^{45}$
1828+487	0.692	1.270	1.183	$3.0 \cdot 10^{45}$
1901+319	0.635	0.790	0.212	$6.3 \cdot 10^{44}$
1921-293	0.352	13.11	2.069	$2.1 \cdot 10^{45}$
1928+738	0.303	0.840	0.656	$2.8 \cdot 10^{44}$
1954+513	1.223	0.560	0.279	$3.0 \cdot 10^{45}$
2037+511	1.687	1.790	0.345	$1.8 \cdot 10^{46}$
2121+053	1.941	2.090	...	2.150	0.414	$2.0 \cdot 10^{46}$
2128-123	0.501	1.650	...	0.500	...	$2.5 \cdot 10^{44}$
2200+420	0.069	1.420	1.220	2.270	...	$7.3 \cdot 10^{43}$
2201+315	0.298	2.520	0.817	$3.7 \cdot 10^{44}$
2216-038	0.901	0.290	1.430	2.020	...	$7.2 \cdot 10^{46}$
2223-052	1.404	...	3.490	3.530	0.642	$1.3 \cdot 10^{46}$
2234+282	0.795	1.800	1.220	0.230	0.405	$1.3 \cdot 10^{45}$
2255-282	0.927	0.890	5.990	5.650	...	$2.3 \cdot 10^{46}$
2345-167	0.576	1.130	1.520	0.780	...	$3.2 \cdot 10^{44}$

Notes: Column designation: 1 - source name; 2 - redshift; 3 - core flux density at 2 GHz; 4 - core flux density at 8 GHz; 5 - core flux density at 15 GHz; 6 - core flux density at 86 GHz; 7 - calculated synchrotron luminosity.

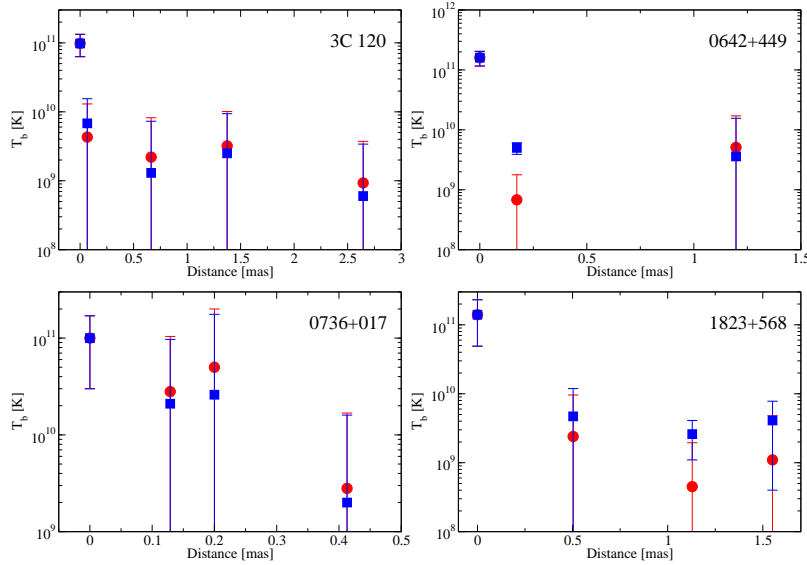


Figure 5.5: Brightness temperatures of individual emitting component in 3C 120, 0642+449, 0736+017, 1823+568. Blue squares and red triangles denote the measured and predicted values of the brightness temperatures, respectively.

relativistic AGN jets are reported in the cases of NGC 6251 (Sudou et al. 2000) with moderately relativistic speeds ($0.13c \sim 0.42c$), of Cygnus A (Bach et al. 2005) for apparent relativistic speeds ($0.2 \sim 0.5 h^{-1}c$), and of 3C 345 (Unwin et al. 1997; Lobanov & Zensus 1999) for highly relativistic speeds ($\gamma_\infty \approx 35$).

5.4 Do Jets expand adiabatically?

From the observed brightness temperatures of relativistic jets, we can investigate the adiabatic expansion of the jets. Following the argument in Marscher (1990), we assume that the individual jet component is an independent relativistic shock with adiabatic energy losses dominating the radio emission. The assumption that the jet is adiabatic leads to the following power law distribution of the relativistic electron energy:

$$N(E) = K(r)E^{-s}, [E_1(r) < E < E_2(r)], \quad (5.14)$$

where $K(r) \propto r^{-1(s+2)/3}$ and $E_{1,2} \propto r^{-2/3}$. The magnetic field falls off as $B(r) \propto r^{-a}$. The Doppler factor is assumed to be constant or varying slightly along the jet. These assumptions enable us to relate the brightness temperatures $T_{b,J}$ of the jet components to the brightness temperature $T_{b,C}$ of the core:

$$T_{b,J} = T_{b,C}(d_J/d_C)^\xi, \quad (5.15)$$

where $d_{J,C}$ are the measured sizes of the core and jet components, and $\xi = [2(2s+1) + 3a(s+1)]/6$. We have taken here $s = 2.0$ for a typical spectral index $\alpha = -0.5$ of synchrotron emission and $a = 1$ for the transverse structure of the magnetic field in the jet. The brightness temperature of the core components for all sources is used for the core. The predicted values are shown in Figure 5.5. The measured and model values of brightness temperatures agree well despite the large uncertainties, suggesting that the jet components may indeed be relativistic plane shocks.

5.5 Conclusion

Due to their highly relativistic physical environments, the compact jets of extragalactic radio sources are Doppler boosted, making it impossible to measure directly their intrinsic properties: the intrinsic brightness temperature T_0 , the Lorentz factor γ_j , and the viewing angle θ_j . Under assumptions that all jets have the same Lorentz factor and the intrinsic brightness temperature, and the jet is straight with no bends, the intrinsic parameters are simply related to the observed values: the observed brightness temperature T_b and the

apparent jet speed β_{app} . Using the method by Homan et al. (2006), we have found the intrinsic brightness temperature of $T_0 = 6.5_{-0.8}^{+1.1} \times 10^9$ K for 85 sources selected from our 3 mm-survey data. This value is less than the one found by (Homan et al. 2006) in the case of the median-low state by a factor of ~ 5 . Despite the difference in both samples, the decrease of T_0 may imply that the ultra compact cores in AGN at 86 GHz are magnetic field dominated.

The VLBI cores of the compact radio sources are optically thick at a given frequency. The distance of the core from the central engine is inversely proportional to the frequency, $r_c \propto \nu^{-1/k_r}$ (Königl 1981). Under the equipartition condition between the magnetic field energy and particle energy density, the absolute distance of the VLBI core can be predicted. From the database of VLBI surveys at lower frequencies (2, 8, 15 GHz) and our measurements, the brightness temperatures in the rest frame are investigated in the sub-parsec regions of the compact radio sources. From the vicinity of the central engine, the brightness temperatures increase slowly and then rise with steeper slope. This implies that the jets are collimated and accelerated by the magnetically driven force, as predicted by Vlahakis & Königl (2004).

The relativistic jets can be explained as a collection of relativistic shocks. As shown in Lobanov et al. (2000) the intrinsic brightness temperatures deduced by their population model differs significantly (by a factor of 2-10) between the VLBI cores and the jet components. The difference of the intrinsic brightness temperatures derived leads to the fact that the jet emission should evolve substantially already on the sub-milliarcsecond scales. The observed brightness temperatures of the jet components in our survey are in a good agreement with the predicted values of the brightness temperatures obtained from a single set of model parameters with the assumption that each of the jet components is an independent relativistic shock with adiabatic energy losses dominating the emission. The agreement can be improved by taking into account changes in the opacities and magnetic fields of the jet component.

Chapter 6

Conclusions

Studies of compact radio sources since the discovery of quasars have revealed a variety of physical properties: both in morphology and kinematics from sub-parsec to Mega-parsec scales, radiation mechanisms at frequencies from the radio to γ -rays, theoretical models for relativistic jets, etc. The frontier discovery of VLBI observations for the compact extragalactic radio sources have triggered the extensive studies to investigate the underlying physics of the relativistic jets. In this context, the highest resolution VLBI surveys of ultra-compact radio sources provides the potentially important statistical basis for future study.

There are over 100 extragalactic compact radio sources detected and imaged at sub-milliarcsecond resolution from a global 3 mm-VLBI with the largest sample at 86 GHz. A majority of them have a total VLBI flux density at 86 GHz of ≥ 0.2 Jy. Almost 70% of the sources have resolved VLBI cores with sizes of 0.02 – 0.07 mas. Most of them have flux densities of 0.2 – 1 Jy. Not all of the sources are core dominated, with some dominated by jet structures. In accordance with parsec-scale morphology, the quasars and BL Lac objects are more compact than the radio galaxies, which is in agreement with the unification paradigm of AGN. The cores of intra day variable (IDV) sources are actually more compact than non-IDV sources in angular size, and hence have higher brightness temperatures. However, we do not find any difference of compactness in sub-milliarcsecond and milliarcsecond scales for the IDV and non-IDV sources.

Modeling the visibility functions of the uv -data with simple Gaussian components gives reliable estimates of flux densities and sizes of sub-components of the compact radio sources. Taking into account the signal-to-noise ratio of the fitted model of individual components, reasonable lower limits can be determined, preventing us from estimating the intrinsic physical properties of the compact radio sources on the line of limitation. The estimated flux densities and sizes lead to the brightness temperatures of sub-components in the sources under the assumption that the individual sub-components are represented by 2-dimensional elliptical Gaussian models. The distribution of the core brightness temperatures peaks at $\sim 10^{11}$ K and only 1% have brightness temperatures higher than 10^{12} K, exceeding the inverse Compton limits. The observed brightness temperatures are relatively lower than those derived from other VLBI surveys at lower frequencies (e.g., 2, 8, and 15 GHz).

The observed brightness temperatures of sub-milliarcsecond VLBI cores enable us to investigate the intrinsic physical properties of extragalactic compact jets. Despite the Doppler boosting effect due to their relativistic environments, the intrinsic properties such as the intrinsic brightness temperature T_0 , the Lorentz factor γ_j , and the viewing angle θ_j can be related to the observed values: the observed brightness temperature T_b and the apparent jet speed β_{app} . Here we should assume that all jets have the same Lorentz factor and the intrinsic brightness temperature, and the jet is straight with no bends. The deduced intrinsic brightness temperature is $T_0 = 6.5^{+1.1}_{-0.8} \times 10^9$ K for 85 sources selected from our 3 mm-survey data. This value is less than the one found by (Homan et al. 2006) in the case of the median-low state by a factor of ~ 5 . Despite the difference in both samples, the decrease of T_0 may imply that the ultra compact cores in AGN at 86 GHz are magnetic field dominated. Under the equipartition condition between the magnetic field energy and particle energy density, the absolute distance of the VLBI core can be predicted. From the database of VLBI surveys at lower frequencies (2, 8, 15 GHz) and our measurements, the brightness temperatures in the source frame are investigated in the sub-parsec scale of the compact radio sources. From the vicinity of the central engine, the brightness temperatures increase slowly and then rise with a steeper slope. This implies that the jets are collimated and accelerated by the magnetically driven force, as predicted by Vlahakis & Königl (2004). The relativistic jets can be explained as a collection of relativistic shocks. The difference in the intrinsic brightness temperatures derived leads to the fact that the jet emission should have already evolved

substantially on sub-milliarcsecond scales. The observed brightness temperatures of the jet components in our survey are in a good agreement with the predicted values of the brightness temperatures obtained from a single set of model parameters with the assumption that each of the jet components is an independent relativistic shock with adiabatic energy losses dominating the emission.

Bibliography

- Agudo, I., Krichbaum, T. P., Bach, U., et al. 2005, astro-ph/0511268
- Alef, W. & Graham, D. A. 2002, in Proceedings of the 6th EVN Symposium, ed. E. Ros, R. W. Porcas, A. P. Lobanov, & J. A. Zensus, 31
- Alef, W., Graham, D. A., Zensus, J. A., Müskens, A., & Schlüter, W. 2000, in Proceedings of the 14th Workshop Meeting on European VLBI for Geodesy and Astrometry. Consiglio Nazionale delle Ricerche - Istituto di Radioastronomia, 2000. Edited by P. Tomasi, F. Mantovani, M. Perez Torres, ed. P. Tomasi, F. Mantovani, & M. Perez Torres
- Alfvén, H. & Herlofson, N. 1950, *Physical Review*, 78, 616
- Antonucci, R. 1993, *ARA&A*, 31, 473
- Attridge, J. M. 2001, *ApJ*, 553, L31
- Baade, W. & Minkowski, R. 1954, *ApJ*, 119, 215
- Bach, U., Kadler, M., Krichbaum, T. P., et al. 2005, in ASP Conf. Ser. 340: Future Directions in High Resolution Astronomy, ed. J. Romney & M. Reid, 30–34
- Barvainis, R. & Phillips, R. B., eds. 1997, *Millimeter-VLBI Science Workshop*
- Beasley, A. J., Dhawan, V., Doeleman, S., & Phillips, R. B. 1997, in *Millimeter-VLBI Science Workshop*, ed. R. Barvainis & R. B. Phillips, 53–56
- Beasley, A. J., Gordon, D., Peck, A. B., et al. 2002, *ApJS*, 141, 13
- Begelman, M. C., Blandford, R. D., & Rees, M. J. 1984, *Reviews of Modern Physics*, 56, 255
- Benford, G. & Lesch, H. 1998, *MNRAS*, 301, 41K4
- Bevington, P. R. & Robinson, D. K. 1992, *Data reduction and error analysis for the physical sciences* (New York: McGraw-Hill, —c1992, 2nd ed.)
- Blandford, R. D. & Königl, A. 1979, *ApJ*, 232, 34
- Blandford, R. D. & Payne, D. G. 1982, *MNRAS*, 199, 883
- Blandford, R. D. & Rees, M. J. 1974, *MNRAS*, 169, 395
- Blandford, R. D. & Znajek, R. L. 1977, *MNRAS*, 179, 433
- Blumenthal, G. R. & Gould, R. J. 1970, *Reviews of Modern Physics*, 42, 237
- Bogovalov, S. & Tsinganos, K. 2005, *MNRAS*, 357, 918
- Bower, G. C., Backer, D. C., Wright, M., et al. 1997, *ApJ*, 484, 118
- Bridle, A. H. & Perley, R. A. 1984, *ARA&A*, 22, 319
- Burbidge, G. R. 1956, *ApJ*, 124, 416
- Burbidge, G. R. & Burbidge, E. M. 1957, *ApJ*, 125, 1

- Cawthorne, T. V. 2006, *MNRAS*, 367, 851
- Celotti, A. & Fabian, A. C. 1993, *MNRAS*, 264, 228
- Clark, B. G. 1980, *A&A*, 89, 377
- Clark, B. G., Kellermann, K. I., Bare, C. C., Cohen, M. H., & Jauncey, D. L. 1968, *ApJ*, 153, L67+
- Cohen, M. H., Jauncey, D. L., Kellermann, K. I., & Clark, B. G. 1968, *Science*, 162, 88
- Cohen, M. H., Lister, M. L., Homan, D. C., et al. 2007, *ApJ*, 658, 232
- Colgate, S. A. 1967, *ApJ*, 150, 163
- Cornwell, T., Braun, R., & Briggs, D. S. 1999, in *ASP Conf. Ser. 180: Synthesis Imaging in Radio Astronomy II*, ed. G. B. Taylor, C. L. Carilli, & R. A. Perley, 151–170
- Cornwell, T. J. 1995, in *Very Long Baseline Interferometry and the VLBA*, ed. J. A. Zensus & N. P. Diamond, P., 39–56
- Cornwell, T. J. & Fomalont, E. 1999, in *Synthesis Imaging in Radio Astronomy II*, ed. G. B. Taylor, C. L. Carilli, & R. A. Perley, 187–199
- Cotton, W. D. 1995, in *ASP Conf. Ser. 82: Very Long Baseline Interferometry and the VLBA*, ed. J. A. Zensus, P. J. Diamond, & P. J. Napier, 189–208
- Curtis, H. D. 1918, *Publications of Lick Observatory*, 13, 55
- Daly, R. A. & Marscher, A. P. 1988, *ApJ*, 334, 539
- Di Matteo, T., Perna, R., & Narayan, R. 2002, *ApJ*, 579, 706
- Doeleman, S. S. & Claussen, M. 1997, in *Millimeter-VLBI Science Workshop*, ed. R. Barvainis & R. B. Phillips, 37–38
- Dunn, R. J. H., Fabian, A. C., & Celotti, A. 2006, *MNRAS*, 372, 1741
- Fadda, D., Jannuzi, B. T., Ford, A., & Storrie-Lombardi, L. J. 2004, *AJ*, 128, 1
- Falcke, H., Bower, G. C., Lobanov, A. P., et al. 1999, *ApJ*, 514, L17
- Fath, E. A. 1913, *ApJ*, 37, 198
- Fender, R., Wu, K., Johnston, H., et al. 2004a, *Nature*, 427, 222
- Fender, R. P., Belloni, T. M., & Gallo, E. 2004b, *MNRAS*, 355, 1105
- Ferrari, A. 1998, *ARA&A*, 36, 539
- Fey, A. L. & Charlot, P. 1997, *ApJS*, 111, 95
- Fey, A. L. & Charlot, P. 2000, *ApJS*, 128, 17
- Fey, A. L., Clegg, A. W., & Fomalont, E. B. 1996, *ApJS*, 105, 299
- Fomalont, E. B. 1999, in *ASP Conf. Ser. 180: Synthesis Imaging in Radio Astronomy II*, ed. G. B. Taylor, C. L. Carilli, & R. A. Perley, 301–319
- Fomalont, E. B., Frey, S., Paragi, Z., et al. 2000, *ApJS*, 131, 95
- Fomalont, E. B., Petrov, L., MacMillan, D. S., Gordon, D., & Ma, C. 2003, *AJ*, 126, 2562
- Gomez, J. L., Marti, J. M. A., Marscher, A. P., Ibanez, J. M. A., & Marcaide, J. M. 1995, *ApJ*, 449, L19
- Greiner, J., Klose, S., Reinsch, K., et al. 2003, *Nature*, 426, 157
- Greve, A. & Krichbaum, T. P., eds. 1999, 2nd millimeter-VLBI science workshop

- Gurvits, L. I., Kellermann, K. I., & Frey, S. 1999, *A&A*, 342, 378
- Heckman, T. M., Kauffmann, G., Brinchmann, J., et al. 2004, *ApJ*, 613, 109
- Henstock, D. R., Browne, I. W. A., Wilkinson, P. N., et al. 1995, *ApJS*, 100, 1
- Hey, J. S., Parsons, S. J., & Phillips, J. W. 1946, *Nature*, 158, 234
- Hirabayashi, H., Fomalont, E. B., Horiuchi, S., et al. 2000, *PASJ*, 52, 997
- Högbom, J. A. 1974, *A&AS*, 15, 417
- Homan, D. C. 2005, in *ASP Conf. Ser. 340: Future Directions in High Resolution Astronomy*, ed. J. Romney & M. Reid, 133–139
- Homan, D. C., Kovalev, Y. Y., LMister, M. L., et al. 2006, *ApJ*, 642, L115
- Homan, D. C. & Lister, M. L. 2006, *AJ*, 131, 1262
- Homan, D. C., Lister, M. L., Kellermann, K. I., et al. 2003, *ApJ*, 589, L9
- Homan, D. C. & Wardle, J. F. C. 1999, *AJ*, 118, 1942
- Homan, D. C. & Wardle, J. F. C. 2004, *ApJ*, 602, L13
- Horiuchi, S., Fomalont, E. B., Taylor, W. K., et al. 2004, *ApJ*, 616, 110
- Hoyle, F. & Fowler, W. A. 1963, *Nature*, 197, 533
- Hughes, P. A. 1991, *Beams and jets in astrophysics (Beams and Jets in Astrophysics)*
- Hughes, P. A. & Miller, L. 1991, *Introduction: synchrotron and inverse-Compton radiation (Beams and Jets in Astrophysics)*, 1–51
- Hujeirat, A., Livio, M., Camenzind, M., & Burkert, A. 2003, *A&A*, 408, 415
- Impey, C. D. & Neugebauer, G. 1988, *AJ*, 95, 307
- Jackson, J. D. 1975, *Classical electrodynamics (92/12/31, New York: Wiley, 1975, 2nd ed.)*
- Jansky, K. G. 1932, *Proceedings of the Institute of Radio Engineers*, 20, 1920
- Jennison, R. C. 1958, *MNRAS*, 118, 276
- Jorstad, S. G., Marscher, A. P., Lister, M. L., et al. 2005, *AJ*, 130, 1418
- Jorstad, S. G., Marscher, A. P., Mattox, J. R., et al. 2001, *ApJS*, 134, 181
- Jukes, J. 1967, *Nature*, 216, 461
- Junor, W., Biretta, J. A., & Livio, M. 1999, *Nature*, 401, 891
- Kadler, M., Ros, E., Lobanov, A. P., Falcke, H., & Zensus, J. A. 2004, *A&A*, 426, 481
- Kardashev, N. S. 2000, *Astronomy Reports*, 44, 719
- Kellermann, K. I. 2002, *Publications of the Astronomical Society of Australia*, 19, 77
- Kellermann, K. I. 2003, in *ASP Conf. Ser. 300: Radio Astronomy at the Fringe*, ed. J. A. Zensus, M. H. Cohen, & E. Ros, 185–192
- Kellermann, K. I., Lister, M. L., Homan, D. C., et al. 2004, *ApJ*, 609, 539
- Kellermann, K. I. & Pauliny-Toth, I. I. K. 1969, *ApJ*, 155, L71
- Kellermann, K. I. & Pauliny-Toth, I. I. K. 1981, *ARA&A*, 19, 373
- Kellermann, K. I., Vermeulen, R. C., Zensus, J. A., & Cohen, M. H. 1998, *AJ*, 115, 1295

- Klare, J., Zensus, J. A., Lobanov, A. P., et al. 2005, in ASP Conf. Ser. 340: Future Directions in High Resolution Astronomy, ed. J. Romney & M. Reid, 40–44
- Koide, S., Shibata, K., Kudoh, T., & Meier, D. L. 2002, *Science*, 295, 1688
- Komissarov, S. S. 2005, *MNRAS*, 359, 801
- Königl, A. 1981, *ApJ*, 243, 700
- Kovalev, Y. Y., Kellermann, K. I., Lister, M. L., et al. 2005, *AJ*, 130, 2473
- Kovalev, Y. Y., Petrov, L., Fomalont, E. B., & Gordon, D. 2007, *AJ*, 133, 1236
- Krichbaum, T. P., Agudo, I., Bach, U., Witzel, A., & Zensus, J. A. 2006a, ArXiv Astrophysics e-prints
- Krichbaum, T. P., Britzen, S., Standke, K. J., et al. 1995, *Proceedings of the National Academy of Science*, 92, 11377
- Krichbaum, T. P., Graham, D. A., Bremer, M., et al. 2006b, *Journal of Physics Conference Series*, 54, 328
- Krichbaum, T. P., Graham, D. A., Witzel, A., et al. 2007, *Towards the Event Horizon: High Resolution VLBI Imaging of Nuclei of Active Galaxies (Exploring the Cosmic Frontier, ESO Astrophysics Symposia European Southern Observatory, Volume . ISBN 978-3-540-39755-7. Springer, 2007, p. 189)*, 189–+
- Krichbaum, T. P., Witzel, A., & Zensus, J. A. 1999, in *2nd Millimeter-VLBI Science Workshop*, ed. A. Greve & T. Krichbaum, 5–8
- Krishan, V. & Wiita, P. J. 1994, *ApJ*, 423, 172
- Kulkarni, S. R., Djorgovski, S. G., Odewahn, S. C., et al. 1999, *Nature*, 398, 389
- Lesch, H. & Pohl, M. 1992, *A&A*, 254, 29
- Lind, K. R. & Blandford, R. D. 1985, *ApJ*, 295, 358
- Lister, M. 2003a, in *Future Directions in High Resolution Astronomy: A Celebration of the 10th Anniversary of the VLBA*, edited by J. D. Romney and M. J. Reid. Socorro, N.M. : National Radio Astronomy Observatory, 2003., p.5, 5–9
- Lister, M. L. 2003b, *ApJ*, 599, 105
- Lister, M. L. & Homan, D. C. 2005, *AJ*, 130, 1389
- Lister, M. L. & Marscher, A. P. 1999, *Astroparticle Physics*, 11, 65
- Lister, M. L. & Smith, P. S. 2000, *ApJ*, 541, 66
- Lobanov, A. 2007, *Ap&SS*, 307
- Lobanov, A. & Zensus, J. A. 2007, *Active Galactic Nuclei at the Crossroads of Astrophysics (Exploring the Cosmic Frontier, ESO Astrophysics Symposia European Southern Observatory, Volume . ISBN 978-3-540-39755-7. Springer, 2007, p. 147)*, 147
- Lobanov, A. P. 1996, Ph.D. Thesis
- Lobanov, A. P. 1998a, *A&AS*, 132, 261
- Lobanov, A. P. 1998b, *A&A*, 330, 79
- Lobanov, A. P. 2005, *A&ASubmitted (astro-ph/0503225)*
- Lobanov, A. P., Krichbaum, T. P., Graham, D. A., et al. 2000, *A&A*, 364, 391
- Lobanov, A. P., Krichbaum, T. P., Witzel, A., & Zensus, J. A. 2006, *PASJ*, 58, 253
- Lobanov, A. P. & Zensus, J. A. 1999, *ApJ*, 521, 509
- Lobanov, A. P. & Zensus, J. A. 2006, *astro-ph/0606189*

- Longair, M. S. 1981, *High energy astrophysics* (Cambridge and New York, Cambridge University Press, 1981. 420 p.)
- Lonsdale, C. J., Doeleman, S. S., & Phillips, R. B. 1998, *AJ*, 116, 8
- Lovell, J. E. J., Moellenbrock, G. A., Horiuchi, S., et al. 2004, *ApJS*, 155, 27
- Ly, C., Walker, R. C., & Junor, W. 2007, *ApJ*, 660, 200
- Lynden-Bell, D. 1969, *Nature*, 223, 690
- Maraschi, L., Ghisellini, G., & Celotti, A. 1992, *ApJ*, 397, L5
- Marscher, A. P. 1990, in *Parsec-scale radio jets*, ed. J. A. Zensus & T. J. Pearson, 236–249
- Marscher, A. P. 1995, *Proceedings of the National Academy of Science*, 92, 11439
- Marscher, A. P. 2006, in *AIP Conf. Proc. 856: Relativistic Jets: The Common Physics of AGN, Microquasars, and Gamma-Ray Bursts*, ed. P. A. Hughes & J. N. Bregman, 1–22
- Marscher, A. P. & Gear, W. K. 1985, *ApJ*, 298, 114
- McKinney, J. C. 2005, *ArXiv Astrophysics e-prints*
- Meier, D. L. 2003, *New Astronomy Review*, 47, 667
- Meier, D. L., Koide, S., & Uchida, Y. 2001, *Science*, 291, 84
- Melia, F. & Königl, A. 1989, *ApJ*, 340, 162
- Melrose, D. B. 2002, *Publications of the Astronomical Society of Australia*, 19, 34
- Meszáros, P. & Rees, M. J. 1997, *ApJ*, 482, L29
- Miley, G. 1980, *ARA&A*, 18, 165
- Miller-Jones, J. C. A., Fender, R. P., & Nakar, E. 2006, *MNRAS*, 367, 1432
- Mirabel, I. F. & Rodríguez, L. F. 1994, *Nature*, 371, 46
- Mirabel, I. F. & Rodríguez, L. F. 1998, *Nature*, 392, 673
- Mirabel, I. F. & Rodríguez, L. F. 1999, *ARA&A*, 37, 409
- Moellenbrock, G. A., Fujisawa, K., Preston, R. A., et al. 1996, *AJ*, 111, 2174
- Moffet, A. T., Gubbay, J., Robertson, D. S., & Legg, A. J. 1971, in *IAU Symposium, Vol. 44, External Galaxies and Quasi-Stellar Objects*, ed. D. S. Evans, D. Wills, & B. J. Wills, 228–+
- Moran, J. M. & Dhawan, V. 1995, in *ASP Conf. Ser. 82: Very Long Baseline Interferometry and the VLBA*, ed. J. A. Zensus, P. J. Diamond, & P. J. Napier, 161–188
- Narayan, R. & Nityananda, R. 1986, *ARA&A*, 24, 127
- Pacini, F. & Rees, M. J. 1970, *Nature*, 226, 622
- Pagels, A., Krichbaum, T. P., Graham, D. A., et al. 2004, in *European VLBI Network on New Developments in VLBI Science and Technology*, ed. R. Bachiller, F. Colomer, J.-F. Desmurs, & P. de Vicente, 7–10
- Pearson, T. J. 1995, in *ASP Conf. Ser. 82: Very Long Baseline Interferometry and the VLBA*, ed. J. A. Zensus, P. J. Diamond, & P. J. Napier, 268–286
- Pearson, T. J. & Readhead, A. C. S. 1988, *ApJ*, 328, 114
- Petrov, L., Kovalev, Y. Y., Fomalont, E., & Gordon, D. 2005, *AJ*, 129, 1163
- Petrov, L., Kovalev, Y. Y., Fomalont, E. B., & Gordon, D. 2006, *AJ*, 131, 1872

- Piran, T. 2005, *Reviews of Modern Physics*, 76, 1143
- Polatidis, A. G., Wilkinson, P. N., Xu, W., et al. 1995, *ApJS*, 98, 1
- Press, W. H., Teukolsky, S. A., Vetterling, W. T., & Flannery, B. P. 1992a, *Numerical recipes in C. The art of scientific computing* (Cambridge: University Press, —c1992, 2nd ed.)
- Press, W. H., Teukolsky, S. A., Vetterling, W. T., & Flannery, B. P. 1992b, *Numerical recipes in FORTRAN. The art of scientific computing* (Cambridge: University Press, —c1992, 2nd ed.)
- Punsly, B. 1996, *ApJ*, 473, 178
- Rantakyro, F. T., Baath, L. B., Backer, D. C., et al. 1998, *A&AS*, 131, 451
- Readhead, A., Mason, C., Moffet, A., & et al. 1983, *Nature*, 303
- Readhead, A. C. S. 1994, *ApJ*, 426, 51
- Readhead, A. C. S., Walker, R. C., Pearson, T. J., & Cohen, M. H. 1980, *Nature*, 285, 137
- Reber, G. 1940, *ApJ*, 91, 621
- Rees, M. J. 1966, *Nature*, 211, 468
- Rogers, A. E. E., Phillips, R. B., & Lonsdale, C. J. 1995, in *Bulletin of the American Astronomical Society*, 1300
- Ros, E., Zensus, J. A., & Lobanov, A. P. 2000, *A&A*, 354, 55
- Ruszkowski, M. & Begelman, M. C. 2002, *ApJ*, 573, 485
- Rybicki, G. B. & Lightman, A. P. 1979, *Radiative processes in astrophysics* (New York, Wiley-Interscience, 1979. 393 p.)
- Ryle, M. & Hewish, A. 1960, *MNRAS*, 120, 220
- Salpeter, E. E. 1964, *ApJ*, 140, 796
- Scheuer, P. A. G. & Williams, P. J. S. 1968, *ARA&A*, 6, 321
- Schmidt, M. 1963, *Nature*, 197, 1040
- Schwab, F. R. & Cotton, W. D. 1983, *AJ*, 88, 688
- Schwinger, J. 1949, *Physical Review*, 75, 1912
- Scott, W. K., Fomalont, E. B., Horiuchi, S., et al. 2004, *ApJS*, 155, 33
- Semenov, V., Dyadechkin, S., & Punsly, B. 2004, *Science*, 305, 978
- Seyfert, C. K. 1943, *ApJ*, 97, 28
- Shaver, P. A., Wall, J. V., Kellermann, K. I., Jackson, C. A., & Hawkins, M. R. S. 1996, *Nature*, 384, 439
- Shepherd, M. C., Pearson, T. J., & Taylor, G. B. 1994, *BAAS*, 26, 987
- Shklovskii, I. S. 1963, *AZh*, 40, 972
- Shu, F. H. 1991, *Physics of Astrophysics, Vol. I* (Physics of Astrophysics, Vol. I, by Frank H. Shu. Published by University Science Books, ISBN 0-935702-64-4, 429pp, 1991.)
- Sikora, M. & Madejski, G. 2000, *ApJ*, 534, 109
- Slipher, V. M. 1917, *Lowell Observatory Bulletin*, 3, 59
- Slysh, V. I. 1992, *ApJ*, 391, 453
- Stevens, J. A., Litchfield, S. J., Robson, E. I., et al. 1994, *ApJ*, 437, 91

- Sudou, H., Taniguchi, Y., Ohyama, Y., et al. 2000, PASJ, 52, 989
- Taylor, G. B., Carilli, C. L., & Perley, R. A., eds. 1999, *Synthesis Imaging in Radio Astronomy II*
- Taylor, G. B., Fassnacht, C. D., Sjouwerman, L. O., et al. 2005, ApJS, 159, 27
- Taylor, G. B., Vermeulen, R. C., Pearson, T. J., et al. 1994, ApJS, 95, 345
- Taylor, G. B., Vermeulen, R. C., Readhead, A. C. S., et al. 1996, ApJS, 107, 37
- Teräsranta, H., Tornikoski, M., Mujunen, A., et al. 1998, A&AS, 132, 305
- Thakkar, D. D., Xu, W., Readhead, A. C. S., et al. 1995, ApJS, 98, 33
- Thompson, A. R., Moran, J. M., & Swenson, G. W. 1991, *Interferometry and synthesis in radio astronomy* (Malabar, Fla. : Krieger Pub., 1991.), 47
- Tingay, S. J., Jauncey, D. L., Preston, R. A., et al. 1995, Nature, 374, 141
- Twiss, R. Q., Carter, A. W. L., & Little, A. G. 1960, The Observatory, 80, 153
- Unwin, S. C., Cohen, M. H., Pearson, T. J., et al. 1983, ApJ, 271, 536
- Unwin, S. C., Wehrle, A. E., Lobanov, A. P., et al. 1997, ApJ, 480, 596
- Urry, C. M. & Padovani, P. 1995, PASP, 107, 803
- Urry, C. M. & Treister, E. 2005, in *Growing Black Holes: Accretion in a Cosmological Context*, ed. A. Merloni, S. Nayakshin, & R. A. Sunyaev, 432–440
- Vermeulen, R. C. & Cohen, M. H. 1994, ApJ, 430, 467
- Véron-Cetty, M.-P. & Véron, P. 2006, A&A, 455, 773
- Vlahakis, N. & Königl, A. 2003, ApJ, 596, 1104
- Vlahakis, N. & Königl, A. 2004, ApJ, 605, 656
- Walker, R. C. 1989, in *ASP Conf. Ser. 6: Synthesis Imaging in Radio Astronomy*, ed. R. A. Perley, F. R. Schwab, & A. H. Bridle, 355–378
- Walker, R. C., Benson, J. M., Unwin, S. C., et al. 2001, ApJ, 556, 756
- Wardle, J. F. C., Homan, D. C., Ojha, R., & Roberts, D. H. 1998, Nature, 395, 457
- Weatherall, J. C. & Benford, G. 1991, ApJ, 378, 543
- Whitney, A. R., Shapiro, I. I., Rogers, A. E. E., et al. 1971, Science, 173, 225
- Wiita, P. J. 2006, in *Astronomical Society of the Pacific Conference Series, Vol. 350, Blazar Variability Workshop II: Entering the GLAST Era*, ed. H. R. Miller, K. Marshall, J. R. Webb, & M. F. Aller, 183–+
- Wilkinson, P. N. 1989, in *NATO Advanced Science Institutes (ASI) Series C: Mathematical and Physical Sciences, Proceedings of the NATO Advanced Study Institute on Very Long Baseline Interferometry (VLBI), Bologna, September 12-23, 1988*, Dordrecht: Kluwer, 1989, edited by Felli, Marcello; Spencer, Ralph E., ed. M. Felli & R. E. Spencer
- Xu, W., Readhead, A. C. S., Pearson, T. J., Polatidis, A. G., & Wilkinson, P. N. 1995, ApJS, 99, 297
- York, D. G., Adelman, J., Anderson, Jr., J. E., et al. 2000, AJ, 120, 1579
- Zeldovich, Y. B. 1964, Dokl. Akad. Nauk SSSR, 155, 67
- Zensus, J. A. 1997, ARA&A, 35, 607
- Zensus, J. A., Cohen, M. H., & Ros, E., eds. 2003, *Astronomical Society of the Pacific Conference Series, Vol. 300, Radio Astronomy at the Fringe*

Zensus, J. A., Cohen, M. H., & Unwin, S. C. 1995a, *ApJ*, 443, 35

Zensus, J. A., Diamond, P. J., & Napier, P. J., eds. 1995b, *Very Long Baseline Interferometry and the VLBA*

Zensus, J. A. & Pearson, T. J., eds. 1987, *Superluminal radio sources; Proceedings of the Workshop, Pasadena, CA, Oct. 28-30, 1986*

Zensus, J. A., Ros, E., Kellermann, K. I., et al. 2002, *AJ*, 124, 662

Acknowledgements

I would like to thank many people who have given me countless support and encouragements for my PhD research. I thank Prof. Dr. Uli Kein for his official support from the beginning of my PhD research. He has always kindly advised and encouraged me regarding my thesis. I also owe Priv. Doz. Dr. Walter Huchtmeier, who has given me valuable scientific comments and optimistic advise on my work. I also thank Prof. Dr. Hans Kroha and Priv. Doz. Dr. Axel Nothnagel, who agreed to my proposal for being a member of my thesis committee. I owe Arno Witzel and Anton Zensus, who received me with open arms in the VLBI group and have treated me as an equal from the beginning.

This thesis would have not happened without the encouragements of Andrei Lobanov, who has always given me the essential clues to find out a way to go through for any scientific problem during my research, and of Thomas Krichbaum, whose critiques on the observational data improved extensively this thesis; thanks to them I started working on great data from the global mm-VLBI array. I owe gratitude to Walter Alef and the correlator team, who had correlated the survey data and kindly exported the archival data when I encountered a problem on the data. I thank Alan Roy for his kind answers and comments on my questions. I owe Richard Porcas who has come to my office and asked fundamental scientific questions to fresh my astrophysical knowledge. I thank John McKeen and Dharam Vir Lal for their reading my thesis, which made the thesis more understandable. I owe my gratitude to Yuri Kovalev, who has kindly given me the brightness temperatures at lower frequencies, and commented on the brightness temperatures estimation. I also thank Manolo Perucho for his comments on the intrinsic brightness temperatures in his 'simulational' point of view.

I thank my friends in our group for their friendship during my PhD years. I thank Manolis with all my heart. He has constantly encouraged me to "keep it real". Some of his knowledge on LINUX, SHELL, etc has been very much helpful for my work, and his consult on my life has motivated myself. I will not forget what Simone has help me for. Discussion that we have had on DIFMAP and AIPS, triggered countless ideas with which I could solve the encountered problems during my PhD. I thank Violetta for her warm answers to my question on many stuffs, and many memories with her in our office. I owe Anupreeta, who gave me chances to think carefully about fundamental facts. I thank Rusen for his questions that refreshed my brain. I thank Nadia and Nicola for their contributions to my lectures in Korea and their friendship.

I would like to thank Bong Won Sohn who had helped me a lot for almost everything that I needed in the beginning of my German life and research. He has been like an "angel" for my family and me. I thank my wife, Jae-Chun, for her countless and weightless support. Her just being with me for the PhD years has been extensively encouraged me. My little, 'terrorist', Solhee has been a source of the motivation for my research. I would not forget the love and support that my parents have constantly expressed and given.

Curriculum Vitae

Sang-Sung Lee

Date and Place of Birth : 17 April 1976, Taegu, Republic of Korea

Education :

Since Dec. 2003

PhD research at the Max-Planck-Institut für Radioastronomie,
in the research division of Prof. Dr. J.A. Zensus, Bonn, Germany
Supervisors : Andrei P. Lobanov, Thomas P. Krichbaum
Topic : *A Global 86 GHz VLBI Survey of Compact Radio Sources*

Feb. 2003

M.Sc. at Astronomy Program, School of Earth and Environmental Science,
Seoul National University, Seoul, Korea
Supervisor : Yong-Sun Park
Topic: *Surface Adjustment of the SRAO 6-m Antenna based on Near-Field
Radio Holography at 86 GHz*

Aug. 1998

B.Sc. at Department of Astronomy, Seoul National University, Seoul, Korea
Supervisor : Sang-Gak Lee
Topic: *Study of Gamma Ray Bursts*

Feb. 1994

Graduation of Simin High School, Deagu, Korea

Feb. 1991

Graduation of Gamsam Middle School, Deagu, Korea

Feb. 1988

Graduation of Gamsam Primary School, Deagu, Korea

Experience

1. Research

- A Global 86 GHz VLBI Survey of Compact Radio Sources (PhD Thesis Project)
*in collaboration with A. P. Lobanov, T. P. Krichbaum, A. Witzel, J. A. Zensus (MPIfR)
A. Greve, M. Grewing (IRAM).*
- Polarization Imaging of QSO 1633+382 with VLBI at 22 GHz
in collaboration with Thomas P. Krichbaum (MPIfR) and Bong Won Sohn (KASI).
- Holographic Surface Measurement of the SRAO 6m antenna
in collaboration with Do-Young Byun (KASI), Yong-Sun Park (SRAO), Suk-Tae Han (KASI).
- CO Molecular Line Mapping around Supernova Remnant HB9
in collaboration with Bon-Chul Koo (SNU), Do-Young Byun (KASI).

- The Origin of Mixed Morphology Supernova Remnants

in collaboration with Bon-Chul Koo (SNU).

2. Observations

- **Effelsberg 100-m** : VLBI Observation assistant for Regular GMVA Sessions (2004-present)
- **Effelsberg 100-m** : VLBI Bi-Monthly Observation for 1633+382 (2004-2005)
- **SRAO 6-m** : $^{12}\text{CO}(J = 1 - 0)$ Observation around Supernova Remnant HB 9 (2002)

3. Teaching

- **Lecturer** at Kangwon University, Choonchun, Korea (Mar. 2003 – Jun. 2003)
Two lectures on **Astronomical Observation** and **Galaxy and Cosmology**

4. Schools

- **European Radio Interferometry School**, Manchester, UK, 5-9 Sep. 2005
- **Fourth IRAM Millimeter Interferometry school**, Grenoble, France, 22-27 Nov. 2004

5. Military

- Military Service as KATUSA (Korean Attached to the United States Army), Dongduchun, Korea (Jan. 1999 – Mar. 2001)